



University of Fort Hare
Together in Excellence

**Sedimentology, Petrography and Geochemistry of the Kuruman
Banded Iron Formation in the Prieska area, Northern Cape
Province of South Africa**

By

Mainly Abongile Mbongonya

(200505372)

Dissertation submitted in fulfilment of the requirements for the degree



Of
University of Fort Hare
Together in Excellence

Masters of Science in Geology

Faculty of Science and Agriculture

University of Fort Hare, Alice, South Africa

Supervisor: Prof K. Liu

January 2021

DECLARATION

I, Mainly Abongile Mbongonya, pronounce that the research reported in this thesis is my independent work except where otherwise stated. I am fully aware of the University of Fort Hare's plagiarism policy, and I have taken every precaution to comply with the regulations. Where other sources of information have been used, they have been acknowledged and appropriately referenced. The dissertation contains original study findings and has not been previously approved or concurrently submitted to any other university for a degree award or examination.

Name: Mainly Abongile Mbongonya

Signature:



At Geology Department

University of Fort Hare

Alice campus



University of Fort Hare
Together in Excellence

ACKNOWLEDGEMENTS

I would wish to acknowledge and offer appreciation to my Supervisor, Prof K. Liu, for his continued support and guidance throughout the research project, including field and laboratory studies.

I want to give my postgraduate colleague Nondumiso Ndlazi special gratitude for her assistance in performing geochemical analysis. I recognize the rest of the academic staff and postgraduate colleagues within the Department of Geology for their assistance and support during my studies. A warm appreciation to the Department of Geology, UFH, for offering strategic assistance for the span of my studies. I likewise want to express gratitude towards Govan Mbeki Research and Development Centre (GMRDC) of UFH for providing financial assistance through Supervisor linked bursary to conduct this study.

I thank Litshedzani Mutele from the Council for Geoscience for his assistance during the writing of the thesis. Last and foremost, I would like to express appreciation to my mother and sister for their adoration, prayers, support, and encouragement throughout my studies



University of Fort Hare
Together in Excellence

ABSTRACT

The sedimentary sequences hosted by the Griqualand West Basin within the Transvaal Supergroup, Northern Cape Province of South Africa, contain several iron and manganese ore deposits. Many studies have been conducted in the Griqualand West basin, particularly within the northern Ghaap plateau compartment where most iron and manganese mines are located, with less attention to the southern Prieska Compartment. Thus, the current study is targeted at the Kuruman Formation in the Prieska area to investigate the geological occurrence, including sedimentology, geochemistry, origin, and post-depositional alteration of the banded iron formation (BIF).

Four stratigraphic sections were measured, and the fifth section was only mapped for lithology and sedimentary facies. These sections constitute portions of the stratigraphic sequence of the Transvaal Supergroup that occurs within the study area. The stratigraphic sequence of the area comprises nine successional cycles with five upward fining cycles and four upward-coarsening cycles. These cycles reflect fluctuation of the sea level and shallowing- and filling-up processes of the final basin.

Four mineral paragenetic groups constituting primary minerals, diagenetic minerals, low-grade minerals, and weathering mineral assemblages were encountered in the area. The primary mineral assemblage includes magnetite, hematite, siderite, chert, quartz, and smectite. The diagenetic assemblage minerals in the area are martite, quartz (cement), illite, calcite, ankerite, and stilpnomelane. Low-grade assemblage minerals are riebeckite, crocidolite, and minnesotaite, whereas goethite, limonite, calcite (calcrete), quartz (silcrete), and clay minerals are the supergene (weathering) assemblage minerals. These mineral assemblages were confirmed by microscope petrography, XRD, SEM-EDX, and diagenesis studies.

Eight sedimentary facies including Horizontal-laminated BIF facies (Hlb), Horizontal thin to medium bedded BIF facies (Hbb), Ripple laminated BIF facies (Rlb), Thin to medium bedded mudstone facies (Mbm), Medium to thick-bedded mudstone facies (Tbm), Medium to thick-bedded fine-sandstone facies (Mts), Laminated dolomite stromatolite facies (Ld), and Dome-shaped stromatolitic BIF facies (Dbif) were identified in the field. Five facies associations including Facies association 1 (Hlb + Hbb), Facies association 2 (Hlb + Hbb + MbM + Tbm), Facies association 3 (Hlb + Hbb + MbM + Tbm + Rlb), Facies association 4 (Mbm + Tbm + Mts), and Facies association 5 (Ld + Dbif + Mts) have been recognised.

Mineralogy, petrography, and geochemical studies indicate that the studied samples have all been subjected to recent weathering that altered the primary mineralogy and the geochemical composition. Mineral assemblages of the Kuruman BIF within the Prieska area are dominated by quartz, which constitutes about 53 wt.%, followed by the iron oxides averaging about 44 wt.%. Other minerals such as carbonates and silicates are only occurring in concentrations of less than 3 wt. % combined. The Prieska BIF is enriched in cobalt, tungsten, molybdenum, barium (Ba), and nickel compared to the BIF in the northern parts of the Griqualand West basin and other localities.

Post-depositional mineral alteration studies show that most of the primary minerals had suffered various degrees of alteration. The bulk of quartz, silicate, and iron oxide minerals in the area have been recrystallized, partially replaced, dissolved, or leached out.

Multiple formation processes were involved in the origin of the banded iron formation: (1). Deposition of iron-rich mud material in the deep ocean floor and formation of a mixture of iron-rich mud (ferruginite) on the seafloor; (2). Differentiation of ferruginite and formation of disseminated iron-oxide from mud; (3). Cohesion and diagenesis of disseminated iron-oxide and formation of iron-rich (magnetite/hematite) and silica-rich (chert/quartz) patches, lenses (pod), microbands, and laminations; (4). Consolidation and compaction, leading to the formation of the final banded iron formation (BIF).

Keywords: Kuruman Formation; Banded Iron Formation (BIF); Mineral paragenesis; BIF geochemistry; Post-depositional alteration.

TABLE OF CONTENTS

DECLARATION	ii
ACKNOWLEDGEMENTS.....	iii
ABSTRACT	iv
TABLE OF CONTENTS	vi
LIST OF TABLES	xii
TABLE OF FIGURES	xiii
CHAPTER 1: INTRODUCTION	1
1.1. Background information	1
1.1.1. Types of banded iron formation	2
Algoma type	2
Superior type	2
1.1.2. Distribution in space and time	3
1.1.4. Economic significance	7
1.2. Study location.....	7
1.3. Previous studies	8
1.4. Problem statement	10
1.5. Aims and objectives.....	11
1.6. Potential impact	11
1.7. Structure of the thesis	12
CHAPTER 2: GEOLOGICAL BACKGROUND	13
2.1. Regional Geology.....	13
1.7.1. The Griqualand West Basin	15
The Ghaap Group.....	18
Asbestos Hills Subgroup.....	19
<i>Kuruman Formation</i>	21

Kliphuis Member	22
Groenwater Member.....	23
Riries Member.....	24
Ouplaas Member.....	24
1.8. Local Geology	25
CHAPTER 3: MATERIALS AND METHODS	27
3.1. Desktop Studies	27
3.2. Field investigation and sampling.....	27
3.3. Stratigraphic measurements	28
3.4. Sedimentary facies analysis	28
3.5. Laboratory analysis Methods	29
3.5.1. X-Ray Diffraction (XRD) Techniques.....	30
3.5.2. Optical Microscope Studies.....	30
3.5.3. Scanning Electron Microscope (SEM) studies	31
3.5.4. X-Ray Fluorescence (XRF) analyses.....	31
CHAPTER 4: STRATIGRAPHIC OCCURRENCES.....	32
4.1. Introduction	32
4.2. Stratigraphic section one.....	33
4.3. Stratigraphic section two.....	36
4.4. Stratigraphic section three.....	38
4.5. Stratigraphic Section four	40
4.6. Stratigraphic Section five.....	43
CHAPTER 5: SEDIMENTARY FACIES AND DEPOSITIONAL ENVIRONMENT	44
5.1. Introduction	44
5.2. Facies analysis of the Kuruman Formation.....	44
5.2.1. Horizontally laminated BIF facies (Hlb)	45
5.2.2. Horizontal thin to medium bedded BIF facies (Hbb).....	46
5.2.3. Ripple laminated BIF facies (Rlb)	47

5.2.4. Thin to medium bedded mudstone facies (Mbm)	48
5.2.5. Medium to thick-bedded mudstone facies (Tbm)	49
5.2.6. Medium to thick-bedded fine-grained sandstone facies (Mts)	50
5.2.7. Laminated dolomite stromatolite facies (Ld).....	51
5.2.8. Dome-shaped stromatolitic carbonate facies (Dbif).....	52
5.3. Facies Associations (FAs).....	53
5.3.1. Facies association 1 (FA 1, Hlb + Hbb)	54
5.3.2. Facies association 2 (FA 2, Hlb + Hbb + Mbm + Tbm).....	54
5.3.3. Facies association 3 (FA 3, Hlb + Hbb + Mbm + Tbm + Rlb).....	55
5.3.4. Facies association 4 (FA 4, Mbm + Tbm + Mts)	55
5.3.5. Facies association 5 (FA 5, Ld + Dbif + Mts)	55
5.4. Depositional environment	56
5.5. Facies model.....	57
CHAPTER 6. MINERALOGY AND PETROGRAPHY OF WEATHERED BIF	58
6.1. Mineralogy	58
6.1.1. Iron oxides	60
Hematite.....	60
Martite.....	61
Magnetite	62
Goethite.....	62
Limonite.....	63
6.1.2. Silica and silicate minerals	64
Quartz	64
Silicate minerals	65
Stilpnomelane.....	65
Riebeckite.....	66
Minnesotaite.....	67



Clay minerals.....	67
6.1.3. Carbonate minerals	68
6.2. BIF Petrography and occurrence	69
6.2.1. Iron-oxides occurrence	70
Iron oxides with chert (quartz) occurrence	70
Iron oxides with carbonate occurrence	72
Iron-oxides with silicate occurrence.....	72
6.2.2. Iron-oxide-rich bands	73
Partially ferruginous bands	73
Laminated iron oxide-rich bands.....	74
Uniform iron-rich bands	75
Patchy iron-rich bands	75
Bands with disseminated iron-rich crystals in a quartz cement	76
Highly leached iron oxide-rich bands.....	77
CHAPTER 7: GEOCHEMISTRY OF WEATHERED BANDED IRON FORMATION	79
7.1. Introduction	79
7.2. Major element geochemistry of the weathered BIF	79
7.2.1. Spider diagrams of major element compositions	81
7.2.2. Major element geochemistry relative to Kuruman BIF.....	82
7.2.3. Major element geochemistry relative to Superior-Type BIF.....	84
7.2.4. Major element scatter plots.....	86
7.3. Trace element geochemistry of the weathered BIF	87
7.3.1. Trace element spider diagrams	90
7.3.2. Trace element geochemistry relative to Kuruman BIF	91
7.3.3. Trace element geochemistry relative to Superior-Type BIF	93
7.2.4. Trace element scatter plots	95
7.4. Source area weathering	97

CHAPTER 8: POST-DEPOSITIONAL ALTERATION	102
8.1. Introduction	102
8.2. Diagenesis	102
8.2.1. Mineral cohesion and growth	103
8.2.2. Mechanical and chemical compaction	104
8.2.3. Pore spaces and pore network	106
8.2.4. Mineral overgrowth	107
8.2.5. Cementation.....	108
Hematite cement.....	108
Goethite cement.....	109
Quartz cement	110
Clay cement.....	110
8.2.6. Authigenic minerals	111
8.2.7. Recrystallization	112
8.2.8. Mineral replacement	115
Hematite replacement	115
Goethite replacement	117
Quartz replacement.....	119
8.2.9. Dissolution.....	120
8.2.10. Tectonic overprint	122
8.3. Supergene modification- surficial weathering and oxidation	122
8.3.1. Field observations	123
8.3.2. Petrographic evidence	124
8.4. Mineral paragenesis	126
8.4.1. Primary mineral assemblage.....	127
8.4.2. Diagenetic mineral assemblage	128
8.4.3. Low-grade metamorphic assemblage.....	130



8.4.4. Weathering mineral assemblage	131
8.5. The origin and formation process of the BIF	132
CHAPTER 9: DISCUSSIONS AND CONCLUSION	134
9.1. Discussion	134
9.2. Conclusions	138
9.3. Recommendations.....	139
REFERENCES	141
APPENDIX I	161
A. Approximate mineral abundances based on XRD results	161
B. Photomicrographs of the samples.....	162
APPENDIX II.....	166
A. Average major element chemical composition of the samples against published average data	166
B. Average trace element composition of the samples against published data	167
C. Scatter diagrams	168
D. Weathering Index of Parker (WIP).....	169



University of Fort Hare
Together in Excellence

LIST OF TABLES

Table 1.1: Table showing the thesis structure.	12
Table 2. 1: Simplified stratigraphy of the Transvaal Sequence in the Griqualand West Basin	16
Table 2. 2: A simplified stratigraphy of the Kuruman Formation	22
Table 5. 1: Summary of sedimentary facies and their respective depositional environments.	57
Table 6. 1: Major minerals of the weathered Kuruman BIF outcrops in the Prieska area identified by XRD, optical microscopy, and SEM-EDX analysis.....	58
Table 6. 2: Table of mineral abbreviations.....	59
Table 7. 5: Whole-rock trace element compositions of the BIF expressed in parts per million (ppm).	89
Table 7. 6: Summary of the trace element compositions of the Prieska BIF (in ppm) compared with the average compositions of the published Kuruman BIF and Superior-Type BIF.....	91
Table 7. 7: The normalized trace element values of the weathered Prieska BIF using Kuruman BIF averages	92
Table 7. 8: The normalized trace element values of the weathered Prieska samples using Superior-Type BIF averages.....	94
Table 7. 9: Chemical weathering indices and their respective calculation formulas.....	98
Table 7. 10: Weathering indices of the samples.	99



University of Fort Hare
Together in Excellence

TABLE OF FIGURES

Figure 1. 1: Distribution of BIFs across geological time and hosting countries.	4
Figure 1. 4: Map showing the Prieska study area	8
Figure 2.1: Regional geology map showing the distribution of the Basins of the Transvaal Supergroup.....	14
Figure 2.2: Geological map showing stratigraphic and structural occurrences in the Griqualand West Basin.....	17
Figure 4. 1: Google earth map showing the location of the five stratigraphic sections.	33
Figure 4. 2: Field photographs showing (A) Deformed and folded formation containing dark iron-rich (red arrows) layers alternating with brownish chert and carbonate layers.	34
Figure 4. 3: Field photograph displaying intense differential weathering and folding.....	34
Figure 4. 4: Measured Stratigraphic Section 1.	35
Figure 4. 5: Field photograph showing (A) dark magnetite and reddish hematite microbands	36
Figure 4. 6: Measured Stratigraphic Section 2.....	37
Figure 4. 7: Field photographs showing a weathered and deformed hematite (black arrows), limonite, and goethite-rich (red arrows) formation.....	38
Figure 4. 8: Measured Stratigraphic Section 3.	39
Figure 4. 9: Field photographs showing a	40
Figure 4. 10: Field photograph displays (A) Highly deformed BIF and mudstone formation	41
Figure 4. 11: Measured Stratigraphic Section 4.	42
Figure 4. 12: Field photographs showing a thin to medium bedded BIF.....	43
Figure 5. 1: Field photograph from section one illustrating the horizontal laminated BIF facies of the Kuruman Formation in Prieska.	46
Figure 5. 2: Field photograph illustrating the horizontal thin to medium bedded BIF facies of the Kuruman Formation in Prieska.	47
Figure 5. 3: Field photograph from section four showing a ripple laminated, weathered brownish BIF	48
Figure 5. 4: Field photograph illustrating the thin and medium bedded mudstone of the Kuruman Formation	49
Figure 5. 5: Field photograph illustrating the thick-bedded mudstone facies of the Kuruman Formation in Prieska	50

Figure 5. 6: Field photograph illustrating the fine sandstone facies of the Kuruman Formation in Prieska	51
Figure 5. 7: Field photograph illustrating laminated dolomite stromatolite facies of the Kuruman Formation in Prieska.....	52
Figure 5. 8: Field photograph illustrating the dome-shaped bio-carbonate facies (red arrows) of the Kuruman Formation in Prieska.	53
Figure 5. 9: Field photograph from section one illustrating the FA1	54
Figure 5. 10: Field photograph illustrating FA5	56
Figure 5. 11: Depositional model of the Kuruman Formation in the Prieska area	57
Figure 6. 1: Variation diagram showing the mineral types and abundances of the weathered Kuruman BIF in the Prieska area.....	59
Figure 6. 2: Reflected light photomicrographs showing porous microcrystalline hematite ...	61
Figure 6. 3: Reflected light photomicrographs showing a massive, less porous martite (Mat) with goethite (Gth)	61
Figure 6. 4: Reflected light photomicrographs showing (A) Martitizing grains containing magnetite (Mag) at the centre and rims of specular hematite (Hem) at the grain boundaries;	62
Figure 6. 5: Reflected light photomicrographs showing (A) Porous goethite (Gth) crystals..	63
Figure 6. 6: Transmitted light photomicrograph (A) and SEM photomicrograph (B) showing detrital quartz (Qz) grains occurring with hematite (Hem).	64
Figure 6. 7: SEM-EDX photomicrograph showing quartz (Qz) grains	65
Figure 6. 8: Transmitted light photomicrographs showing stilpnomelane (Stp, red-brownish) and quartz (Qz) occurrence.....	66
Figure 6. 9: Transmitted light photomicrographs showing blueish riebeckite (Rbk), whitish quartz, pinkish calcite (Cal), and dark magnetite (Mag) crystals.	67
Figure 6. 10: SEM-EDX photomicrograph showing the occurrence of iron-oxide.....	68
Figure 6. 11: Transmitted light (A) and reflected light (B) photomicrographs showing rhombic iron-oxide (hematite) pseudomorphs	69
Figure 6. 12: Transmitted light photomicrographs showing (A) Iron oxide (Mag, dark area) subordinate grains and minor iron silicates in quartz-rich mesoband.....	71
Figure 6. 13: Transmitted light photomicrographs showing the dark iron oxide-rich (Hem) and white chert/quartz-rich (Qz) micro and mesobands.	71
Figure 6. 14: Reflected light photomicrographs showing (A) A dull, porous band consisting of the iron minerals mixed with silicate minerals (mud) and chert (Qz). There are also various sized hematite-rich patches and isolated grains (Hem); (B) Porous, loose disseminated hematite	

(Hem) grains at the top alternating with hematite-rich lamination and the mixed band of iron minerals, silicate, and chert (quartz) at the bottom. These bands have been cross-cut by a later quartz vein.	72
Figure 6. 15: Reflected light photomicrographs showing (A) Horizontal to wavy contacts between iron oxide-rich (whitish) and quartz-rich (dark) microbands	73
Figure 6. 16: Reflected light photomicrographs showing (A) Magnetite-rich (Mag) band at the centre alternating with quartz-rich (Qz) band and hematite-rich (Hem) at the bottom	74
Figure 6. 17: Reflected light photomicrographs showing a massive less porous martite (Mat) forming a uniform iron-rich band.	75
Figure 6. 18: Reflected light photomicrographs showing (A) Porous microcrystalline	76
Figure 6. 19: Reflected light photomicrographs showing (A) Disseminated porous hematite (Hem) and porous goethite (Gth) crystals	77
Figure 6. 20: Reflected light photomicrograph showing porous goethite (Gth) occurring with subhedral to euhedral magnetite (Mag) grains	78
Table 7. 1: Major elemental variation of the samples expressed in weight percentages (wt. %).	80
Figure 7. 1: Major element variation diagram of the weathered Prieska BIF samples.	81
Table 7. 2: Summary of the major element compositions compared with the Kuruman BIF and Superior Type BIF's average compositions by Gutzmer et al. (2008) and McClung (2006), .	82
Table 7. 3: The normalized major element values of the samples using Kuruman BIF protolith averages	83
Figure 7. 2: Spider plot of major elements composition, normalized against Kuruman BIF .	84
Table 7. 4: The normalized values using Superior-Type BIF averages	85
Figure 7. 3: Spider plot of major element compositions for the weathered Prieska BIF normalized against Superior-Type BIF	85
Figure 7. 6: The variation bar diagram showing trace element concentrations of the weathered BIF in the Prieska area.	90
Figure 7. 7: Kuruman BIF normalized trace element distribution of the weathered Prieska samples.	93
Figure 7. 8: Superior-Type normalized trace element distribution of the weathered Prieska samples.	95
Figure 7. 9: Trace element scatter plots showing positive relationships.	96
Figure 7. 10: Cross-plots displaying negative correlations between the trace elements.	97
Figure 7. 11: A variation diagram showing CIA and CIW intensities across the samples. ..	100

Figure 7. 12: The CIA against the Al ₂ O ₃ plot shows the samples' weathering intensity	101
Figure 8. 1: Transmitted light photomicrograph (A) showing original sediment mix of iron-oxide, chert (quartz) and mud material	104
Figure 8. 2: Photograph showing grain to grain contact patterns influenced by burial depth	105
Figure 8. 3: Transmitted light photomicrograph showing the long contacts (orange arrows) and concave-convex contact patterns (red arrows) of the quartz grains in a chert-rich band.....	106
Figure 8. 5: Reflected light photomicrographs showing	108
Figure 8. 6: Transmitted light photomicrograph showing hematite (Hem) cement (dark areas) around the quartz grains in a quartz-rich band	109
Figure 8. 8: SEM-EDX photomicrograph showing the detrital quartz grains (Qz, point 1 and 3 at the top right and lower right), matrix, and cement.....	111
Figure 8. 9: Reflected light (A) and transmitted light (B) photomicrographs showing authigenic martite (Mat) with subhedral to euhedral crystalline shapes	112
Figure 8. 10: Transmitted light photomicrographs showing (A) different quartz sizes and shapes.	113
Figure 8. 11: Transmitted light photomicrograph showing horizontal and vertical quartz veinlets related to recrystallization during diagenesis.	113
Figure 8. 12: Textural generations of the iron oxides that form BIFs	114
Figure 8. 13: Reflected light photomicrograph showing the inner magnetite/kenomagnetite and outer hematite in the martitising bands.	116
Figure 8. 14: Transmitted light (A) and reflected light photomicrographs (B) showing (A) Hematite (Hem) pseudomorphs of carbonate minerals in the quartz-rich mesoband.....	117
Figure 8. 15: Reflected light photomicrographs showing goethite replacing magnetite/kenomagnetite in the martitising bands	118
Figure 8. 16: Reflected light photomicrograph showing the replacement of the rhomb-shaped carbonate minerals by goethite.	119
Figure 8. 17: Reflected light photomicrograph showing the replacement of the rhombic-shaped carbonate minerals by quartz (rhomb shapes shown by red arrows).	120
Figure 8. 18: SEM-EDX photomicrograph showing a dissolution hole filled with quartz. It is also showing the remains of the micropores	121
Figure 8. 19: Transmitted light (A) and reflected light (B) photomicrographs showing (A) microcrack filled with fine hematite	121
Figure 8. 20: Reflected light photomicrographs showing (A) Broken kink folds	122

Figure 8. 21: Field photographs showing a weathering formation consisting of leaching carbonate minerals (carb), calcrete (white area), and limonite (reddish-brown area on B).. 123

Figure 8. 22: Field photographs showing (A) Original dark BIF gradually changes to yellowish goethite-hematite after weathering..... 124

Figure 8. 23: Reflected light photomicrograph showing (A) highly leached vuggy microband with pore-filling secondary martite (Mat) and fibrous goethite (Gth) in the supergene zone 125

Figure 8. 24: Reflected light photomicrograph showing (A) weathering of magnetite to form goethite (Gth)..... 126

Figure 8. 25: Mineral paragenetic assemblages of the Kuruman BIF the in Prieska area. ... 127

Figure 9. 1: Comparison of major element average compositions between Prieska BIF, Kuruman BIF 166

Figure 9. 2: Average trace element variations between Prieska BIF, Kuruman protolith 167



University of Fort Hare
Together in Excellence

CHAPTER 1: INTRODUCTION

1.1. Background information

Banded Iron Formations (BIFs) are very fine-grained chemical sedimentary rocks containing iron carbonates, iron oxides, and iron silicates in their mineral assemblage (James, 1954; Trendall & Blockley, 1970; Thorne et al., 2008). They are finely laminated to thinly bedded (James, 1954, 1966; Isley & Abbott, 1999), with about 15% or more iron content and silica (greater than 40%) proportion (Woodward & Knoll, 2009). The mm to cm-scale iron-rich and iron-poor meso and microbands are alternating (Isley, 1995; Spier et al., 2007; Rasmussen et al., 2014). Hematite, subordinate magnetite, sometimes siderite, pyrite, iron silicates, and quartz are the typical mineral constituents of the BIF (Hagemann et al., 2008; Pecoits et al., 2009; Evans et al., 2013; Bolarinwa, 2018).

The BIFs were formed within the continental crusts that have been stable since the Precambrian time. They were deposited in the marine environment during the Archean and Early Paleoproterozoic Periods (Trendall, 2002; Simonson, 2003; Klein, 2005; Beukes & Gutzmer, 2008; Bekker et al., 2010). The majority of the Archean BIFs are deformed, metamorphosed, and associated with greenstone belts (Klein, 2005), making their basinal setting' reconstruction difficult. Conversely, the Paleoproterozoic BIFs such as the Transvaal Supergroup of South Africa are less deformed and metamorphosed and allowing for proper evaluation of the original basinal setting (Klein, 2005).

The formation and depositional environments of the iron and related minerals have been extensively researched and debated, although the early studies supported terrestrial weathering as the source of iron. Garrels et al. (1973; 1987) proposed that the BIFs were generated from the aqueous Fe^{2+} originated from the weathering of land rocks transported to the ocean by fluvial systems. On the other hand, Holland (1973, 1984) proposed that the Fe^{2+} was released into deep seawater from the ocean-floor sediments, transported for large distances by the upwelling bottom current to the shallower parts of the oceans such as continental shelves, oxidized by the dissolved O_2 , and deposited as ferric hydroxides. Jacobsen and Pimentel-Klose (1988) argued that the Fe^{2+} is hydrothermal in origin based on the Nd isotopes data.

1.1.1. Types of banded iron formation

The Algoma and the Superior types are the two currently used BIF classes (Gross, 1965). These classes are distinguished based on their tectonic setting, mineralization, size, and lithological associations (Gross, 1965).

Algoma type

BIFs of the Algoma-type are relatively small with less than 10 km lateral extents and thicknesses of 10 to 100 m (Gross, 1965; Goodwin, 1973; Appel, 1980; Condie, 1981). They are commonly associated with the Archean greenstone belts (Isley & Abbott, 2009) and are typically highly deformed due to mid to high regional tectonic movement and metamorphism (Klein, 2005). They were deposited in active tectonic settings and consist of large volcanic components (Gross, 1965; Goodwin, 1973; Appel, 1980; Condie, 1981; Miyano, 1982; Miyano & Beukes 1984). The volcanic components commonly comprise magnesium and iron-rich mafic to ultramafic units (Isley & Abbott, 2009). The mafic component consists of pillow lavas. The geochemistry of the Algoma type BIFs also reflects high-temperature hydrothermal activity associated with mid-ocean ridge crests and back-arc basins (Isley & Abbott, 2009). They usually grade into volcanogenic massive sulfide deposits and contain remnant hydrothermal chimneys (Isley & Abbott, 2009).

Superior type

The deposition of the Superior-type BIFs took place between 2.7 and 1.8 Ga, with the peak occurring in 2.5 Ga. The peak deposition represents some of the world's major BIF-hosting sequences, such as the Hamersley Group in Australia and Transvaal Supergroup in South Africa (Klein, 2005). The Superior type deposits are vast and laterally extensive compared to the Algoma-type and are associated with passive continental settings (Gross, 1965; Beukes & Gutzmer, 2008). Most of these deposits have above 100 m thicknesses, with the largest extending over 105km² (Trendall & Blockley, 1970; Beukes, 1973).

The Superior type BIFs have variable depositional environments, such as the Archean Pongola BIF (~2.9 Ga) forming on the continental shelf (Isley & Abbott, 2009). Other BIFs like the Labrador Trough formed in foreland basins, whereas the Brockman Super sequence of the Hamersley Basin was formed in back-arc basins (Isley & Abbott, 2009).

The Superior-type BIFs display granular or oolitic textures indicating the deposition above the wave base. The sedimentary units accumulated below the wave base show a banding thickness ranging from a few millimetres to tens of meters (Isley & Abbott, 2009). The Superior-type BIFs are distinguished by their general lack of deformation and are related to lithologies like the platform carbonates, carbonaceous shales, and quartz-arenites (Beukes & Gutzmer, 2008).

1.1.2. Distribution in space and time

The BIF distribution in time and space is much punctuated (Beukes & Gutzmer, 2008).

They occur periodically and are abundant across 3.8 - 2.5 Ga geological records (James, 1954; Gross, 1965; Trendall, 1968; James & Trendall, 1982 Klein & Beukes, 1992; Cisne, 1984; Klein, 2005). However, BIFs are absent or scarce in the Mesoproterozoic time but make a brief re-appearance in the Neoproterozoic era, closely associated with glaciogenic deposits (Klein, 2005) (Fig. 1.1). Their global volume is largest around 2.5 Ga and diminishes approximately 1.8 Ga, and they reappear between 0.8 and 0.6 Ga. (Klein, 2005). The 2.5 Ga Transvaal supergroup that hosts the Kuruman Formation of the Griqualand West basin contains some enormous BIF sequences of the world (Beukes, 1983; Klein & Beukes, 1992). The other well-known BIF occurrences are the 3.8 Ga (Isua, West Greenland), 2.5 Ga (Hamersley Province, Western Australia), 2.2-2.0 Ga (Superior-Labrador Trough), and 0.7 Ga (Rapitan) (Trendall & Blockley, 1970; Klein & Beukes, 1992; Barley et al., 1999) (Fig 1.1). The Archean iron formations are mostly found in greenstone belts, while the late Neoproterozoic-Paleoproterozoic iron formations are associated with cratonic sedimentary successions. The Witwatersrand successions contain some of the only known Mesoarchean iron formations (Smith, 2007).

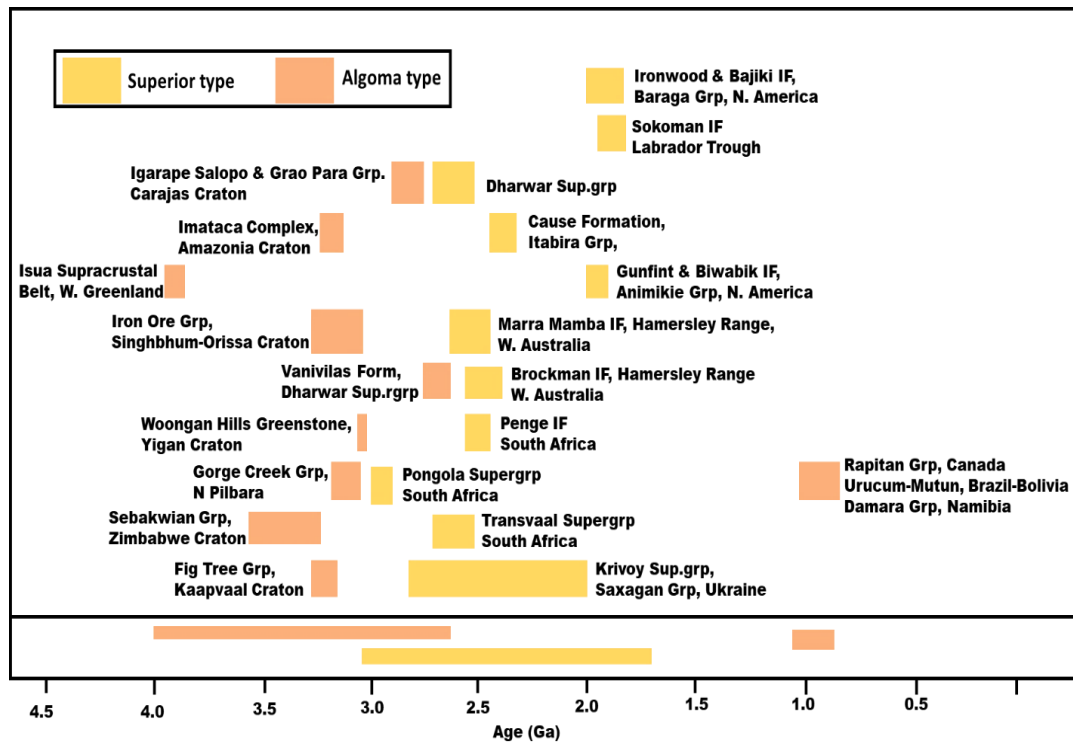


Figure 1. 1: Distribution of BIFs across geological time and hosting countries. Note that the Algoma type occurs between 3.9 and 2.6 Ga and then again from 1.0 to 0.85 Ga. The Superior type occurs from 1.7 to 3.0 Ga. (After Koehler et al., 2010).

1.1.3. Mineralization

The high-grade (greater than 60wt% iron) ore deposits hosted in the BIFs result from the enrichment of the iron formation host rock. The enrichment was facilitated by supergene processes, hydrothermal activities, and a combination of the two processes. The enrichment of the BIFs resulted in the global existence of three major types of high-grade BIF-hosted iron ore deposits. These major deposit types are enriched by silica (quartz) leaching from the BIF host rock or replacement of silica by iron oxide minerals (hematite or magnetite) or a combination of both (Gutzmer et al., 2008). The BIF-hosted deposits of the Maremane Dome in the Northern Cape Province of South Africa are the prime example of the supergene deposit (Van Schalkwyk & Beukes, 1986; Beukes et al., 2003; Dalstra & Rosiere, 2008, Gutzmer et al., 2008). A typical example of the hydrothermal iron deposit in South Africa was mined in Thabazimbi (Beukes et al., 2003; Gutzmer et al., 2008). The supergene-modified hydrothermal examples include the

Quadrilatero Ferrifero of Brazil (Rosiere et al., 2008) and India (Beukes et al., 2008; Mukhopadhyay et al., 2008) (Fig. 1.2).



Figure 1. 2: Global distribution of significant high-grade iron deposits. (Adopted from Hagemann et al., 2015). Circle sizes indicate the size of mineral resources contained in the respective districts. The iron grade is indicated by the cumulative length of the bar graphs beneath each locality.

The Griqualand West basin in the Northern Cape Province is a host to many ore deposits such as copper, zinc, diamonds, manganese, and iron ore (Fig. 1.3). The majority of these ore deposits have been exploited from the northern Ghaap Plateau basin compartment, which supplies the world with iron and manganese ores. The iron ore is mainly extracted through open cast mining. The iron ore's open cast mining indicates that the iron ore is shallow and has been massively affected by supergene processes and surficial weathering. The recovered friable, porous, or goethite-rich supergene modified ores occur as laminated, massive, brecciated, and conglomeratic ore types (Van Schalkwyk & Beukes, 1986; Carney & Mienie, 2003; Alchin et al., 2008; Chisonga, 2012). Hydrothermal ores are also BIF-hosted and show laminated, massive, and brecciated texture (Netshiozwi, 2002). The laminated ore from both the supergene and hydrothermal ores was formed by enriching the microbanded BIF (ferhythmite).

The massive ores represent the enriched clastic-textured muddy BIF (lutite) (Beukes & Gutzmer, 2008). The ores mostly comprise fine-grained, compact microplaty hematite aggregates that occur in lathlike and tabular texture. The hematite form patches, and it occurs as magnetite pseudomorphs (martite) and replacement of iron-rich carbonates. Variable textural hematite types are encountered with the massive iron ore. The laminated ore comprises alternating bands of microplaty hematite and martite. Bands with ample microplaty hematite occasionally contain voids. The hematite plates are commonly randomly orientated and can be bedding parallel. Other minerals present include minor quartz and rare micas, clays, and apatite. Brecciated ore consists of laminated and massive ore angular blocks set in a fine-grained hematite and quartz matrix. Conglomeratic ore comprises subrounded to angular clasts of laminated and massive ore in a muddy, hematite-rich matrix. Specularite veinlets comprise coarser-grained microplaty hematite (specularite) in random orientations, along with major quartz and calcite in some cases, and crosscut the underlying oxidized BIF and the ore. They are common in brecciated ore. The southern Prieska compartment's mineral potential has not yet been fully recognized, although the largest global blue asbestos (crocidolite) deposits were previously recovered from the area (Beukes, 1980).

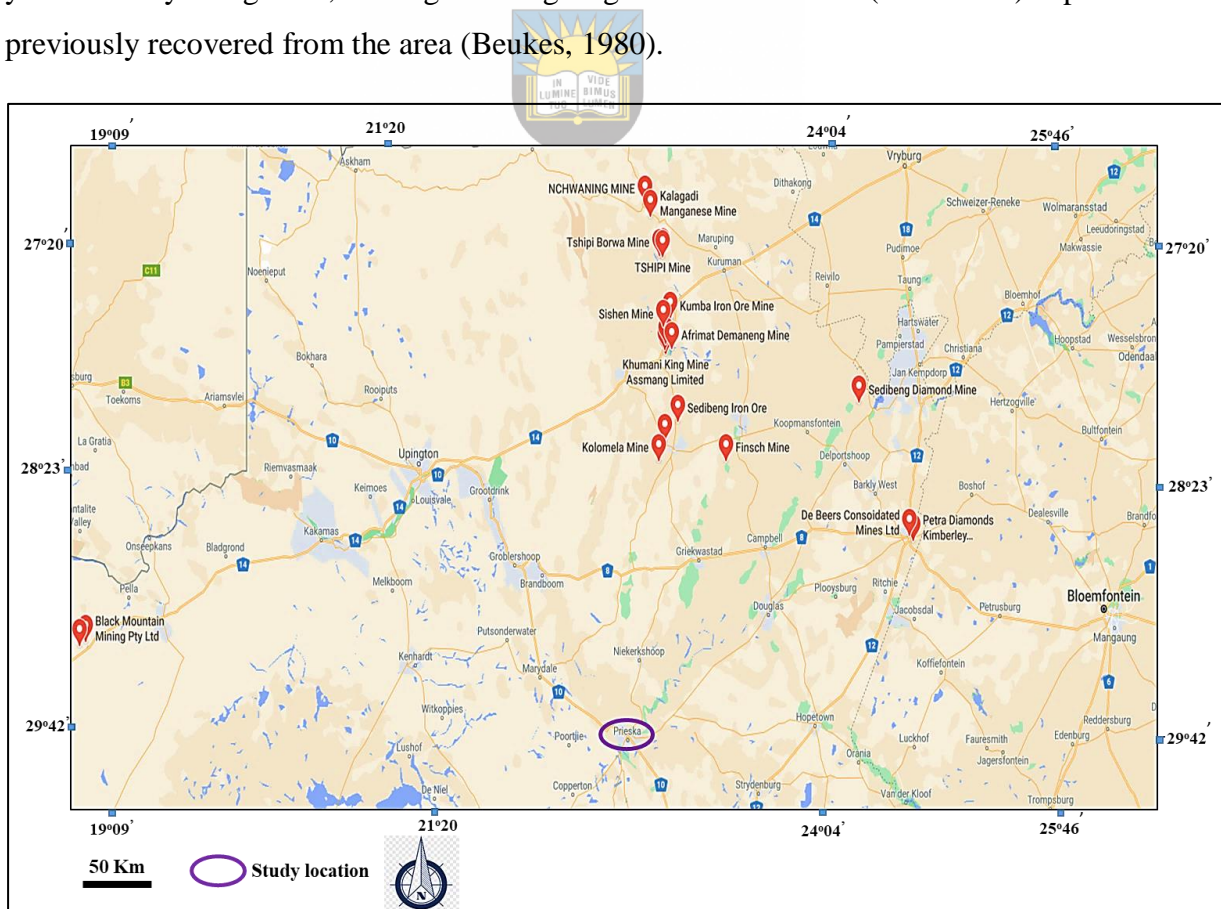


Figure 1. 3: Map showing the distribution of different mines in the Griqualand West basin, Northern Cape Province (Modified from Google maps).

1.1.4. Economic significance

Banded iron formations (BIF) are a critical source of iron because they host most of the world's significant iron deposits and are extensively distributed within large sedimentary basins (Meyer, 1985; Trendall, 2002; Dalstra & Flis, 2008; Li et al., 2015). These iron formations generally comprise 25 to 35 % of total iron (Lewy, 2011, Evans et al., 2013). The enriched BIF-derived higher-grade iron ore bodies containing 58–69 wt % Fe form one of the major single metal concentrations in the Earth's crust (Hagemann et al., 2007). Their iron content and economic value are improved by alteration processes like post-depositional alteration and supergene modifications, promoting intensive chemical and sedimentological research of the altered sequences to reconstruct their origin (Lewy, 2011). Furthermore, iron ore has been mined and smelted across South Africa, with a high concentration pronounced in the Northern Cape Province (Taylor et al., 1988). The small iron ore mining was mainly for specular hematite used to manufacture body paint and smelting purposes. Extensive local iron ore mining took place in Thabazimbi, where about 400 tons of ore was extracted (Taylor et al., 1988). South Africa became the seventh world's largest iron ore producer in 2014, with the size of its BIF-hosted high-grade iron ore deposits globally significant with high economic value (USGS, 2015). In addition to their economic potential, the BIFs are also essential for understanding the ocean and atmosphere's chemical evolution, especially the atmosphere's oxygen level during Precambrian time (Dimroth, 1975; Holland, 1984, Bau, 1993; 1999; Ohmoto, 1997).

1.2. Study location

The investigation was carried out along the N10 road cuts from Prieska towards Marydale in the Northern Cape Province of South Africa (Fig. 1.4). It geographically lies between 29°41'50.26"S (latitude) and 22°44'14.24"E (longitude) at an elevation of about 960m. The study area's climatic conditions are temperate to semi-arid with humid and hot summer and dry and cold winter seasons.

The Prieska study area is tectonically located on the Kaapvaal craton's margin on the east of the Namaqua Natal province and south-east of the Kheis Province (Fig. 1.4). The research targeted the well-exposed Kuruman Banded Iron Formation, Griqualand West Sequence of the

Transvaal Supergroup (see Chapter 2). The outcrops' exposure quality and accessibility along road N10 between Prieska and Marydale are considerably better than private farms and game reserves.

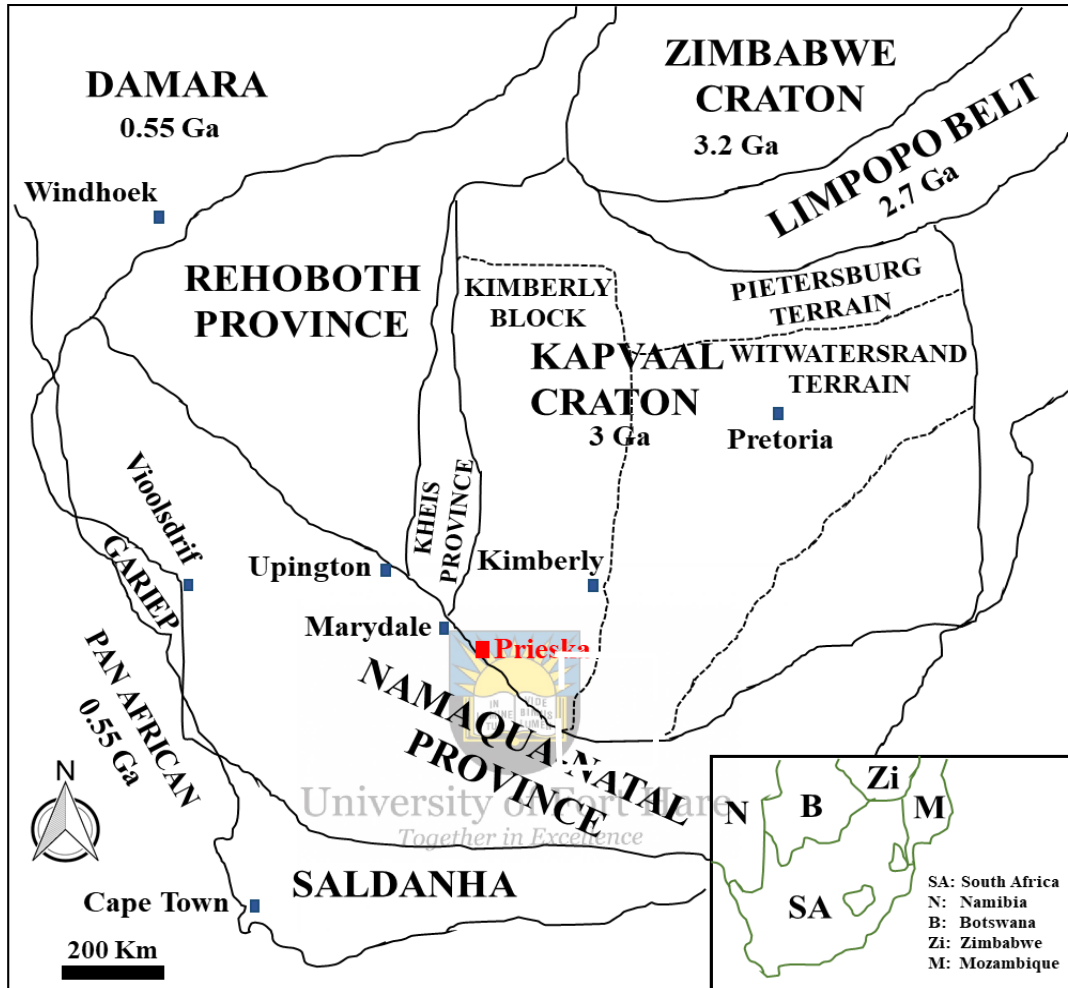


Figure 1. 4: Map showing the Prieska study area (Highlighted in red) (Modified from Cornel et al., 2018).

1.3. Previous studies

The studies on the Transvaal Supergroup and its BIF started around 1812 by the early pioneers such as Burchell (1822), Moffat (1858), and Harger (1934), who investigated both the Griqualand West Basin and the Transvaal Basin. The nomenclature of the two basins' rock units became a popular research subject resulting in many publications (e.g., Stow, 1874; Penning, 1885; Gibson, 1892). These studies dropped between 1844 and 1904 due to a widespread belief that the iron ore reserves were adequate to support future industrialization

(Morey, 1983). The foundation of the Geological Survey of South Africa in 1912 invigorated extensive geological mapping and stratigraphic description of the Griqualand West and Transvaal basin (e.g., Rogers, 1907; Rogers & Du Toit, 1909; Nel, 1929; Visser, 1944, 1958; De Villiers, 1960, 1970). The attention and subsequent publications on the Transvaal Supergroup's geology grew considerably from the 1960s (Engelbrecht, 1962; Trendall, 1965; Berge, 1966; Fockema, 1967).

Du Toit (1945) performed a study of the mineralogical and petrographic characterization of the Kuruman banded iron formation, and his focal interest was the origin of economic Na-amphibole asbestos deposits. Further studies were done by *inter alia*, Harrington (1962), Backstrom (1963), Cullen (1963), Cilliers & Genis (1964), Berge (1966), Malherbe (1970). Beukes (1973, 1978) and Halbich and Altermann (1992) provided a detailed sedimentological description and development of the BIFs. These studies were later joined by Button (1976), Klemm (1979), Beukes (1980a, 1984), Klein and Beukes (1989), Beukes and Klein (1990), and Schröder et al. (2011). The studies conducted by Beukes and Klein (1990) also focused on the geochemical composition and petrographical investigation of Kuruman and Griquatown formation, looking at evidence of the transition between the formations. Other geochemical-related studies on the Kuruman Formation were done by Horstmann and Halbich (1995), Klein and Beukes (1989), Polteau et al. (2006), and Schröder et al. (2006). Carbonate-banded iron formation transition from the Campbellrand carbonates to the Kuruman Iron Formation was studied by Halbich et al. (1992).

Other researchers who contributed to the BIF petrography and mineralogy studies of the Kuruman Formation are Beukes (1973, 1978, 1980, 1984) and Dimroth and Chauvel (1973). The Transvaal Supergroup was recently investigated by Carney and Mienie (2003), Gutzmer et al. (2005), De Kock et al. (2008), and Gutzmer et al. (2008).

Holland and Beukes (1990) investigated the paleoweathering of the Kuruman Formation and the underlying Campbellrand dolomite in the Wolhaarkop (south-west of Postmasburg). Weathering effects on the banded iron formation studies were performed by Lantink et al. (2019), who investigated the influence of climate on banded iron formation covering Prieska, Whitebank, and Woodstock areas. Banded Iron formation-hosted high-grade hematite iron ore deposits occurring on the Maremane Dome in the Northern Cape Province of South Africa between Sishen and Postmasburg were also investigated by Smith & Beukes (2016). Beukes

(1978) was the first to describe the detailed full stratigraphy of the Kuruman BIF in the Prieska area who also provided a detailed description of the BIF facies from a deep drill core intersection.

The majority of the studies mentioned above were mainly focused on the north-eastern parts of the Griqualand West basin in the Northern Cape Province, such as the Sishen and Khumani areas. There was, therefore, less or rather lack of detailed research in the southern part of the Griqualand West basin in the Northern Cape Province, such as Prieska, Nauga East, and Bovenzeekoebaart areas. The distribution, lithology, occurrence, and post-depositional alteration of the BIF in these areas were less informative or unclear. Also the effects of weathering to the Kuruman BIF mineralogy and geochemistry was not studied into detail. Therefore, a research project that could fill the gap left by the previous studies of the BIF in the Northern Cape Province (Fig. 1.4) was proposed.

1.4. Problem statement

The Griqualand West basin contains significant iron resources and hosts numerous iron and manganese mines, including, among others, the Kumba Resources, Sishen iron mine, Kalahari Manganese mines, and Assmang Beeshoek mine (Alchin & Botha, 2006). Published data provides comprehensive information about the geology, stratigraphy, geochemistry, and petrology of the Griqualand West basin's BIFs; however, the BIFs in the Prieska-Marydale (study area), which form the southern part of Griqualand West Basin, received only casual attention. There is a shortage of detailed stratigraphic investigation and integrated studies about the geological occurrence, petrographic, geochemical characteristics, and post-depositional alteration processes in the research area. The previous studies insufficiently clarify the mineral types, the role of diagenesis, supergene alteration, and surficial weathering in ore-genesis for those areas.

Moreover, new iron-ore deposits need to be discovered to expand iron ore reserves and develop new exploration targets in less explored areas. Thus, this research can provide new insights into the banded iron ore deposits. The research output could also benefit local and national economic development.

1.5. Aims and objectives

The research project aims to provide new insight into the geological occurrence, mineral and rock types, geochemical characteristics, and post-depositional alterations of the weathered banded iron formation in the Prieska area. The aim is also to investigate the effects of weathering on the petrography and geochemical composition of the Kuruman Iron formation in the Prieska area.

The specific objectives are:

- To measure the BIF stratigraphic sequence in the study area;
- To study the geological occurrences of the banded iron formation (BIF);
- To study mineral types and lithology characteristics of the BIF;
- To study sedimentary structures and sedimentary facies;
- To study the geochemistry of the BIF hosting unit in the Prieska area;
- To study the depositional environment of the sediments;

The data will be compared with known fresh ore-bearing BIFs, and a general model for a high-grade iron ore formation will be generated.


University of Fort Hare
Together in Excellence

1.6. Potential impact

The current research project will provide new data and insights on the banded iron formation of the southern part of the Griqualand West Basin, particularly for the mineral and rock types, geochemical characteristics, and the origin of the banded iron formation in the study area. The study will also contribute to the Kuruman BIF database by providing a detailed stratigraphy, mineralogy, and geochemical framework to test the previous formation models. Although the study is conducted on the Kuruman BIF, the findings will have important consequences for understanding other BIF-bearing successions. Besides providing new insight into the BIF in the study area, it could provide an opportunity for local and national economic development. Meanwhile, the candidate will also get improved research training and a route to becoming a professional geologist. The research on outcrop material could advance our knowledge of the iron formation in general, specifically regarding data available in the literature on the fresh deep drill core material of the same succession at the nearby old Koegas asbestos mine.

1.7. Structure of the thesis

The thesis consists of eight chapters, references, and appendices, as highlighted in Table 1.1. Abstract, references, and appendices are not included in Table 1.1 below.

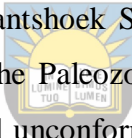
Table 1.1: Table showing the thesis structure.

CHAPTER 1	CHAPTER 2	CHAPTER 3	CHAPTER 4	CHAPTER 5	CHAPTER 6	CHAPTER 7	CHAPTER 8	CHAPTER 9
Introduction	Geological background	Materials and methods	Stratigraphic occurrences	Sedimentary facies and depositional environment	Mineralogy and petrography	Geochemistry of the BIF	Post-depositional alteration	Discussion and conclusion
BIF Background		Desktop studies	Stratigraphic section 1			Major elements	Diagenesis	
Study location	Regional geology	Fieldwork and sampling	Stratigraphic section 2	Facies associations		Trace elements	Post-depositional alteration	
Previous studies		Stratigraphic measurements	Stratigraphic section 3					
Problem statement	Local geology	Sedimentary facies analysis	Stratigraphic section 4	Depositional environments		Source area weathering	Mineral paragenesis	
Aims and objectives		XRD techniques	Stratigraphic section 5	Facies model				
Potential impact	Mineralization	Optical microscopic studies						
Structure of the thesis		SEM studies						
		XRF studies						

CHAPTER 2: GEOLOGICAL BACKGROUND

2.1. Regional Geology

The Paleoproterozoic (2.7 -2.2 Ga) sedimentary sequences of the Transvaal Supergroup covers approximately 250 000 km² on the Kaapvaal Craton, stretching from South Africa Botswana. These sedimentary sequences are partitioned within three basins, including Transvaal Basin, Griqualand West Basin, and Kanye Basin. The Transvaal Basin is located in the northeast, Griqualand West Basin in the western margin of the Kaapvaal Craton, and Kanye Basin covered by Botswana's Kalahari sediments (Eriksson et al., 2006). The Transvaal Supergroup unconformably overlies the 3.0 Ga crystalline basement of Archean gneisses, granites, and greenstone belts (Altermann & Hälbich, 1990) or the Ventersdorp volcanic, and the younger Witwatersrand Supergroup (Tsikos, 1994). It is unconformably covered by the Mapedi shales of the siliciclastic-rock package (Olifantshoek Supergroup), which succeeds the 2 715 Ma Ventersdorp Supergroup (Fig. 2.1). The Paleozoic-Mesozoic Karoo Supergroup covers the Transvaal Supergroup along a regional unconformity on the south while it has been broadly eroded down to the Archean basement on the east.



University of Fort Hare
Together in Excellence

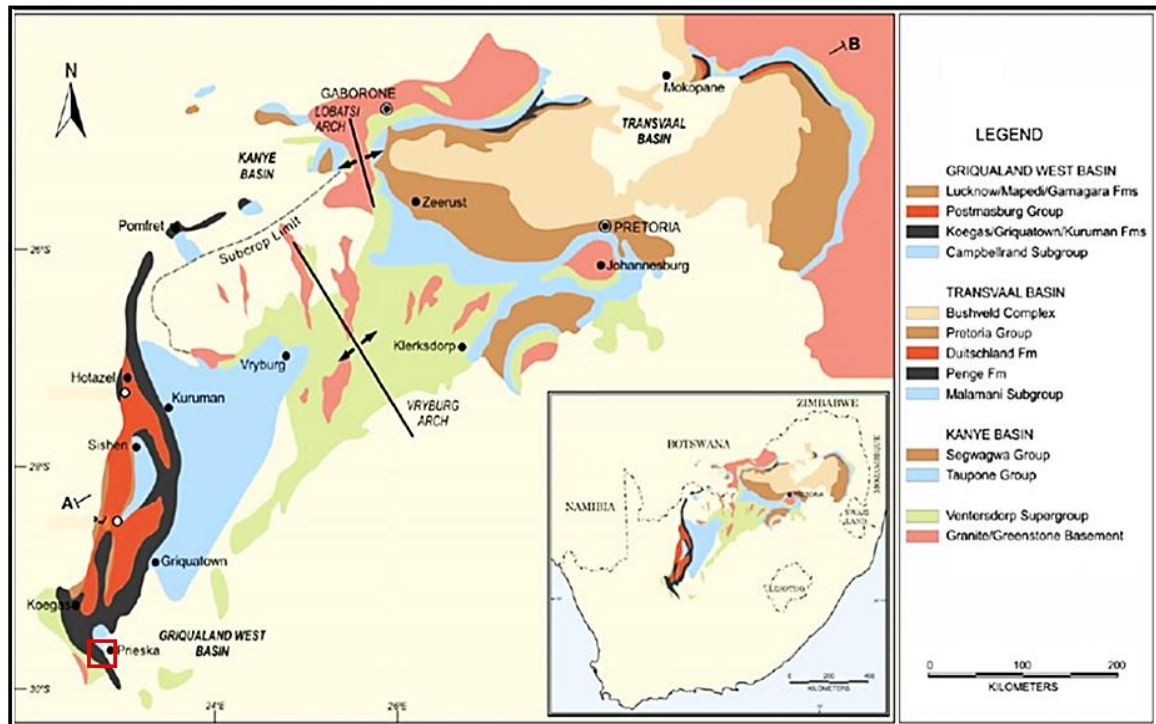


Figure 2.1: Regional geology map showing the distribution of the Basins of the Transvaal Supergroup. The Vryburg Arch separates the Griqualand West and Kanye Basins. The Prieska study area is indicated by a red square in the bottom left. The map was adapted from Moore et al. (2012).

University of Fort Hare

The Transvaal Supergroup comprises carbonate, glacial, detrital, and volcanic sequences (Beukes & Smit, 1987). There are apparent thrust faults and intense folding that resulted from the major tectonic events. Those events in the Griqualand West basin are the post-Olifantshoek period that destroyed some areas' lithostratigraphic successions. Following its deposition, the Transvaal Supergroup's geology experienced mild open folding deformation that resulted in the Maremane dome's formation (Beukes, 1983). The majority of the Supergroup experienced below the zeolite grade of metamorphism, which reaches hornblende to hornfels facies adjacent to the Bushveld Complex (Saggerson & Turner, 1992).

The preserved strata experienced structural disruptions such as gentle wrapping over most of the craton with localized steeper dips around the Bushveld Complex. The intense folding and faulting within the Kheis Belt and Dooringberg Fault Zone along the boundary west of the Kaapvaal Craton cut sedimentary facies illuminating that deposition persisted beyond this boundary during Transvaal time (Beukes, 1987; Beukes & Smit, 1987; Stowe, 1986) (Fig. 2.2).

The preserved Transvaal Supergroup develops in the Kaapvaal Craton within two separate structural successions in the northeast and western basinal segments (Beukes, 1983; Moore et al., 2001; Tsikos, 1999). The first basinal segment is the north-eastern Transvaal sub-basin (Button, 1986). This sub-basin is located on the western margin of the Kaapvaal Craton, extending into southern Botswana beneath Kalahari cover as the Kanye Basin (Moore et al., 2001). The other is the southwestern Griqualand West sub-basin covering the Kaapvaal Craton on the western margin and adjoining Botswana parts (Button, 1986; Moore et al., 2001) (Fig. 2.1). The Vryburg Arch is separating the two sub-basins (Moore et al., 2001).

The two sub-basins contain similar gross stratigraphic subdivisions (Altermann & Nelson, 1998; Armstrong et al., 1991; Beukes 1977, 1986; Eriksson et al., 1995; Halbich et al., 1993; Martin et al., 1998). They consist of a mixed siliciclastic and volcanic unit at the base that is conformably followed by a chemical sedimentary unit. The top comprises a mixed chemical volcanic-siliciclastic rock unit, which unconformably overlies the chemical sedimentary unit. This top unit is characterized by more pronounced facies change than the bottom units. It comprises the Pretoria Group's siliciclastic rocks in the Transvaal basin, while it contains the mixed volcanogenic-chemical sedimentary succession of the Postmasburg Group in Griqualand West (Beukes, 1983).

The Transvaal Supergroup has temporal correlative BIFs that stretch from the south-west Griqualand West sequence to the north-east Transvaal sub-basin in the Kaapvaal craton (Beukes, 1983; Eriksson et al., 1993). The Griqualand West sequence's well-known units are the Griquatown (now Danielskuil on the Council for Geoscience 1:1M Geology of SA map) and Kuruman BIFs, whereas in the Transvaal–Bushveld Basin is the correlative Penge Iron Formation.

1.7.1. The Griqualand West Basin

The Griqualand West Basin is developed on the southwestern rim of the Archaean Kaapvaal Craton. The basin comprises a succession of minor volcanic, siliciclastics, carbonates, and BIFs (Beukes & Gutzmer, 2008; Horstmann & Halbich, 1995; Knoll & Beukes, 2009; Polteau et al., 2006). These successions are grouped into Ghaap Group and Postmasburg Group (Table 2.1).

Table 2. 1: Simplified stratigraphy of the Transvaal Sequence in the Griqualand West Basin modified from Beukes and Smit (1987), Dorland (1999), and Tsikos (1999). The ages were taken from Beukes (1987), Eriksson et al. (1993, 1995), Cheney and winter (1995), Cheney (1996), Cornell et al. (1996), Summer and Bowring (1996), Martin et al. (1998), Romer and Bau (1998), Bau et al. (1999), Catuneanu and Eriksson (2002), Bekker et al. (2004), Polteau et al. (2006), Lewy (2011), and Moore et al. (2012).

Supergroup	Group	Subgroup	Formation	Lithology	Approx. thickness (m)
Transvaal	Postmasburg	Voelwater	Mooidraai (2.394 Ga)	Carbonate, chert	300
			Hotazel	BIFs, Mn	250
			Ongeluk	Andesitic lava	900
			Makganyene	Diamictite	50 - 150
	Ghaap	Koegas (2.415 Ga)	Rooinekke	BIFs, dolomite	100
			Naragas	Shale, siltstone	240 - 600
			Kwakwas	Riebeckitic slate	
			Doradale	BIF	
			Pannetjie	Quartz wacke, shale	
		Asbestos Hills	Griquatown (2.432 Ga)	Clastic textured BIFs	200 - 300
			Kuruman (2.465 Ga)	Microbanded BIFs	150 - 750
		Campbellrand	(2.557 Ga)	Carbonate, shale, chert	1500 - 1700
		Schmidtsdrif	(2.642 Ga)	Shale, quartzite, lava, carbonate	10 -250



The Griqualand West Basin experienced burial temperatures ranging from 120 to 210°C and pressures below 2 kb, causing slight deformation (Miyano & Beukes, 1987; Cornell et al., 1996; Johnson et al., 2003; Klein, 2005; Knoll & Beukes 2009). Metamorphism does not exceed the low grade in the much-affected areas, according to Miyano and Beukes (1984). These rocks of the Griqualand West basin are highly deformed in the southwestern corner, adjacent to the Namaqualand Metamorphic Belt (Altermann & Hälbich, 1991). They are delimited to the west by the sharp NW-SE trending tectonic Doringberg Fault System that runs on their southwestern termination (Fig. 2.2). The Kaapvaal Craton's western margin marks the separation of the Griqualand West Sequence from the easternmost Namaqualand Metamorphic Province. This separation is also known as the Kheis Province, in the marginal area (Stowe, 1986) (Fig. 2.2).

The basal Ghaap Group of the Griqualand West sequence comprises a clastic and chemical sedimentary rock sequence that is unconformably overlain by a mixed siliciclastic-volcanic Postmasburg Group rock package and the Voelwater Subgroup's chemical sediments at the stratigraphic top (Beukes, 1986; Grobbelaar et al., 1995). A glacial tillite directly overlies the angular unconformity (Makganyene Diamictite) segregated from the above Postmasburg

Group by an unconformity with a low-angle (Altermann & Hälbich, 1991) (Table. 2.1). The Griqualand West sub-basin is also subdivided into the Ghaap Plateau and the Prieska compartments (Beukes, 1983) because of their distinct developments (Altermann & Nelson, 1998). The two compartments are separated by the NW-SE trending Griquatown Fault Zone (GFZ) (Altermann, 1997) (Fig. 2.2). They show indistinguishable lithological successions of partly varying ages in their basal stratigraphic levels and contrasting mineral potential (Altermann, 1996; Altermann & Nelson, 1998).

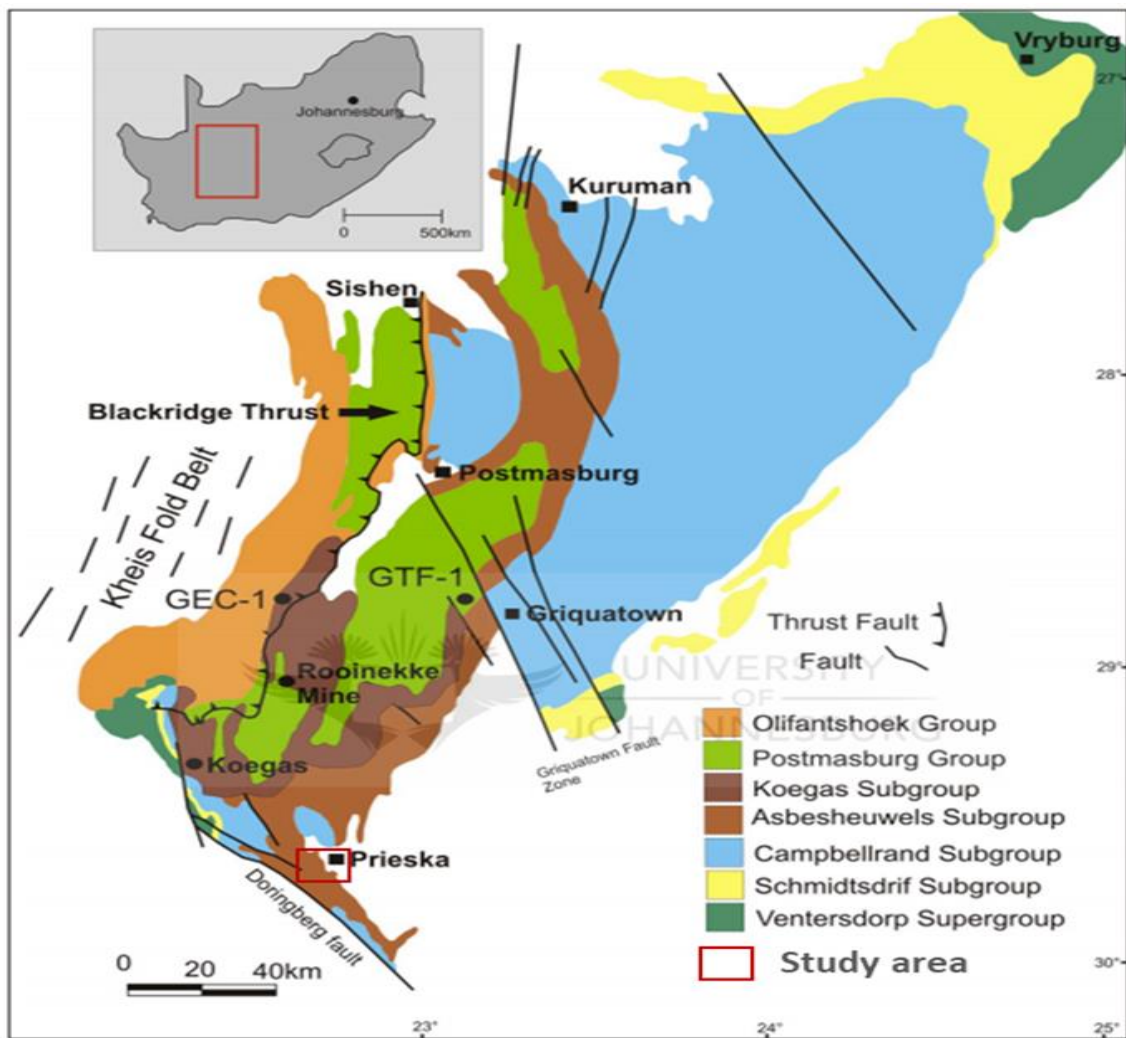


Figure 2.2: Geological map showing stratigraphic and structural occurrences in the Griqualand West Basin (After Nel, 2013).

The Griqualand West basin has well-developed iron formation units, such as the well-studied Kuruman formation, which incorporates the Prieska study area and Griquatown iron-formations, Asbestos Hills Subgroup. Griqualand West basin attains a maximum thickness of 1000m (Beukes, 1983). Therefore, it is essential to briefly describe the Griqualand West Sequence geology, primarily tracking the banded iron-formations (BIFs) while not making any further references to the Transvaal basin.

The Ghaap Group

The Ghaap Group of the Griqualand West Sequence contains a relatively pure chemical sedimentary succession occurring towards the western edge of the Kaapvaal Craton (Beukes, 1986a). The sedimentary group correlated with the Pretoria Group of the Transvaal basin (Beukes, 1983) is overlain by the Postmasburg Group, comprising a mixture of volcanic and chemical rocks (Beukes, 1986a).

The Ghaap Group is subdivided from the bottom to the top into the Schmidtsdrif, Campbellrand, Asbesheuwels (Asbestos Hills), and Koegas Subgroups (Beukes, 1983) (Fig. 2.3). The basal Schmidtsdrif Subgroup comprises interbedded siliciclastic and carbonate rocks. It is directly on top of the crystalline Archean basement or lavas of the Ventersdorp Supergroup along a regional unconformity (Beukes, 1983; Beukes & Smit, 1987). The principal clastic characteristic of the Schmidtsdrif Subgroup does not match with the rest of the Ghaap Group. The basal protobasinal Schmidtsdrif Subgroup's rocks are related to the Ventersdorp and Limpopo events (Catuneanu & Eriksson, 1999; Eriksson et al., 2001).

The Schmidtsdrif Subgroup is followed at the top by the Campbellrand Subgroup carbonate succession platform, which is about 1.7 km thick (Table 2.1). The Campbellrand Subgroup comprises stromatolitic, shallow-shelf deposits that thin out along the SW margin of the Kaapvaal Craton and finely laminated non-stromatolitic carbonate succession deposits (Klein & Beukes, 1989; Beukes & Klein, 1990). The carbonate deposits mainly comprise dolomite and less limestone, with reworked micritic and biogenic material and mostly pyrite-rich carbonaceous shales, particularly at the top (Beukes, 1983, 1984, 1987; Klein & Beukes, 1989; Horstman & Hälbich, 1995; Beukes & Gutzmer, 2009). The sequence is terminated by a regional unconformity that separates the Ghaap Group's rocks from the Makganyene Formation diamictite beds.

The Campbellrand Subgroup is conformably covered by a 1000 m thick BIF of the transgressive Asbesheuwels Subgroup (Asbestos Hills Sub-group) (Grobelaar et al., 1995). The south and southwestern Koegas Subgroup overlies the Asbestos Hill Subgroup (Table 2.1). It is composed of a mixed sequence of terrigenous clastic sediments with subordinate iron-formations, dolomite bioherms, and lavas (Beukes, 1983). The Koegas Subgroup is also succeeded by a 150m thick Makganye Formation, which constitutes glacial diamictite and is unconformably followed by the 900 m thick Ongeluk Andesite Formation above (Altermann & Hälbich, 1991; Cornell et al., 1996; Tsikos & Moore, 1997). There are seven recognized banded iron formation units out of the ten existing beds or members from the basal Ghaap Group towards the top of the overlying Postmansburg Group (Beukes, 1983).

Asbestos Hills Subgroup

The Asbestos Hills Subgroup (Asbesheuwels Subgroup) sediments are predominantly composed of two banded iron formation (BIF) sequences. These BIF sequences include the rhythmically microbanded Kuruman Iron Formation, which constitutes the Prieska study area, and the overlying predominantly clastic-textured shallow-water Griquatown Formation (Fig. 2.3; Table 2.1). These BIFs extend over 500 km north-south below the siliciclastic rocks of the Koegas Subgroup (Beukes, 1978, 1980, 1983, 1984). The BIF deposition in a basin-slope environment indicates the basin's progressive deepening (Martin et al., 1998). The rising of the sea level was attributed to a major transgression (Beukes, 1987).

The Kuruman Iron Formation represents deep-water facies, while the Griquatown Iron Formation reflects a shallow-water depositional environment (Eriksson et al., 2006; Moore et al., 2001). Beukes (1984, 1986a) argues that sediments of the Griquatown Iron Formation grade up to quartz-chlorite mudstones and wackes of the Koegas deposited in a fresh-water lake. The shallowing-upward cycle started when the Griquatown Iron Formation was deposited (Beukes & Klein, 1990). These iron formations grade upwards into the Koegas Subgroup's siliciclastic rocks within the Prieska sub-basin (Beukes, 1986). This iron formation was deposited mainly in shallow marine to the deltaic environment (Altermann & Hälbich, 1991). According to Beukes (1983) and Beukes and Klein (1990), the grain size increase of the iron formation reflects the filling of the depositional basin, with resultant upward shallowing and an increase in the water energy (storm-dominated deposits).

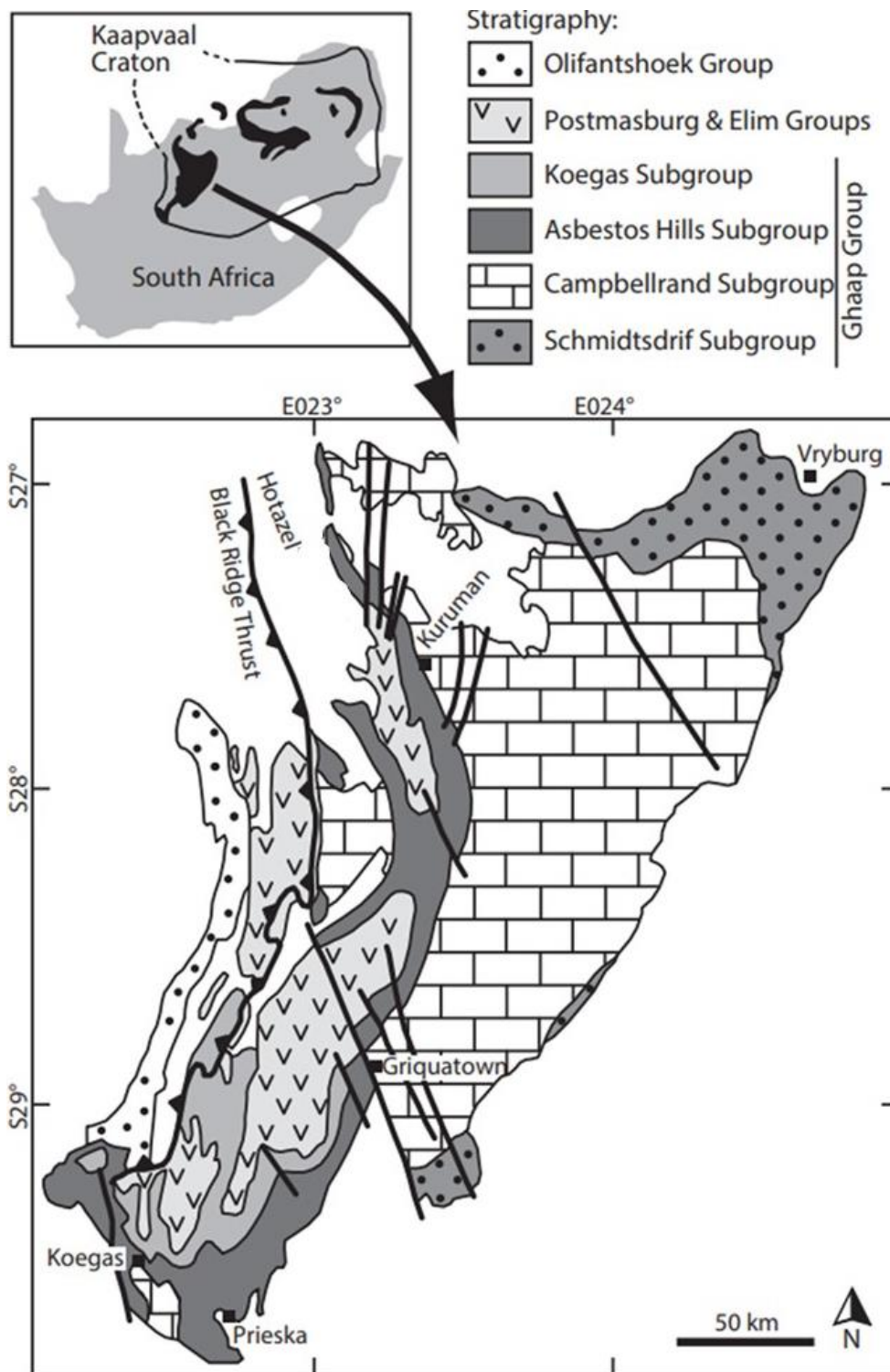


Figure 2. 1: Structural and geological map showing the distribution of Asbestos Hills sub-group and facies change from the shelf area at Danielskuil towards the thicker Prieska facies in the Prieska-Koegas area within the Griqualand West Basin in the Kaapvaal Craton (modified from Schröder, et al., 2011).

Kuruman Formation

The ~ 210m thick Kuruman Iron Formation, which was named after the town of Kuruman, is a Superior-type of a typical Precambrian cherty iron-formation (IF) formed on a continental platform (Gross, 1965, 1980). It overlies the Campbellrand Subgroup carbonate rocks below the Griquatown Iron-Formation (Beukes, 1980). The formation has variable thicknesses across the basin, with approximately 150m north of the synsedimentary Griquatown Fault Zone and 750m south of the fault, where there is a rapid increase in sedimentation rate, resulting in considerable thickening of the formation (Beukes, 1983).

The Kuruman and Griquatown Iron Formations comprise up to 30m thick cherty layers, enriched in blue riebeckite, and 3-40 cm thick of stilpnomelane bands intercalated in the BIF sequence. The stilpnomelane bands are brown to black on fresh outcrops and terminate sedimentary macrocycles (Beukes, 1978, 1980a). The autochthonous Kuruman Banded Iron Formation consists predominantly of very fine (mm-scale) thin composition and colour-banded rhythmically bedded macrocycles of fine-grained mudrock, chert, and iron minerals (siderite, magnetite, and hematite) that grades upward the stratigraphy becoming more granular chert-carbonate-magnetite BIF (Beukes, 1983, 1984; Beukes & Klein, 1990). The micro-banded (finely laminated) Kuruman BIF was deposited in an offshore, intermittently anoxic environment that grades upwards into more granular-textured and mesobanded upper BIF of the Griquatown Formation. Such rare facies transitions in the geological record were only described from the Transvaal Supergroup (Beukes 1980, 1983, 1984; Beukes & Klein, 1990). The two formations are challenging to separate on a geochemical basis; hence they are inferred to have been deposited under broadly similar palaeo-environmental conditions (Beukes & Klein, 1990).

In the Prieska-Koegas area on the south, the Kuruman Iron Formation is separated from the Campbellrand Subgroup by Naute Shale that comprises mainly pelites and a few intercalated cherts. It is chemically continuous over hundreds of kilometres (Beukes, 1983; Horstmann & Halbich, 1995; Cheney, 1996). The Kuruman Iron Formation's highest metamorphic temperatures were 110–170°C (Miyano & Beukes, 1984). The formation was deposited in an open-shelf environment below the wave base, and it contains multiple cycles of shallowing upwards in the succession (Beukes, 1984). The formation is cross-cut by two sills of basaltic andesitic nature. The thinner sill is about 3m thick and situated between the mesobanded BIF

and a thicker interval near the Kuruman-Griquatown transition. The BIFs immediately around these sills are depleted in carbonate as an effect of contact metamorphism. The Kuruman and Griquatown Iron Formations have been greatly impacted by thrust faults in the south of the Griquatown Fault zone (Beukes, 1980). The fault movements that mainly affected the Banded Iron Formations (BIFs) were directed east, north-east, and south-east. The BIFs were impacted because of the incompetency of some of their beds and their laminated character

The Kuruman Iron Formation is divided into several sedimentological members based on the basinal outcrops (Beukes, 1984). These members are harder to distinguish at the carbonate platform top and in drill core sections. The formation is subdivided into Kliphuis Member at the base, Groenwater Member, Riries Member, and Ouplaas Member at the top (Beukes, 1984) (Table 2.2).

Table 2. 2: A simplified stratigraphy of the Kuruman Formation (modified from Beukes, 1984 and Lewy, 2011).

Member	Description
Ouplaas	Clastic textured siderite lutite, grainstones, and disc stones
Riries	Greenalite-siderite Less chert
Groenwater	Magnetite-siderite, stilpnomelane lutite Magnetite-Hematite; Chert-oxide-rich
Kliphuis	Ankerite and chert; shale & claystone partings Dark stilpnomelane lutite; Riebeckite & crocidolite

Kliphuis Member

The basal Kliphuis Member is a transitional zone from the underlying Campbellrand carbonate sequence (Beukes, 1980). It comprises ankerite-rich banded cherts with shale or claystone partings looking like the ankeritized carbonate turbidites of the Campbell Rand Sequence

(Beukes, 1980, 1983). It is composed of interbedded shale and siderite-rich banded iron formations, containing decreasing Ca–Mg carbonate rock abundances and increasing iron contents towards the top of the sequence (Beukes et al., 2003).

The Kliphuis member contains multiple dark-coloured stilpnomelane lutite bands linked to the volcanic input into deep waters (Beukes, 1984; Klein & Beukes, 1989). This linkage is based on their lateral continuity, close association with deep-shelf carbonates, and the preservation of their fine micro-banding (Beukes & Gutzmer, 2008). Riebeckite and crocidolite are preferentially concentrated next to the stilpnomelane lutite mesobands and macro-bands. Crocidolite is only developed in the magnetite-bearing rhythmite. The macrocycles can be correlated over tens of kilometres, making defining the potential crocidolite-bearing zones in the Kuruman Iron-Formation more accurate (Beukes, 1980).

Groenwater Member

The magnetite-siderite Groenwater Member overlies the Kliphuis Member, and it displays cyclic deposits of stilpnomelane lutite and magnetite–hematite banded iron formation (BIF) (Beukes, 1983). These cycles of deposition reflect alternating volcanic ash and iron formation deposition (Beukes, 1983). The stilpnomelane lutite - ferhythmite macrocycles of the Groenwater Member indicate deposition in an open shelf environment (Beukes, 1984). Rhythmic chert and oxide-rich bands of the Groenwater Member are typified by deposition that shallows upward from the deepwater (Beukes, 1984; Pickard, 2003). The four subunits, including Matlipani zone, Whitebank zone, Elgan zone, and Derby zone, constitute Groenwater Member, representing three clastic sediment and BIF cycles. The last two cycles are dominantly composed of volcanically derived stilpnomelane mudrock interbedded with chert. The same coupling occurs again in the overlying Riries Member, comprising three clastic sediment and BIF cycles, with the uppermost Alphen zone containing grainstone bands.

The thickness and content of chert mesobands decrease upward from stilpnomelane lutite beds and sharply increase going down below those beds (Beukes, 1983, 1984). The stilpnomelane lutite beds indicate the deposition of altered acidic volcanic ash beds during explosive volcanic periods. The macrocyclicality described above is believed to have a mixed volcanic-biological origin (Beukes, 1983). During periods of volcanic quiescence, the flourishing of photosynthesizing organisms would promote the precipitation of siderite and hematite bands

in the form of seasonal geochemical varves. Mesobanding in the ferhythmites is attributed to diagenetic processes, leading to magnetite, stilpnomelane, and riebeckite development (Beukes, 1983, 1984).

Riries Member

The greenalite-rich and siderite-rich iron formation of the Riries Member (Beukes et al., 2003) are immediately above the Groenwater Member (Table 2.2). The Riries member comprises the greenalite-siderite rhythmites almost devoid of chert mesobands. A shift towards well-established, neutral-weakly alkaline precipitation conditions due to the abundance of greenalite is evident in this member (Beukes, 1983). The greenalite-siderite ferhythmites deposition occurred at the toe of a slope, below wave-base. Parts of these greenalite-siderite-rich sediments were deposited along a platform slope.



Ouplaas Member

University of Fort Hare
Together in Excellence

The top and capping Ouplaas Member consists of clastic textured iron formation (Beukes et al., 2003). It is constituted by orthochemical (siderite lutite) and allochemical (grainlutites, disclutites grainstones) iron-formation (Beukes, 1980). It is an intraclastic iron formation and was formed in a shallow-water platform environment. It is characterized by the rapid transition from greenalite rhythmites to orthochemical and allochemical iron-formations that marks an abrupt change in the depositional environment towards the top of the Kuruman sequence. Siderite lutites and siderite-rich grainstones, and disc-stones were deposited in a shallow-water platform above wave-base under alkaline conditions (Beukes, 1978, 1983, 1984). This deposition completed the upward-shallowing progradational sedimentary cycle, which characterizes the Kuruman Iron-Formation (Beukes, 1983).

1.8. Local Geology

The study area is covered by the Kuruman Formation, Asbestos Hills Subgroup, of the Ghaap Group (Beukes, 1980, 1983, 1984). The area comprises weathered, highly calcretised and deformed banded iron-formation that occurs with shale and claystone partings (Fig. 2.4). There is also dark stilpnomelane lutite, jaspilite, and riebeckite-amphibolite, with much calcrete exposed on the surface or between the bedding.

There are diamictites with varved shale, mudstones with dropstones, and fluvioglacial gravel of the Dwyka Group of the Karoo Supergroup on the northeast of the area. There is dolomite/limestone (generally stromatolitic), subordinate chert, minor quartzite, shale, and banded iron formation of Campbell rand subgroup of the Transvaal Supergroup East and South East of the area. The shales, sandstones, andesite, and dolomites of the Ghaap Group of the Transvaal Supergroup occur in the South East. There are lightly grey, weakly foliated, and medium to coarse-grained homogeneous porphyritic biotite-muscovite granite of the Skalkseput granite on the Southwest corner (Fig. 2.4).



The BIFs in the study area are medium to fine-grained. They exhibit atypical banded texture and comprise iron bands with variegated grain size. The bands are nearly parallel to the alternate layers of iron minerals and silica (quartz).

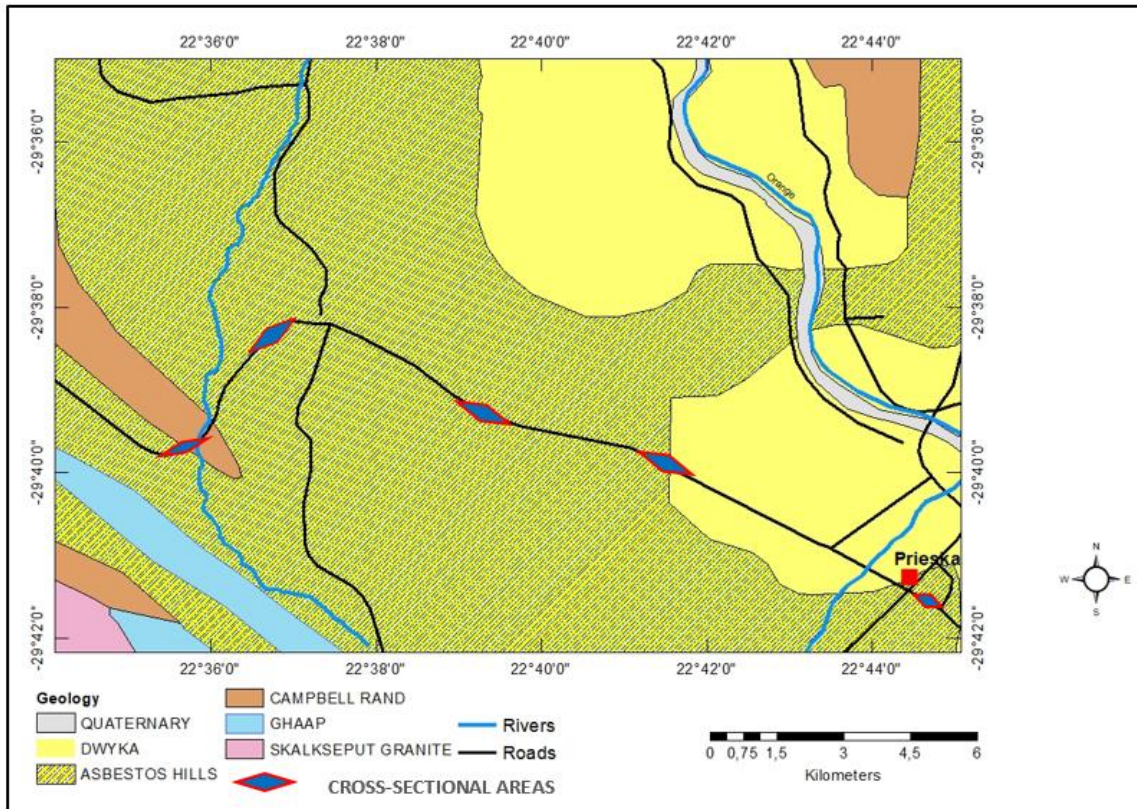


Figure 2. 2: Geological map showing the cross-sectional areas and local geology of the Prieska area. (Modified from 1:1 000 000 scale map from the Council for Geoscience of South Africa).

University of Fort Hare
Together in Excellence


CHAPTER 3: MATERIALS AND METHODS

Various methods, including desktop studies, field investigation, stratigraphic measurement, and laboratory studies, were carried out to achieve the research aim and objectives.

3.1. Desktop Studies

Various activities, such as consulting online information, technical reports, journal papers, and degree thesis, were carried out to provide a good understanding of the geological background of the Prieska area. Previous work related to the banded iron formation on both local and regional scales was consulted to view the approach and techniques to plan the research project properly.

3.2. Field investigation and sampling



Fieldwork and sampling were carried out from Prieska towards Marydale. These were concentrated on the Kuruman Formation road-cut exposures because it was challenging to access private game reserves and farms. The instruments used included the handheld global positioning system, compass, digital camera, measuring tape, geological hammer, sample bags, hand lens, permanent marker, pencils, pen, and field notebook. Different lithologies, sedimentary structures, vertical packing styles, and sedimentary facies were observed and identified. The observed outcrops' sedimentary structures were described, and photographs were taken where necessary. The thicknesses of stratigraphic units were measured using a measuring tape. Samples from the least altered and deformed outcrops were obtained based on the field observations. They were marked and placed in labelled sample bags for further geological studies, petrographic examinations, and geochemical analysis. GPS coordinates were taken and recorded for the positions of the stratigraphic sections.

3.3. Stratigraphic measurements

The Kuruman Formation outcrops in the study area were examined from the road-cut exposures. Different lithologies and sedimentary structures were described. Stratigraphic sections were measured within the limits of the roadcut outcrop based on field observations using a measuring tape. Petrographic parameters such as colour, grain size, mineral composition, bedding thicknesses, sedimentary structures, and facies were used to separate the various stratigraphic units. Sedimentary facies analysis was carried out using a modified version of the lithofacies classification scheme by Miall (1988a, 1988b, 1996) developed for siliciclastic sedimentary rocks with no direct application to chemical sedimentary rocks like Iron formations, except for the coding system. The description of the individual facies was adopted from Miall (1995, 1997), Bordy and Catuneanu (2001), Bordy et al. (2005), James (1954) and Beukes and Gutzmer (2008). Facies association (FAs) was integrated from the individual facies based on the vertical stacking styles and depositional environments' variation during the sediment deposition. Lithostratigraphy illuminates both vertical and lateral lithological variations that reflect changing depositional environments. A comprehensive review of the spatial stratigraphic changes of the sedimentary successions from the Kuruman BIF was performed. Based on the banding thickness and cyclicity, the BIF has been subdivided into macro-bands with meter scale, centimetre scale mesobands, and millimetre-scale microbands (Trendall, 1983). The processing tools used for stratigraphic data include Surfer Software and Microsoft Office PowerPoint. The outcomes were conveyed in the stratigraphic sections.

3.4. Sedimentary facies analysis

Recording of lithological features and sedimentary structures is an essential part of facies analysis. A combination of lithology and sedimentary structure, and other rock characteristics give rise to facies. The stratigraphic units' facies analysis was carried out using a lithofacies classification scheme modified version by Miall (1988a, 1988b, 1996) based on a bit-part or letter lithofacies coding system. However, these sedimentary facies schemes were developed for siliciclastic sedimentary rocks with no direct application to chemical sedimentary rocks like Iron formations, except for the coding system. The description of the individual facies is

adapted from Miall (1995, 1997), Bordy and Catuneanu (2001), Bordy et al. (2005), James (1954) and Beukes and Gutzmer (2008). The individual facies cannot wholly reconstruct or interpret the depositional environment and conditions that prevailed during their deposition. Hence the facies association was deduced from them. The identified sedimentary facies were grouped into facies associations (FAs) and used to deduce the possible depositional paleo-environments. Petrographic features such as the rock texture, grain size, and mineral compositions were used to identify and distinguish different lithofacies. Petrographic variations based on non-analytical techniques such as colour and banding's nature permitted the differentiation of the iron formation sub-facies across stratigraphy. Lithostratigraphy IUGS classification after Murphy and Salvador (1999) has been employed for the study.

Sedimentary facies deal with mineral composition, rock texture, fossil content, rock geometry, colour, sedimentary structures, and paleo-current patterns, reflecting the depositional process and environment. Sedimentary facies is a concept that is used in a descriptive and interpretative way to deduce the formation processes and depositional environments from which a particular sedimentary rock was sourced or derived. Steno (1669) introduced the term "facies," whereas, Gressly (1838) and Walker and Cant (1984) used the word "facies" to define the lithological and paleontological aspects of stratigraphic units. Since then, the word has been used by numerous geologists in diverse ways.

The term "facies" is defined as a body of sedimentary rock with specific characteristics such as a combination of lithological, physical, and biological aspects to differentiate it from neighbouring rock bodies. There are two types of sedimentary facies, i.e., lithofacies and biofacies. Lithofacies deals with lithological features, such as colour, mineral composition, rock texture, and sedimentary structures. In contrast, the biofacies describe biological characteristics, such as fossil types, fossil reserve and burial condition, the proportion of a specific fossil, and fossil assemblage.

3.5. Laboratory analysis Methods

The laboratory work was carried out following the fieldwork. Samples were prepared for mineralogical, petrographic, diagenesis, and geochemical analysis.

3.5.1. X-Ray Diffraction (XRD) Techniques

The whole-rock mineralogical examination of the samples' major mineral phases was achieved using X-ray diffraction (XRD) performed in the Faculty of Science at the University of Pretoria.

The samples were prepared for XRD analysis using a standardized Panalytical back-loading system, which provides a nearly random distribution of the particles. They were analyzed using a PANalytical X'Pert Pro powder diffractometer in θ - θ configuration with an X'Celerator detector and variable divergence and fixed receiving slits with Fe filtered Co-K α radiation ($\lambda=1.789\text{\AA}$). The mineralogy was determined by selecting the best fitting pattern from the ICSD database to the measured diffraction pattern, using X'Pert Highscore plus software. The relative phase amounts (weight% of the crystalline portion) were estimated using the Rietveld method (X'Pert Highscore Program).

It is important to note that mineral abundances below 1% remain undetectable by the powdered XRD method. In contrast, those between 1 and 5% exhibit minor spectra peaks, and their intensities are too low for accurate identification. Thus, approximate mineral abundances were inferred by integrating semi-qualitative XRD and petrographic methods such as SEM and optical microscopy.

3.5.2. Optical Microscope Studies

The optical microscope studies were carried out using thin-section slides in the Department of Geology, University of Fort Hare. Ten polished representative thin section slides were prepared and examined using the Olympus and Leica MC 170 HD optical microscope. Mineral assemblages and their common textural attributes and relations were studied with the optical microscope. The mineral types, rock textures, cement types, and diagenetic features such as authigenic minerals, compaction and recrystallization, overgrowth, and mineral alterations of the BIF were also determined with optical microscope's aid.

The rigorous petrographic examinations and descriptions were carried out using transmitted light microscopy for gangue minerals (chert/ quartz) and reflected light microscopy for the iron minerals.

3.5.3. Scanning Electron Microscope (SEM) studies

The scanning electron microscope (SEM) was used in the study to investigate grain-surface texture, rock petrological textures, authigenic minerals, types of cement, mineral replacement, and semi-quantity of the mineral's chemical compositions.

This study was performed at the University of Fort Hare with a Tescan Vega 3 scanning electron microscope (SEM) machine, equipped with an energy dispersive X-ray spectrometry (EDX). Six representative samples were carbon coated and studied for semi-quantity chemical composition analysis and element distribution mapping.

The SEM was used to identify mineral phases, rock textures, and post-depositional alterations accurately than a microscope study. It was carried out to identify minor minerals and conduct detailed textural studies.



3.5.4. X-Ray Fluorescence (XRF) analyses

University of Fort Hare
Together in Excellence

X-ray fluorescence (XRF) was performed in the Faculty of Science at the University of Pretoria. It was used to study the whole-rock major and trace element compositions. XRF was also used to study the weathering intensities of the samples. The BIF rock samples were neatly cleaned and crushed into powder of less than 50 µm grain size. The pressed pellets were used for the major oxides and trace elements analyses. The samples were prepared as pressed powders. 10-30g powdered sample, mixed with 20 drops Moviol (PVA), pressed to 10 tons. The Thermo Fisher ARL Perform'X Sequential XRF instrument with Uniquant software was used for analyses. The software analyses for all elements in the periodic table between Na and U, but only elements found above the detection limits (0.01 wt. % for majors and trace elements) were reported. The values were normalized, and no LOI was done to determine crystal water and oxidation state changes. Standard sample material was prepared and analyzed in the same manner as the samples and is reported as such.

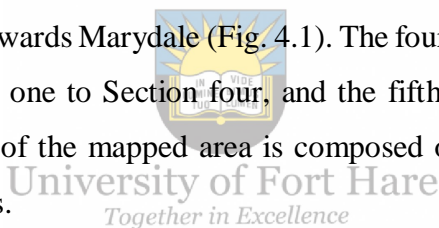
CHAPTER 4: STRATIGRAPHIC OCCURRENCES

4.1. Introduction

The field mapping was carried out along the N10 road cutting from Prieska towards Marydale and covered four main cross-sectional areas and one sub-cross section area with accessible outcrops (Fig. 4.1). Four stratigraphic successions were measured and described. Each stratigraphic section was measured until the limit of the outcrop. The fifth section was very short, and as a result, it was not measured but only mapped and described for the Prieska BIF.

It should be noted that how the sections relate to each other in stratigraphic sense or order remains unknown or highly speculative. Thus the sections do not represent the entire thickness of the Kuruman Iron Formation in the area.

The first stratigraphic section is situated south-east of Prieska, and the fifth section was mapped on the far west of Prieska towards Marydale (Fig. 4.1). The four measured stratigraphic sections are presented from Section one to Section four, and the fifth mapped section is given under Section five. The majority of the mapped area is composed of deformed and weathered BIF rocks with fresher road cuts.



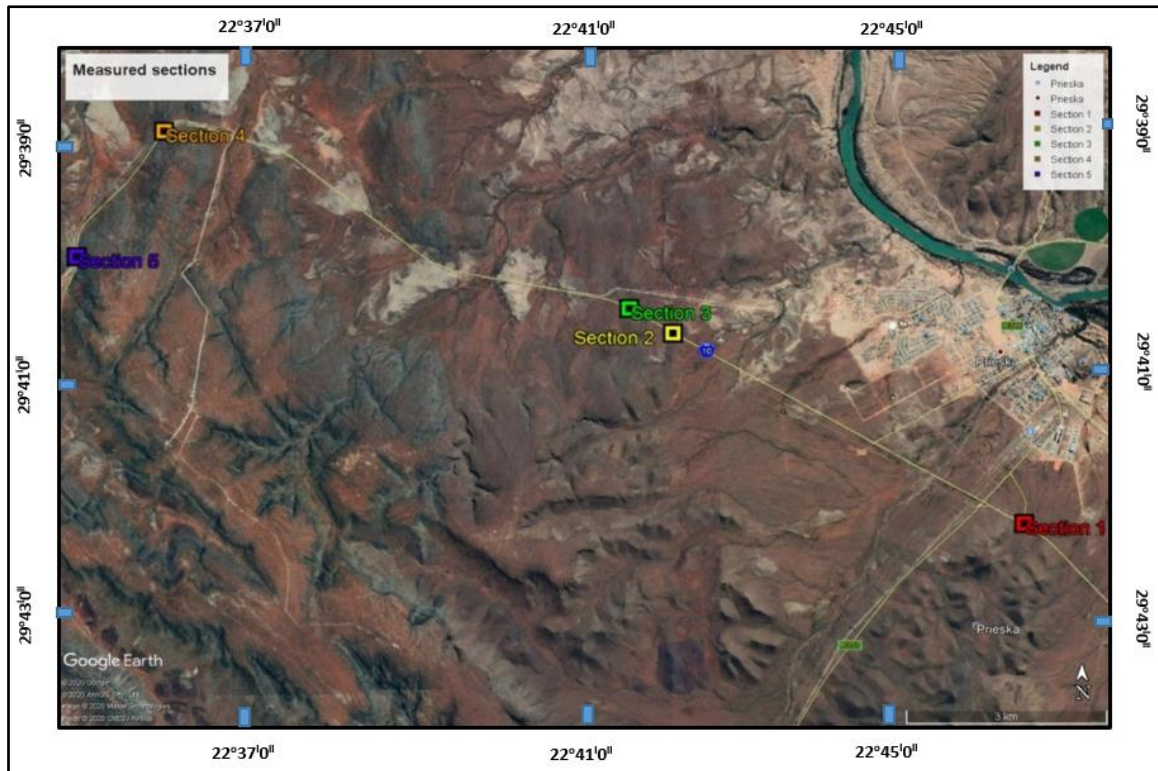


Figure 4. 1: Google earth map showing the location of the five stratigraphic sections.



4.2. Stratigraphic section one

University of Fort Hare
Together in Excellence

The first measured stratigraphic section is geographically South East of Prieska (Fig. 4.4). Section 1 has a thickness of about 54.6m and a slightly deformed base. The section is composed of the BIF and mudstone with two coarsening up cycles. The base of the section is more laminated and becomes thinly bedded towards the top. The deformation extent increases going up the formation. The formation has dark to black layers of magnetite, hematite, and small varying concentrations of goethite (Fig.4.2). Chert (quartz), iron oxides, clay minerals, and carbonate layers are the dominant constituents of some stratigraphic units (Fig. 4.2). There are highly weathered zones characterized by significant contents of limonite and goethite (Fig. 4.3). There is folding displayed in some of the zones (Fig. 4.2).

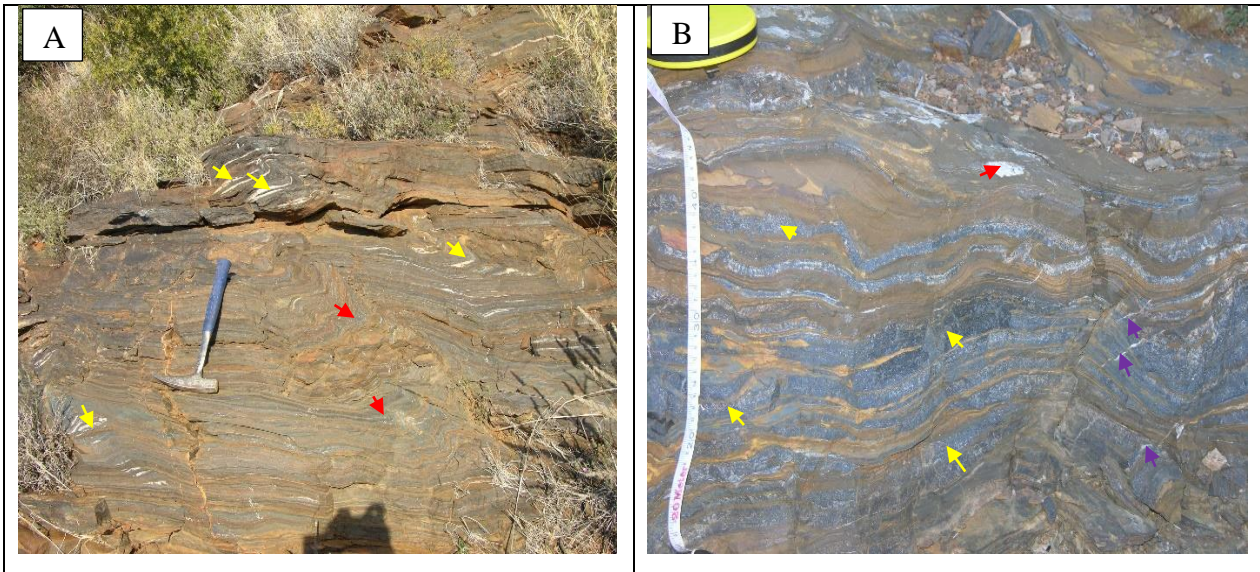


Figure 4. 2: Field photographs showing (A) Deformed and folded formation containing dark iron-rich (red arrows) layers alternating with brownish chert and carbonate layers. There are also white quartz-rich lenticular laminations (yellow arrows); (B) Dark magnetite/hematite-rich layers (yellow arrows) occurring with whitish quartz (red arrow) and brownish mud-weathered iron-rich layers. The formation shows strong deformation and secondary quartz veinlets (purple arrows).

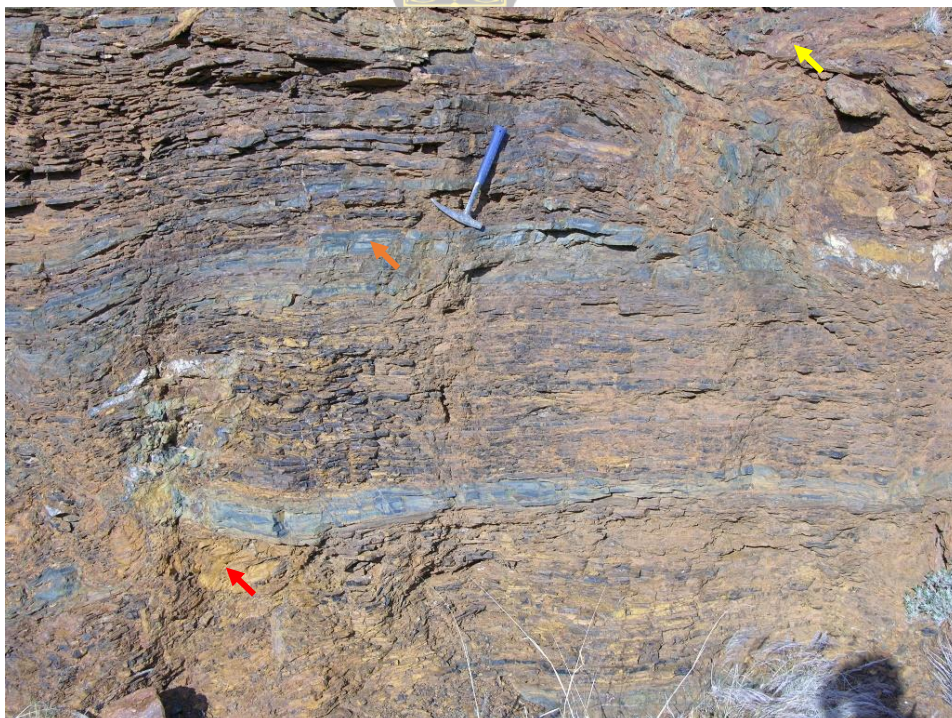


Figure 4. 3: Field photograph displaying intense differential weathering and folding. It also shows a significant amount of blackish or grey magnetite (orange arrow), yellowish goethite/limonite (red arrow), reddish-brown hematite (yellow arrow), and chert (light brownish).

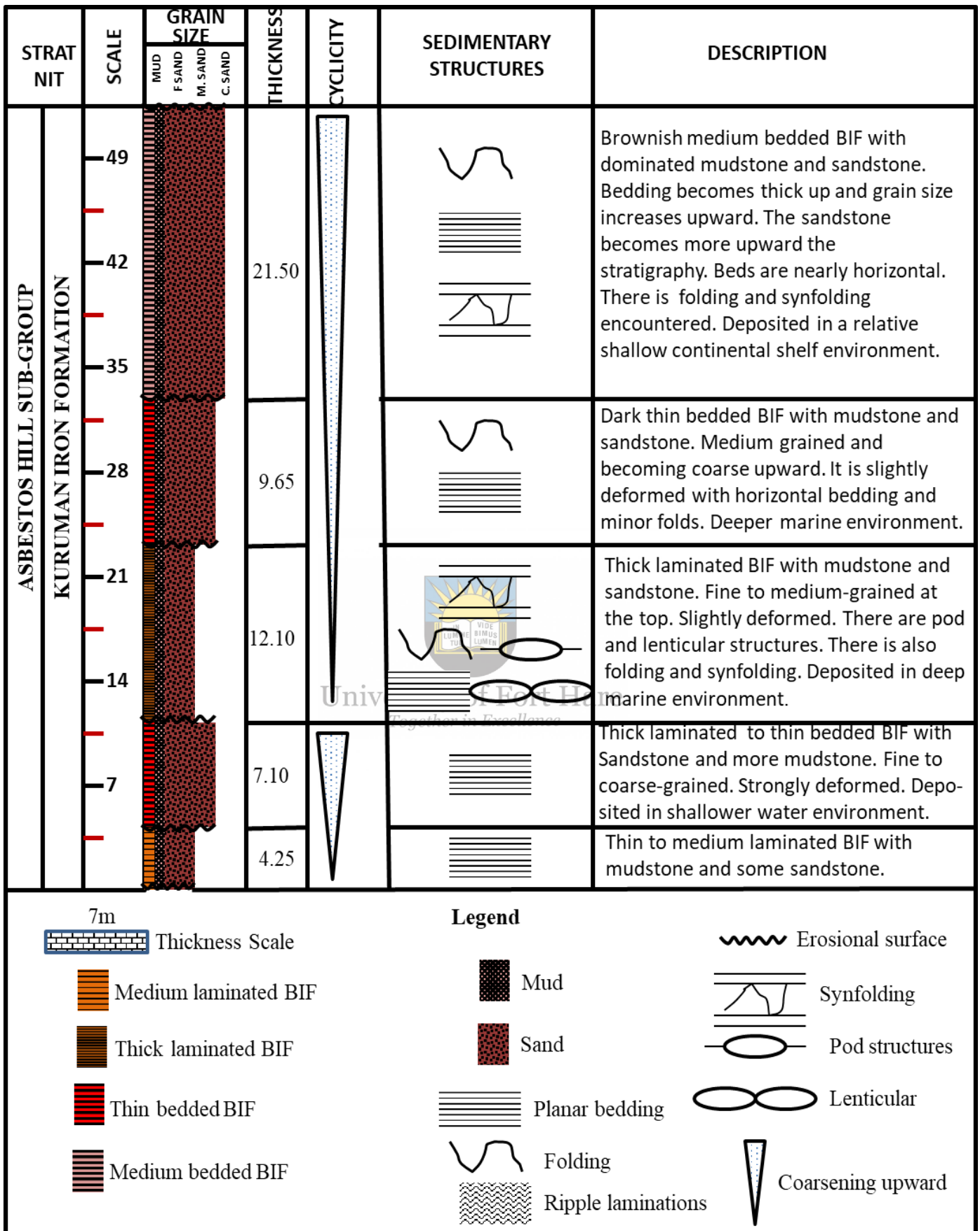


Figure 4. 4: Measured Stratigraphic Section 1.

4.3. Stratigraphic section two

The second stratigraphic section is a bit further from Prieska town. It is geographical West of the Prieska town along Road N10 (Fig. 4.1). The section is 52.4m thick, and it comprises five units (Fig. 4.6). The section is generally composed of the typical laminated BIF units, which are interlayered with mudstone. It is constituted by three fining up cycles. The section consists of magnetite layers interlayered with hematite, goethite, chert, and carbonate-rich microbands (Fig. 4.5). It is faulted and filled with secondary calcrete present within the openings (joints, faults, cracks, and bedding planes) of some of the layers. There are blackish to reddish-brown colour variations encountered from the different layers.

This section represents a relatively slow, quiet, deeper water depositional environment changing to a shallower water depositional environment at the top. There are sedimentary structures like iron-rich lenticulars, rill marks, and planar bedding present within this stratigraphic sequence. There are also faults and fault cut-offs, which are coupled with highly deformed formation. The rocks are generally dipping about 14° towards NW, and some phyllites are observed (Fig. 4.5).

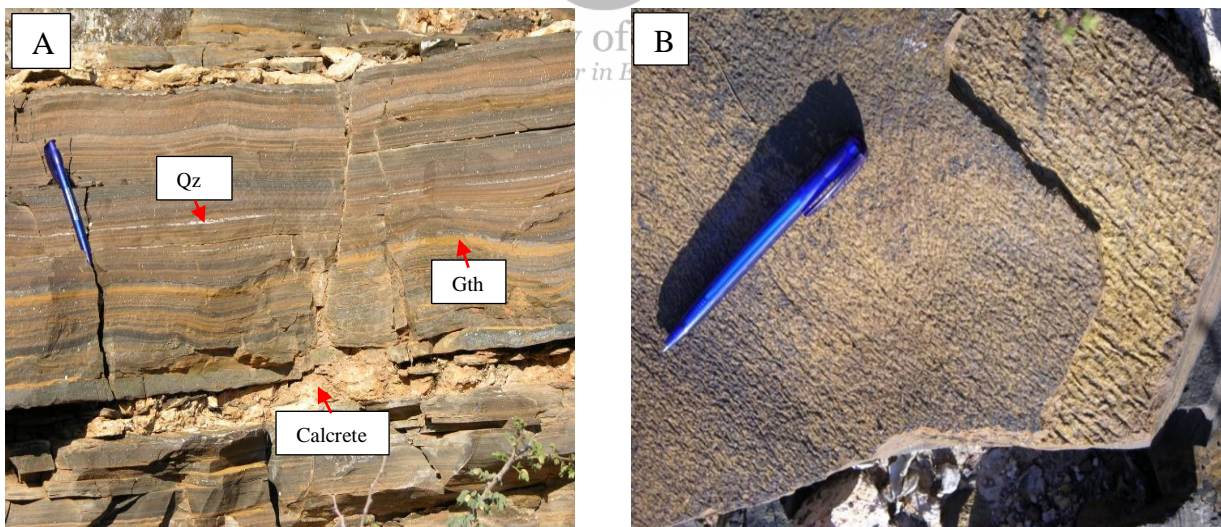


Figure 4. 5: Field photograph showing (A) dark magnetite and reddish hematite microbands, yellow to brownish goethite-rich/ limonite microbands (Gth), and light-coloured quartz (Qz) and carbonate-rich microbands; (B) A phyllite with limonite/goethite (yellowish) and rill marks on the bedding surface.

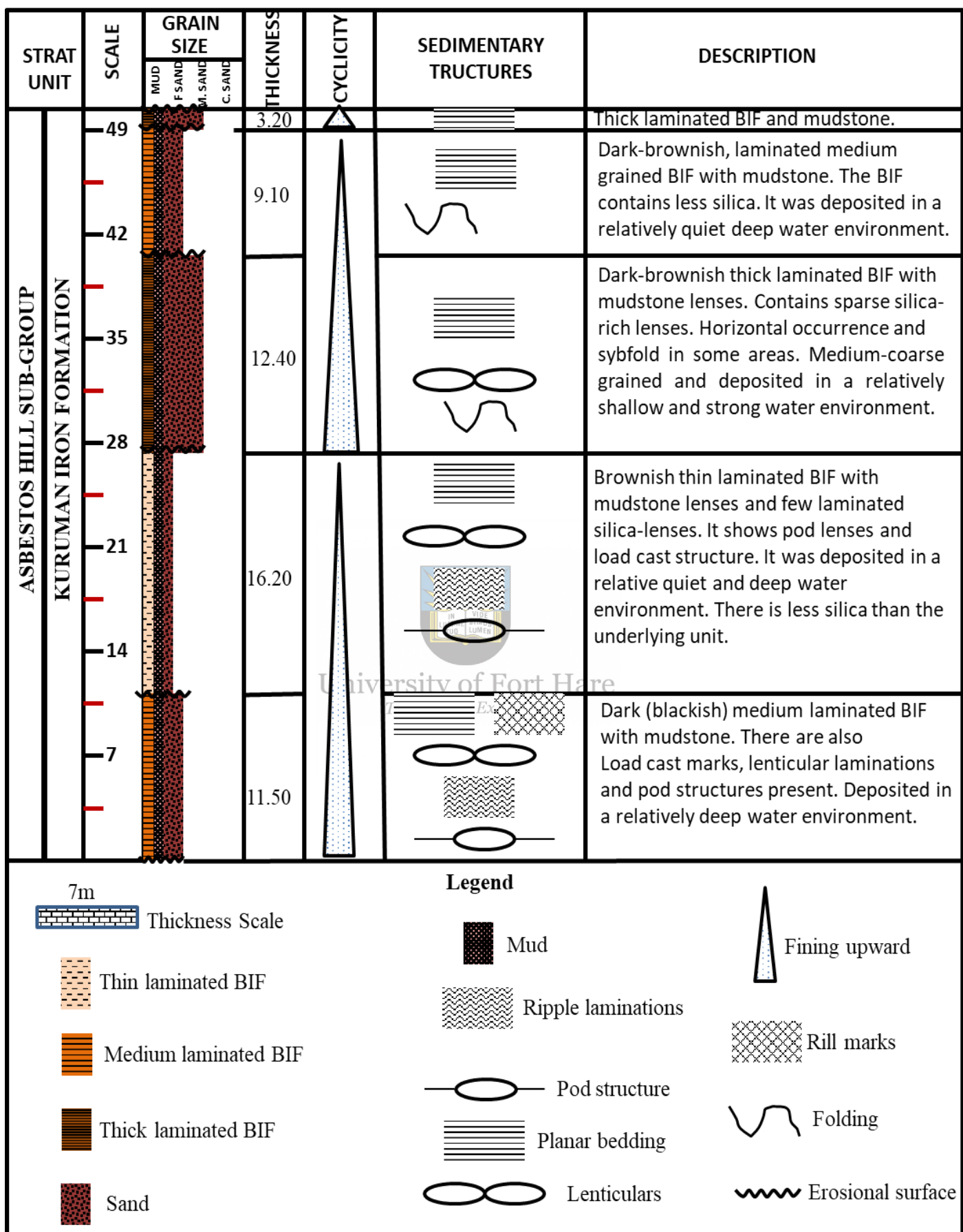


Figure 4. 6: Measured Stratigraphic Section 2.

4.4. Stratigraphic section three

The third stratigraphic section is North West of Section 2 along Road N10 (Fig. 4.8). The section has six units with a combined thickness of 151.20m. This section and the previous section form the two limbs of a syncline, while this section is through to younger rocks than those in section two. It also comprises the BIF and mudstone. The base has a coarsening-up cycle that is fining up towards the top. The stratigraphic section generally comprises planar bedding with ripple laminations and synfolding in some areas (Fig 4.7). There is also folding that is encountered, and the beds are becoming near-horizontal towards the NW. The laminations are thicker than those experienced in Section one. There are, however, thin laminations of mudstone, iron, and sandstone layers. There is a transitional bed present from the thick to medium beddings. There are more pronounced sand and iron layers than Section one. The rocks are deformed and highly weathered, and the formation is dipping towards South East. The formation is generally deformed and highly weathered. It is dominated by hematite and goethite in some places. It comprises weathered magnetite laminations, hematite, and goethite laminations. The hematite appears to be intermixed with goethite. Some areas contain more hematite and goethite with less magnetite. Ripple laminations and synfolding are appearing in some zones. There is a green tint that is associated with the chert and magnetite layers.



Figure 4. 7: Field photographs showing a weathered and deformed hematite (black arrows), limonite, and goethite-rich (red arrows) formation.

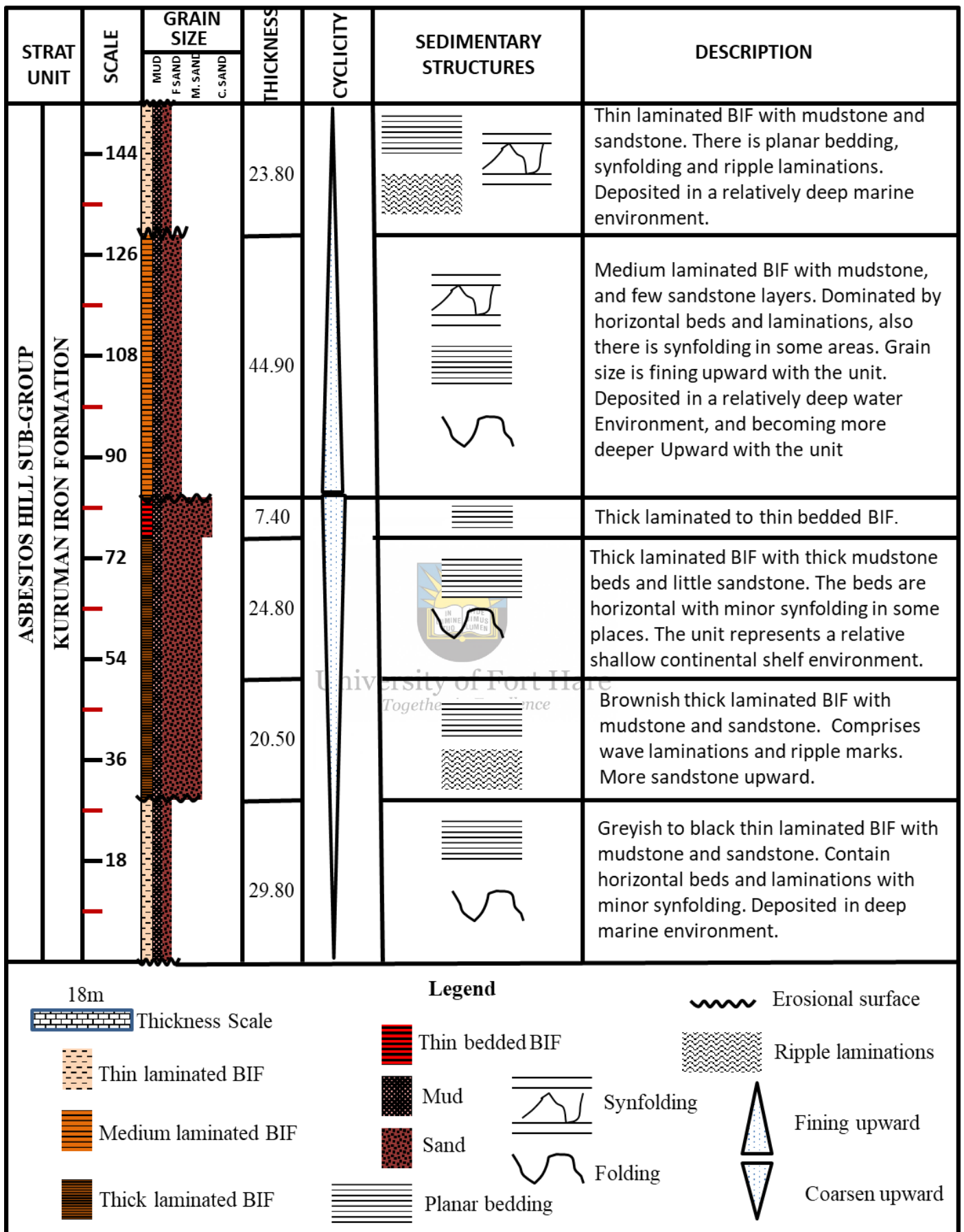


Figure 4. 8: Measured Stratigraphic Section 3.

4.5. Stratigraphic Section four

The fourth and the last measured Stratigraphic Section is 342.61m thick, and it consists of eleven distinct units (Fig. 4.11). This section comprises one of the excellent and well-exposed outcrops. The rocks are generally folded and highly deformed. The section comprises laminated BIF layers and mudstone with three fining-up cycles and one coarsening-up cycle. There is the presence of synfolding and multiple lenticular and pod structures.

The section is contained in an anticline comprising a smaller laminated stromatolite BIF on the older limb (SE) and a larger stromatolite BIF on the younger side (NW). The BIF is thin to medium laminated with a dark colour that changes to brownish colour towards the North West (top). The laminations increase to thin beds and back to medium laminations towards the younger side. The formation is separated by the road and is thin-laminated on one side and thick laminated on the other side. There are waves and ripple laminations with folding at some places (Fig. 4.9). There are thin to medium BIF laminations of mostly chert-rich bands interlayered with hematite and carbonate-rich laminations.

Some of the BIF rocks have bands comprising a mixture of hematite and goethite. Most of those bands are hematite-rich. They either occur as continuous bands, lenticulars, or pod structures (Fig. 4.10). The other bands and laminations are rich in chert, while others are more magnetite-rich.



Figure 4. 9: Field photographs showing a deformed and weathered chert, hematite, goethite, carbonate-rich mudstone with ripple laminations (red arrows) and folding (yellow arrow).

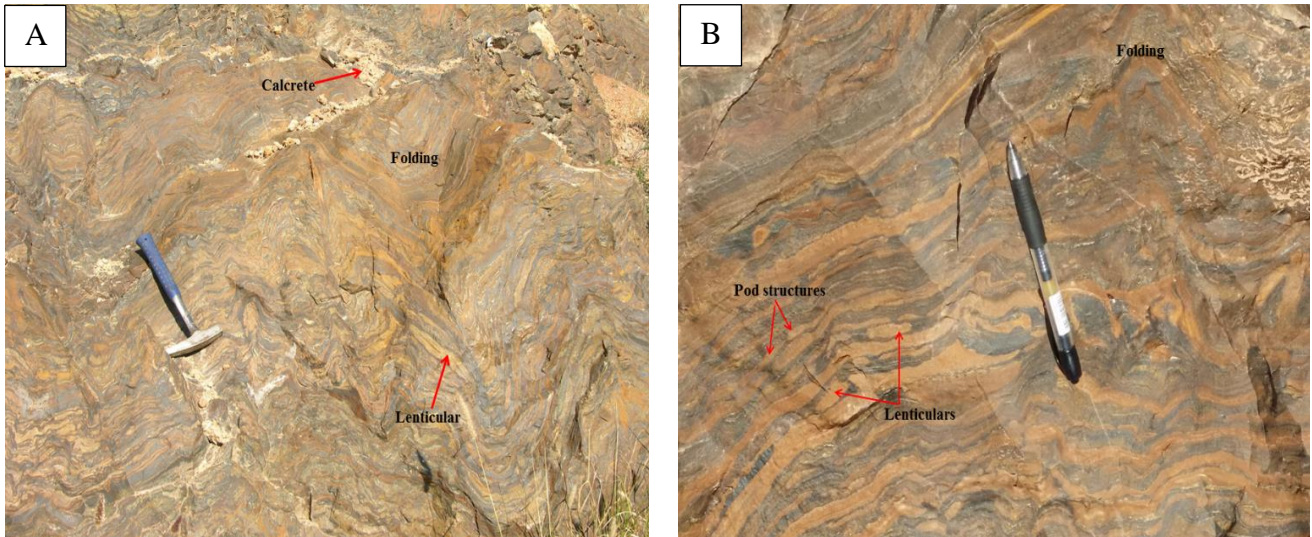


Figure 4. 10: Field photograph displays (A) Highly deformed BIF and mudstone formation that comprises syndepositional folding and multiple lenticular structures; (B) Deformed formation consisting of broken BIF laminations, lenticular and pod structures. The formation comprises a brownish alternating bands rich in goethite and hematite.



University of Fort Hare
Together in Excellence

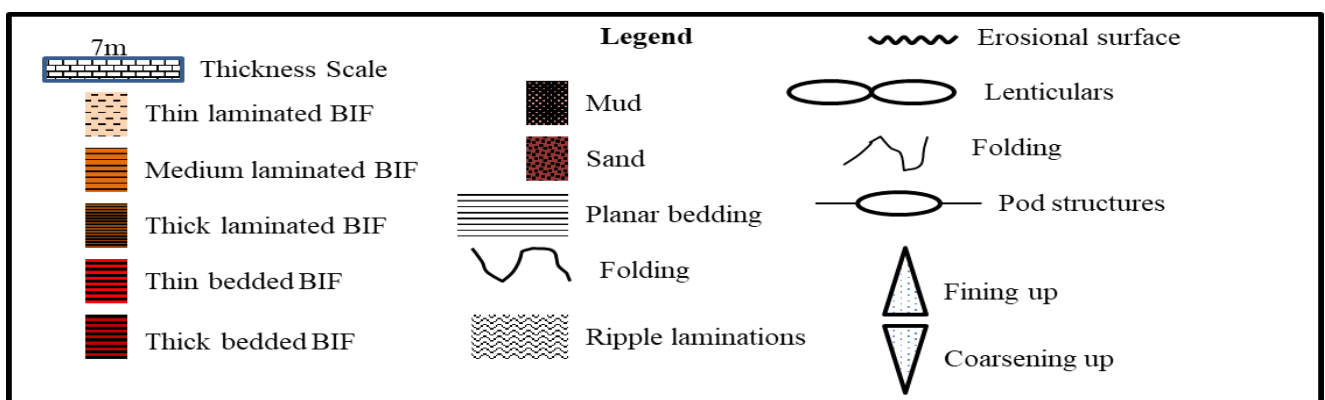
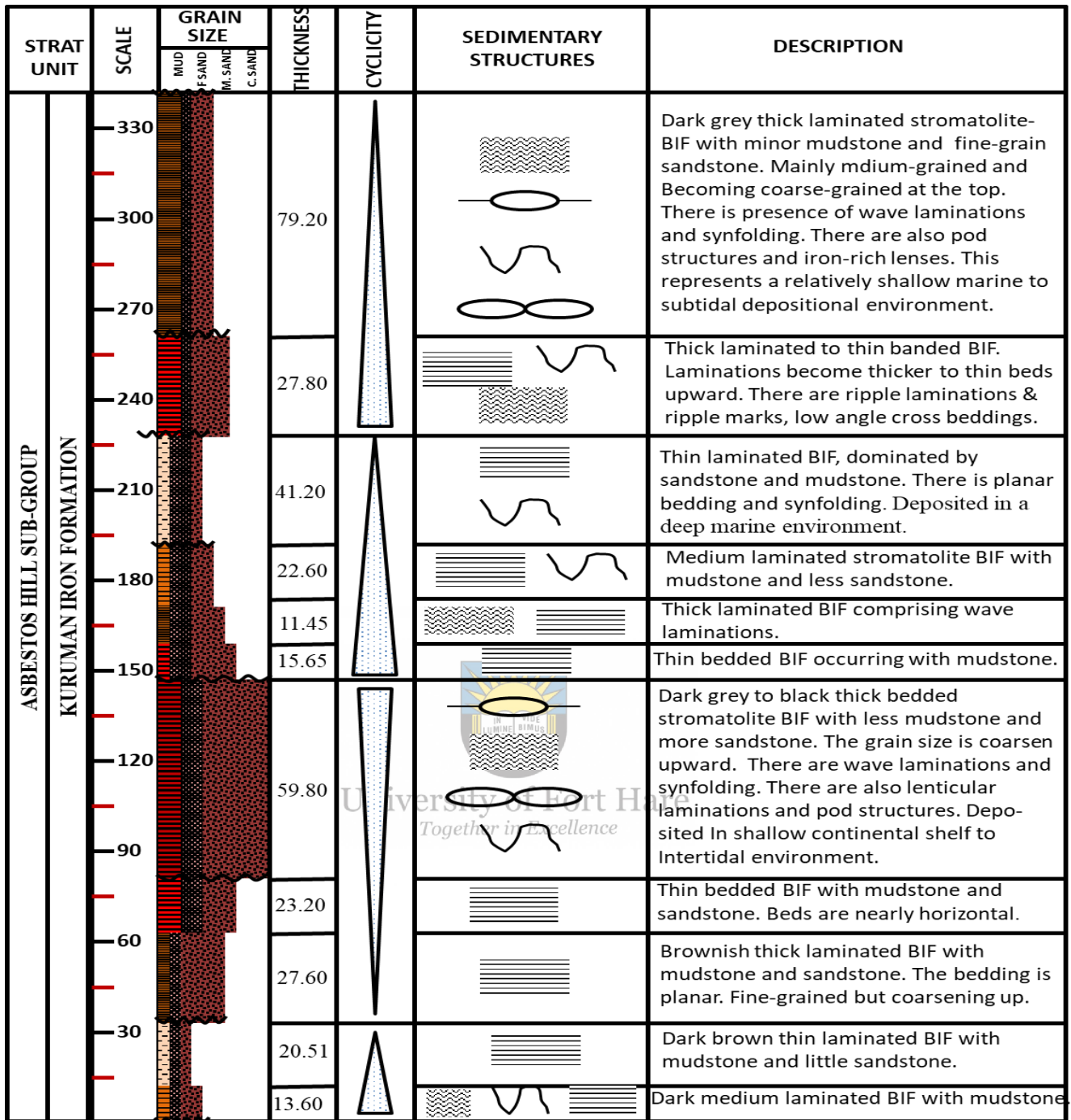


Figure 4. 11: Measured Stratigraphic Section 4.

4.6. Stratigraphic Section five

The fifth section, which was only mapped and not measured to different units, represents the last section of the study. It is situated on the NW of Prieska towards Marydale, representing the youngest (top of overall BIF sequence) of the mapped sections. It was not measured because only a few outcrops were exposed, which would result in a very short traverse.

The phyllite was observed with thin laminated BIF that is contoured. The BIF also consists of deformed bedding. The magnetite is exposed to the surface, and it changes to reddish hematite. The BIF appears with calcrete on the surface due to leaching and evaporation. There is a huge fault that is evident in the area. The formation is highly weathered towards the North West, and there is more calcrete visible towards the younger side.

There are also some quartz veins visible. There are chert (greyish) layers that are interbedded with iron and mud-rich layers. The chert layer is related to the deepwater depositional environment. The chert layer is about 1 to 5cm thick (Fig. 4.12). Some of the chert layers are lenticular, while some are deformed. Some of the faults and folds are visible with the faults containing quartz fills.

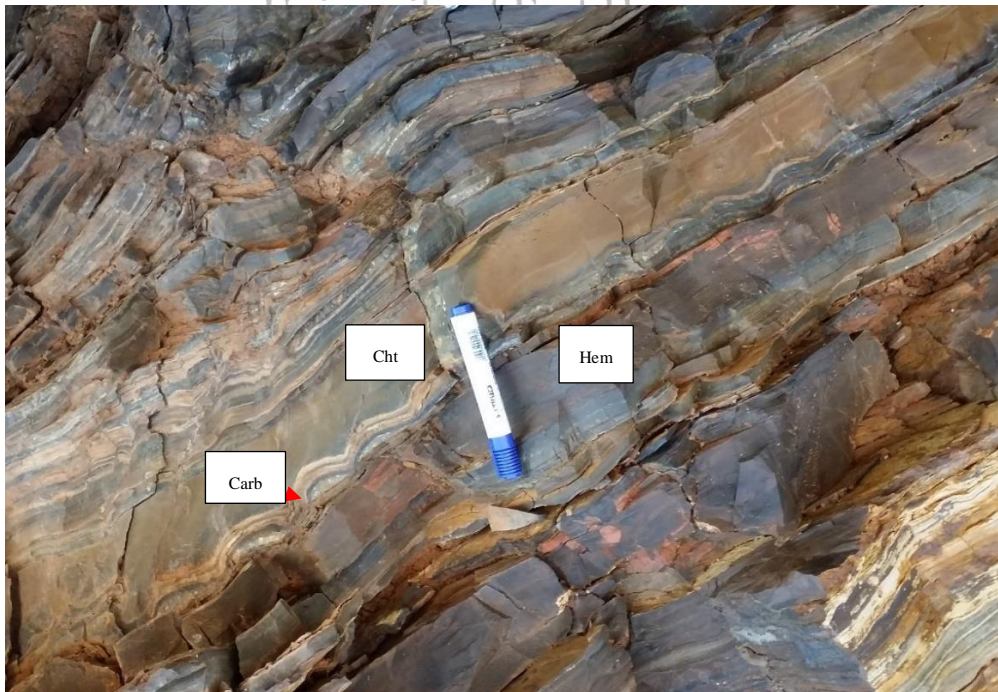


Figure 4. 12: Field photographs showing a thin to medium bedded BIF composed of chert-rich (Cht) bands interlayered with hematite (Hem) and carbonate-rich (Carb) laminations. The carbonate laminations display ripple laminations.

CHAPTER 5: SEDIMENTARY FACIES AND DEPOSITIONAL ENVIRONMENT

5.1. Introduction

This chapter presents a description of the weathered Kuruman Formation sedimentary facies recognized and identified in the Prieska study areas. Descriptions of the sedimentary facies were done from the outcrops along the N10 road. The observations assisted in determining and interpreting depositional environments. The interpretation of depositional environments was inferred from the lithologies, sedimentary structures, and contact relationships between the sedimentary facies and rock units. These features are a good reflection of the depositional processes, hydrodynamic conditions, and depositional environments.

5.2. Facies analysis of the Kuruman Formation



The specific characteristic geometry, colour, bedding, lithology, mineral composition, texture, grain size, sedimentary structures, and paleocurrent patterns of the weathered roadside Prieska geology, including the BIF, was studied employing facies analysis after Miall (1995, 1997), Bordy and Catuneanu (2001), Bordy et al. (2005), James (1954) and Beukes and Gurtzmer (2008). These were used in the study to delineate the formation processes and depositional environments of the different lithologies of the Kuruman Formation.

The well-exposed and weathered Kuruman Formation in the study area comprises BIF and associated sedimentary rocks with the thickness of a single rock unit ranging from a few centimetres to more than ten meters, depending on the depth of the depositional environment. There are well-developed sedimentary structures in the sequence, such as cross-bedding, laminations, lenticular bedding, horizontal bedding, pod structures, and ripple marks, reflecting a specific type of depositional environment. Different sedimentary facies were defined within the Kuruman Formation based on the lithologies, sedimentary structures, and grain-size variations. A modified version of sedimentary facies codes proposed by Miall (1977, 1983, 2000) was used for the current study.

The observable petrological features of sedimentary rocks, such as mineral composition, biological features, and grain size, were thoroughly studied. These studies were conducted to deduce the origin and nature of the Kuruman formation's depositional environments. The current chapter presents a description of the lithofacies and biofacies of the Kuruman Formation identified in the Prieska area. The observations helped determine and interpret the depositional environments based on the lithologies, sedimentary structures, fossil types, and contact relationships.

Eight sedimentary facies were recognized and identified in the study area. The sedimentary facies identified include horizontally laminated BIF facies (Hlb), horizontal thin to medium bedded BIF facies (Hbb), ripple laminated BIF facies (Rlb), thin to medium bedded mudstone facies (Mbm), medium to thick-bedded mudstone facies (Tbm), medium to thick-bedded fine sandstone facies (Mts), laminated dolomite stromatolite facies (Ld), and dome-shaped stromatolitic BIF facies (Dbif).

5.2.1. Horizontally laminated BIF facies (Hlb)



The horizontal laminated BIF facies (Fig. 5.1) comprises thin, medium, or thick horizontal laminations of iron oxide layers alternating with chert layers. In some areas, the chert laminations are dominating while the iron oxide laminations are dominating in others. This facies is encountered at the top unit of section 1. It is found towards the top and bottom of section 2. The same facies appears in almost all the units of section 3 and section 4 (see Chapter 4). The formation is slight to strongly deformed with minor folding and synfolds in some areas of the sequence. The colour associated with these facies is dark (black), dark brown, or dark grey.



Figure 5. 1: Field photograph from section one illustrating the horizontal laminated BIF facies of the Kuruman Formation in Prieska.



University of Fort Hare
Together in Excellence

5.2.2. Horizontal thin to medium bedded BIF facies (Hbb)

The horizontal thin to medium bedded BIF facies (Fig. 5.2) comprise thin to medium interbedded BIF layers (iron oxides and chert). The beds' thickness range from a few centimetres to tens of meters in the field outcrops. This facies is encountered at the bottom of section 1 and towards the top of section 4. The bedding thickness increases going up the unit. The grain size also increases towards the stratigraphic top. The formation is originally dark or greyish but becomes brownish when exposed to the surface due to weathering and oxidation. There is synfolding observed in the strata.



Figure 5. 2: Field photograph illustrating the horizontal thin to medium bedded BIF facies of the Kuruman Formation in Prieska.



5.2.3. Ripple laminated BIF facies (Rlb)

University of Fort Hare
Together in Excellence

Ripple laminated BIF facies (Rlb) comprise BIF containing ripple laminations and synfolding (Fig. 5.3). This facies is found at the bottom and top of stratigraphic section 3. It is also contained at the bottom and middle of section 4. The facies is sometimes constituted by minor folds that overlap on the ripple lamination. These minor folds make the bedding structures more complicated. The formation is mostly brownish.

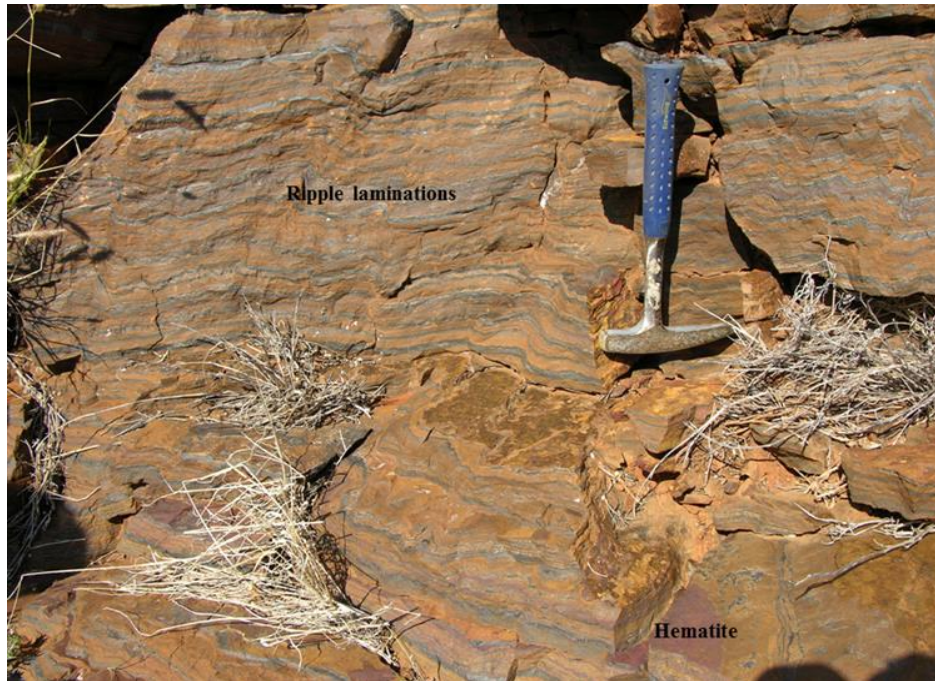


Figure 5. 3: Field photograph from section four showing a ripple laminated, weathered brownish BIF comprising magnetite, hematite, limonite, and goethite laminations with syn-depositional folds.



University of Fort Hare
 together we advance

5.2.4. Thin to medium bedded mudstone facies (Mbm)

Thin to medium bedded mudstone facies (Fig. 5.4) comprises horizontally bedded mudstone and sometimes a ferruginous shale occurring in different colours from the different sections. The rock shows fine to very fine grain textures and sometimes intercalated with thin banded iron formation layers. The fine grain size and thin bedding structure indicate that these facies were deposited in a relatively deeper water environment. The mudstone also occurs as chemically precipitated ferulite or stilpnomelane lutite beds (Probably volcanic ash). The thickness of each bed is varied between 1-30 cm.



Figure 5. 4: Field photograph illustrating the thin and medium bedded mudstone of the Kuruman Formation. The thickness of the individual beds varies between 1-30 cm.



5.2.5. Medium to thick-bedded mudstone facies (Tbm)

University of Fort Hare
Together in Excellence

The thick-bedded mudstone facies (Fig. 5.5) with bedding thickness variation from 25-80 cm commonly occur in the study area. This facies shows occur dark grey, dark brown colour, and brown or reddish-brown colour when weathered. These mudstones are also called lutite, shale, or claystone in the previous literature. These facies could be intercalated with thin-bedded mudstone, sandstone, or banded iron formation in the stratigraphic sequence.



Figure 5. 5: Field photograph illustrating the thick-bedded mudstone facies of the Kuruman Formation in Prieska. The thickness of each bed varies from 20 to 80 cm.



5.2.6. Medium to thick-bedded fine-grained sandstone facies (Mts)

University of Fort Hare
Together in Excellence

Medium to thick-bedded fine-grained sandstone facies (Fig. 5.6) shows a variable bedding thickness from 20 to 100 cm and comprises dominantly fine-grained quartz with minor other detrital grains. The sandstone exhibits various colours influenced by mineral composition, such as clay minerals and matrix. Horizontal bedding or lenticular bedding are very common within these facies. Lenticular bedding structure could reflect the original shallow water channelized depositional environment. Large scale lenticular sets represent wide and large channel deposits, whereas small scale lenticular sets represent shallow and small channel deposits. Grain size increase from mudstone to sandstone reflects hydrodynamic energy increase.



Figure 5. 6: Field photograph illustrating the fine sandstone facies of the Kuruman Formation in Prieska. The thickness of each bed varies from 20 to 100 cm.



5.2.7. Laminated dolomite stromatolite facies (Ld)

University of Fort Hare
Together in Excellence

The laminated dolomite stromatolite facies (Fig. 5.7) is composed of horizontal dolomite beds with lamination structures inside. The laminated dolomite is fine grain-sized; it could be formed by chemical precipitation or by biochemical precipitation. The latter is also called laminated stromatolite, formed by cumulation and precipitation of blue-green algae. In the later stage after deposition, the laminated carbonate facies could be replaced by iron oxides due to stromatolite has high porosity and is easily replaced by the iron-rich pore-water. Then the stromatolite carbonate changes to stromatolite banded iron formation. These facies was found at the bottom and middle of section 4. It is characterized by wave laminations and folding with pod and lenticular structures in the field outcrops. The grain size is usually fine, with medium to coarse grains after recrystallization. The colour is dark grey to light grey.



Figure 5. 7: Field photograph illustrating laminated dolomite stromatolite facies of the Kuruman Formation in Prieska.



5.2.8. Dome-shaped stromatolitic carbonate facies (Dbif)

University of Fort Hare
Together in Excellence

Dome-shaped stromatolitic carbonate facies occur in the Kuruman Formation with banding thickness variable from medium to thick. It is usually greyish coloured when fresh but could be red-brownish after weathered due to containing sparse iron-rich layers (Fig 5.8). Dome or cone-shaped stromatolite is very common within the study areas, with the dome size variable from 10-30 cm wide and 10-45 cm in height, whereas cone size is usually smaller with 4-10 cm in width and 8-20 cm in height. This facies appears in medium to the coarse-grained pale greyish banded iron formation. Stromatolites are biogenetic sedimentary structures. They are different forms and shapes, such as laminated, wave-shaped, cone and dome-shaped, and spherical-shaped (oncolite). These stromatolites were formed in shallow water environments, such as intertidal and supratidal environments by algae and bacteria. They are usually carbonated in chemical composition, but iron, phosphorus, and manganese stromatolites are found in the geological records. It is not clear the iron, phosphorus, or manganese types of stromatolite were formed by replacement of carbonate stromatolite, or they were originally formed by iron, phosphorus, or manganese eating bacteria and algae in the geological past.



Figure 5. 8: Field photograph illustrating the dome-shaped bio-carbonate facies (red arrows) of the Kuruman Formation in Prieska.

5.3. Facies Associations (FAs)



University of Fort Hare
Together in Excellence

The lithofacies and biofacies, which occur together and are viewed as genetically or environmentally related, were grouped as facies association based on the lithologies, sedimentary structures, and vertical and lateral alteration relationship of the different facies. The internal and external geometry strata of the Kuruman Formation in the study area have been grouped into five distinct facies associations (FA1-5). The five identified facies associations (FA) are:

Facies association 1 (Hlb + Hbb),

Facies association 2 (Hlb + Hbb + Mbm + Tbm),

Facies association 3 (Hlb + Hbb + Mbm + Tbm + Rlb),

Facies association 4 (Mbm + Tbm + Mts), and

Facies association 5 (Ld + Dbif + Mts).

5.3.1. Facies association 1 (FA 1, Hlb + Hbb)

Facies association 1 (Fig. 5.9) is made up of horizontal laminated BIF facies (Hlb), and horizontal thin to medium bedded mudstone facies (Hbb). It is encountered at the bottom of Section 1. This facies association reflects a deposition in a deep marine environment.



Figure 5. 9: Field photograph from section one illustrating the FA1: Horizontal laminated BIF facies (Hlb, bottom) and Horizontal thin to medium bedded mudstone facies (Mbm, middle) of the Kuruman Formation in Prieska. This facies association represents formation in a deep marine environment.

5.3.2. Facies association 2 (FA 2, Hlb + Hbb + Mbm + Tbm)

Facies association 2 is encountered in the middle of section 3 and at the bottom, middle, and the top of section 4. It comprises the horizontal laminated BIF facies (Hlb), the horizontal thin to medium bedded BIF facies (Hbb), thin to medium bedded mudstone facies (Mbm), and medium to thick-bedded mudstone facies (Tbm). This association was probably deposited in a lower hydrodynamic deep marine environment, such as a deep marine plain, where lamination and horizontal bedding could be developed.

5.3.3. Facies association 3 (FA 3, Hlb + Hbb + Mbm + Tbm + Rlb)

Facies association 3 is encountered at the top of sections 1, 3, and 4, at the bottom of sections 2, 3, and 4, and in section 5. It is composed of horizontal laminated BIF facies (Hlb), the horizontal thin to medium bedded BIF facies (Hbb), thin to medium bedded mudstone facies (Mbm), medium to thick-bedded mudstone facies (Tbm), and ripple laminated BIF facies (Rlb). This facies association represents a relatively shallower marine deposit. The water energy was higher than FA2, as reflected by ripple laminations.

5.3.4. Facies association 4 (FA 4, Mbm + Tbm + Mts)

Facies association 4 is encountered at the bottom of section 2. It comprises thin to medium bedded mudstone facies (Mbm), medium to thick-bedded mudstone facies (Tbm), and medium to thick-bedded fine sandstone facies (Mts). This facies association indicates a relatively shallow marine depositional environment. Hence grain size is coarser than facies association 3.

5.3.5. Facies association 5 (FA 5, Ld + Dbif + Mts)

Facies association 5 (Fig. 5.10) is encountered at the bottom and towards the top of section 3. The same facies association is found at the bottom and in the middle of section 4. It consists of laminated dolomite stromatolite facies (Ld), dome-shaped stromatolitic banded iron formation facies (Dbif), and medium to thick-bedded fine sandstone facies (Mts). This facies association reflects a shallow marine depositional environment. The grain size is coarser and could be near the subtidal to the intertidal environment. Thus where the dome-shaped stromatolite could have developed.

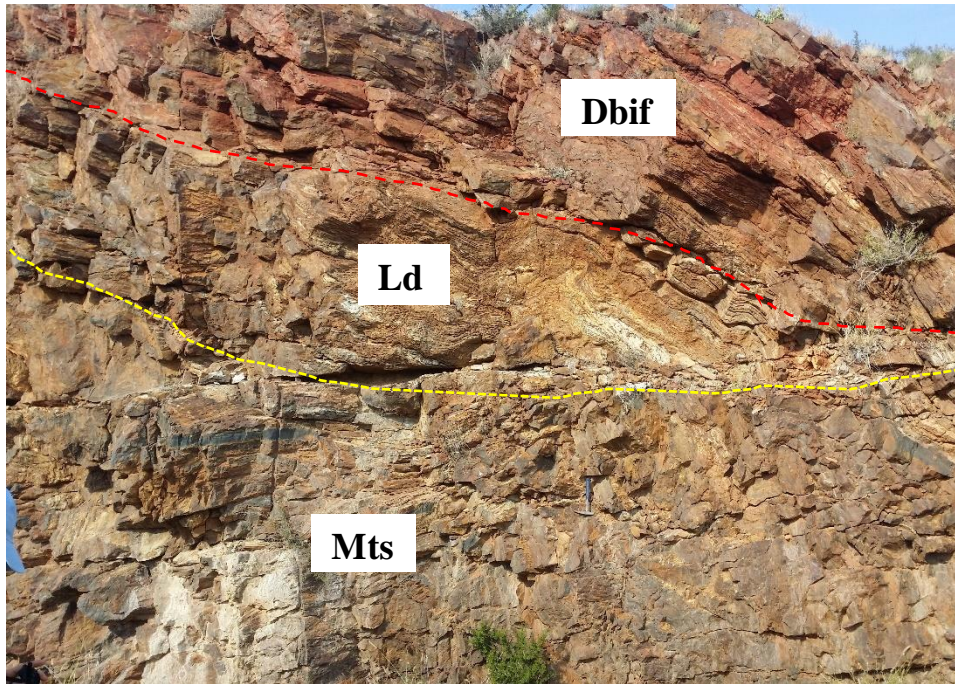


Figure 5. 10: Field photograph illustrating FA5: The dome-shaped stromatolitic banded iron formation facies (Dbif), laminated dolomite stromatolite facies (Ld), mudstone, and medium to thick-bedded fine sandstone facies (Mts) of the Kuruman Formation in Prieska.



University of Fort Hare
Together in Excellence

5.4. Depositional environment

A depositional environment is a geographic terrain where sediments can be deposited and cumulated for a considerable time and thickness. A specific environment can be deduced from the rock types (lithology), sedimentary structures, sedimentary facies, and facies associations. Table 5.1 summarizes sedimentary facies, facies associations, and their respective depositional environments for the Kuruman Formation at the Prieska-Marydale area.

Table 5. 1: Summary of sedimentary facies and their respective depositional environments.

Facies Association	Depositional environment
FA 1 (Hlb + Hbb)	Deep marine basin.
FA 2 (Hlb + Hbb + Mbm + Tbm)	Deep marine plain.
FA 3 (Hlb + Hbb + Mbm + Tbm + Rlb)	Relatively shallow marine, such as lower parts of continental shelf.
FA 4 (Mbm + Tbm + Mts)	Relatively shallow marine, such as upper parts of continental shelf.
FA5 (Ld + Dbif + Mts)	Shallow marine/ subtidal and intertidal zone

5.5. Facies model

With considering the grain-size distribution and variation, sedimentary structures and facies, as well as lateral facies arrangement, an integrated depositional model that formed Kuruman Formation in the study area has been proposed (Walker, 1976; Anderton, 1985) (Fig 5.11).

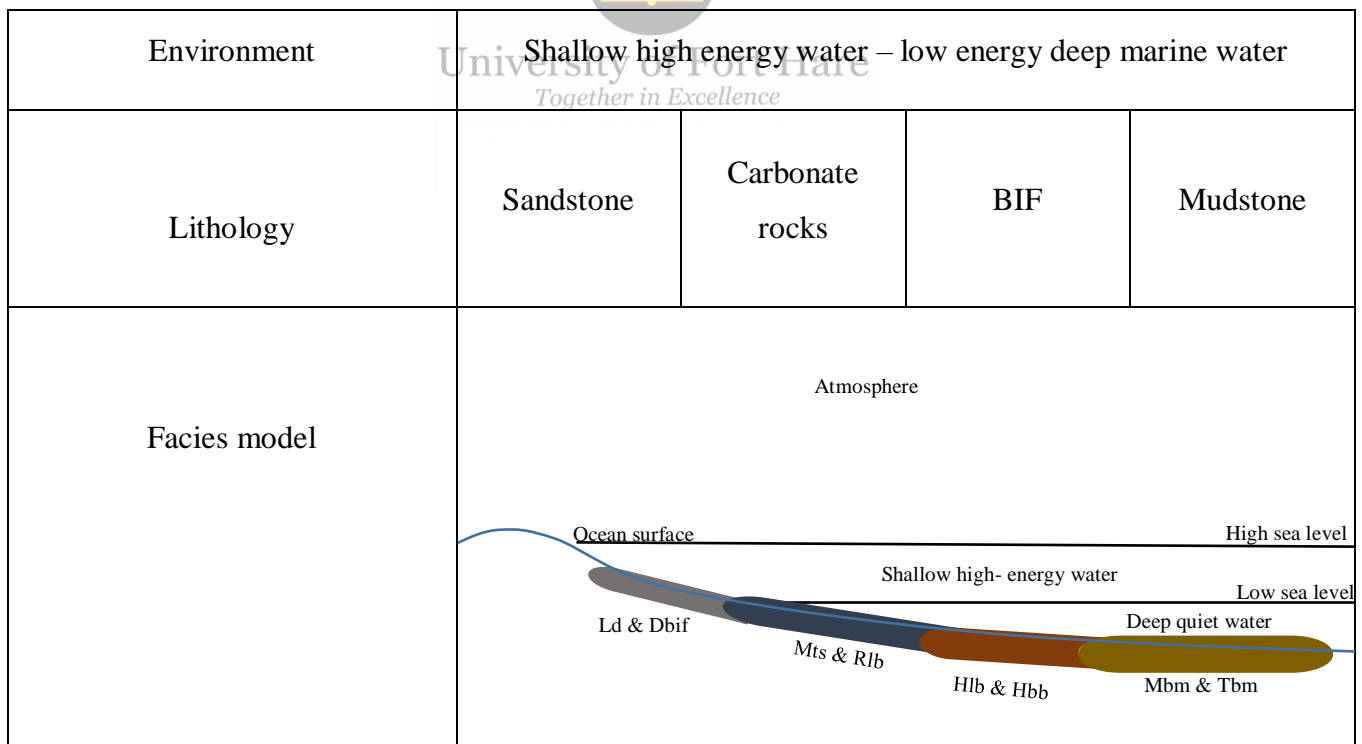


Figure 5. 11: Depositional model of the Kuruman Formation in the Prieska area, showing different facies distribution and their respective depositional environments (adopted from Walker, 1976 and Anderton, 1985).

CHAPTER 6. MINERALOGY AND PETROGRAPHY OF THE BIF

6.1. Mineralogy

The mineral assemblages found from the weathered Kuruman Formation outcrops in the Prieska area are iron oxides, silica (quartz), iron silicates, and carbonates. The different types of minerals encountered are listed in Table 6.1, and their abundances are displayed in Figure 6.1. The mineral abbreviations for the different mineral types are listed in Table 6.2.

Table 6. 1: Major minerals of the weathered Kuruman BIF outcrops in the Prieska area identified by XRD, optical microscopy, and SEM-EDX analysis. The minerals are listed with their chemical compositions.

Iron oxides	Hematite	Fe_2O_3
	Magnetite	Fe_3O_4
	Martite	Fe_2O_3
	Goethite	$\text{FeO}(\text{OH})$
	Limonite	$\text{Fe}_3\text{O}_4 \cdot n\text{H}_2\text{O}$
Silica and Silicates	Quartz	SiO_2
	Stilpnomelane	$\text{KFe}^{2+}_{4.3}\text{Mg}_{1.4}\text{Fe}^{3+}_{2.3}\text{Si}_{10}\text{Al}_2\text{O}_{24}(\text{OH})_3 \cdot 2(\text{H}_2\text{O})$
	Riebeckite	$\text{Na}_2\text{Fe}^{2+}_3\text{Fe}^{3+}_2(\text{Si}_8\text{O}_{22})(\text{OH})_2$
	Minnesotaite	$\text{Fe}^{2+}_{2.5}\text{Mg}_{0.5}\text{Si}_4\text{O}_{10}(\text{OH})_2$
	Illite	$(\text{K}, \text{H}_3\text{O})(\text{Al}, \text{Mg}, \text{Fe})_2(\text{Si}, \text{Al})_4\text{O}_{10}[(\text{OH})_2, (\text{H}_2\text{O})]$
Carbonates	Ankerite	$(\text{FeCaMg})\text{CO}_3$
	Siderite	FeCO_3
	Calcite	CaCO_3
	Dolomite	$(\text{CaMg})\text{CO}_3$

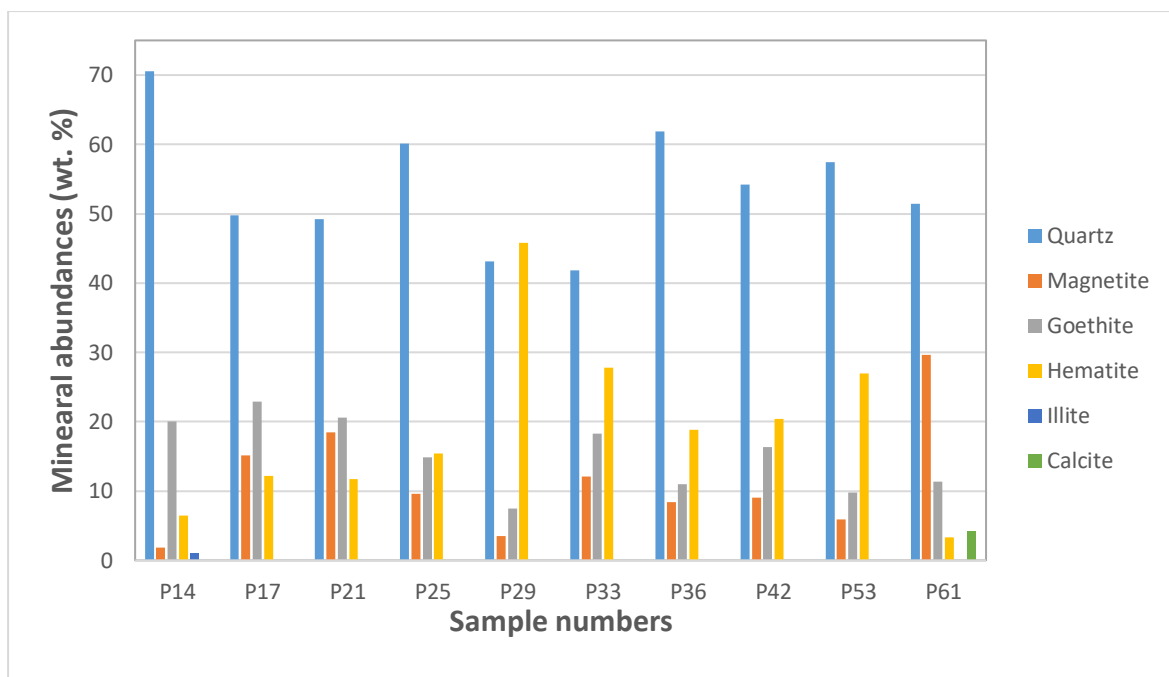


Figure 6. 1: Variation diagram showing the mineral types and abundances of the weathered Kuruman BIF in the Prieska area. The plot was generated from X-Ray Diffraction (XRD) results.



Table 6. 2: Table of mineral abbreviations.

Mineral name	Abbreviation
Hematite	Hem
Goethite	Gth
Magnetite	Mag
Martite	Mat
Quartz	Qz
Stilpnomelane	Stp
Minnesotaite	Mns
Riebeckite	Rbk
Calcite	Cal
Siderite	Sd
Ankerite	Ank

6.1.1. Iron oxides

The iron oxides are the other dominant mineral assemblage after the quartz, constituting about 45.5 wt-% (Fig. 6.1). Hematite represents about 41 % of the iron oxides, goethite (34 %), and magnetite (25%) (Fig. 6.1). Limonite was also observed from the field investigations. The hematite, magnetite, and goethite from the samples appear in different textures and sizes as grains, matrix, and cement.

Hematite

The hematite occurs as the dominant iron oxide supported by the XRD, SEM, and microscope study. It appears bright white in reflected light while opaque in transmitted light photographs displaying a reddish colouration due to weathering (Fig. 6.2). It occurs as a primary mineral while it also appears as a secondary mineral replacing other iron oxides, silica, iron silicates, and carbonate minerals during diagenesis. Hematite displays different forms and textural patterns between the samples and various bands. Under the microscope, hematite appears as subhedral grains and euhedral crystals due to recrystallization, whereas the anhedral forms are the common components of the hematite matrix and cement. This diversity makes the distinction between primary and secondary hematite challenging in highly modified martite and hematite bands. Microcrystalline platy hematite is the most common pattern, occurring as grains, matrix, and cement (Fig. 6.2). The specular hematite is mainly found in the martitizing zones. The hematite crystals are associated with quartz, riebeckite, and altered carbonates.

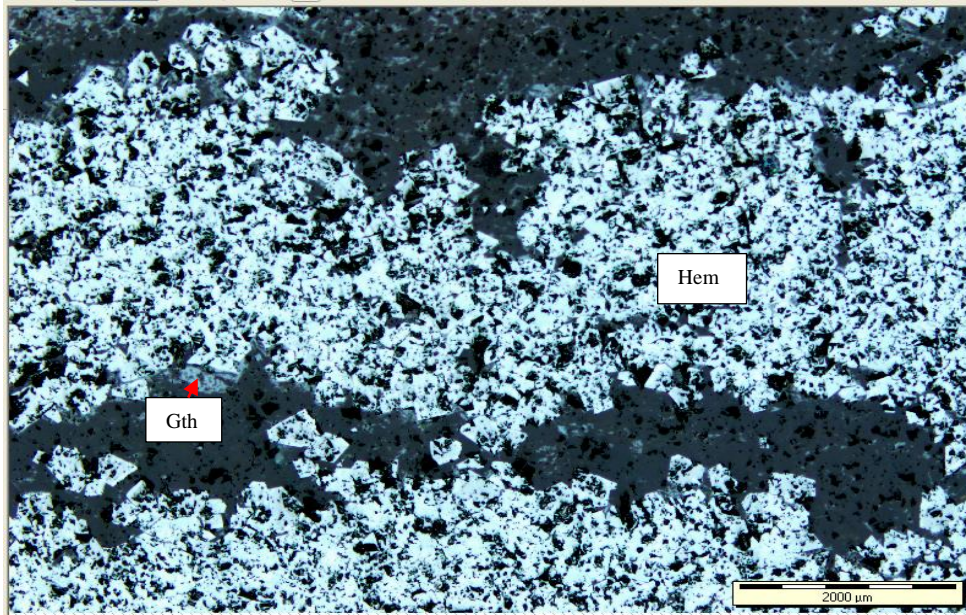


Figure 6. 2: Reflected light photomicrographs showing porous microcrystalline hematite (Hem) occurrence.

Martite

Martite is a secondary hematite pseudomorph that occurs in the Prieska BIF rocks (Fig. 6.3). Martite occurs in hematite-magnetite and hematite-goethite coexistences. The maghemite pseudomorph after magnetite and specularite are closely associated with martite.

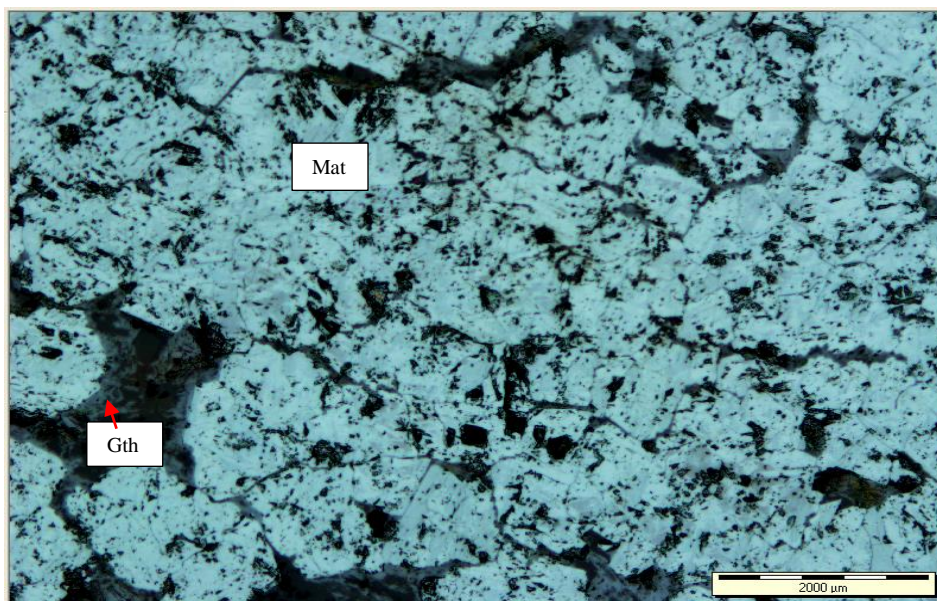


Figure 6. 3: Reflected light photomicrographs showing a massive, less porous martite (Mat) with goethite (Gth).

Magnetite

Magnetite occurs as one of the major iron oxides in the study area. It appears opaque under transmitted light showing black colour in the micro and mesobands while pale greenish in reflected light (Fig. 6.3). Magnetite is commonly coarser-grained than hematite. It occurs as a primary precipitate even though secondary forms are also present. Magnetite occurs as subhedral to euhedral well-formed crystals in some iron-rich bands (Fig. 6. 3B). Magnetite commonly occurs with hematite and goethite in the strongly altered bands. Magnetite can be oxidized to hematite, martite, and goethite upon exposure to the Earth's surface. Specular hematite is the common variety associated with magnetite from the samples (Fig. 6.3A).

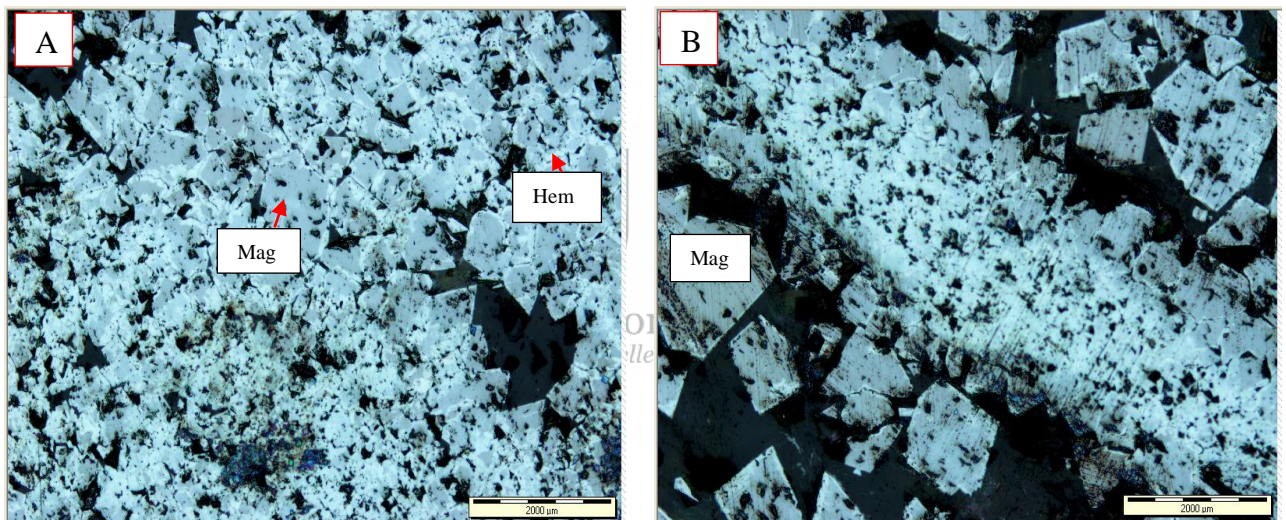


Figure 6. 4: Reflected light photomicrographs showing (A) Martitizing grains containing magnetite (Mag) at the centre and rims of specular hematite (Hem) at the grain boundaries; (B) Magnetite (Mag) grains forming a dense martitising microband in the centre and large euhedral magnetite crystals at the top and bottom corners of the photograph.

Goethite

Goethite is the second abundant iron oxide mineral after hematite in the study area (Fig. 6.1). It appears opaque in transmitted light while pale blueish under reflected light microscopy (Fig. 6.4). Goethite appears as a secondary mineral replacing the other iron oxides, silica, silicates,

or carbonate minerals. It is commonly cryptocrystalline to microcrystalline, and it occurs as small, porous isolated subhedral to anhedral crystals or xenomorphic blasted shapes. Goethite is commonly occurring as matrix and cement (Fig. 6.4B), although rare coarse goethite grains are encountered.

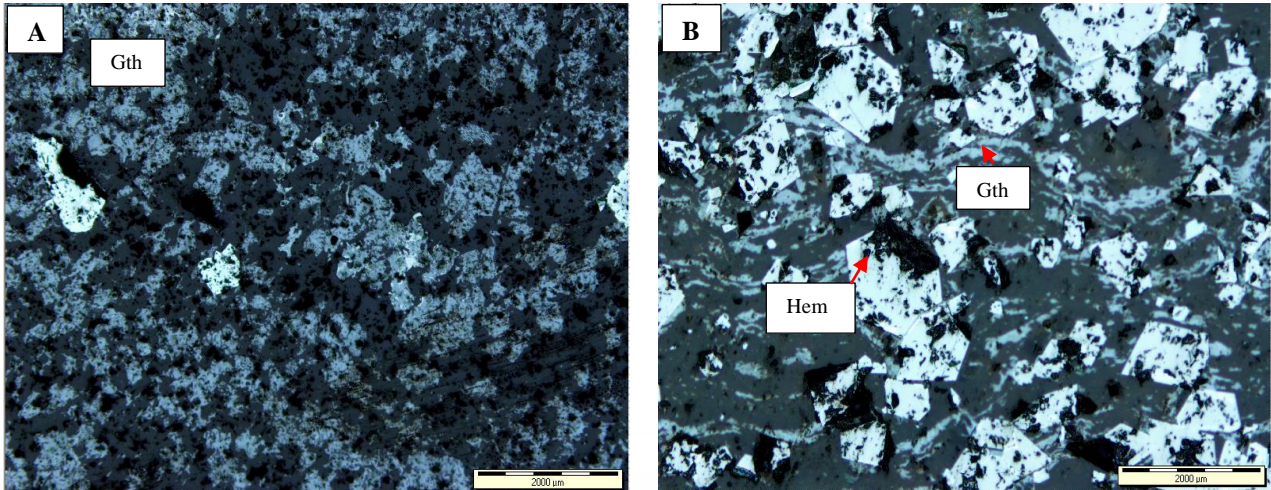


Figure 6. 5: Reflected light photomicrographs showing (A) Porous goethite (Gth) crystals; (B) Goethite (Gth) matrix and cement occurring with white subhedral to euhedral hematite (Hem) grains.

University of Fort Hare
Together in Excellence

Limonite

Limonite is another iron oxide identified in the field and confirmed by optical microscope and SEM-EDX. It is an impure hydrated iron mineral (with variable water content) with a colloidal, soil/ powder-like, or amorphous character. Limonite is often brownish to orange-yellow coloured and earthy. It is a secondary mineral formed by alteration of other iron oxides. It could be formed from the hydration of hematite or magnetite. Its formation is related to oxidation and hydration of the iron oxides or iron carbonate minerals such as siderite on the weathering crust. Figure 4.9, 4.10, and Figure 8.22 show the occurrence of limonite.

6.1.2. Silica and silicate minerals

A silicate mineral assemblage is a big group of minerals with silica composition in the formula. The silica and silicate minerals are described in detail below.

Quartz

Quartz is a major mineral constituent amongst the samples constituting about 53.95 average wt.% (Fig. 6.5). It appears whitish in transmitted light while dark or greyish in reflected light and SEM photomicrographs (Fig. 6.5 & 6.6). Quartz is a primary and also secondary mineral constituent formed from the recrystallization of the cryptocrystalline chert. It exists as polycrystalline, monocrystalline grains, as well as quartz cement. In the BIF, the quartz grains display different grain sizes and shapes from rounded, sub-rounded, sub-angular to angular and irregular. The flaky and chalcedonic quartz are also encountered within the BIF samples under the microscope. During diagenesis, chert could be changed to chalcedony, microcrystalline quartz, and fine quartz with increased temperature and burial depth. The quartz is associated with rhomb-shaped, mostly hematite and goethite pseudomorphs of the carbonate minerals (Fig. 6.5). The flaky, fibrous quartz and long quartz fringes are more pronounced parallel to deformation and pressure shadows adjacent to the iron oxide micro-bands.

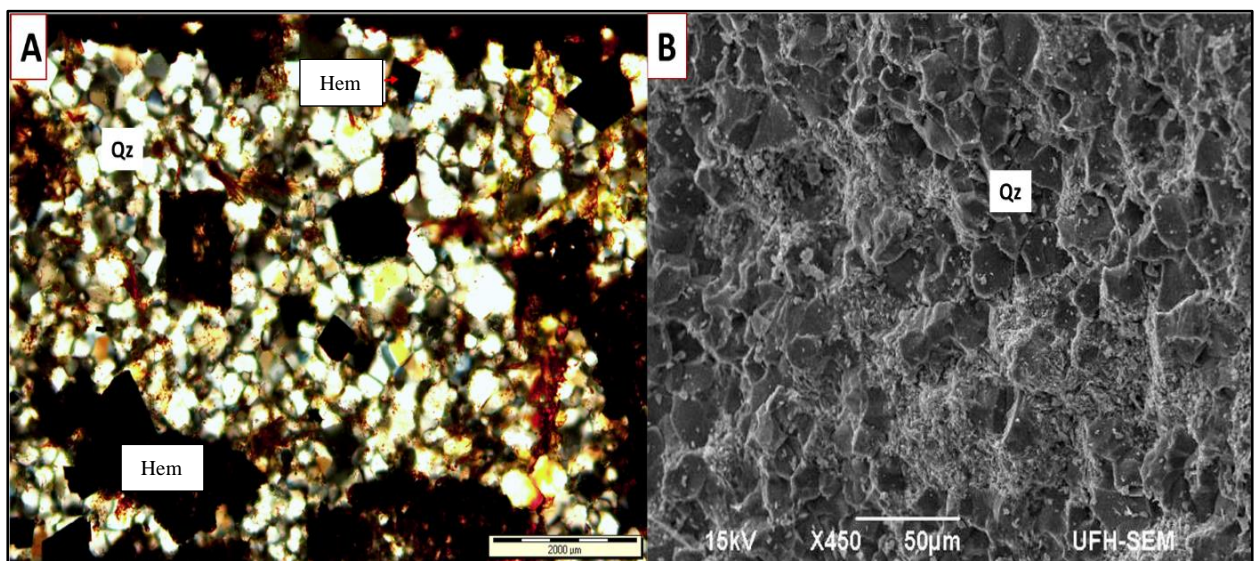


Figure 6. 6: Transmitted light photomicrograph (A) and SEM photomicrograph (B) showing detrital quartz (Qz) grains occurring with hematite (Hem).

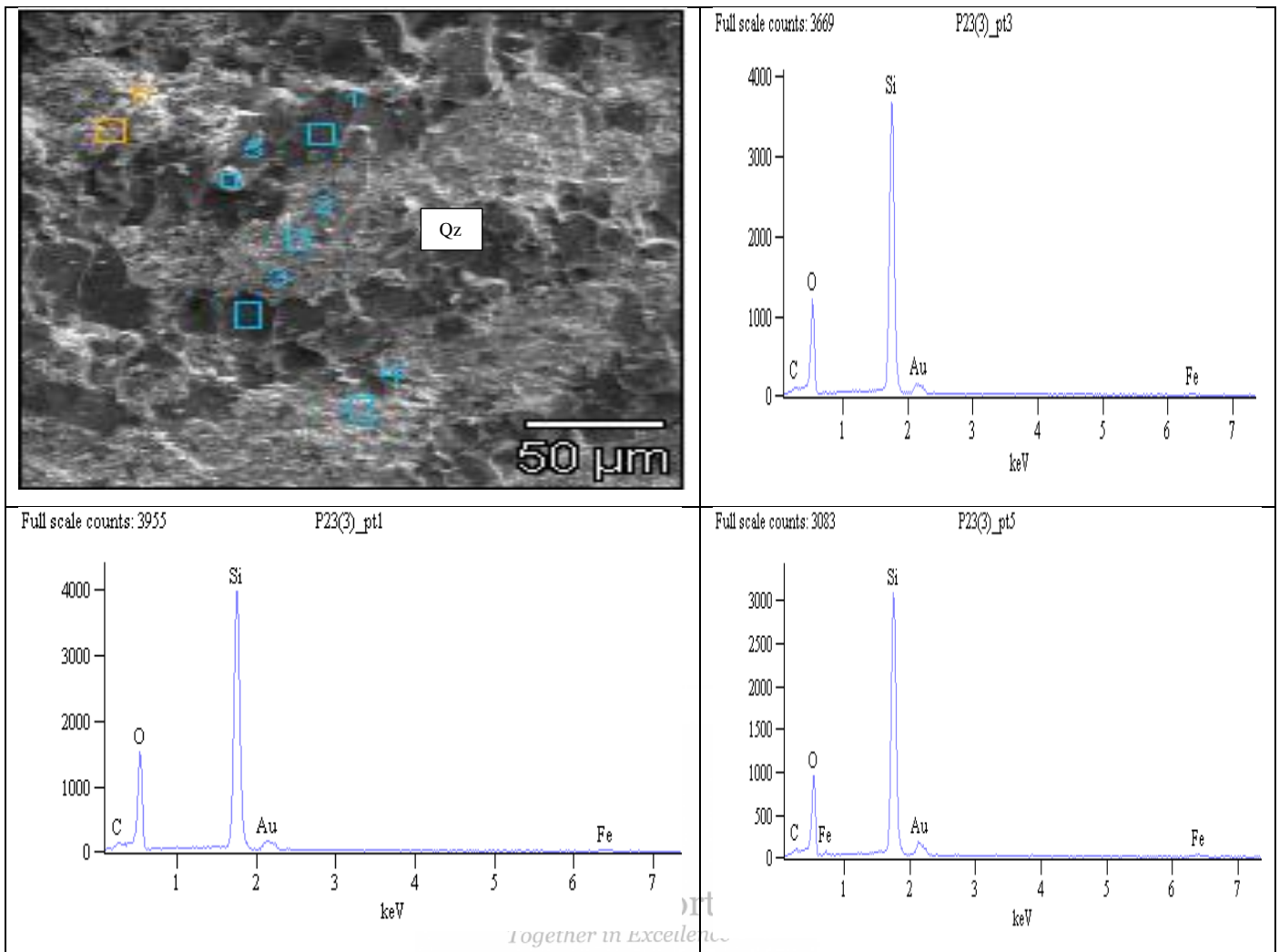


Figure 6. 7: SEM-EDX photomicrograph showing quartz (Qz) grains (dark coloured). Au peak is due to Au-coating.

Silicate minerals

The silicate minerals identified within the BIF samples include stilpnomelane, riebeckite, minnesotaite, and clay minerals.

Stilpnomelane

Stilpnomelane is one of the main silicate minerals of the Prieska BIF. It appears as the common silicate mineral shown by the optical microscope and SEM. Stilpnomelane occurs as pale

yellowish, pale brownish, blackish, or light greenish-yellow colours in the transmitted light microscope (Fig.6.7).

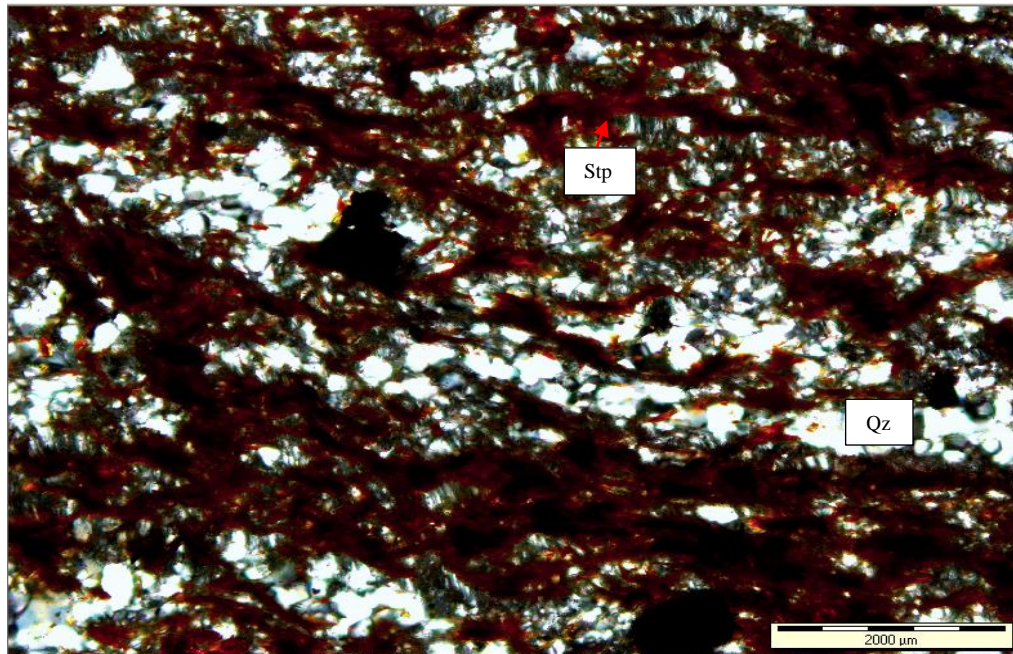


Figure 6. 8: Transmitted light photomicrographs showing stilpnomelane (Stp, red-brownish) and quartz (Qz) occurrence.

University of Fort Hare
Together in Excellence

Riebeckite

Riebeckite is the other silicate mineral after stilpnomelane found in the BIF sequence. Minor riebeckite crystals occur as circular or flaky tiny crystals randomly distributed in the quartz-rich micro and mesobands (Fig. 6.8). The dark blue, dense riebeckite crystals were spotted predominantly within chert-rich micro and mesobands and at the interface between chert and iron oxide microbands (Fig. 6.8). It is associated with chert and magnetite microbands containing randomly dispersed brownish stilpnomelane.

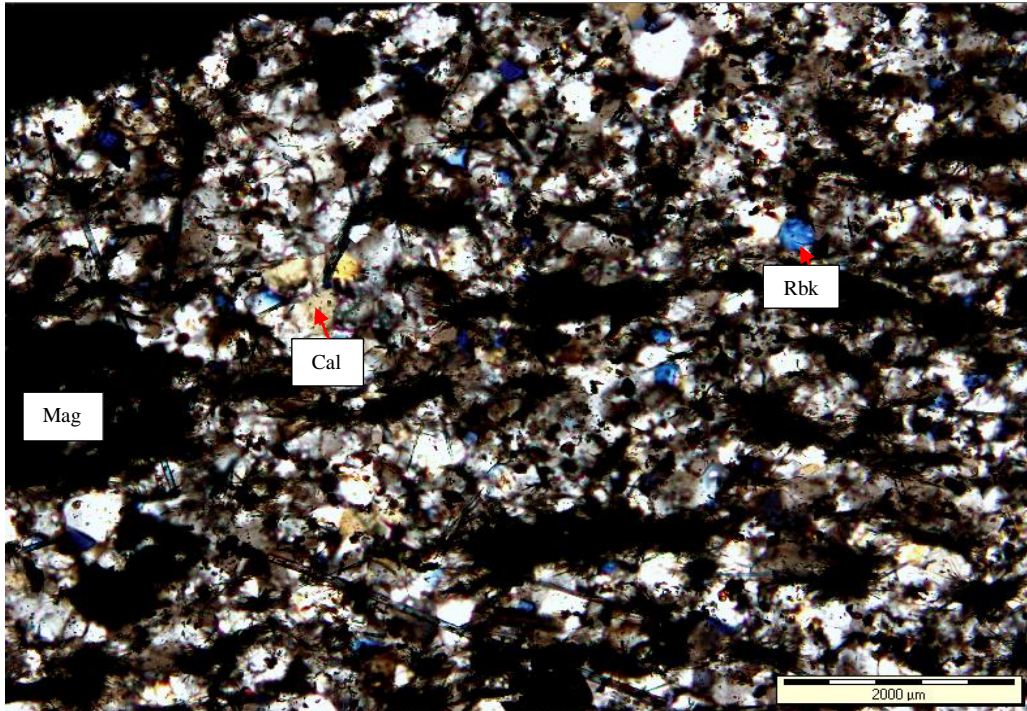


Figure 6. 9: Transmitted light photomicrographs showing blueish riebeckite (Rbk), whitish quartz, pinkish calcite (Cal), and dark magnetite (Mag) crystals.



University of Fort Hare
Together in Excellence

Minnesotaite

Minnesotaite also represents the silicate minerals within the samples, although it appears in a minor amount. It occurs as fine needles and platelets of colourless to pale greenish-yellow crystals with other silicates. Traces of minnesotaite are rarely spotted in the quartz-rich bands. It was identified based on the microscope studies.

Clay minerals

Smectite and illite are the common clay minerals representing the silicate assemblage. These clay minerals are found within the samples and could become the major minerals in the clay-rich bands. Illite and smectite were identified by the XRD, SEM-EDX, and microscope (Fig. 6.9), and they are primary and could be secondary minerals in origin. Smectite is a primary mineral deposited in a relatively deep water environment. In contrast, illite is usually a secondary mineral that recrystallized from smectite during diagenesis with the temperature

increase due to deep buried. Illite can change to sericite and muscovite if the burial temperature increases in the diagenetic environment.

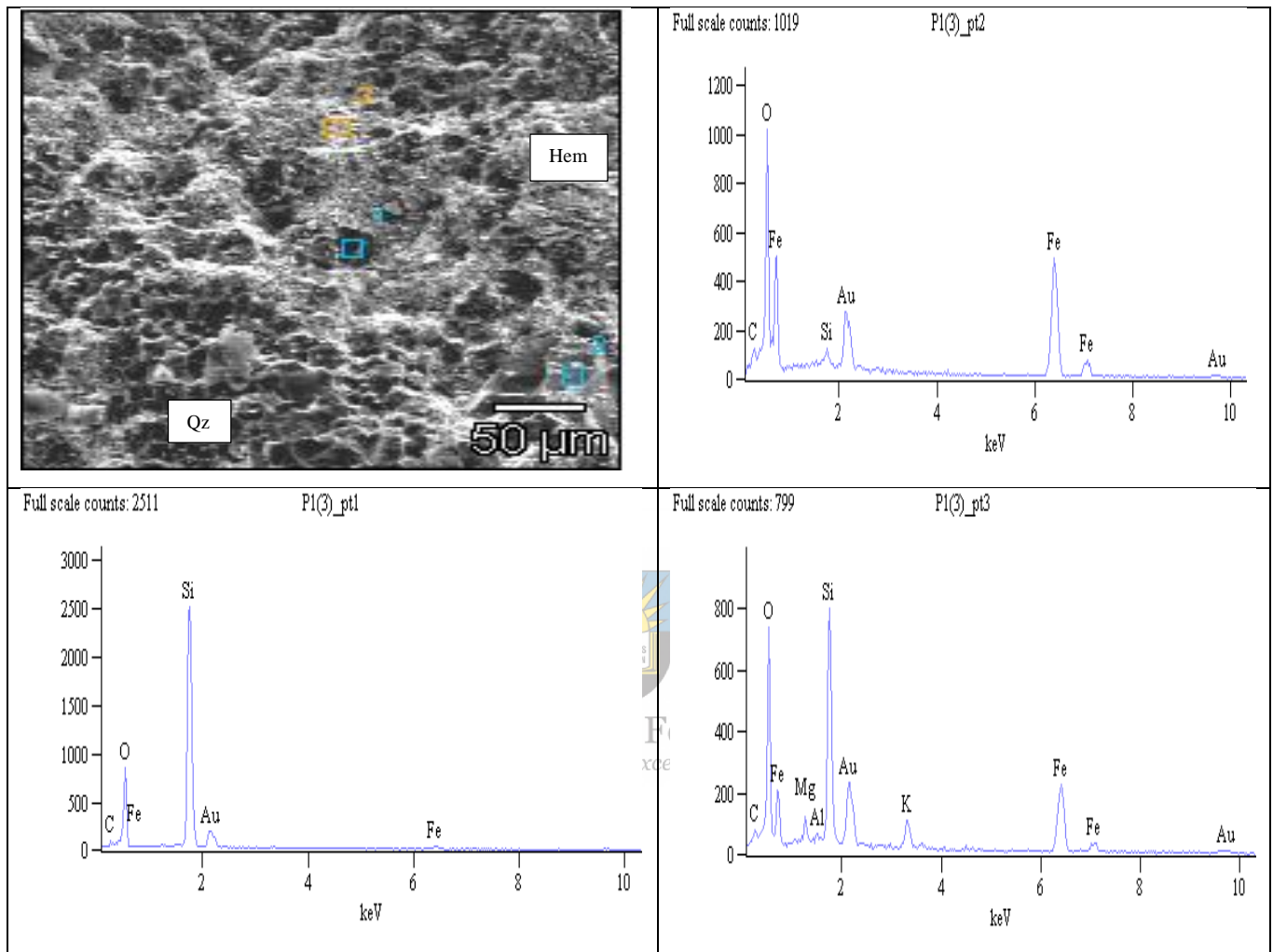


Figure 6. 10: SEM-EDX photomicrograph showing the occurrence of iron-oxide (Point 1, top-right), Quartz (Point 2, bottom left), and iron-bearing clay minerals (Point 3, bottom right)) in the BIF samples. Au peak is due to Au-coating.

6.1.3. Carbonate minerals

Different types of carbonate minerals were encountered in the rock samples during lab analyses. These carbonates were in minor concentrations compared to iron oxides and silicate minerals, accounting for less than 2 wt.% of the mineral assemblages (Fig. 6.10). The carbonate assemblages' existence is inferred from the rhombic-shaped crystals that have sometimes been

replaced by quartz and iron-oxides (Fig. 6.8). These carbonate minerals include siderite, ankerite, calcite, and dolomite, which constitute the dominant carbonate fraction of the Kuruman Iron Formation (Beukes, 1983, 1984; Lewy, 2011). Ankerite is commonly coarser-grained than siderite. Siderite appears in varieties that include the brighter iron-rich and the dull magnesium-rich types under the reflective light microscope. Calcite and dolomite presence was also confirmed by the XRD and microscope studies. These carbonate minerals appear with porosity differences due to post-depositional alteration (dissolution).

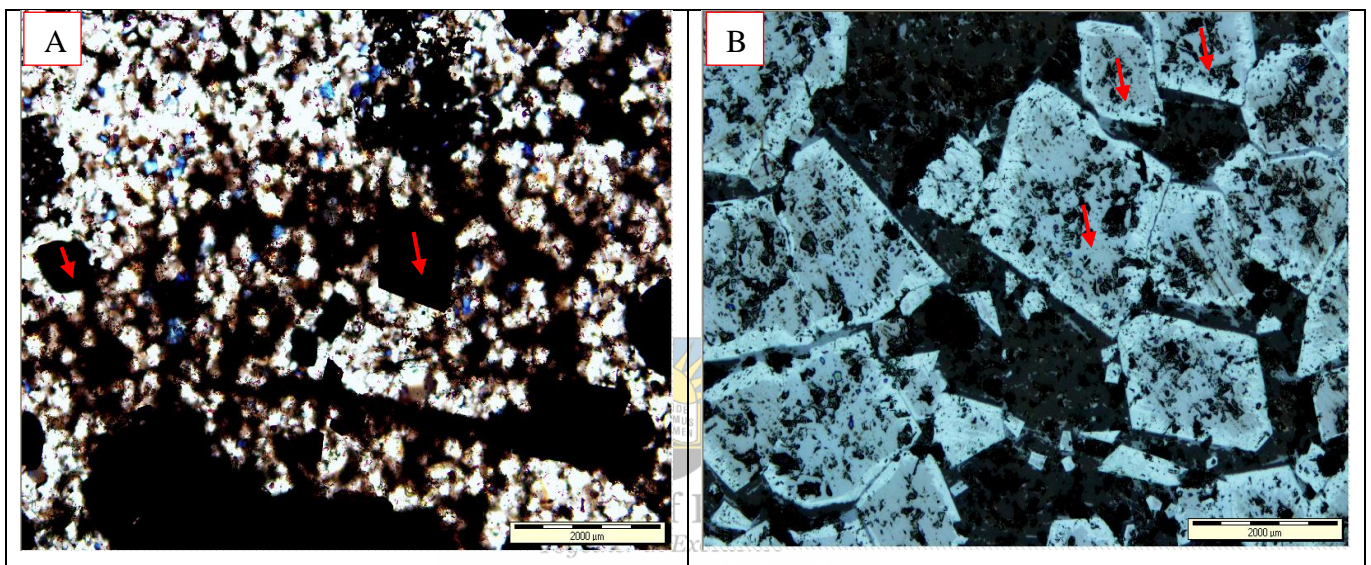


Figure 6. 11: Transmitted light (A) and reflected light (B) photomicrographs showing rhombic iron-oxide (hematite) pseudomorphs (red arrows) after replacing carbonate mineral precursor.

6.2. BIF Petrography and occurrence

The Prieska BIF comprises the iron-rich minerals (hematite, martite, goethite, and magnetite) occurring with chert (quartz)-rich, mud-rich, and carbonate-rich minerals. These mineral assemblages occur mixed in the same micro- or mesobands. They also occur as micro or mesobands that alternate together.

6.2.1. Iron-oxides occurrence

The iron-oxide minerals occur with chert (quartz), mud (silicate minerals), and carbonate minerals.

Iron oxides with chert (quartz) occurrence

Subordinate iron oxides that occur as lenticulars, stringlike laminations, or form braided microband texture occur with chert (quartz). The chert (quartz) contain minor carbonate minerals and traces of iron silicate minerals that impregnate them and impart characteristic tints of dark brown, yellowish-brown, or blue colours in plane polarised light (Fig. 6.12B). These colours highlight the presence of stilpnomelane, minnesotaite, and riebeckite, respectively.

The iron-rich bands are alternating with 0.1 mm to 0.5 mm thick chert (quartz)-rich microbands and 0.75mm to 1.2 mm thick chert (quartz)-rich mesobands (Fig 12 & 13). The chert-rich microbands occur in thin bands of various sizes separated by iron oxide-rich bands (Fig. 6.12). They appear as continuous bands (Fig. 6.12A) and as lenticulars separated by iron oxides (Fig. 6.12B). The quartz-rich lenticulars could be formed due to shear stress, but there are also primary originated lenticular bands in the BIF sequence. The contacts between the iron-rich and chert (quartz)-rich micro and mesobands are abrupt between some bands while they are semi-gradational in others.

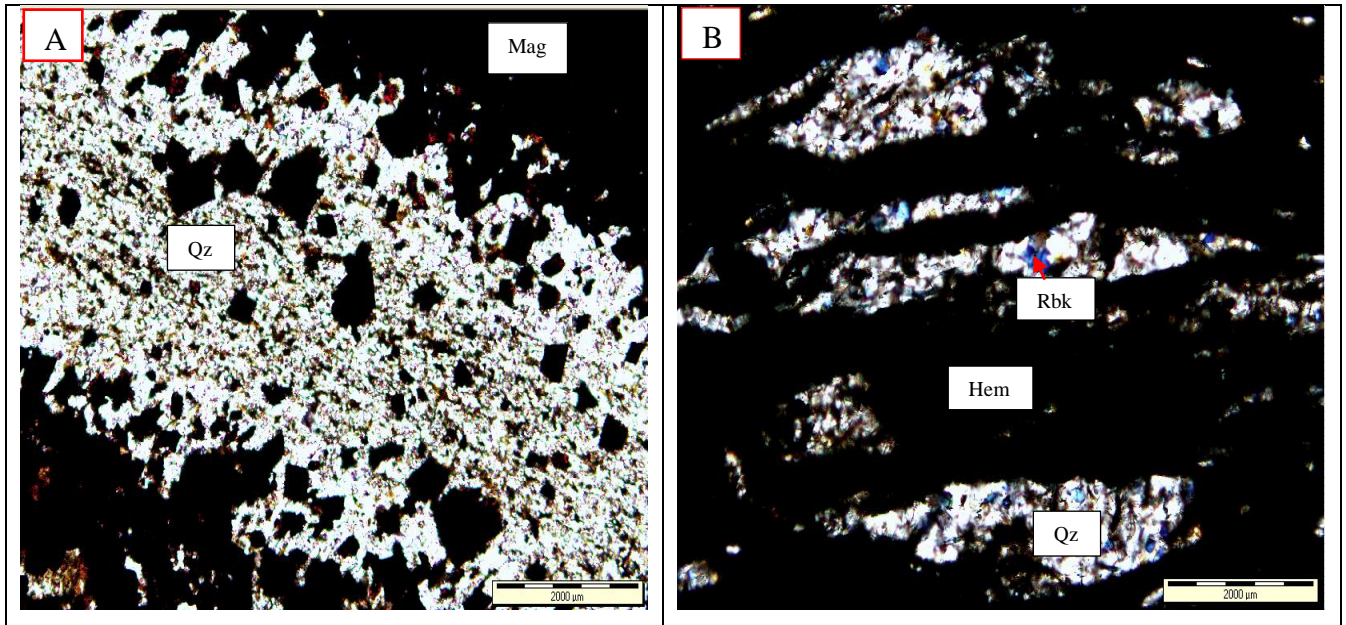


Figure 6. 12: Transmitted light photomicrographs showing (A) Iron oxide (Mag, dark area) subordinate grains and minor iron silicates in quartz-rich mesoband (Qz, white area); (B) Chert (quartz)-rich lenticular bands (Qz, white) with minor riebeckite (Rbk, blue) between hematite-rich microbands (Hem, dark area).

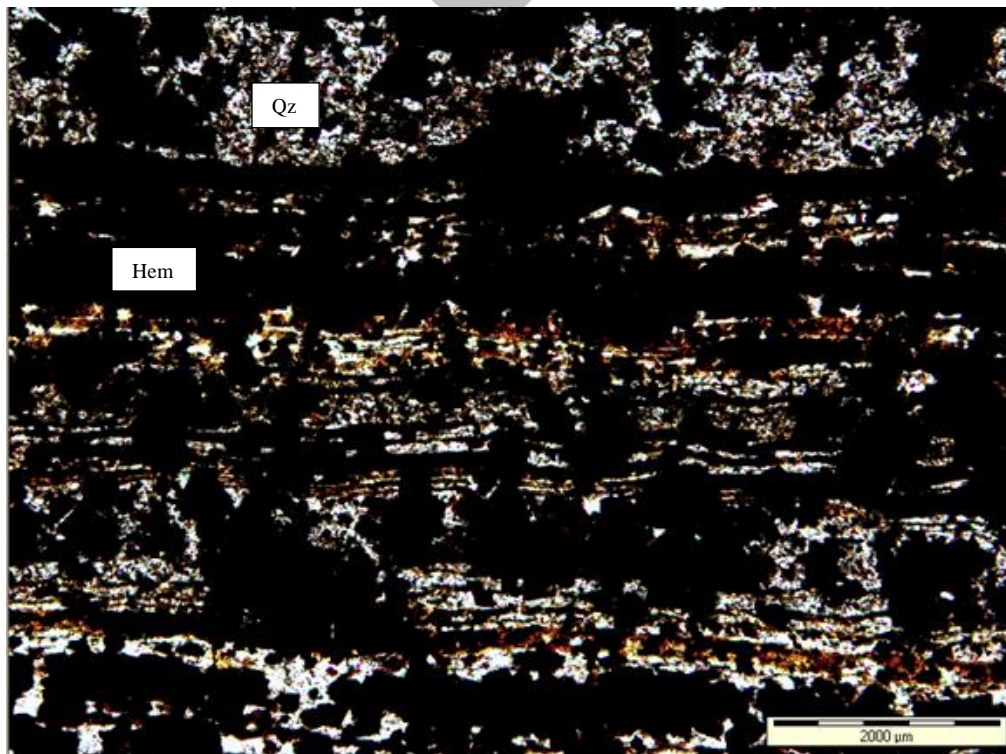


Figure 6. 13: Transmitted light photomicrographs showing the dark iron oxide-rich (Hem) and white chert/quartz-rich (Qz) micro and mesobands.

Iron oxides with carbonate occurrence

The co-occurrence of the iron oxide and carbonate minerals is indicated by the presence of hematite and goethite pseudomorphs of the carbonate minerals (siderite, ankerite, and calcite) within the iron-rich micro and mesobands (Fig. 6.10). These iron oxide-carbonate bands occur with minor quartz. They contain finely disseminated chert inter-grown with hematite. The micro and mesobands exhibit relatively planar to wavy contacts, either sharp or graded. These bands occur in zones or patches and as isolated grains.

Iron-oxides with silicate occurrence

The iron-oxides are found in the same micro or mesoband with the silicate minerals (stilpnomelane, riebeckite, or clay minerals) (Fig. 6.14). These bands commonly contain varying chert (quartz) contents. They occur alternating with the iron-rich micro and mesobands (Fig. 6.14B).

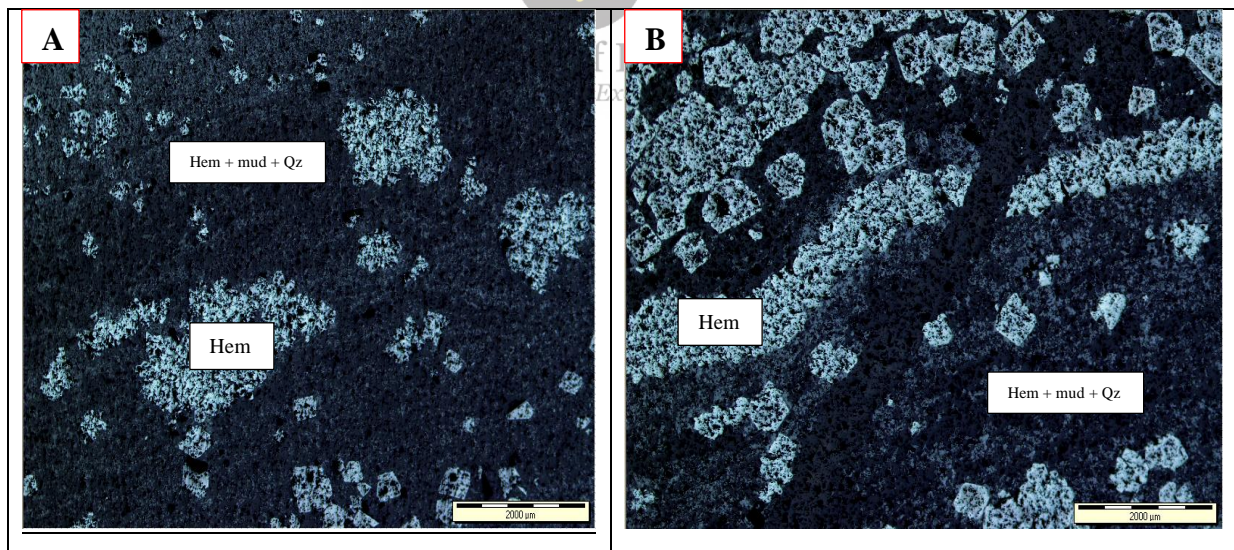


Figure 6. 14: Reflected light photomicrographs showing (A) A dull, porous band consisting of the iron minerals mixed with silicate minerals (mud) and chert (Qz). There are also various sized hematite-rich patches and isolated grains (Hem); (B) Porous, loose disseminated hematite (Hem) grains at the top alternating with hematite-rich lamination and the mixed band of iron minerals, silicate, and chert (quartz) at the bottom. These bands have been cross-cut by a later quartz vein.

6.2.2. Iron-oxide-rich bands

The iron-oxide-rich micro and mesobands are dominantly constituted by the iron-oxide minerals (hematite, martite, goethite, limonite, and magnetite) with minor chert (quartz) and traces of carbonate and silicate minerals. These iron-oxide minerals occur as isolated grains or occur close to each other forming micro and mesobands. Thus the iron-rich micro and mesobands in the Prieska BIF occur as partially ferruginous bands, disseminated iron-rich bands, patchy iron-rich bands, laminated iron-rich bands, uniform iron-rich bands, and highly leached iron oxide-rich bands. These bands are discussed below.

Partially ferruginous bands

The partially ferruginous bands are composed of the iron oxide minerals (commonly hematite and goethite) occurring with chert (quartz) (Fig. 6.15A). These minerals are commonly occurring intermixed and displaying fine-grained anhedral textures (Fig. 6.15A&B). The fine iron minerals in these minerals indicate that they replace the silicate minerals in previously chert (quartz)-rich bands. The partially ferruginous bands occasionally contain few isolated coarse-grained hematite crystals (Figure 6.15B).

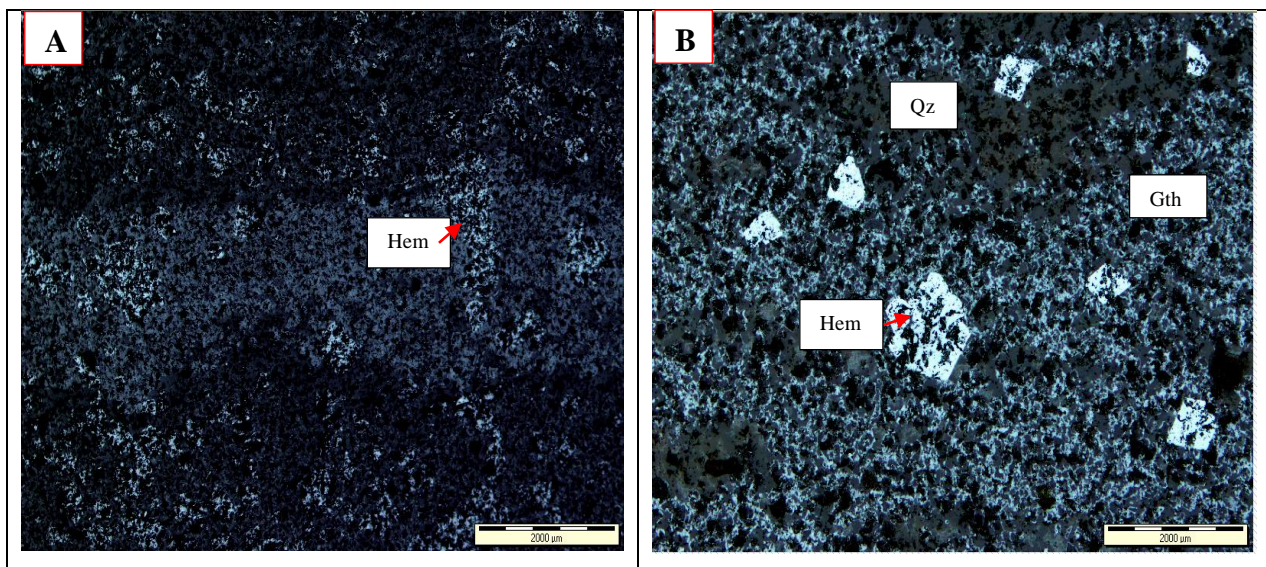


Figure 6. 15: Reflected light photomicrographs showing (A) Horizontal to wavy contacts between iron oxide-rich (whitish) and quartz-rich (dark) microbands; (B) Hematite (Hem), goethite (Gth), and quartz (Qz) in partially ferruginous mesoband.

Laminated iron oxide-rich bands

The laminated iron oxide-rich bands comprise the iron oxide minerals (hematite, magnetite, martite, and goethite) occurring in laminations (Fig. 6.16). The individual lamellae or bands are few millimetres to centimetres thick. The laminations are commonly containing a mixture of two or more iron oxide minerals. Some bands are dominated by magnetite, while others are dominated by hematite (Fig. 6.16A). Other bands are predominantly constituted by martite, while some bands are dominated by goethite (Fig. 6.16B).

The monomineralic laminated iron oxide-rich bands were rarely encountered in the study area. Some of these bands contain the iron oxide minerals mixed with chert (quartz). Some of the mesobands consist of faint and dull goethite-rich microbands with disseminated hematite grains. Small hematite clusters constitute some bands. The bands contain coarse-grained martite crystals with goethite cement (Fig. 6.16B). The bands' boundaries are either sharp or planar while undulating in other bands (Fig. 6.16). Some of the iron-oxide-rich micro and mesobands show small folding resulting from late-stage diagenesis.

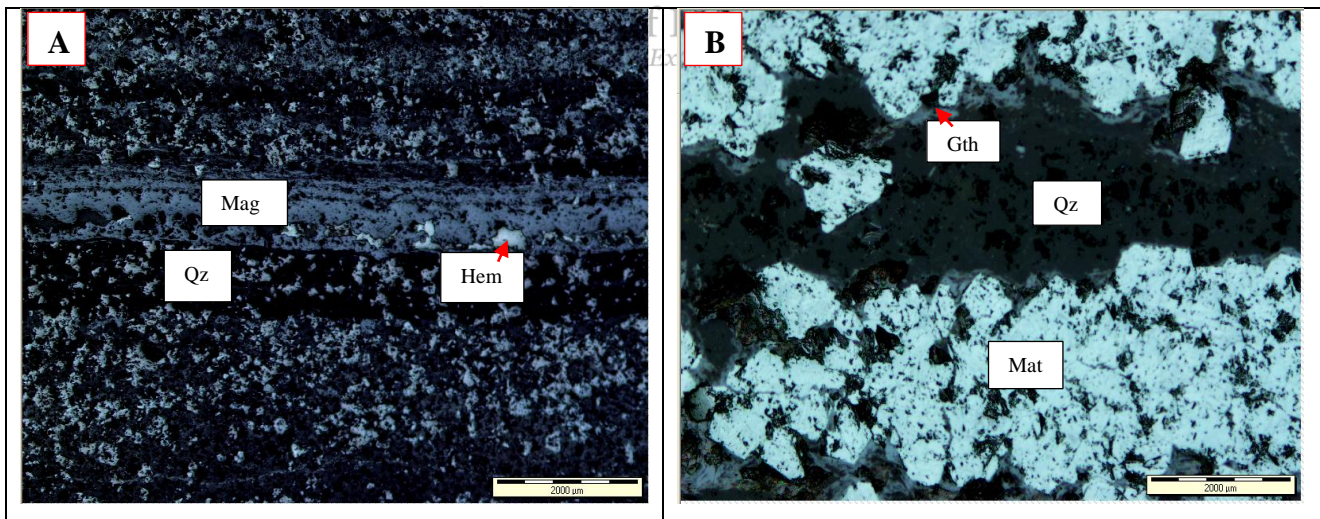


Figure 6. 16: Reflected light photomicrographs showing (A) Magnetite-rich (Mag) band at the centre alternating with quartz-rich (Qz) band and hematite-rich (Hem) at the bottom; (B) Martite-rich bands (Mat) (at the top and bottom) alternating with quartz-rich bands (Qz) (in the middle).

Uniform iron-rich bands

The uniform iron-rich micro and mesobands commonly contain massive martite grains that occur in clusters. These are dense, less porous iron-rich bands containing coarse-grained martite crystals. They occur with varying quartz amounts that occur as either grains, matrix, or cement (Fig. 6.17).

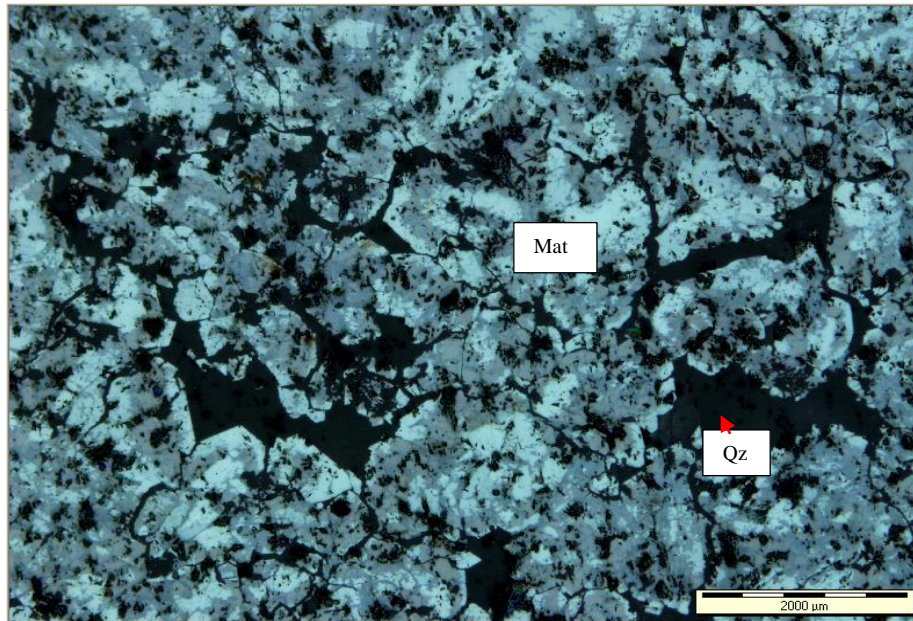


Figure 6. 17: Reflected light photomicrographs showing a massive less porous martite (Mat) forming a uniform iron-rich band. There is a presence of magnetite remains. Hematite appears to be invading magnetite crystals from outside inwards.

Patchy iron-rich bands

The patchy iron-rich bands occur as discrete patches or pockets of iron-rich minerals. The common iron minerals in these bands are hematite and martite (Fig. 6.18). These patchy bands are comprising porous microcrystalline hematite crystals (Fig. 6.18A). Some of these bands are composed of less porous coarse-grained martite grains with goethite cement. The martite is occurring in those bands is massive and subhedral to euhedral (Fig. 6.18B). These bands commonly occur with minor quartz. The bands are interlayered with chert (quartz) or other iron oxide-rich bands.

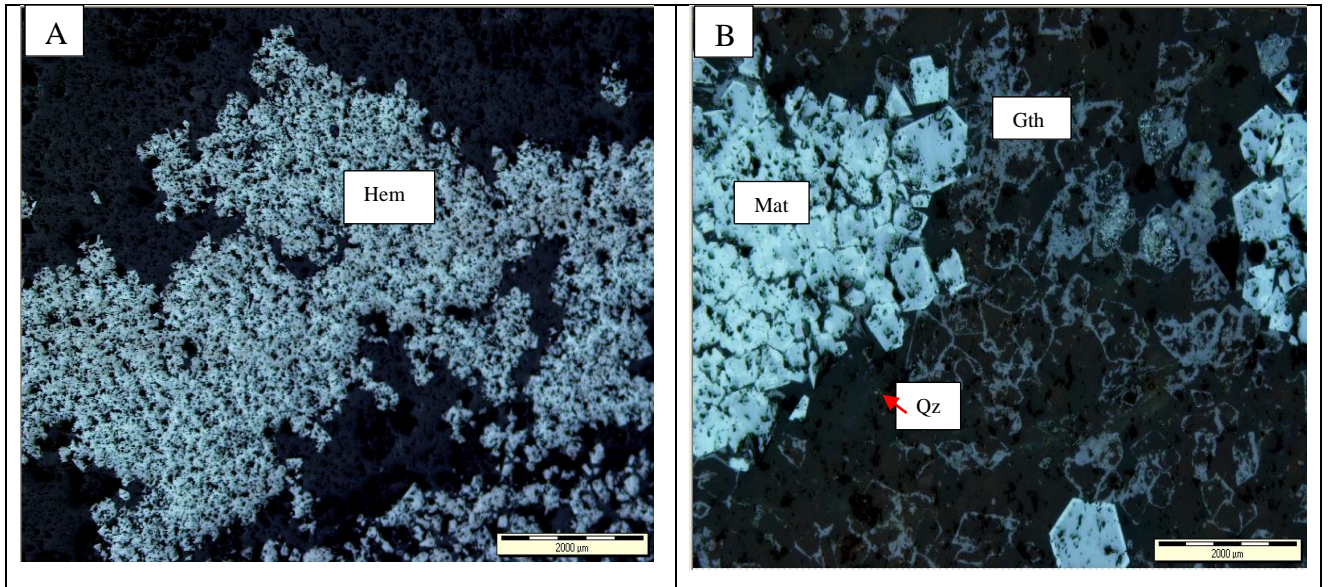


Figure 6. 18: Reflected light photomicrographs showing (A) Porous microcrystalline earlier magnetite replaced by fine hematite (Hem) crystals; (B) Massive coarse-grained martite (Mat) crystals occurring with quartz (Qz) and goethite (Gth).

Bands with disseminated iron-rich crystals in a quartz cement



The disseminated iron-rich bands are comprised of the iron oxide minerals (hematite, magnetite, or goethite) occurring as loose grains or patches in a matrix or cement (Fig. 6.19). These iron-oxide grains commonly occur with minor quartz. The matrix or cement can either be quartz-rich (Fig. 6.19A, B, & C) or iron oxide-rich (Fig. 6.19D). Some of the grains occur following sub-linear to linear trends. Some bands comprise diffusive, massive, dense, microcrystalline hematite crystals that display a weak banding (Fig. 6.19B).

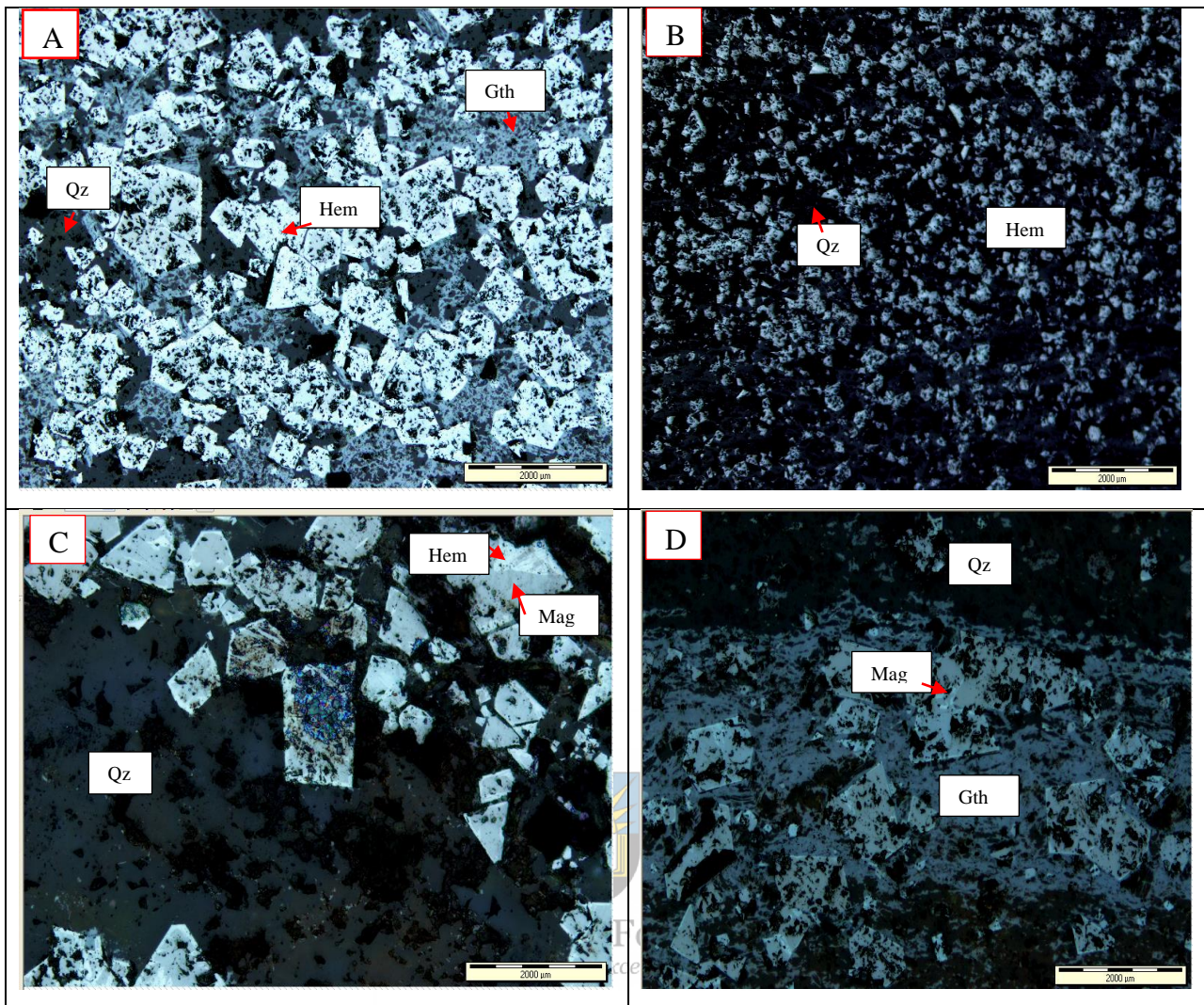


Figure 6. 19: Reflected light photomicrographs showing (A) Disseminated porous hematite (Hem) and porous goethite (Gth) crystals; (B) Diffusive, massive, dense, microcrystalline hematite (Hem) crystals that display a weak banding; (C) Disseminated magnetite crystals (Mag) occurring with quartz (Qz); (D) Disseminated magnetite crystals (Mag) in a goethite-rich matrix (Gth).

Highly leached iron oxide-rich bands

The highly leached iron oxide-rich bands consist of a variety of the above-discussed iron oxide-rich bands (partially ferruginous, laminated, brecciated, irregular, and conglomeratic). These bands have experienced leaching as a result of post-depositional alteration. These bands predominantly consist of porous goethite with subordinate amounts of hematite and martite

(Fig. 6.20). Goethite occurs as filling within the voids and cavities. The iron oxide minerals commonly occur with various quartz quantities.

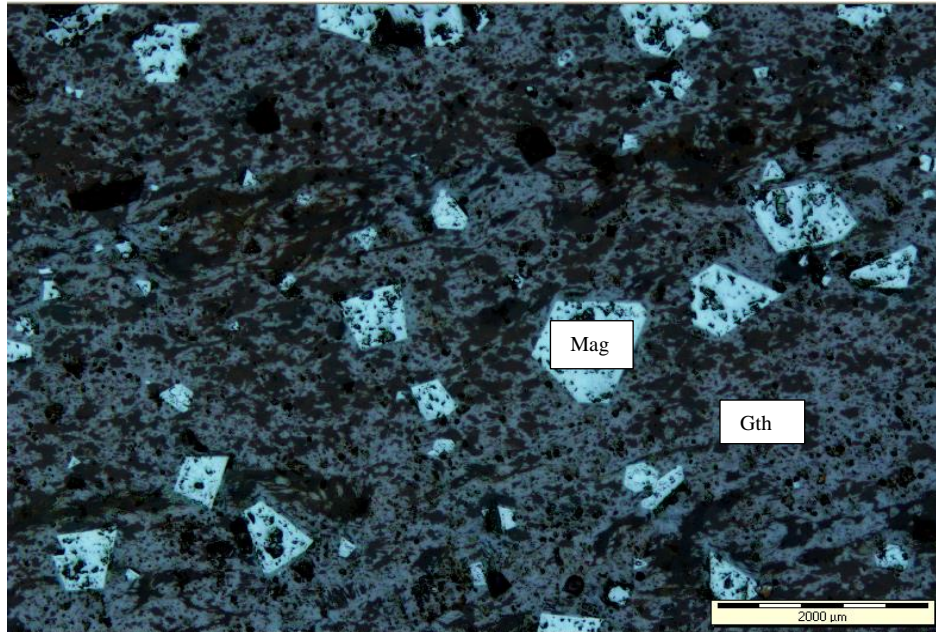


Figure 6. 20: Reflected light photomicrograph showing porous goethite (Gth) occurring with subhedral to euhedral magnetite (Mag) grains in the highly leached band.

University of Fort Hare
Together in Excellence

CHAPTER 7: GEOCHEMISTRY OF THE BANDED IRON FORMATION

7.1. Introduction

The current chapter presents a detailed geochemical description of the slightly weathered Kuruman BIF outcrops near Prieska. The geochemistry of the Kuruman BIF has been studied by a handful of researchers, including Hortsman and Halbich (1995) and Gurtzmer et al. (2008). For the current study, the geochemistry of the weathered BIF outcrops is studied to see the effects of weathering and oxidation on the whole rock chemistry. The study objectives include the impacts weathering, and oxidation has on both major and trace elements of the BIF. The study will also be achieved by comparing the geochemical data of the studied weathered Kuruman BIF with published data of the fresh Kuruman and other BIF from fresher drill cores.

7.2. Major element geochemistry of the weathered BIF

Major element compositions of the examined weathered BIF samples are depicted in the variation diagram (Fig. 7.1). The summarised major element compositions of the Prieska BIF are presented in Table 7.1. The major element compositions are quite variable but still comparable with the average compositions documented by Gutzmer et al. (2008).

The major elemental composition of the Prieska BIF demonstrated by the selected samples is somewhat variable, with dominating SiO_2 and Fe_2O_3 concentrations that account for about 98.92 wt. % of the analyzed samples. The analyzed results show varying but high concentrations of SiO_2 across virtually all the studied samples except P17, P21, and P33, where Fe_2O_3 is dominant. The SiO_2 content from the BIF samples ranges from 45.07 to 78.01 wt. % with an average of 57.74wt. %, and a standard deviation of 8.52. The Fe_2O_3 contents, on the other hand, are moderately high, ranging from 21.17 to 53.59 wt. % with an average of 41.18 wt. % and a standard deviation of 8.41 (Table 7.1).

Other elements are only occurring in minimal abundance accounting for a combined concentration of about 1.08wt. %. These minor elements include MgO, ranging from 0.02 to 0.84 wt. %, a standard deviation of 0.23. P_2O_5 ranges from 0.01 to 0.31 wt. % with a standard deviation of 0.09, K_2O ranges from 0.01 to 0.50 wt.% and a standard deviation of 0.12, CaO

with a range of 0.03 – 3.98 wt. % and a standard deviation of 0.95, MnO is ranging from 0.01 to 0.85 wt. % and a standard deviation of 0.31. All the above major elements were detected and quantified by the XRF across all the BIF samples.

Elements like Al₂O₃, Na₂O, and TiO₂, were not detected in a few samples, and their concentrations and statistical parameters are shown in Table 7.1. The Al₂O₃ was not detected in P29, while its maximum was 0.51 wt. %, an average of 0.22 wt. %, and a standard deviation of 0.16. TiO₂, on the other hand, was not detected in six samples (P21, P29, P36, P42, P53, and P61) with a maximum of 0.02 wt. %, an average of 0.01 wt. %, and a standard deviation of 0.01. Meanwhile, Na₂O was detected only in P 14, recording 0.14 wt. % (Table 7.1, Fig 7.1).

Table 7. 1: Major elemental variation of the samples expressed in weight percentages (wt. %). (-) shows major oxides that were not detected, or their concentrations were below the XRF detection limit.

Sample ID	SiO ₂	TiO ₂	Al ₂ O ₃	Fe ₂ O ₃	MnO	MgO	CaO	Na ₂ O	K ₂ O	P ₂ O ₅	Total wt. %
P1	56.40	0.01	0.34	42.89	0.01	0.05	0.03	-	0.02	0.09	99.83
P2	56.48	0.01	0.48	42.26	0.02	0.07	0.06	-	0.01	0.31	99.71
P3	59.02	0.01	0.28	40.31	0.01	0.02	0.03	-	0.02	0.11	99.81
P4	70.80	0.01	0.43	28.30	0.01	0.07	0.03	-	0.01	0.20	99.85
P5	78.01	0.01	0.38	21.17	0.07	0.16	0.04	-	0.03	0.03	99.90
P6	59.03	0.01	0.17	39.97	0.22	0.32	0.03	-	0.02	0.04	99.81
P7	59.95	0.01	0.14	39.38	0.20	0.12	0.03	-	0.02	0.06	99.91
P14	63.86	0.01	0.33	32.70	0.85	0.76	0.35	0.14	0.50	0.25	99.75
P17	45.65	0.01	0.19	53.59	0.16	0.11	0.04	-	0.02	0.04	99.81
P21	47.35	-	0.05	51.09	0.76	0.21	0.09	-	0.03	0.21	99.79
P27	58.79	0.01	0.08	40.59	0.01	0.23	0.04	-	0.03	0.10	99.88
P29	52.04	0.00	0.00	47.59	0.02	0.10	0.05	-	0.01	0.01	99.82
P33	45.07	0.02	0.51	53.23	0.52	0.23	0.05	-	0.12	0.08	99.83
P36	61.32	-	0.07	38.01	0.15	0.15	0.05	-	0.11	0.02	99.88
P42	51.75	-	0.17	46.92	0.67	0.13	0.05	-	0.04	0.06	99.79
P53	59.27	-	0.05	40.01	0.23	0.17	0.04	-	0.02	0.05	99.84
P61	51.96	-	0.11	42.11	0.81	0.84	3.98	-	0.04	0.01	99.86
Minimum	45.07	0.00	0.00	21.17	0.01	0.02	0.03	0.00	0.01	0.01	
Maximum	78.01	0.02	0.51	53.59	0.85	0.84	3.98	0.14	0.50	0.31	
Mean	57.74	0.01	0.22	41.18	0.28	0.22	0.29	0.01	0.06	0.10	
Standard deviation	8.52	0.01	0.16	8.41	0.31	0.23	0.95	0.03	0.12	0.09	

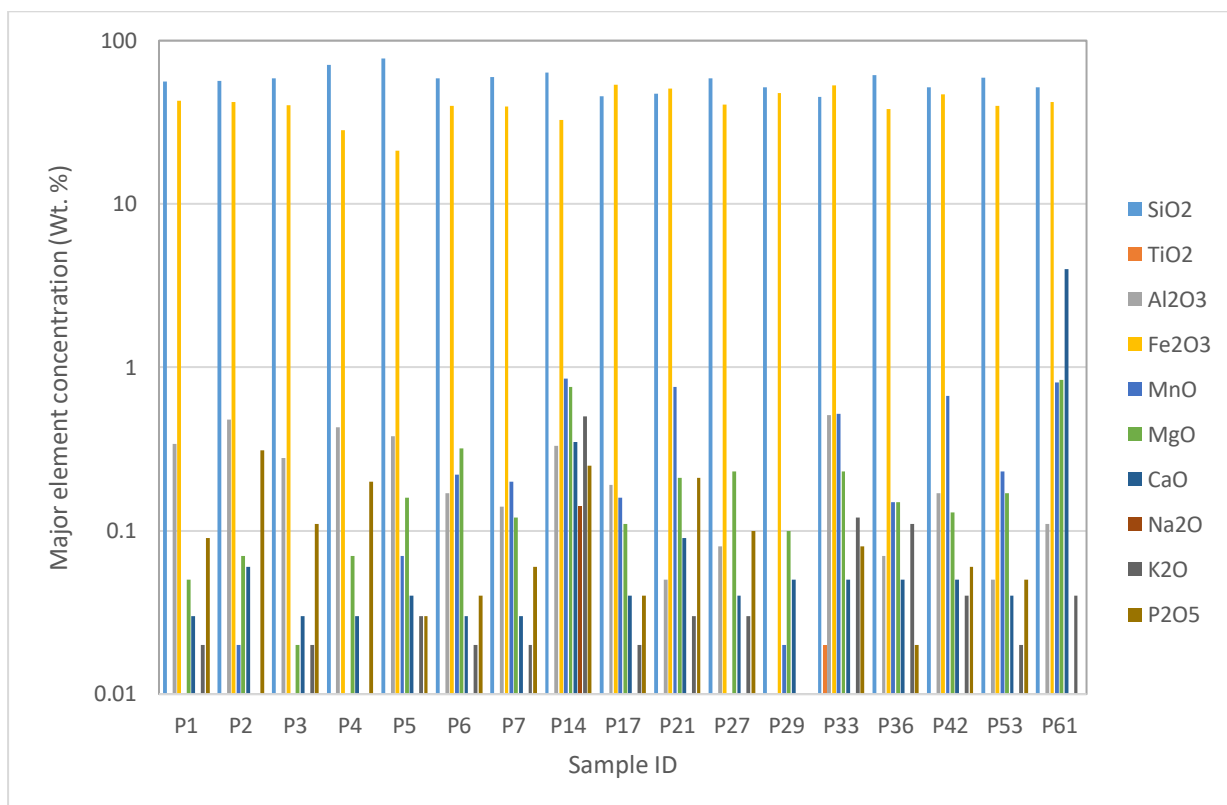


Figure 7. 1: Major element variation diagram of the weathered Prieska BIF samples.

7.2.1. Spider diagrams of major element compositions

The major elements data for the selected samples were normalized to the Kuruman BIF and Superior-type BIF average data extracted from Gutzmer et al. (2008) and McClung (2006), respectively (Table 7.2). The major element concentrations were compared to these two data sets through spider diagrams. Spider plots allowed for visual evaluation of the data sets' elemental characteristics to see their enrichment and depletion relative to each other, which may be influenced by weathering and oxidation. The enriched elements comprise normalization values greater than one, whereas depleted elements are denoted by normalization

values below one. A logarithmic scale was used in the plots to present the different enrichment and depletion magnitudes conventionally.

Table 7. 2: Summary of the major element compositions compared with the Kuruman BIF and Superior Type BIF's average compositions by Gutzmer et al. (2008) and McClung (2006), respectively.

Major oxides	This study (Range) n = 17		Kuruman BIF	Superior-Type BIF
	Min	Max		
SiO ₂	45.07	78.01	51.68	47.30
TiO ₂	0.00	0.02	0.02	0.04
Al ₂ O ₃	0.00	0.51	0.11	1.07
Fe ₂ O ₃	21.17	53.59	39.79	43.10
MnO	0.01	0.85	0.30	0.44
MgO	0.02	0.84	5.14	5.68
CaO	0.03	3.98	5.65	3.03
Na ₂ O	0.00	0.14	0.00	0.33
K ₂ O	0.01	0.50	0.03	0.27
P ₂ O ₅	0.01	0.31	0.09	0.10

7.2.2. Major element geochemistry relative to Kuruman BIF

Average geochemical compositions were calculated and normalized for the samples using Kuruman BIF's average composition compiled by Gutzmer et al. (2008) (Table 7.3). The major element oxides were normalized against the iron ore protolith (Kuruman BIF) (Beukes et al., 2003), and the results are listed in Table 7.3.

The spider diagram displays variable enrichment and depletion in Al₂O₃, K₂O, MnO, and P₂O₅, while TiO₂, CaO, and MgO show complete depletion in all the samples (Fig. 7.2). On the other hand, SiO₂ and Fe₂O₃ show consistent and comparable concentrations with the Kuruman data across the ten samples, although there are slight variations in the Fe₂O₃ concentrations. Other similar contents are the Al₂O₃ (P61), K₂O (P61), K₂O (P21), and P₂O₅ (P27).

The diagram also shows the Al₂O₃, K₂O, MnO, and P₂O₅ enrichment in P14 relative to the Kuruman formation with the same trend observed in P33 except for P₂O₅ levels displaying slight depletion. Al₂O₃ shows enriched content in P17 and P42, while it shows depletion in P27, P29, P21, P53, and P36. P₂O₅, on the other hand, displays enriched concentration in only two samples (P14 and P21), with all the other samples having depleted P₂O₅ concentrations except for P27.

K₂O displays enriched contents in P14, P29, P33, and P42, respectively, while depleted concentrations are observable in P27, P17, P53, and P29. The MnO is enriched in five samples (P14, P61, P21, P42, and P33), while it shows substantial depletion on the other five samples.

Table 7. 3: The normalized major element values of the samples using Kuruman BIF protolith averages from Gutzmer et al. (2008).

Kuruman Normalised major elements	P1	P2	P3	P4	P5	P6	P7	P14	P17	P21	P27	P29	P33	P36	P42	P53	P61
SiO₂	1.09	1.09	1.14	1.37	1.51	1.14	0.88	1.24	0.88	0.92	1.14	1.01	0.87	1.19	1.00	1.15	1.01
TiO₂	0.50	0.50	0.50	0.50	0.50	0.50	0.50	0.50	0.50	0.50	0.50	0.50	1.00	0.50	0.50	0.50	0.50
Al₂O₃	3.09	4.36	2.55	3.91	3.45	1.55	1.73	3.00	1.73	0.45	0.73	0.09	4.64	0.64	1.55	0.45	1.00
Fe₂O₃	1.08	1.06	1.01	0.71	0.53	1.00	1.35	0.82	1.35	1.28	1.02	1.20	1.34	0.96	1.18	1.01	1.06
MnO	0.03	0.07	0.03	0.03	0.23	0.73	0.53	2.83	0.53	2.53	0.03	0.07	1.73	0.50	2.23	0.77	2.70
MgO	0.01	0.01	0.00	0.01	0.03	0.06	0.02	0.15	0.02	0.04	0.04	0.02	0.04	0.03	0.03	0.03	0.16
CaO	0.01	0.01	0.01	0.01	0.01	0.01	0.01	0.06	0.01	0.02	0.01	0.01	0.01	0.01	0.01	0.01	0.70
Na₂O	0.01	0.01	0.01	0.01	0.01	0.01	0.01	14.00	0.01	0.01	0.01	0.01	0.01	0.01	0.01	0.01	0.01
K₂O	0.67	0.33	0.67	0.33	1.00	0.67	0.67	16.67	0.67	1.00	1.00	0.33	4.00	3.67	1.33	0.67	1.33
P₂O₅	1.00	3.44	1.22	2.22	0.33	0.44	0.44	2.78	0.44	2.33	1.11	0.11	0.89	0.22	0.67	0.56	0.11

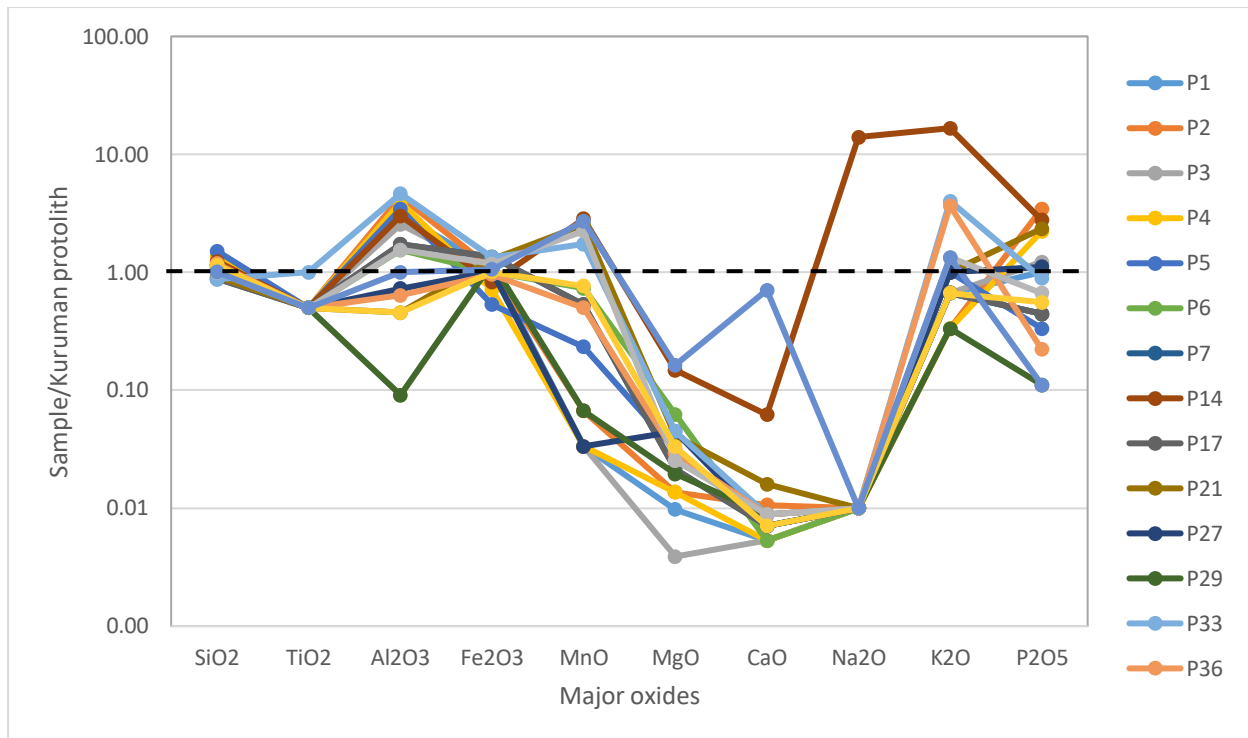


Figure 7. 2: Spider plot of major elements composition, normalized against Kuruman BIF after Gutzmer et al. (2008).



University of Fort Hare

7.2.3. Major element geochemistry relative to Superior-Type BIF

Average geochemical compositions for the Prieska data were also normalized against the Superior-Type BIF average composition compiled by McClung (2006) (Table 6.4 and Fig. 6.3).

Like the normalized spider diagram of the Kuruman Formation, SiO_2 and Fe_2O_3 show consistent and comparable concentrations with Superior-Type data across the samples (Fig. 7.3). Other observed relative concentrations to the Superior-Type BIF are those of P_2O_5 (P27).

The TiO_2 , Al_2O , MgO , K_2O , Na_2O , and CaO show depletion across all the samples except P14 enriched in K_2O , and P61, which shows enriched levels of CaO . P_2O_5 is enriched in P14 and P21, while it displays depletion in the other samples. MnO , on the other hand, has depleted concentrations on P27, P29, P36, P53, and P17 while it shows enrichment in the other five samples (Fig. 7.3)

Table 7. 4: The normalized values using Superior-Type BIF averages from McClung (2006).

Superior-Type normalized major elements	P1	P2	P3	P4	P5	P6	P7	P14	P17	P21	P27	P29	P33	P36	P42	P53	P61
SiO2	1.19	1.19	1.25	1.50	1.65	1.25	1.27	1.35	0.97	1.00	1.24	1.10	0.95	1.30	1.09	1.25	1.10
TiO2	0.25	0.25	0.25	0.25	0.25	0.25	0.25	0.25	0.25	0.25	0.25	0.25	0.50	0.25	0.25	0.25	0.25
Al2O3	0.32	0.45	0.26	0.40	0.36	0.16	0.13	0.31	0.18	0.05	0.07	0.01	0.48	0.07	0.16	0.05	0.10
Fe2O3	1.00	0.98	0.94	0.66	0.49	0.93	0.91	0.76	1.24	1.19	0.94	1.10	1.24	0.88	1.09	0.93	0.98
MnO	0.02	0.05	0.02	0.02	0.16	0.50	0.45	1.93	0.36	1.73	0.02	0.05	1.18	0.34	1.52	0.52	1.84
MgO	0.01	0.01	0.00	0.01	0.03	0.06	0.02	0.13	0.02	0.04	0.04	0.02	0.04	0.03	0.02	0.03	0.15
CaO	0.01	0.02	0.01	0.01	0.01	0.01	0.01	0.12	0.01	0.03	0.01	0.02	0.02	0.02	0.02	0.01	1.31
Na2O	0.03	0.03	0.03	0.03	0.03	0.03	0.03	0.42	0.00	0.03	0.03	0.03	0.03	0.03	0.03	0.03	0.03
K2O	0.07	0.04	0.07	0.04	0.11	0.07	0.07	1.85	0.07	0.11	0.11	0.04	0.44	0.41	0.15	0.07	0.15
P2O5	0.90	3.10	1.10	2.00	0.30	0.40	0.60	2.50	0.40	2.10	1.00	0.10	0.80	0.20	0.60	0.50	0.10

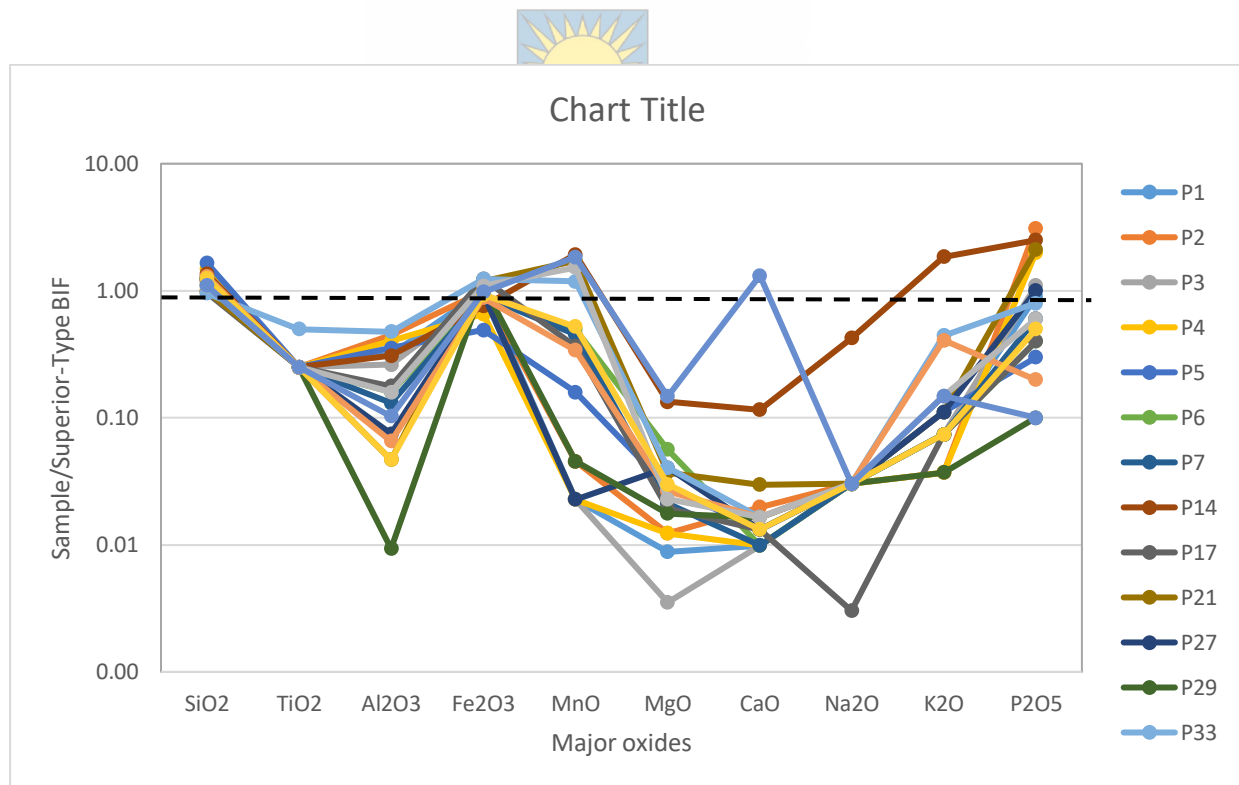


Figure 7. 3: Spider plot of major element compositions for the weathered Prieska BIF normalized against Superior-Type BIF extracted from McClung (2006).

7.2.4. Major element scatter plots

Scatter diagrams for the major element oxides were constructed using the XRF data. Different major elements were plotted against one another to study their geochemical relationships and develop interpretations for the existing trends and groupings. Most of the plots do not show meaningful relationships; hence were not included in the analyses.

The MgO displays a weak positive correlation with SiO₂ (Fig. 7.4). A similar relationship exists between Fe₂O₃ and Al₂O₃(Fig. 7.5 A). The (CaO + MgO) and (Na₂O + K₂O) show a weak positive relationship (Fig. 7.5 B).

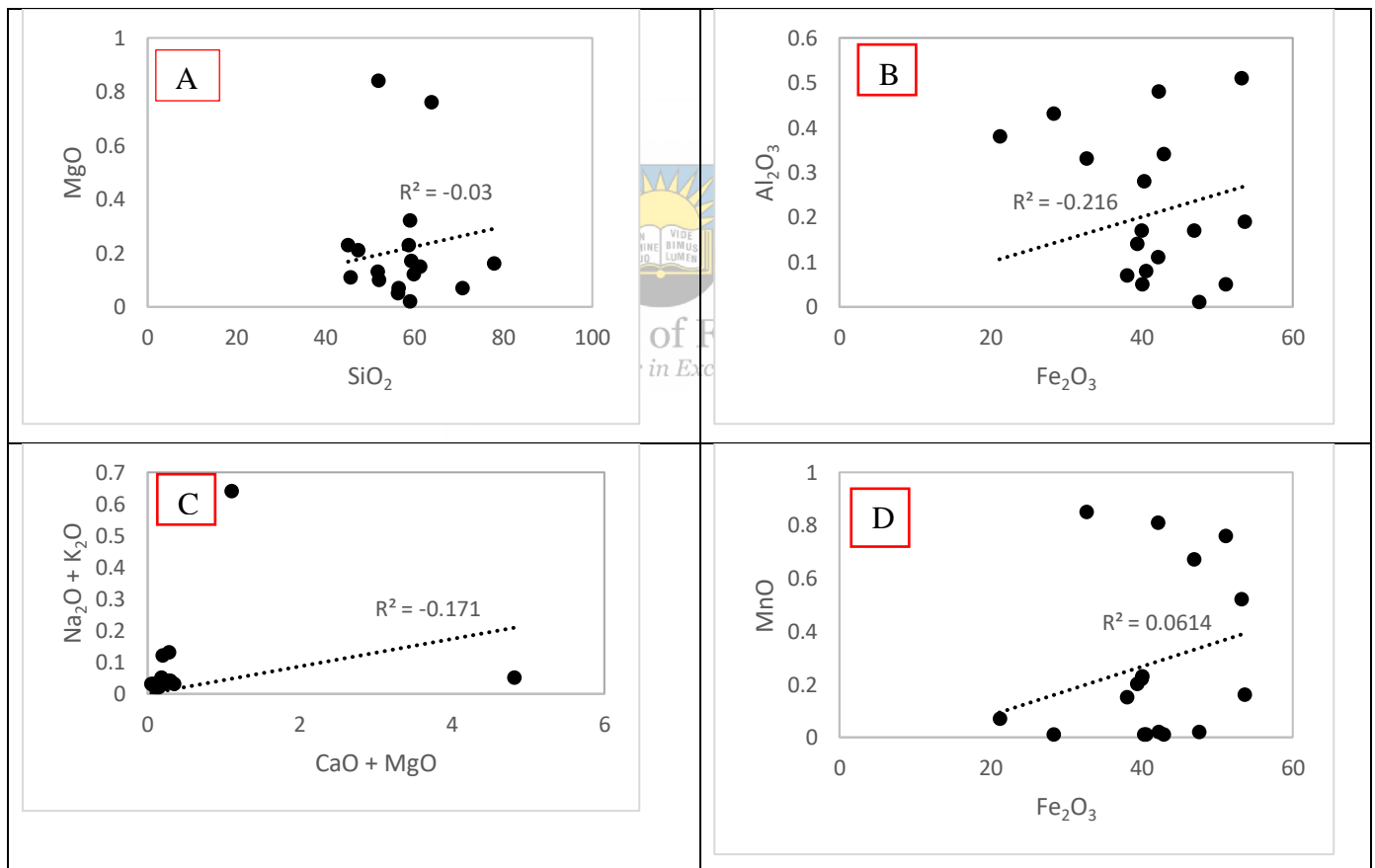


Figure 7. 4: Major element scatter diagram displaying positive correlations between the major oxides.

A strong inverse relationship exists between SiO_2 and Fe_2O_3 (Fig. 7.5A). Similarly, Al_2O_3 displays a negative correlation with SiO_2 (Fig. 7.5 D). A similar relationship exists between MgO and Fe_2O_3 and SiO_2 and MnO (Fig. 7.5 B & C).

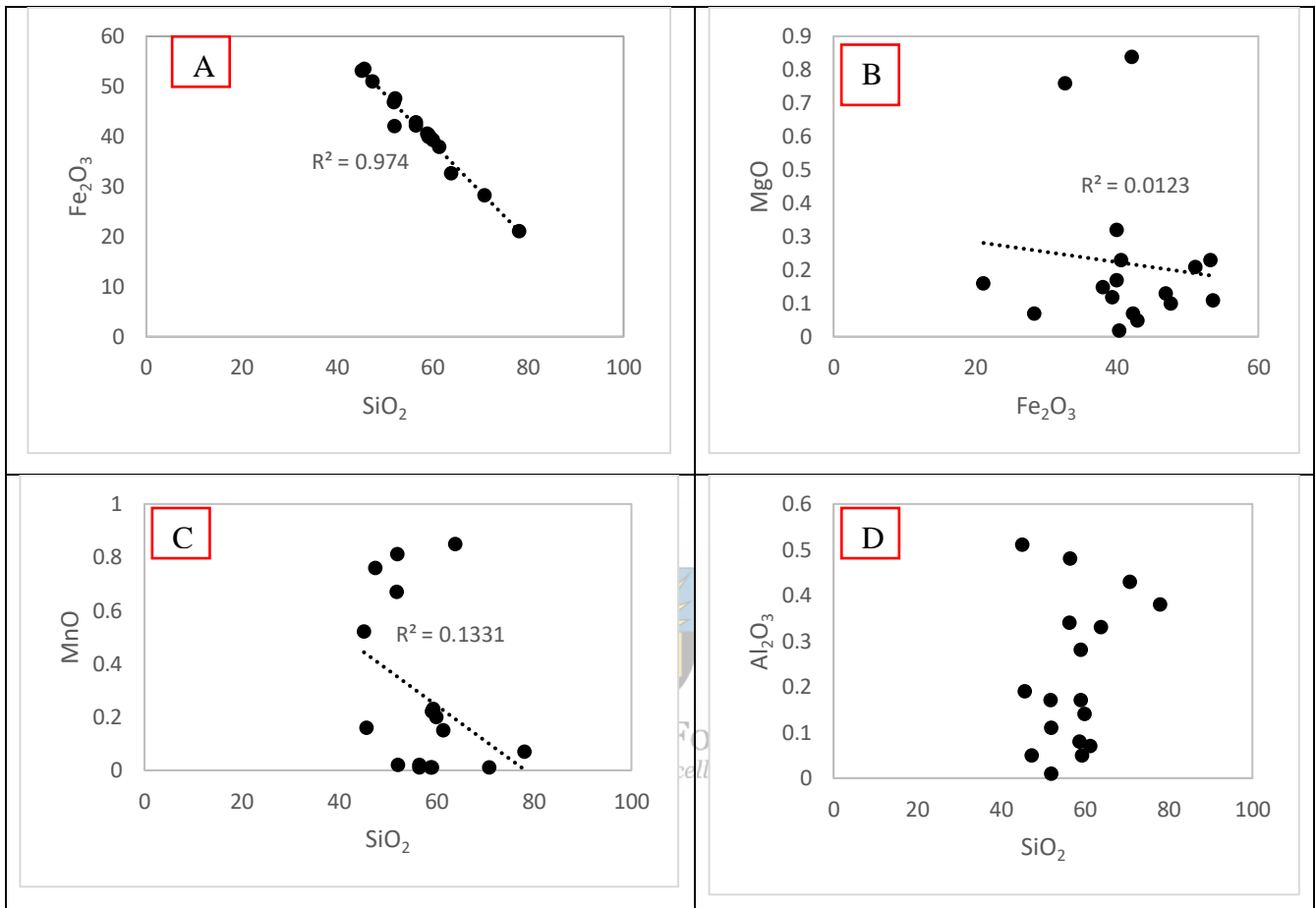


Figure 7. 5: Scatter diagrams displaying negative relationships between the major oxides.

7.3. Trace element geochemistry of the weathered BIF

Trace element compositions of the BIF are listed in table 7.5. The results show that some trace elements were not detected in some of the samples, probably because they were only occurring in negligible concentrations below the XRF detection limits or were not available.

The transition metals tungsten (W) and cobalt (Co) were the most dominant trace elements within the samples. Tungsten concentration ranges from 172 - 828 ppm with an average of 437.3 ppm and a standard deviation of 220.52, while cobalt comprises a concentration range

of 271- 463 ppm, an average of 372.4 ppm, and a standard deviation of 63.41 (Table 6.5, Fig 6.6).

The concentration dominance was followed by a non-metal sulfur (S), an alkali earth metal barium (Ba), and Halogen chlorine (Cl) in that order. Sulfur was not detected in two samples (P21 and P27), while it had a maximum concentration of 816 ppm, an average of 158.9 ppm, and a standard deviation of 271.66. On the other hand, barium was only detected in four samples with a maximum concentration of 475 ppm, an average of 139.6 ppm, and a standard deviation of 191.35. Chlorine was not detected in four samples but had a maximum concentration of 265 ppm with an average of 79.5 ppm and a standard deviation of 95.94 ppm (Table 6.5, Fig 6.6).

The three transition metals, molybdenum (Mo), vanadium (V), and nickel (Ni), were also in relatively high concentrations. However, molybdenum was not detected in P27 and P42. It recorded a maximum concentration of 108 ppm, an average of 62.2 ppm, and a standard deviation of 33.51 ppm. Vanadium was detected in three samples having a maximum concentration of 88 ppm, an average of 22.2 ppm, and a standard deviation of 36.01 ppm. On the other hand, nickel was detected in four samples contributing a maximum concentration of 54 ppm in one of the samples with an average of 17.5 ppm and a standard deviation of 21.94 ppm (Table 6.5; Fig 6.6).

An alkali earth metal strontium (Sr), transition metal yttrium (Y), alkali metal rubidium (Rb), and another transition metal zinc (Zn) followed. Strontium was detected in four samples and had a concentration range of 0 to 114 ppm, an average of 16.9 ppm, and a standard deviation of 33.49 ppm. Yttrium was not detected in four samples but had a maximum concentration of 23 ppm with an average of 9.9 ppm and a standard deviation of 8.77 ppm. Rubidium was detected in three samples with a maximum concentration of 43 ppm, an average of 7.3 ppm, and a standard deviation of 13.29 ppm. On the other hand, zinc was detected in two samples with a maximum concentration of 21 ppm, an average of 3.6, and a standard deviation of 7.32 ppm. The least concentrated trace element is the basic/other metal lead (Pb) detected in only one sample (P33) to contain 23 ppm (Table 7.5, Fig 7.8).

Table 7. 5: Whole-rock trace element compositions of the BIF expressed in parts per million (ppm). (-) shows trace elements that were not detected, or their concentrations were below the XRF detection limit.

Sample ID	S	Cl	V	Co	Ni	Zn	Rb	Sr	Y	Mo	Ba	W	Pb
P1	-	-	84	382	35	-	18	-	18	70	286	182	-
P2	86	-	78	309	52	24	14	19	15	57	423	243	-
P3	-	188	74	411	-	20	17	48	-	73	195	519	-
P4	-	97	-	298	-	-	-	-	18	93	-	367	25
P5	79	112	82	439	51	18	-	32	16	72	391	438	-
P6	112	-	-	397	43	18	38	-	26	84	234	418	-
P7	162	-	-	415	48	16	-	-	15	81	-	316	20
P14	816	265	53	271	-	-	43	114	20	68	475	401	-
P17	97	114	-	427	44	-	-	-	-	108	-	217	-
P21	-	80	-	431	33	-	-	16	23	85	285	211	-
P27	-	-	-	337	-	-	-	-	11	-	-	604	-
P29	58	53	-	463	54	-	-	-	11	68	-	585	-
P33	69	-	-	410	-	21	15	14	-	73	190	633	23
P36	81	-	-	339	-	15	15	-	17	75	-	538	-
P42	73	69	81	387	44	-	-	-	17	-	446	184	-
P53	179	-	-	354	-	-	-	-	-	85	-	828	-
P61	216	214	88	305	-	-	-	25	-	60	-	172	-
Minimum	0.00	0.00	0.00	271.00	0.00	0.00	0.00	0.00	0.00	0.00	0.00	172.00	0.00
Maximum	816.00	265.00	88.00	463.00	54.00	24.00	43.00	114.00	26.00	108.00	475.00	828.00	25.00
Mean	119.29	70.12	31.76	375.00	23.76	7.76	9.41	15.76	12.18	67.76	172.06	403.29	4.00
Standard deviation	185.42	82.85	38.58	55.13	22.96	9.46	13.39	28.22	8.60	27.42	179.05	187.28	8.68

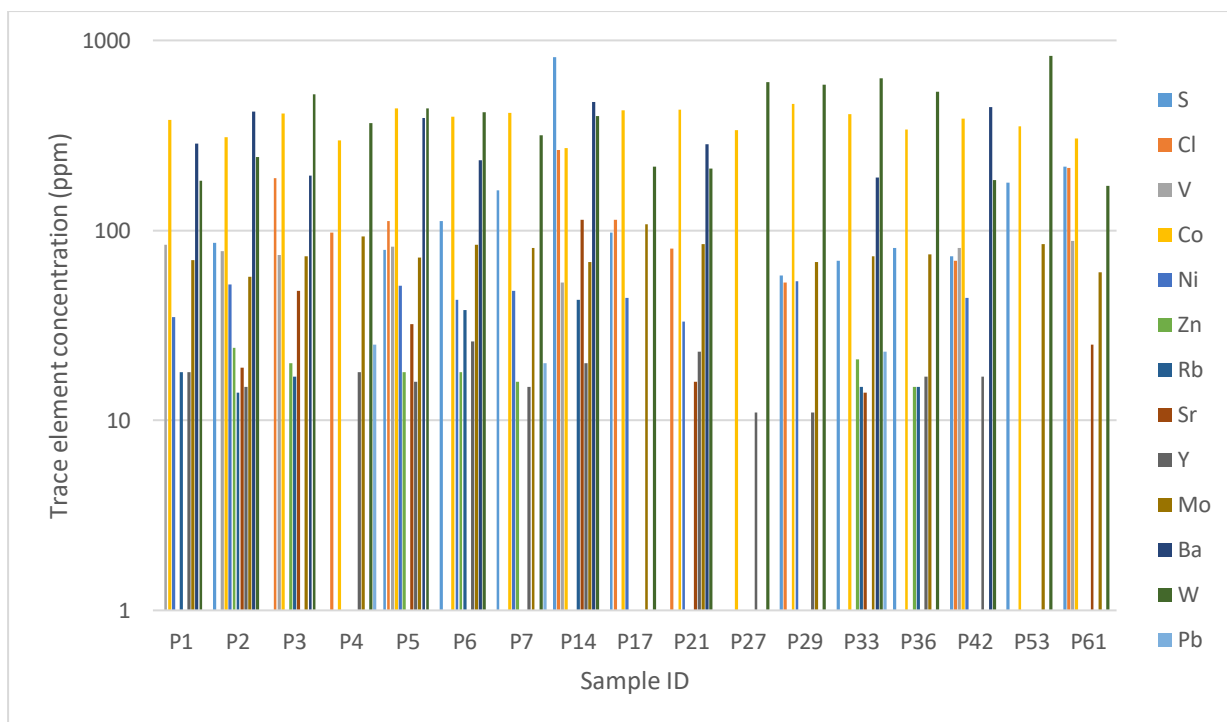


Figure 7. 6: The variation bar diagram showing trace element concentrations of the weathered BIF in the Prieska area. Only those elements with concentrations above the level of detection are included.



University of Fort Hare
Together in Excellence

7.3.1. Trace element spider diagrams

The average trace element compositions were calculated and normalized against the Kuruman and Superior-Type BIF after Gutzmer et al. (2008) and McClung (2006), respectively (Table 7.6). They were plotted on spider diagrams for visual assessment of the samples' enrichment and depletion trends. It should be noted that the most concentrated trace elements (tungsten and molybdenum) were not reported in the BIFs used for normalization (Kuruman and Superior-Type BIF).

Table 7. 6: Summary of the trace element compositions of the Prieska BIF (in ppm) compared with the average compositions of the published Kuruman BIF and Superior-Type BIF by Gutzmer et al. (2008) and McClung (2006).

Trace elements (ppm)	Superior-Type BIF (Mean)	Kuruman BIF (Mean)	Prieska-Marydale BIF (Range) n = 17	
			Min	Max
V	26	10	0	88
Co	24	0.16	271	463
Ni	18	29.3	0	54
Zn	-	25.4	0	24
Rb	36	2.15	0	43
Sr	25	3.45	0	114
Y	25	9.35	0	26
Ba	108	7.13	0	475
Pb	5	2.25	0	25



University of Fort Hare
Together in Excellence

7.3.2. Trace element geochemistry relative to Kuruman BIF

Average trace element concentrations were normalized using the Kuruman BIF average compositions extracted from Gutzmer et al. (2008) (Table 7.7). The study area has not detected Th, Zn, Cu, which were present for the Kuruman BIF. On the other hand, the most dominant trace element (W) was not reported for the Kuruman BIF. Other significant trace elements such as Mo, S, and Cl were also not recorded for the Kuruman BIF. The above trace elements were subsequently not included in the spider plots.

Relative to the Kuruman BIF, Prieska BIF has a high Co enrichment in all the samples by orders of around 2000, while yttrium is enriched by about 2 in six samples. Nickel, strontium, and barium are enriched in four samples (Table 7.7, Fig 7.7). Barium is enriched by orders greater than 30 in four samples, while nickel, on the other hand, is enriched by orders around 1.5 across the four samples.

Vanadium shows enrichment in three samples, P14, P42, and P61, whereas rubidium is enriched in P14, P33, and P36. Vanadium is enriched by orders greater than five in all three samples. On the other hand, lead is enriched in P33 only, while zinc shows complete depletion in all samples (Table 7.7, Fig. 7.9).

Table 7. 7: The normalized trace element values of the weathered Prieska BIF using Kuruman BIF averages from Gutzmer et al. (2008).

Kuruman Normalized trace elements	P1	P2	P3	P4	P5	P6	P7	P14	P17	P21	P27	P29	P33	P36	P42	P53	P61
V	8.40	7.80	7.40	0.01	8.20	0.01	0.01	5.30	0.01	0.01	0.01	0.01	0.01	0.01	8.10	0.01	8.80
Co	2387.50	1931.25	2568.75	1862.50	2743.75	2481.25	2593.75	1693.75	2668.75	2693.75	2106.25	2893.75	2562.50	2118.75	2418.75	2212.50	1906.25
Ni	1.19	1.77	0.00	0.00	1.74	1.47	1.64	0.00	1.50	1.13	0.00	1.84	0.00	0.00	1.50	0.00	0.00
Zn	0.00	0.94	0.79	0.00	0.71	0.71	0.63	0.00	0.00	0.00	0.00	0.00	0.83	0.59	0.00	0.00	0.00
Rb	8.37	6.51	7.91	0.05	0.05	17.67	0.05	20.00	0.05	0.05	0.05	0.05	6.98	6.98	0.05	0.05	0.05
Sr	0.03	5.51	13.91	0.03	9.28	0.03	0.03	33.04	0.03	4.64	0.03	0.03	4.06	0.03	0.03	0.03	7.25
Y	1.93	1.60	0.01	1.93	1.71	2.78	1.60	2.14	0.01	2.46	1.18	1.18	0.01	1.82	1.82	0.01	0.01
Ba	40.11	59.33	27.35	0.01	54.84	32.82	0.01	66.62	0.01	39.97	0.01	0.01	26.65	0.01	62.55	0.01	0.01
Pb	0.04	0.04	0.04	11.11	0.04	0.04	8.89	0.04	0.04	0.04	0.04	0.04	0.04	0.04	0.04	0.04	0.04

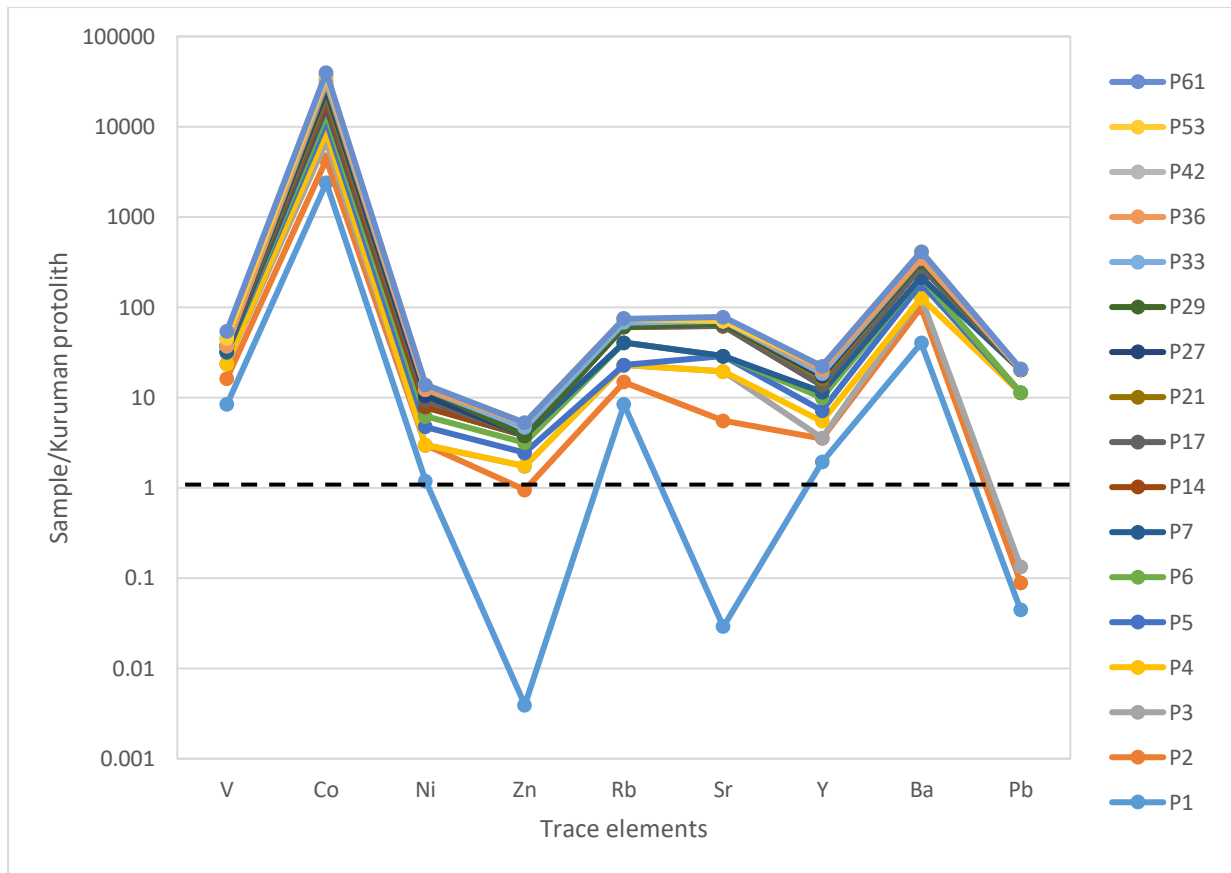


Figure 7. 7: Kuruman BIF normalized trace element distribution of the weathered Prieska samples. The Kuruman BIF values are cited from Gutzmer et al. (2008).

7.3.3. Trace element geochemistry relative to Superior-Type BIF

Average trace compositions were calculated for the samples and normalized against average concentrations of the Superior-type BIF taken from McClung (2006) (Table 7.8). The Prieska BIF does not contain Th, U, Cu, Nb, and Zr trace elements, whereas these elements were reported by McClung (2006) for the Superior-Type BIF. Similarly, there was no reported W, Mo, S, Cl, and Zn for the Superior-Type BIF, whereas these elements were encountered within the Prieska BIF.

Compared with the Superior-Type BIF, cobalt shows enrichment by orders between 11 and 20 across the ten samples (Table 7.8, Fig. 7.10). Barium and nickel are enriched in four samples by orders between 1.5 - 4 and 2 -3 respectively relative to the Superior type BIF, while vanadium is enriched in three samples by orders of around 3.

Strontium and rubidium are both enriched in P14, while lead is only enhanced in P33. Around four orders enrich strontium and lead; meanwhile, rubidium is enriched by orders less than 2. Strontium also has a concentration level similar to the Superior-Type BIF in P61. Yttrium is slightly depleted in six samples, while the other four samples are completely depleted (Table 7.8, Fig 7.10).

Table 7. 8: The normalized trace element values of the weathered Prieska samples using Superior-Type BIF averages from McClung (2006).

Superior-Type normalised trace element	P1	P2	P3	P4	P5	P6	P7	P14	P17	P21	P27	P29	P33	P36	P42	P53	P61
V	3.23	3.00	2.85	0.00	3.15	0.00	0.00	2.04	0.00	0.00	0.00	0.00	0.00	0.00	3.12	0.00	3.38
Co	15.92	12.88	17.13	12.42	18.29	16.54	17.29	11.29	17.79	17.96	14.04	19.29	17.08	14.13	16.13	14.75	12.71
Ni	1.94	2.89	0.01	0.01	2.83	2.39	2.67	0.01	2.44	1.83	0.01	3.00	0.01	0.01	2.44	0.01	0.01
Zn	1.00	240.00	200.00	1.00	180.00	180.00	160.00	1.00	1.00	1.00	1.00	1.00	210.00	150.00	1.00	1.00	1.00
Rb	0.50	0.39	0.47	0.00	0.00	1.06	0.00	1.19	0.00	0.00	0.00	0.00	0.42	0.42	0.00	0.00	0.00
Sr	0.00	0.76	1.92	0.00	1.28	0.00	0.00	4.56	0.00	0.64	0.00	0.00	0.56	0.00	0.00	0.00	1.00
Y	0.72	0.60	0.00	0.72	0.64	1.04	0.60	0.80	0.00	0.92	0.44	0.44	0.00	0.68	0.68	0.00	0.00
Ba	2.65	3.92	1.81	0.00	3.62	2.17	0.00	4.40	0.00	2.64	0.00	0.00	1.76	0.00	4.13	0.00	0.00
Pb	0.02	0.02	0.02	5.00	0.02	0.02	4.00	0.02	0.02	0.02	0.02	0.02	0.02	0.02	0.02	0.02	0.02

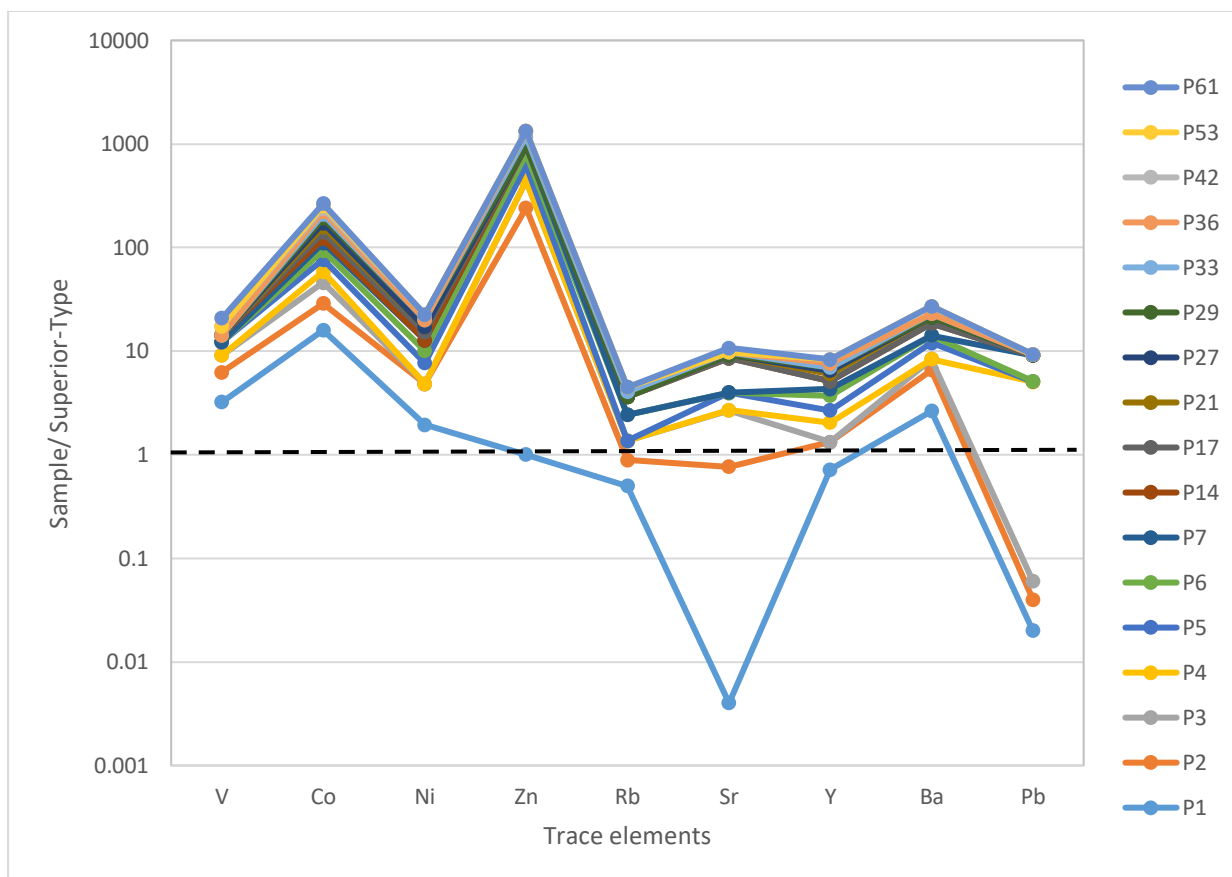


Figure 7. 8: Superior-Type normalized trace element distribution of the weathered Prieska samples. The Superior-Type values are cited from McClung (2006).

7.2.4. Trace element scatter plots

Trace element scatter plots were constructed using XRF data. Trace elements were plotted against one another to compare the different samples, study geochemical relationships, and develop interpretations for existing trends and groupings.

From the scatter plots, Fe_2O_3 displays a strong positive relationship with cobalt (Fig.7.11). It also shows a weak correlation with molybdenum and tungsten. On the other hand, molybdenum displays a weak positive relationship with yttrium and tungsten, while chlorine displays a positive relationship with sulfur. (Fig. 7.11C). Meanwhile, a strong negative relationship occurs between SiO_2 and cobalt (Fig. 7.12).

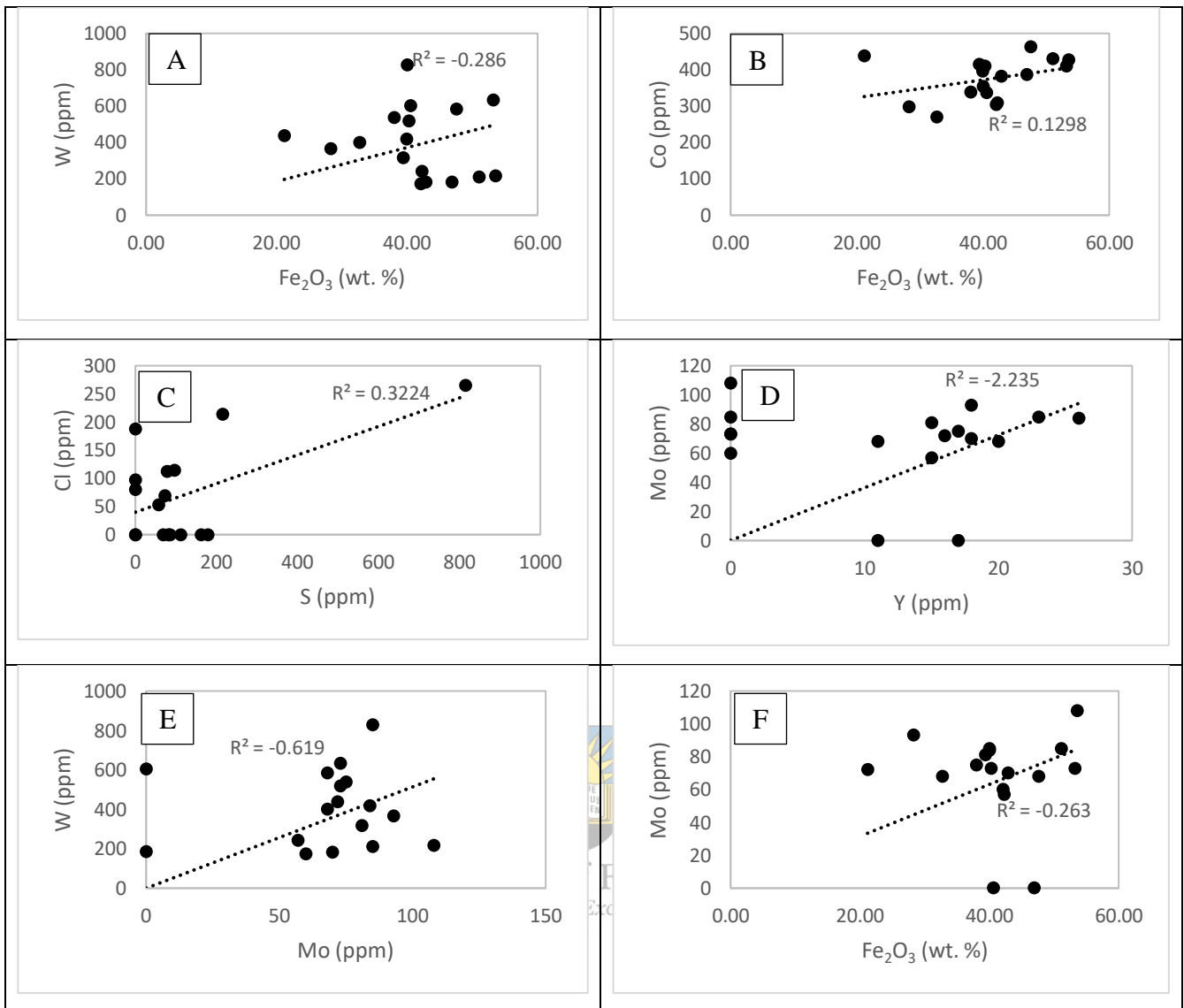


Figure 7. 9: Trace element scatter plots showing positive relationships.

A negative relationship also exists between cobalt and chlorine, tungsten and yttrium, and Fe₂O₃ with barium and yttrium (Fig. 7.13).

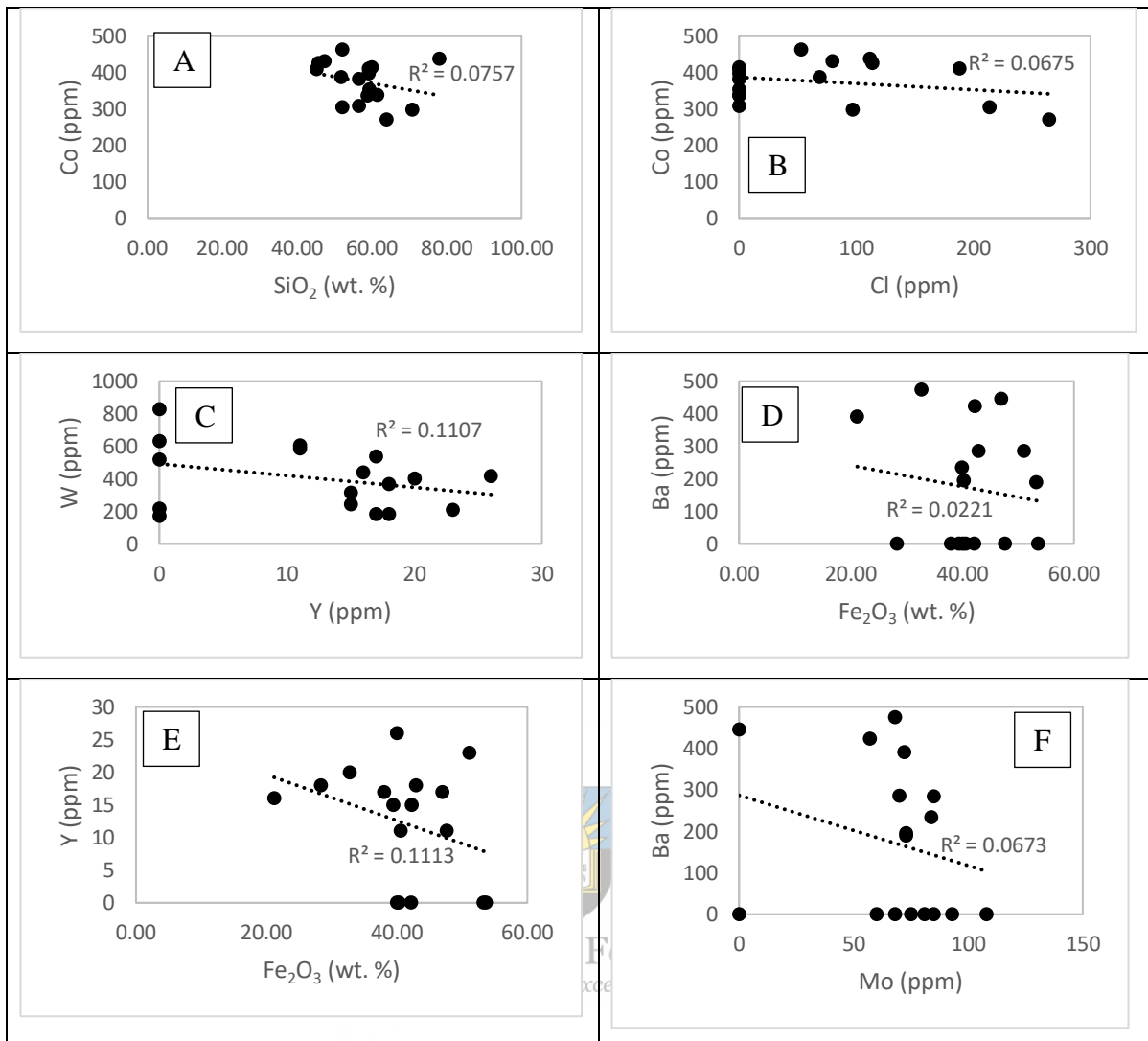


Figure 7. 10: Cross-plots displaying negative correlations between the trace elements.

7.4. Source area weathering

Chemical index of alteration (CIA) from Nesbitt and Young (1982) and chemical index of weathering (CIW) from Harnois (1988) were employed for the study to determine and evaluate the source rock weathering degree and the changes of the weathering profile. These chemical indices were conducted to measure the proportion between the original/primary minerals and secondary mineral products, such as clay minerals. It should be noted, though, that these indices were previously applied in clastic sedimentary rocks (Wronkiewicz & Condie, 1987; Nesbitt & Wilson, 1992; Fedo et al., 1995; Bahlburg & Dobrzinski, 2011, Obasi et al., 2019) and had not been employed in BIFs. They were, however, employed in the study to see their applicability on weathered BIF outcrops.

The chemical weathering indices were calculated based on the molecular proportions of mobile and immobile element oxides (Na₂O, CaO, K₂O, and Al₂O₃) using the formulas in Table 7.9. Their statistical parameters, such as the minimum, maximum, median, mean, and geometric mean, were also determined using Microsoft Excel.

Table 7. 9: Chemical weathering indices and their respective calculation formulas.

Index	Formula	Reference
Chemical Index of Alteration (CIA)	$CIA = [Al_2O_3 / (Al_2O_3 + CaO + Na_2O + K_2O)] \times 100$	Nesbitt & Young (1982)
Chemical Index of Weathering (CIW)	$CIW = [Al_2O_3 / (Al_2O_3 + CaO + Na_2O)] \times 100$	Harnois (1988)

CIA values range from 2.75 to 91.49. They have an average of 58.21, a geometric mean of 45.68, a median of 73.68, and a standard deviation of 28.21 (Table 7.10, Fig 7.14). In comparison, the CIW consist of values ranging from 2.78 to 93.48. The CIW has an average value of 65.84, a geometric mean of 52.95, a median of 80.24, and a standard deviation of 28.04 (Table 7.10, Fig 7.14). These values are mostly influenced by the sample lithology properties, weathering duration, and area climatic conditions.

Table 7. 10: Weathering indices of the samples.

Sample ID	CIA	CIW
P1	87.18	91.89
P2	87.27	88.89
P3	84.85	90.32
P4	91.49	93.48
P5	84.44	90.48
P6	77.27	85.00
P7	73.68	82.35
P14	24.92	40.00
P17	74.86	80.24
P21	29.04	34.45
P27	49.24	58.94
P29	13.30	14.84
P33	73.92	88.94
P36	30.34	53.88
P42	63.44	74.50
P53	41.62	48.34
P61	2.75	2.78
Min	2.75	2.78
Max	91.49	93.48
Mean	58.21	65.84
Geometric mean	45.68	52.95
Median	73.68	80.24
Standard deviation	28.21	28.04

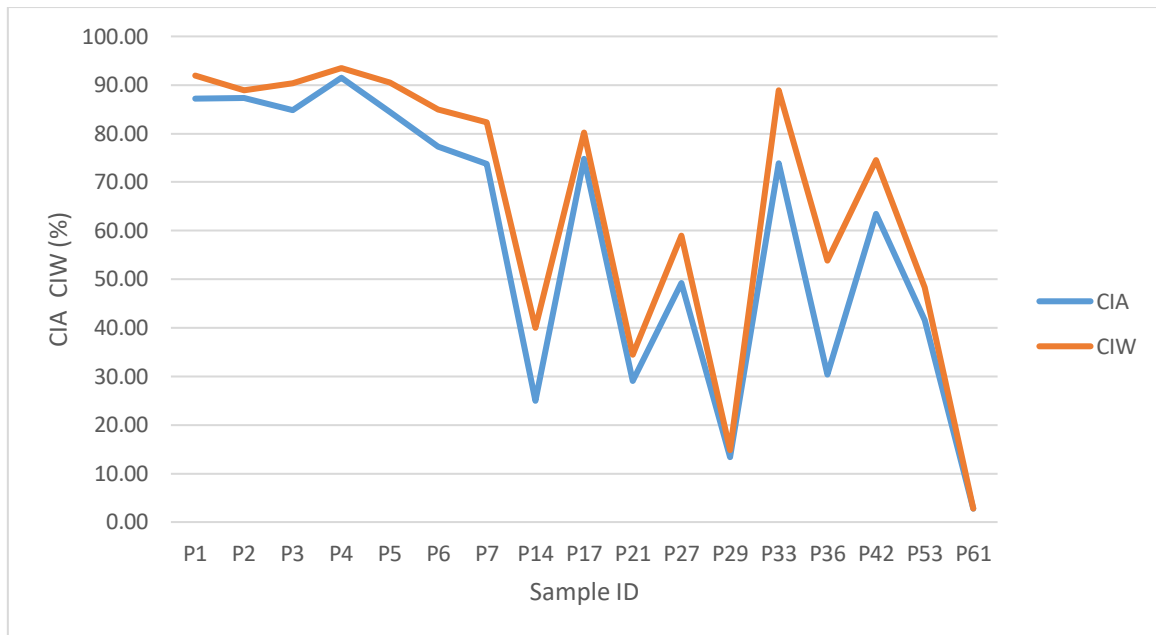


Figure 7. 11: A variation diagram showing CIA and CIW intensities across the samples.

The CIA plot against Al_2O_3 (Fig. 7.12) shows nine samples that include P1, P2, P3, P4, P5, P6, P7, P17, and P33 plotting within the intensive weathering zone. Only two samples, P27 and P42, are plotting in the moderate weathering zone. The remaining six samples, including P53, P29, P21, P14, P36, and P61, plot on the low weathering zone. According to Figure 7.14, sample P61 is the least weathered amongst all the samples.

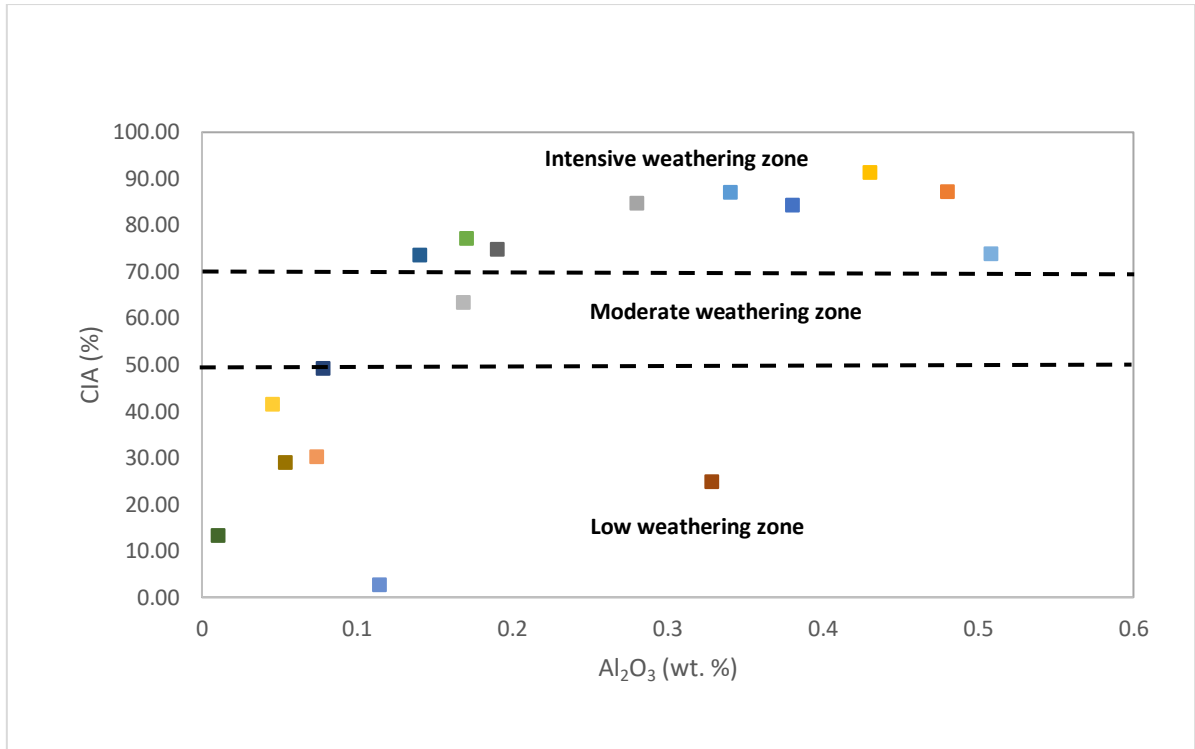


Figure 7. 12: The CIA against the Al₂O₃ plot shows the samples' weathering intensity (after Obasi and Madukwe, 2016, 2020).



University of Fort Hare
Together in Excellence

CHAPTER 8: POST-DEPOSITIONAL ALTERATION

8.1. Introduction

The current chapter investigates the influences of post-depositional alteration processes such as diagenesis, tectonic overprint and metamorphism, and surficial weathering and oxidation on the Kuruman BIF near Prieska. These post-depositional processes are responsible for transforming the rock textures, mineral assemblages and alignments, and geochemistry.

8.2. Diagenesis

Diagenesis incorporates all the rock changes after deposition before metamorphism, including chemical changes and physical transformations of the BIF at a relatively low temperature (below 250°C) and pressure (200Kg/cm²). These modifications involve mineral cohesion and growth, compaction, cementation, and illitization. Other rock changes include mineral inversion and neomorphism, recrystallization, mineral overgrowth, mineral replacement, mineral deformation, oxidation and hydration, and dissolution (Table 6.1). The sediment transformation reflects the variety of environmental temperature and pressure conditions that prevailed during their formation and brings textural and thermodynamic stability to the environment (Worden & Burley, 2003). Diagenesis can be split into two stages, including early diagenesis and burial/late diagenesis (Choquette & Pray, 1970) (Table. 8.1). The diagenetic study was achieved through the use of petrographic studies to determine diagenetic mineral and texture changes.

Table 8. 1: The diagenetic stages experienced by the samples.

DIAGENETIC STAGE	DIAGENETIC PROCESSES
Early Diagenesis	Mineral cohesion and growth Compaction Cementation Illitization Cementation Mineral inversion and neomorphism Authigenic minerals
Late Diagenesis	Replacement Mineral growth Mineral replacement Mineral deformation Oxidation and hydration Dissolution



University of Fort Hare

8.2.1. Mineral cohesion and growth *er in Excellence*

As the Fe-, Mn- and P-bearing soft lutite/argillite have been found on the modern seafloor, particularly in the up-welling current areas (Ye & Miller, 1989; Ye et al., 1989; Liu, 1990). The Fe (or Mn and P) element gradually disperse/differentiate from the ferruginous lutite and move towards a nucleus. These elements go through cohesion together to become an iron-rich patch. Various patches further grow and connect, forming micro- or mesobands of the banded iron formation. The formation process of phosphorite and manganese nodules on the seafloor is similar to the BIF formation. This modern metallogenic process can be traced to the BIF in the Kuruman Formation in the Prieska area. The cryptocrystallinity and microcrystallinity features of the magnetite and hematite in the patches or microbands indicate they were primary minerals and formed in the early diagenetic stage (Fig 8.1). The iron element started to disperse/differentiate from lutite (mudstone) to form magnetite or hematite patches and then connected to become magnetite and hematite microbands as shown by Fig. 8.1, and as well as

in Fig. 6.13 and 6.15. The microbands could be deformed (folded) due to a tectonic movement during the early diagenetic stage.

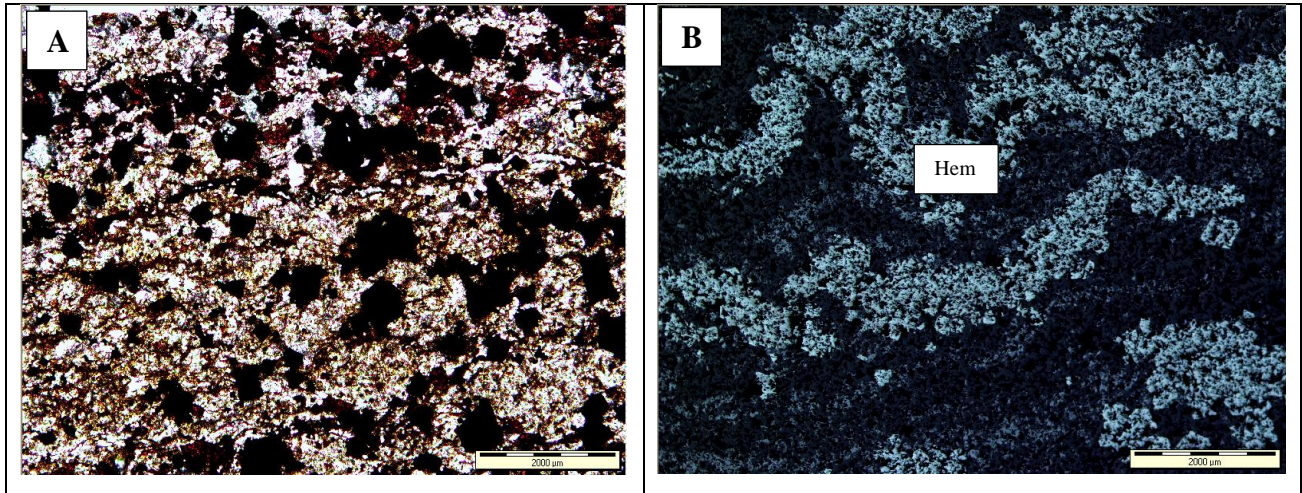


Figure 8. 1: Transmitted light photomicrograph (A) showing original sediment mix of iron-oxide, chert (quartz) and mud material; (B) Reflected light photomicrograph showing cohesive hematite patches and microbands with syndepositional deformation (folding), which indicates that it was formed in a very early diagenetic stage, and sediments were not fully consolidated.

University of Fort Hare
Together in Excellence

8.2.2. Mechanical and chemical compaction

Compaction involves dewatering and close packing of grains facilitated by vertical shear-compressional stresses resulting from the increasing weight of overloading sediments (Burley & Worden, 2009). The overloading pressure causes the sediment grains to be compact, forming a more dense collective material (Boggs, 2009). Mechanical compaction occurs during the initial stages of rock formation. After the sediment deposition, loose detrital grains' intergranular pore spaces are reduced due to overburden weight. This weight causes a change in grain packing by rotation, translation, fracturing, and plastic deformation, thus reducing the strata' porosity and permeability (Pettijohn et al., 1987). The non-contact (free-floating packing grains) changes to point contacts, tangential/long face contacts, then to concavo-convex contacts, and sutured contact patterns with progressive compaction (Boggs, 2009) (Figure 9.1).

Further compaction through overburden pressure may have resulted in the deformation and fracturing of grains (Figure 9.8). Compaction is responsible for developing different grain contact styles, such as tangential to concave-convex and sutured contacts (Fig. 8.2) (Boggs, 2009). The suture contacts occur between the grains of a similar solubility, whereas concavo-convex contacts form where one grain partially dissolves and penetrates another grain.

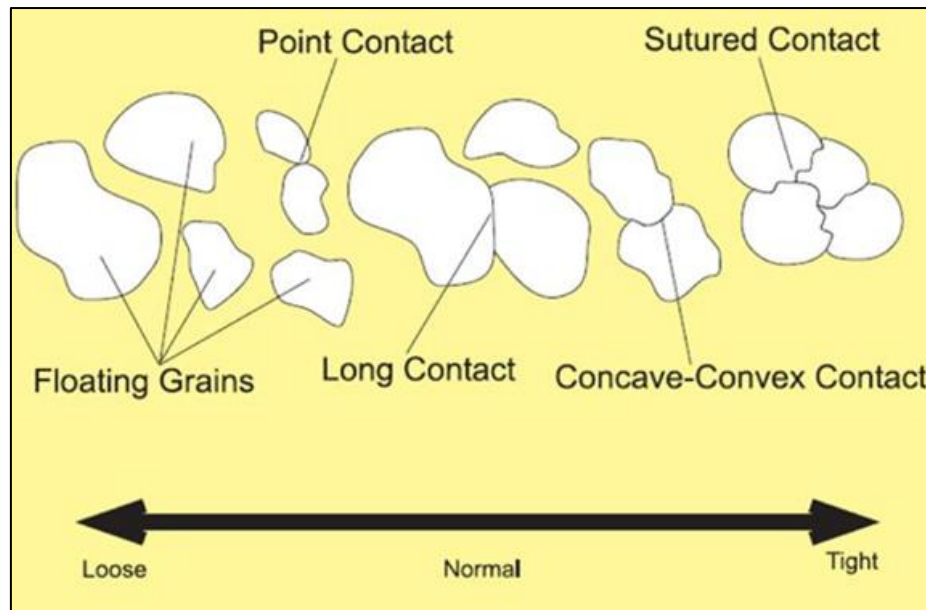


Figure 8. 2: Photograph showing grain to grain contact patterns influenced by burial depth (after Boggs, 2009).

The samples display a range of grain contacts from point to sutured contacts resulting from progressive burial. Long contacts are common in quartz grains, signifying an intermediate burial depth. Other observed grain contacts are the concavo-convex and sutured contacts in quartz and lithic grains resulting from compaction and pressure dissolution processes in the Kuruman formation. The occurrence of sutured and concavo-convex contacts is also attributed to the deep burial diagenetic stage. Some of the quartz grains display parallel orientation, and others comprise chalcedonic texture.

The compaction decreased the porosity and permeability within the samples. There are observed fractures on detrital quartz grains and the mineral deformation observed on the aligned quartz grains. The samples have also undergone chemical compaction responsible for dissolution, recrystallization, and precipitation in response to overburden weight and higher

stress. The compaction has also led to the carbonate minerals being dissolved and leached out of the system without replacement.

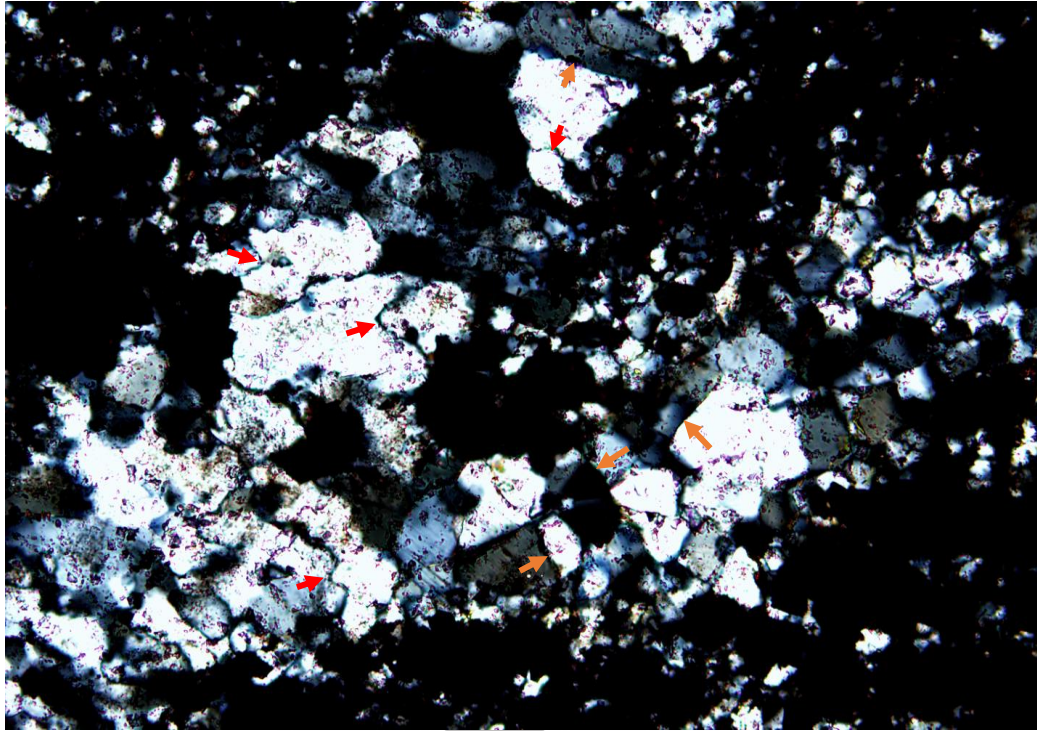


Figure 8. 3: Transmitted light photomicrograph showing the long contacts (orange arrows) and concave-convex contact patterns (red arrows) of the quartz grains in a chert-rich band.

8.2.3. Pore spaces and pore network

The pore spaces are generally grouped into primary pores and secondary pores based on their formation. The primary pores, also called depositional pores, are formed during dissolution, mineral replacement, and recrystallization. Meanwhile, the post-depositional secondary pores are mostly formed during deformation processes. The occurrence of the pore spaces and pore network in the Prieska BIF would mostly be influenced by the dissolution of the carbonate and silicate minerals during diagenesis. They are also impacted when iron oxides and quartz replace the susceptible carbonate and silicate minerals. The pore spaces can be between the grains (inter-pore spaces) and within the crystals (intra-pore spaces). These pore spaces can be later filled by one of the BIF minerals, particularly iron oxides or silica.

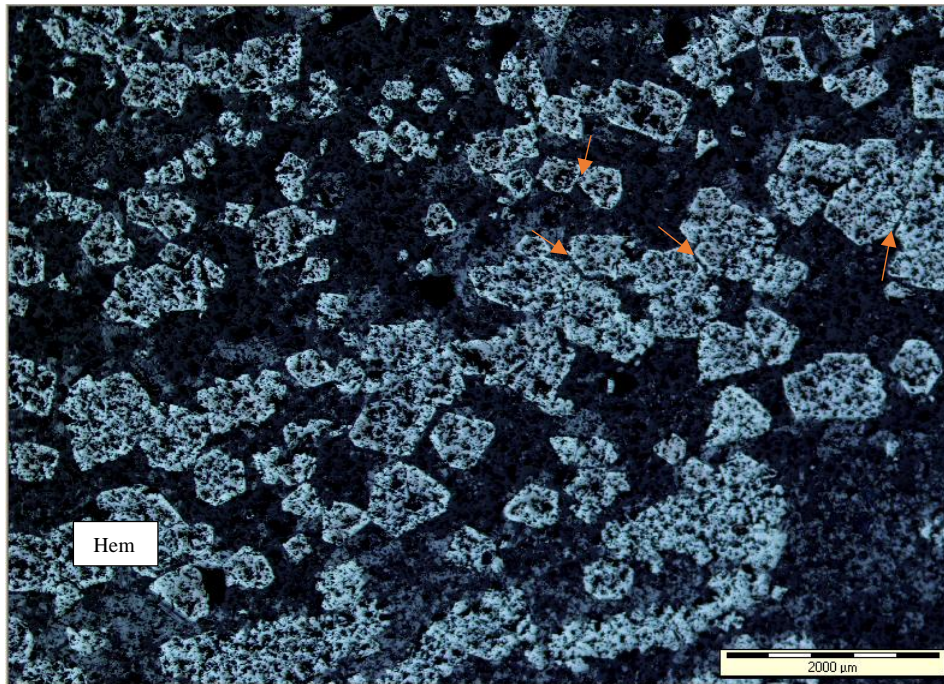


Figure 8. 4: Reflected light photomicrographs showing the inter-pore spaces (red arrows) and intra-pore spaces in the hematite-rich (Hem) mesoband.



University of Fort Hare
Together in Excellence

8.2.4. Mineral overgrowth

Some of the minerals experienced changes in their shapes and sizes without changing their composition. During mineral overgrowth, the anhedral-shaped quartz and iron-oxide grains become more euhedral shaped (Fig. 8.). Quartz and iron-oxide overgrowths are due to temperature increase at burial diagenesis. There are widespread goethite overgrowths at the boundary of paragenetically older martite and hematite crystals (Fig. 8.5).

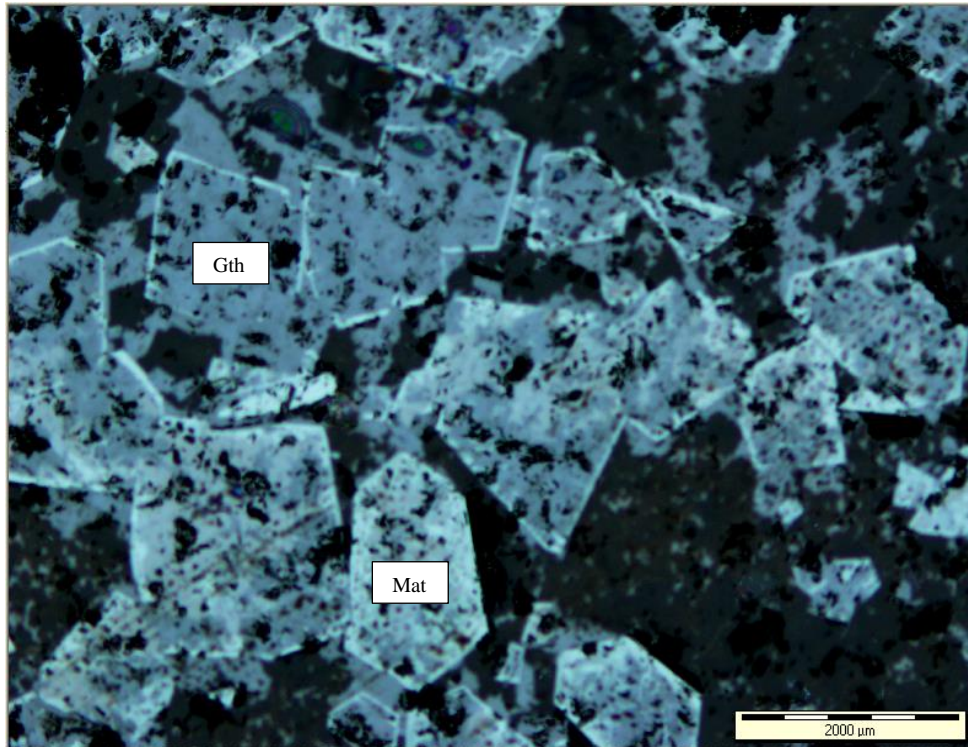


Figure 8. 5: Reflected light photomicrographs showing goethite (Gth) pseudomorph after magnetite with early hematite preserved on crystal faces of original magnetite.



University of Fort Hare
Together in Excellence

8.2.5. Cementation

Cement is the precipitated chemical mineral within the grain pore-spaces that binds the detrital grains together. The cementation process occurs between initial deposition and deep burial stages, and it decreases the rock porosity. Two major cement types are found within the Prieska BIF rocks, including detrital cement and orthogenic cement. The identified cement types are hematite cement, goethite cement, quartz cement, clay cement, and very rare carbonate cement.

Hematite cement

Hematite occurs as pore-filling cement or as rims around coarser quartz in a chert-rich band. It acts as a grain coating and pore-filling mineral in the pore spaces (Fig. 8.6 A). The hematite cement was developed by chemical precipitation and later by pressure solution process during burial diagenesis. Abundant cryptocrystalline hematite is found at the centre of martite euhedral

or within microcracks and small voids caused by dissolution. Some bands develop microcracks filled with crypto- or fine-crystalline hematite and dissolution holes filled with secondary flaky quartz (Fig. 8.8A).

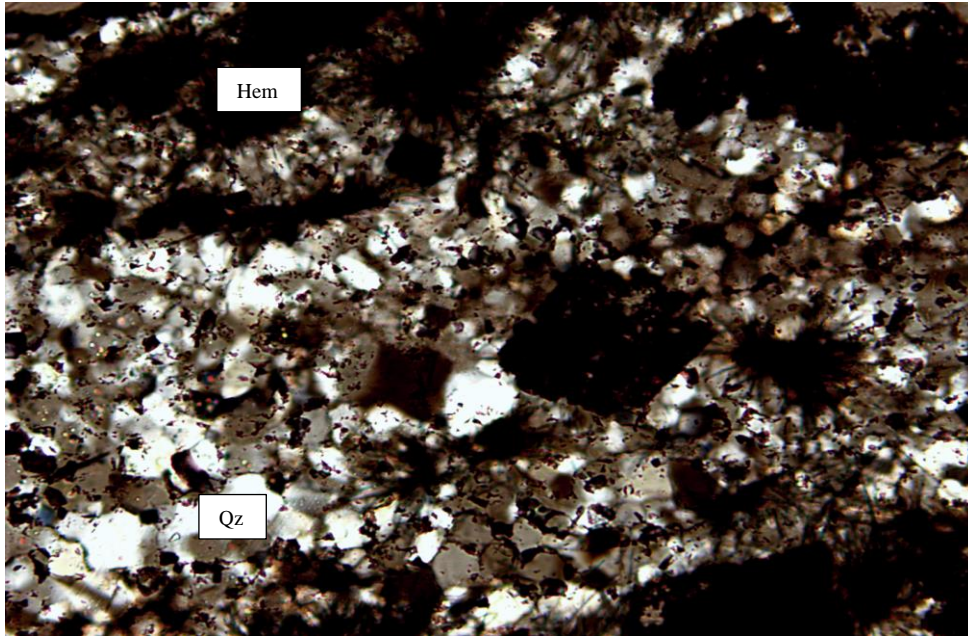


Figure 8. 6: Transmitted light photomicrograph showing hematite (Hem) cement (dark areas) around the quartz grains in a quartz-rich band. The rhombic crystal in the middle of the photo is hematite that replaced a carbonate precursor.

Goethite cement

Goethite in the area occurs as a matrix and as cement (Fig. 8.7A & B). Goethite was replacing an earlier mineral assemblage due to weathering of samples. It appears as pore-filling cement or as rims around detrital grains (Fig. 8.6). Goethite fills intergranular martite pore spaces or the intragranular martite pore spaces commonly at the centre of martite grains in a texture associated with coarse bladed specular hematite.

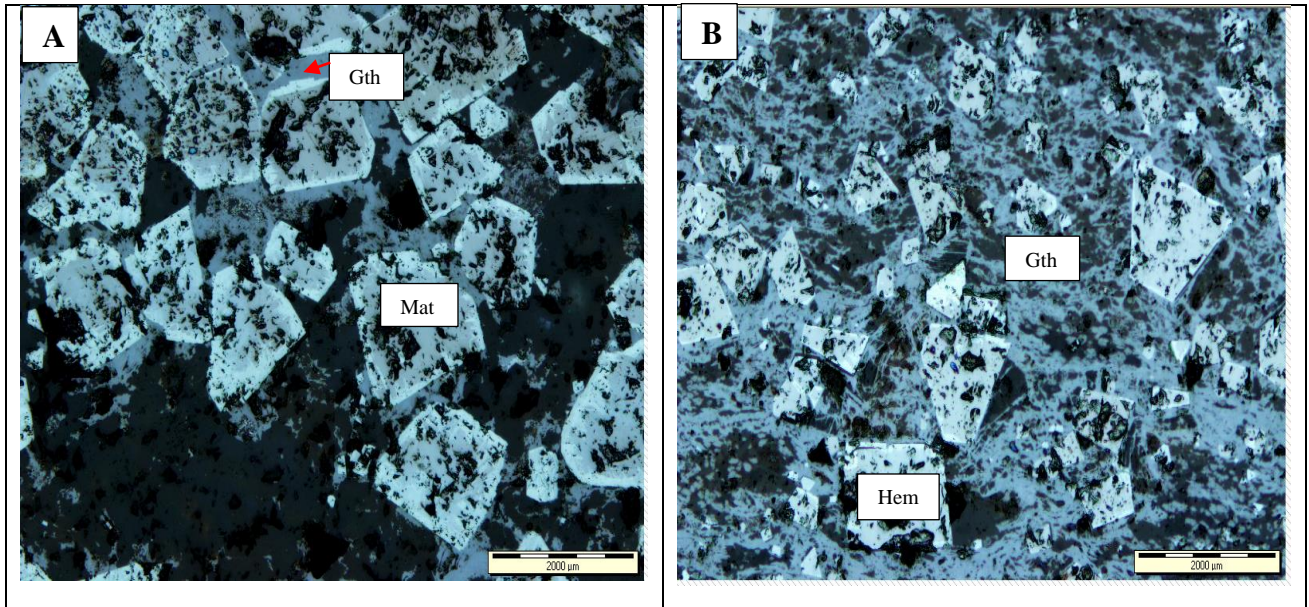


Figure 8. 7: Reflected light photomicrographs showing (A) goethite cement (Gth) occurring as pore-filling cement between martite crystals (mat); (B) Goethite-rich matrix or cement (Gth) occurring with hematite (Hem) grains.



University of Fort Hare

Quartz cement

Diagenetic quartz cement occurs through the silica precipitation within the pore spaces between grains. This cement type was formed early in a shallow marine depositional environment and represented an early diagenetic process. The secondary quartz cement occurs in or adjacent to horizontal pores or cracks. Some quartz also fills veinlets or filling the dissolution holes.

Clay cement

The clay occurs as both detrital and authigenic clay matrix and cement. Smectite represents the clay matrix and coats between grains before the compaction and diagenesis, while illite cement formed before dissolution took place.

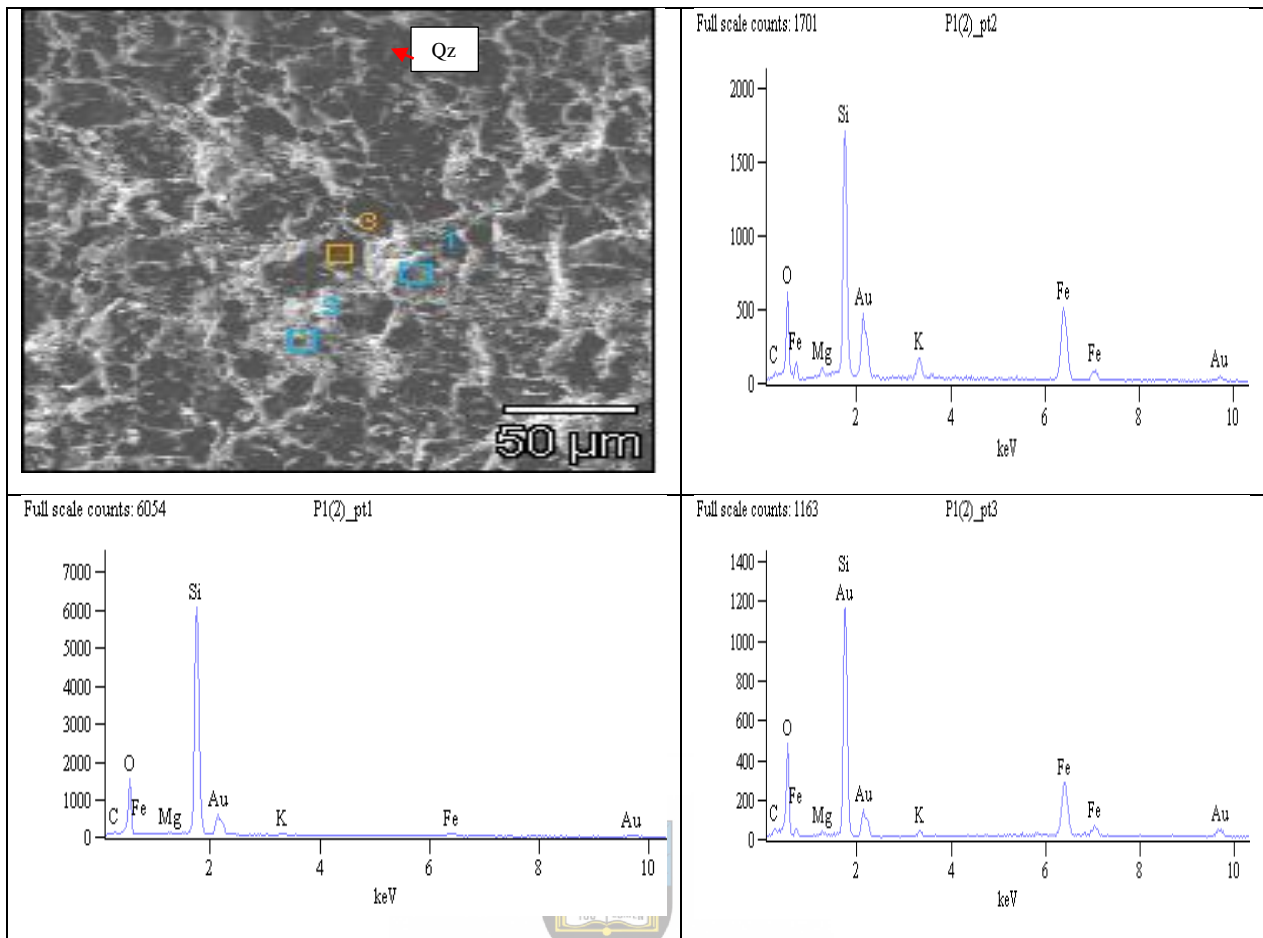


Figure 8. 8: SEM-EDX photomicrograph showing the detrital quartz grains (Qz, point 1 and 3 at the top right and lower right), matrix, and cement formed by quartz, iron oxides, and silicates (point 2, lower left). Au peak is due to Au-coating.

8.2.6. Authigenic minerals

Authigenic minerals are formed during an early diagenetic stage. The minerals automatically grow from the matrix with euhedral or subhedral crystalline shapes. Various authigenic minerals have been found in the BIF of the Kuruman Formation, including authigenic quartz, hematite, martite, and clay minerals, identified through microscope study, SEM, and EDX analyses (Fig. 8.4B, 8.5A & 8.9). The formation of authigenic minerals requires necessary chemical composition and suitable diagenetic environments, such as favourable temperature and pressure of the diagenetic conditions.

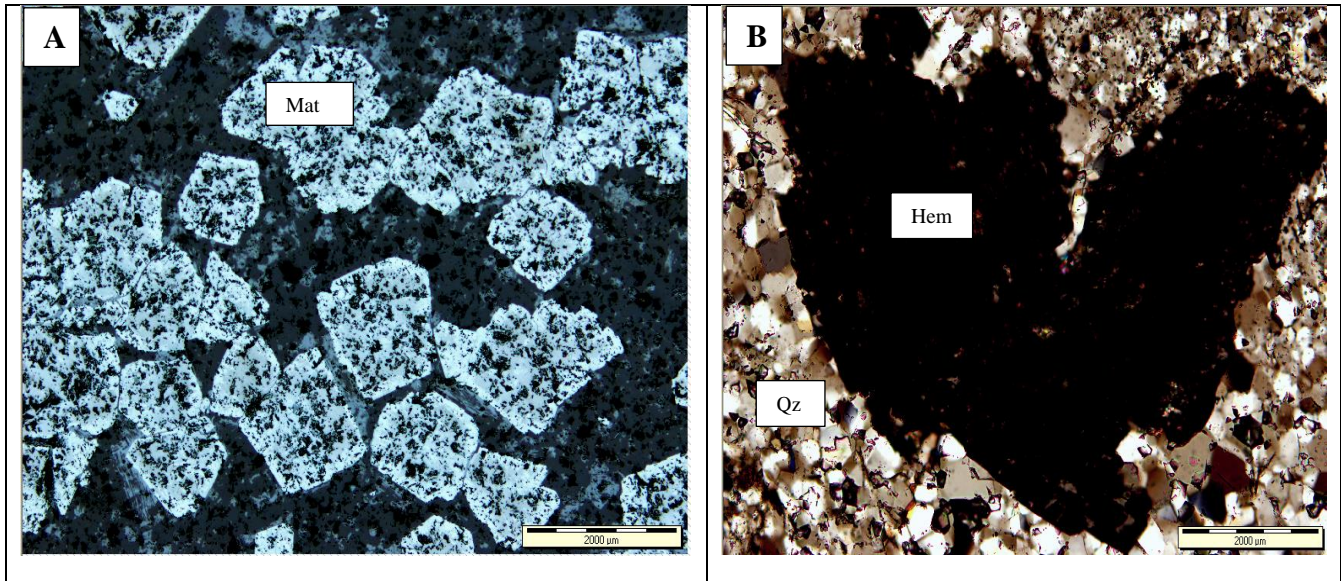


Figure 8. 9: Reflected light (A) and transmitted light (B) photomicrographs showing authigenic martite (Mat) with subhedral to euhedral crystalline shapes; (B) subhedral quartz crystals at the sides occurring with dark hematite (at the centre of the photograph).

8.2.7. Recrystallization



The increase of burial depth increases temperature and pressure, thereby changing the pore fluid compositions. The temperature and pressure increase causes instability in some minerals, and they gradually change their shape or size and compositions to fit the new environment. These changes facilitate the formation of a new mineral that replaces the old one (Folk, 1965). The shape and size changes are usually called neomorphism, whereas mineral type and composition changes are called replacement.

Recrystallization was indicated by the transformation of cryptocrystalline hematite to microcrystalline and fine crystalline hematite into coarse crystalline hematite under increased temperature and pressure.

Notably, within the samples is the recrystallization of cryptocrystalline quartz to form micro- or fine-crystalline, coarse-grained quartz, and chalcedony quartz (Fig 8.10). Quartz shows well-crystallized and coarser grains, which signify recrystallization during late diagenesis (Fig. 8.10 A). The coarse grain quartz also occurs in quartz veinlets representing the late diagenetic features or post-depositional alteration (Fig. 8.11).

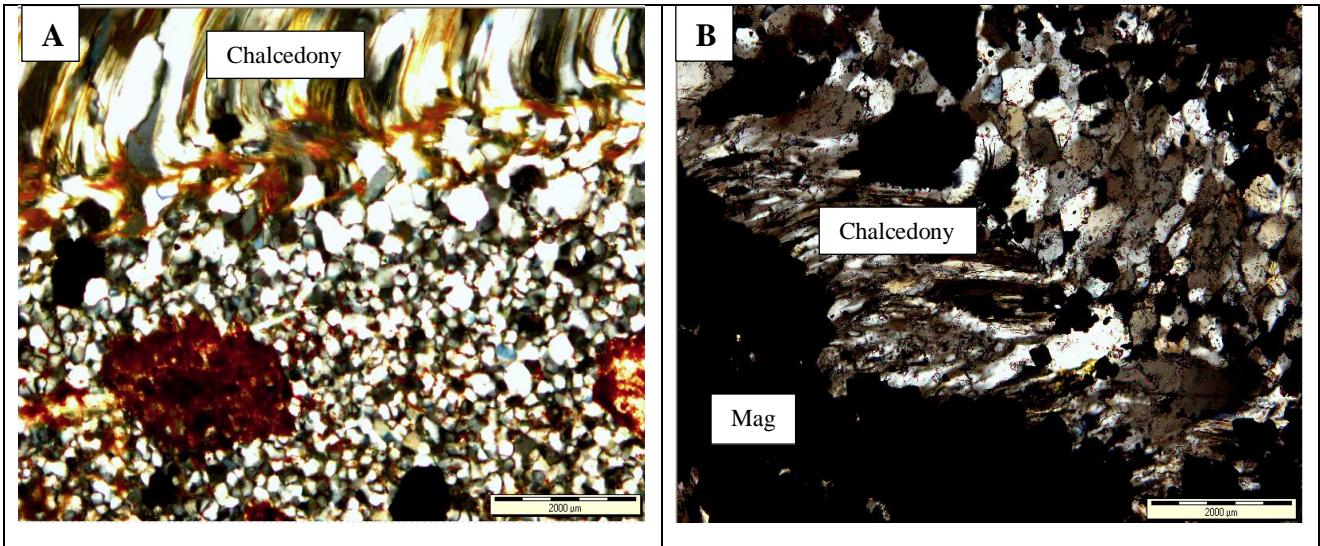


Figure 8. 10: Transmitted light photomicrographs showing (A) different quartz sizes and shapes. The fibrous chalcedony should be noted at the top; (B) various sized and shaped quartz crystals. The bottom is fibrous chalcedony, which grew from the chert band. Chert recrystallized to fibrous chalcedony, then further to quartz.

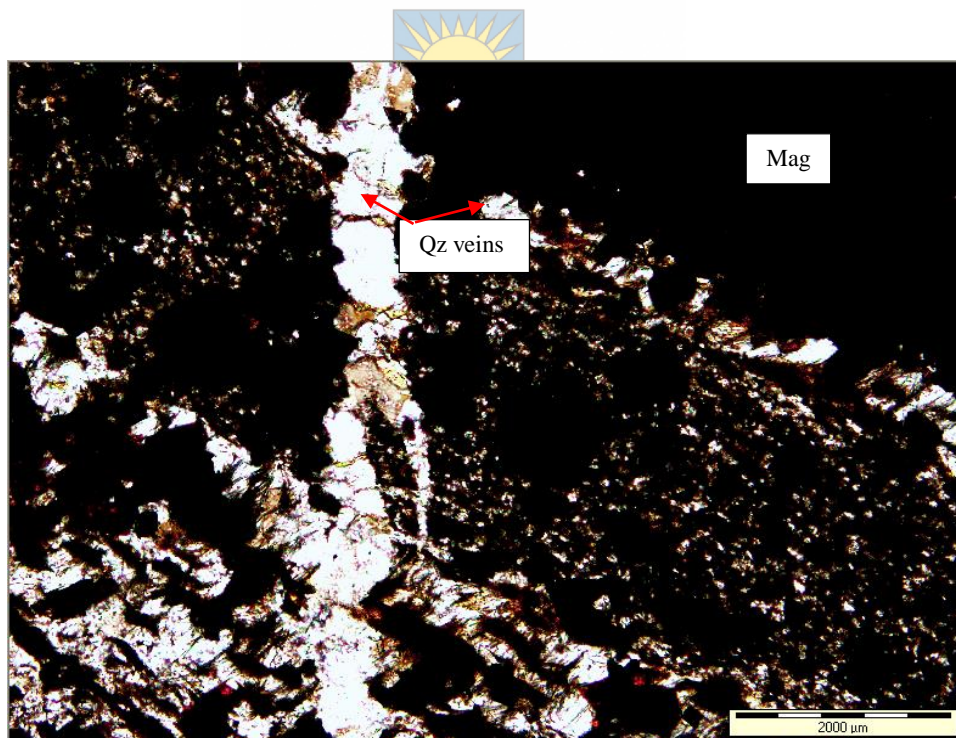


Figure 8. 11: Transmitted light photomicrograph showing horizontal and vertical quartz veinlets related to recrystallization during diagenesis.

Iron oxides experienced recrystallization to accommodate changing structural and diagenetic conditions (Fig. 8.12). They formed from each other during different diagenetic conditions and went through grain merging by growth and oxidation to kenomagnetite/martite or (oxy-) hydration to goethite (Fig. 8.12). With the increase in burial depth, hematite could have gradually recrystallized from the goethite-rich matrix (Fig 8.13). Another common recrystallization phenomenon in the Prieska BIF is siderite transformation with increased burial temperatures to form coarse-grained ankerite. The clay minerals also change, such as the recrystallization of smectite into illite (illitisation) and further to sericite with increasing sediment burial depth of about 3000 meters (Merriman, 2005).

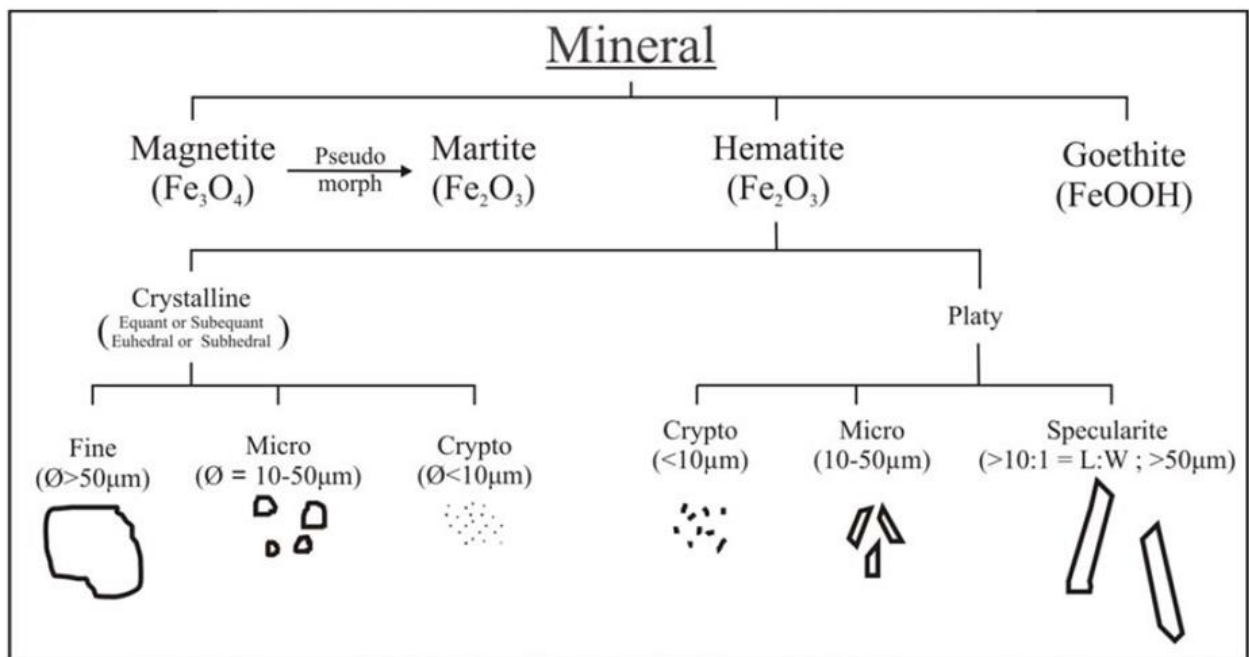


Figure 8. 12: Textural generations of the iron oxides that form BIFs. Magnetite alters to pseudomorphic martite, while goethite is enhanced by surficial weathering. Hematite occurs in various forms (Mukhopadhyay et al., 2008).

8.2.8. Mineral replacement

Mineral replacement is commonly an early to late diagenetic process that transforms the unstable minerals into more stable minerals favoured by the new diagenetic environmental conditions (Folk, 1965). A new mineral replaces a mineral or a group of minerals with different chemical compositions (Fig. 8.14). The new mineral could keep the primary mineral shape (Pseudomorphic shape) or change to a new mineral shape.

The common mineral replacement occurrences in the study area are the replacement of other minerals by hematite, goethite, magnetite, and silica (quartz).

Hematite replacement

Under a microscope, the secondary hematite is formed by replacing the coarser magnetite, while it is also formed through maghemite depending on crystallite size. The original magnetite changes to martite and into laths of specularite or in part to lacunar phases between magnetite and maghemite (kenomagnetite/maghemite), which commonly alters to goethite at a later stage (Dalstra & Rosiere, 2008; Van Schalkwyk & Beukes, 1986) (Fig 8.15). In these changes, magnetite occurs as relicts at the centre of martite crystals. The replacement commences from the periphery inwards and passes through the martite stage to the hematite's final product. The commonly coarser-grained magnetite than coexisting chert and hematite reflects a possible crystallization at the later diagenetic stages from hematite. The break-up of martite crystals after martitization might have distorted the crystal structure.

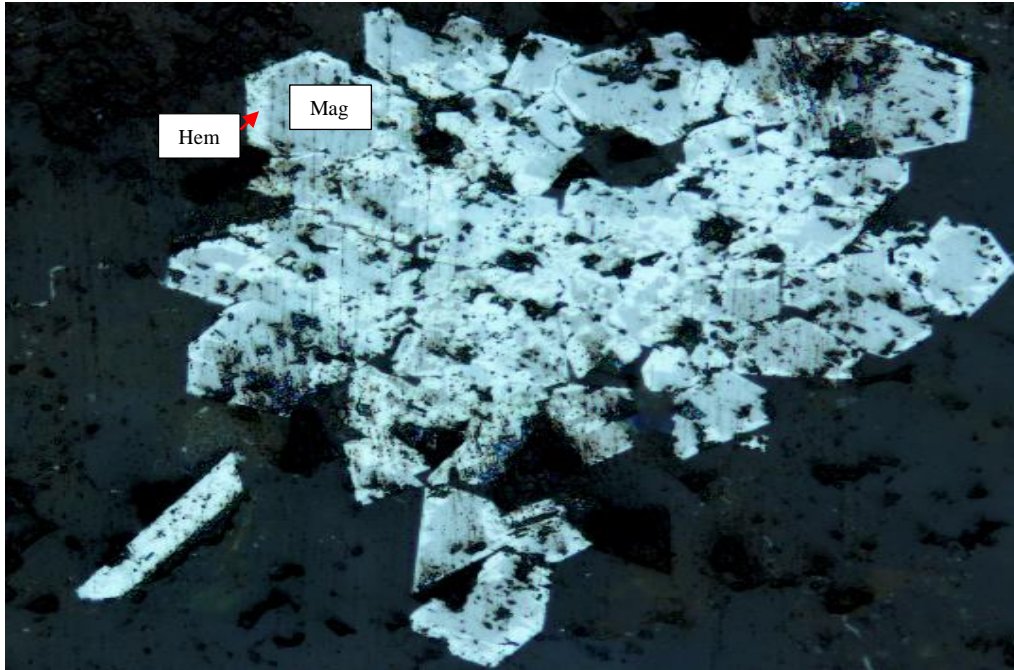


Figure 8. 13: Reflected light photomicrograph showing the inner magnetite/kenomagnetite and outer hematite in the martitising bands.



Hematite also occurs as the secondary replacement mineral for the carbonate minerals and silicates, and part of quartz, as suggested by Clout and Simonson (2005). The carbonate mineral replacement by hematite is reflected by the different sized rhomb-shaped hematite grains (Fig.). The replacement of the silicate minerals by hematite within the quartz-rich bands resulted in hematisation of those bands. Also, the fine-grained hematite present in some of the martite-hematite-goethite bands is a product of goethite conversion.

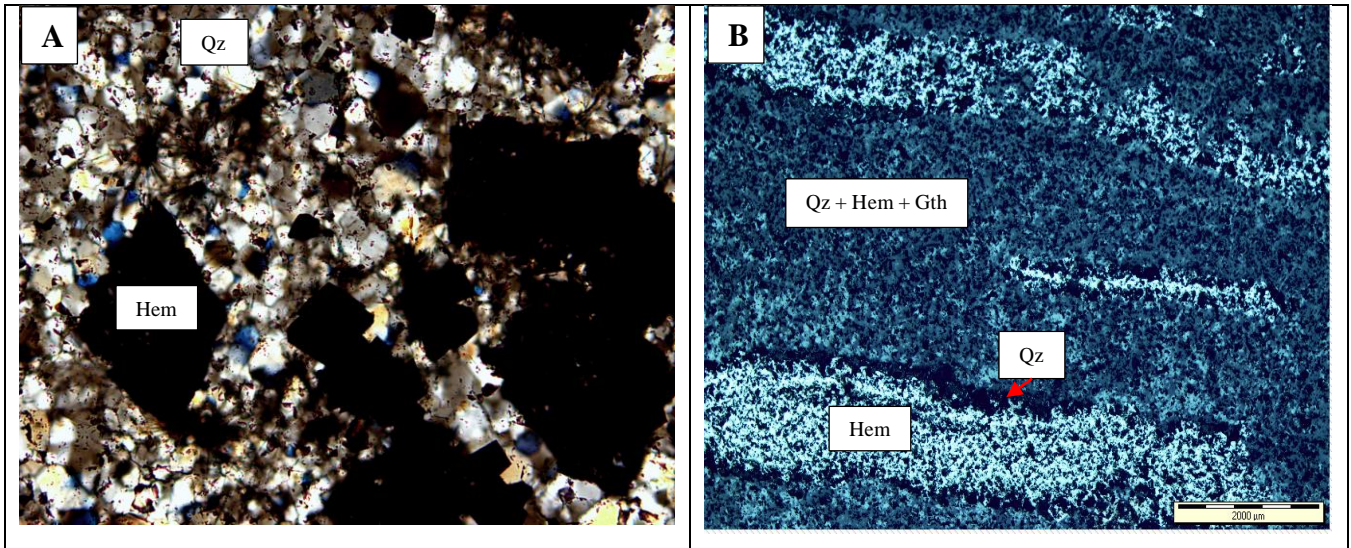


Figure 8. 14: Transmitted light (A) and reflected light photomicrographs (B) showing (A) Hematite (Hem) pseudomorphs of carbonate minerals in the quartz-rich mesoband; (B) Hematite and goethite minerals in partially hematitised bands.

Goethite replacement



Goethite occurs as the secondary mineral replacement for magnetite and hematite/ martite. Magnetite was transformed by hydration into goethite and subsequently into martite by dehydration in a zoning transformation. Goethite replaces maghemite in the martitising areas.

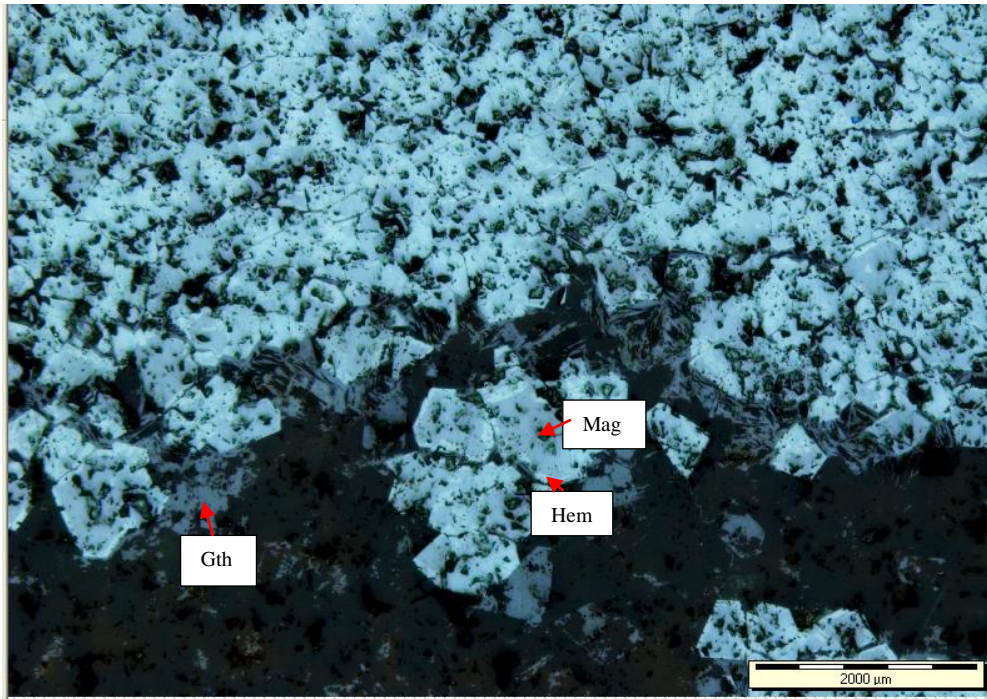


Figure 8. 15: Reflected light photomicrographs showing goethite replacing magnetite/kenomagnetite in the martitising bands. Also shown are the hematite rims around the magnetite crystals.



University of Fort Hare

The carbonates and silicate minerals are susceptible to mineralogical and textural changes. Hence they were later volumetrically replaced by the iron oxides, including goethite, with minor textural changes (Fig. 8.16). Like hematite replacement, goethite replacement for the carbonate assemblage is indicated by the rhomb-shaped goethite crystals. The hematitized original quartz-rich bands also reflect the replacement of the silicates by hematite.

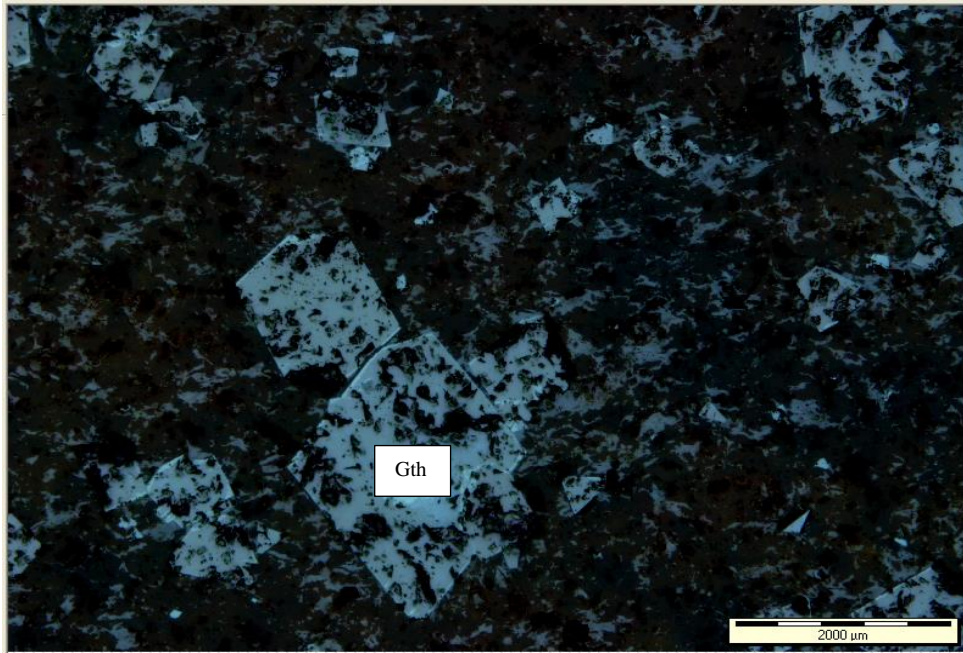


Figure 8. 16: Reflected light photomicrograph showing the replacement of the rhomb-shaped carbonate minerals by goethite.



University of Fort Hare
Together in Excellence

Quartz replacement

Quartz occurs in the Prieska BIF as a replacement mineral in some of the bands. It commonly replaces the susceptible carbonate and silicate minerals (Fig. 8.). The rhombic-shape silica-rich area reflects a typical replacement of the carbonate minerals by quartz. The iron oxides are also rarely replaced by silica during favourable conditions of diagenesis (Fig. 8.14).

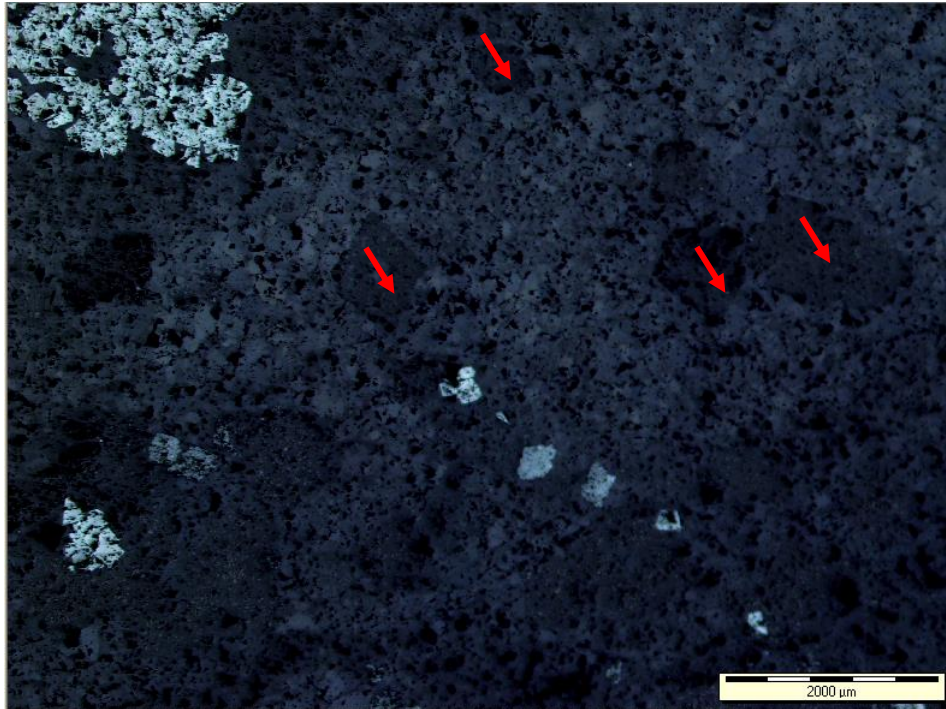


Figure 8. 17: Reflected light photomicrograph showing the replacement of the rhombic-shaped carbonate minerals by quartz (rhomb shapes shown by red arrows).



8.2.9. Dissolution

University of Fort Hare
Together in Excellence

Dissolution is a process where the unstable minerals decompose in liquid due to pH and temperatures, thereby increasing the rock porosity (Fig. 8.18 & 8.19). Dissolution is influenced by mineralogy and the chemistry of the pore waters (Boggs, 2009).

Carbonate and iron silicate minerals are dissolved and destroyed during dissolution, creating cracks or cavity and pore spaces between the mineral grains (Pittman, 1979; Burley & Kantorowicz, 1986). Calcite, siderite, and ankerite are unstable in an acidic environment, while quartz and some silicate minerals are unstable in an alkaline environment. Then, they easily dissolve. The dissolution of the carbonate minerals took place, increasing the porosity of the rocks.

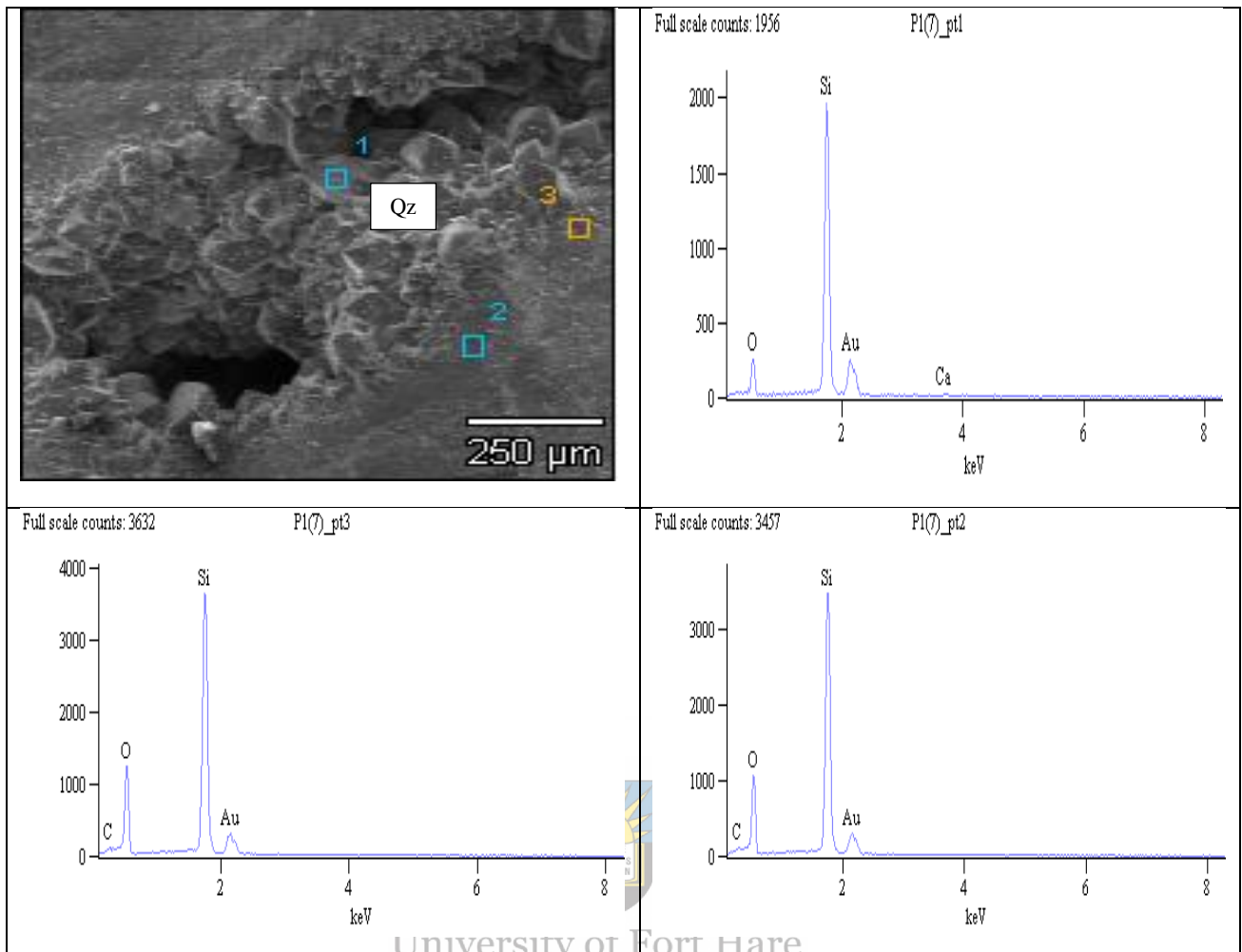


Figure 8. 18: SEM-EDX photomicrograph showing a dissolution hole filled with quartz. It is also showing the remains of the micropores. Au peak is due to Au-coating.

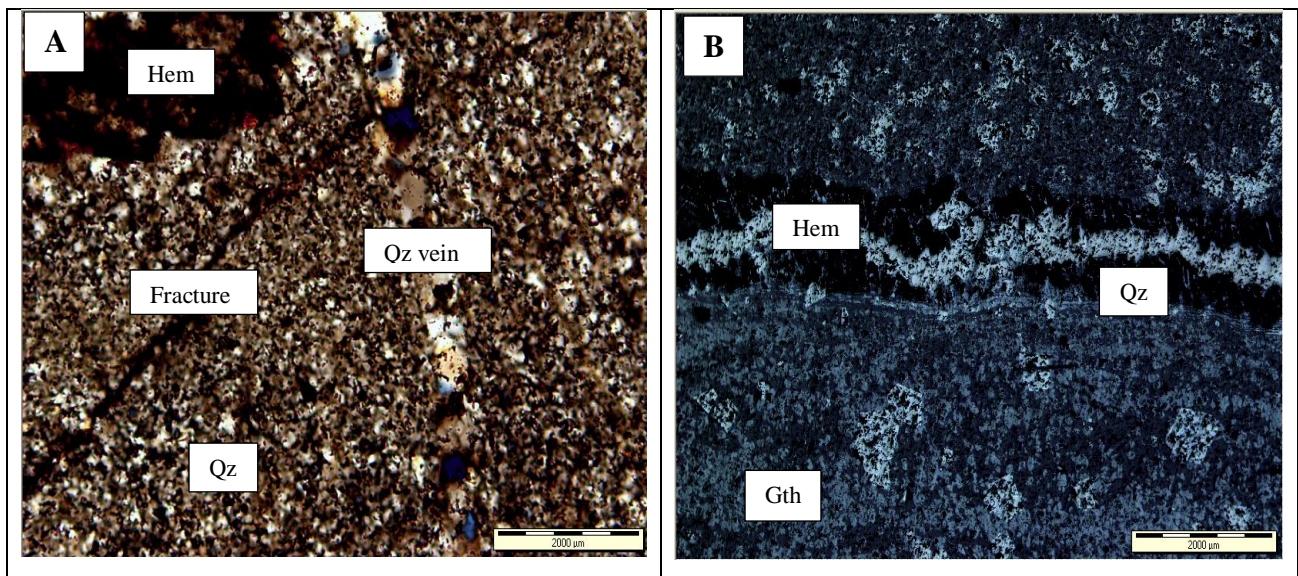


Figure 8. 19: Transmitted light (A) and reflected light (B) photomicrographs showing (A) microcrack filled with fine hematite; (B) Horizontal microcrack filled by fine hematite and dissolution holes that were later filled by quartz.

8.2.10. Tectonic overprint

Some of the mineral transformations and modifications were influenced by the tectonic overprint post-depositionally (Fig. 8.20). Those features are displayed by the irregular folding and pod structures that are exhibited in the different bands. The generally broken and disrupted kink structures in laminated hematite bands are indicated by the fact that hematite micro- or mesobands are fractured along the axial planes of kink folds were formed by brittle deformation. These structures display evidence of previously laminated hematite mesobands. They seem to have occurred in pressure shadow areas and are interlayered with fibrous/chalcedonic and flaky textured quartz (Fig. 8.20A).

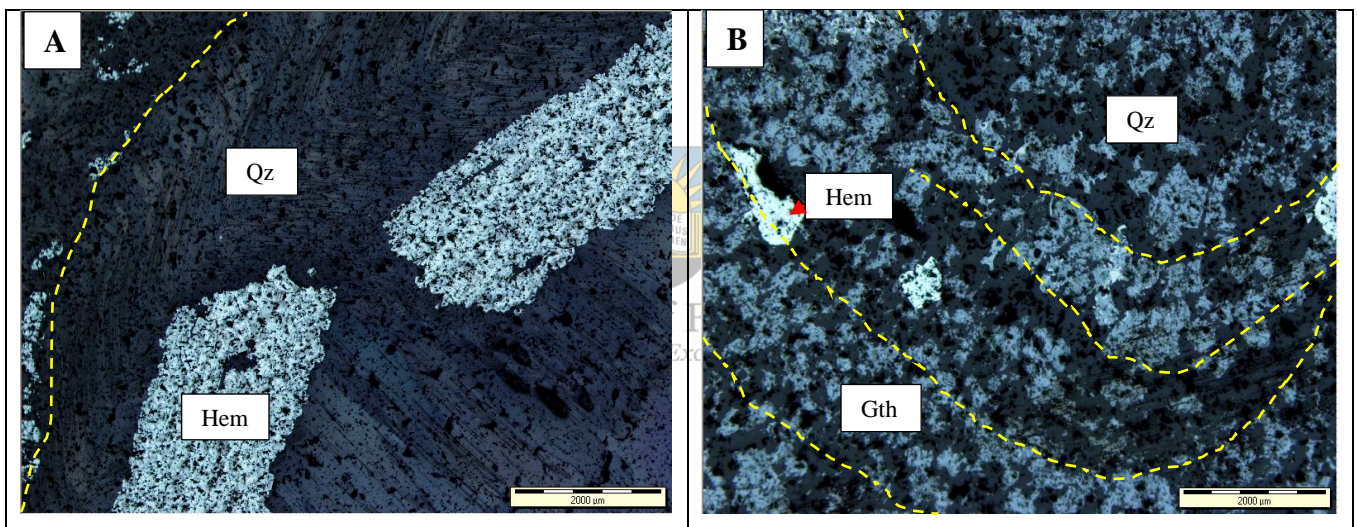


Figure 8. 20: Reflected light photomicrographs showing (A) Broken kink folds; (B) Folded goethite-rich layers (Gth).

8.3. Supergene modification- surficial weathering and oxidation

Supergene modification represents the late stage of alteration like weathering, leaching, dissolution, mineral replacement, grain fracturing, and deformation. This stage takes place when lithified, and buried sediments are uplifted and exposed to the Earth's surface. The samples show evidence of weathering, mineral decomposition, and oxidation from field observations and petrographic examinations. The weak and unstable minerals were weathered

and oxidized or replaced by more stable minerals. Some of the minerals were modified and fractured, resulting in increased porosity.

8.3.1. Field observations

The Prieska BIF displays a white-coloured carbonate bleaching of the rocks. This bleaching results from the leaching out and evaporation of the carbonate minerals (siderite, ankerite, and calcite). The leaching and evaporation of the carbonate minerals also form a carbonate mineral-rich calcrete at the near-surface (Fig. 8.24). The source of calcium could be coming from dolomite, calcite, siderite, or ankerite. These minerals could be leached out from the top layer. It could also be due to the evaporation of Ca-bearing pore water by capillary force from under layers by sunlight evaporation in a semi-arid climate.

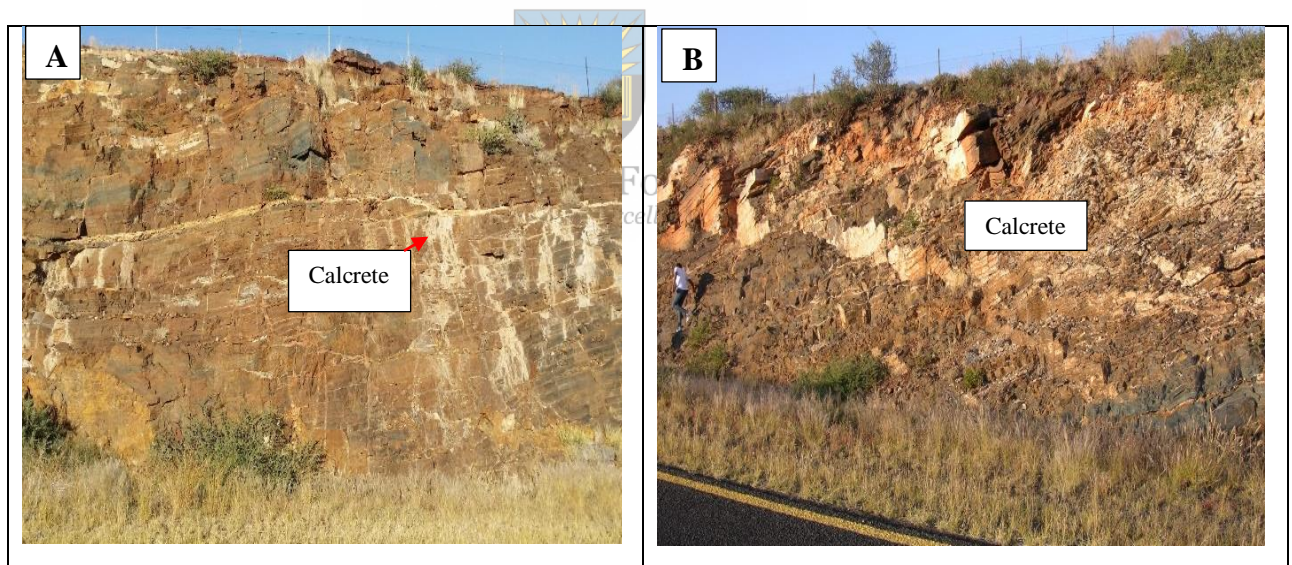


Figure 8. 21: Field photographs showing a weathering formation consisting of leaching carbonate minerals (carb), calcrete (white area), and limonite (reddish-brown area on B). This has to do with soil formation in the area or calcretization that is very common.

The yellow goethite is a weathering product of either hematite or magnetite (Fig. 8.25B). The hard steel grey hematite transforms to earthy red-coloured hematite and yellowish-brown goethite and limonite during weathering, as shown from the field observations (Fig. 8.25A). The yellowish-brown goethite and limonite may also be a result of carbonates or silicates replacement. The effects of differential weathering are evident in Figure 8.25A, causing dissolution cavities in the BIF sequence.

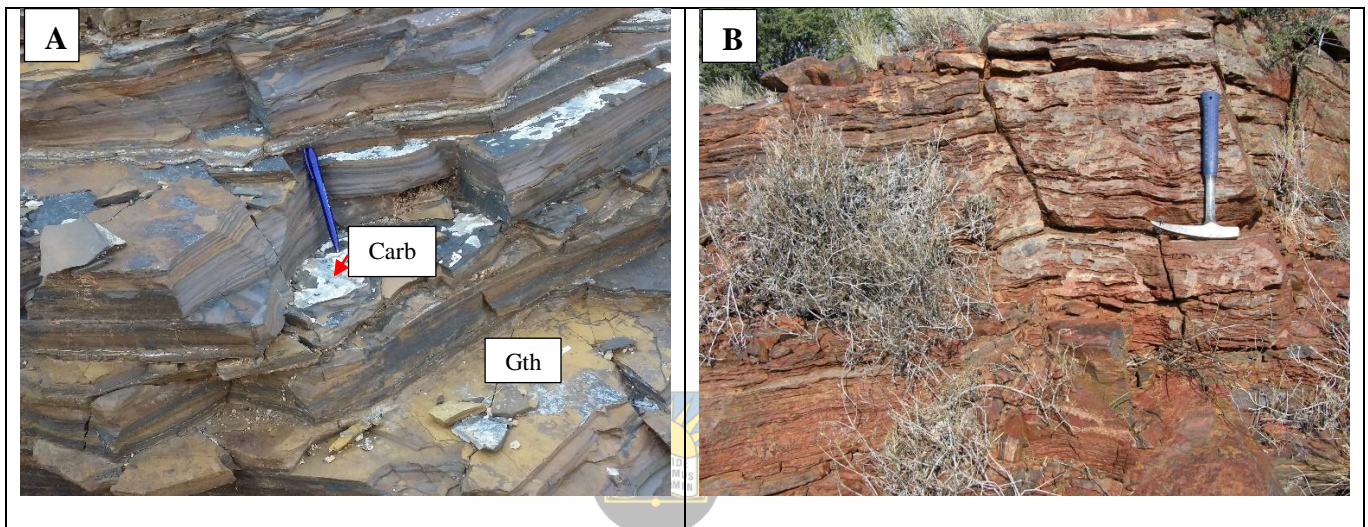


Figure 8. 22: Field photographs showing (A) Original dark BIF gradually changes to yellowish goethite-hematite after weathering; also calcrete (Carb) on the bedding surface; (B) Red-brownish limonite on the weathered surface.

8.3.2. Petrographic evidence

The hematite, goethite, limonite, martite, magnetite, calcrete, and kaolinite mineral assemblages reflect intensive oxidation and weathering above the groundwater table (e.g., LaBerge, 1966). Magnetite is oxidized to martite, while the carbonates and silicates are replaced by goethite. Quartz is rarely altered by weathering (Fig. 8.26). The iron silicates and carbonate minerals appear to diminish with the increase in weathering intensity, while quartz and iron oxides remain the dominant minerals in weathered zones. Further dissolution and leaching caused by weathering destroyed the already altered iron silicates and carbonate minerals (Fig. 8.26B). It also enhanced the oxidation of magnetite to martite and, in part, to goethite. The dissolution and leaching of the iron silicate and carbonate minerals increased

inter-granular porosity. This dissolution and leaching were accompanied by hematite and goethite precipitation since the carbonates and silicates are minor components.

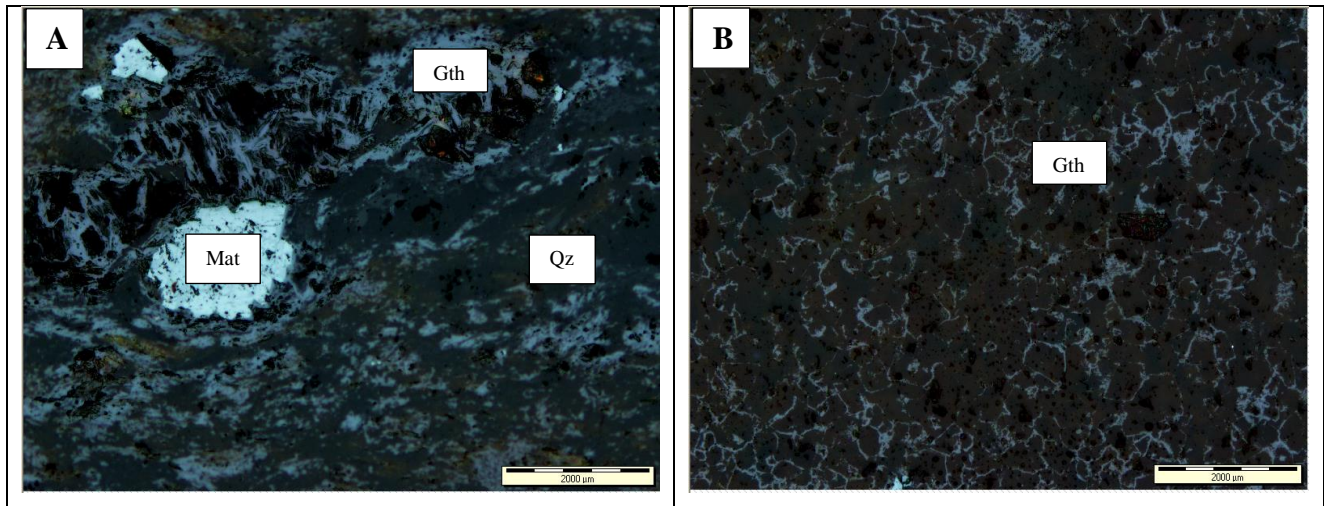


Figure 8. 23: Reflected light photomicrograph showing (A) highly leached vuggy microband with pore-filling secondary martite (Mat) and fibrous goethite (Gth) in the supergene zone; (B) highly weathered and leached goethite-rich (Gth) band.

Goethite appears as a fibrous crystalline mineral or fine-grained groundmass replacing hematite and magnetite (Fig 8.27). It was probably formed at low temperatures by the hydration of magnetite/hematite. Subsequent weathering, including leaching and dissolution of goethite in preference to hematite, gives rise to the typical skeletal or porous texture of the BIF. The significant goethite concentrations in some samples suggest less or no oxidation effects but more hydration influence. Goethite is rarely present in the unaltered samples or bands.

The magnetite also forms overgrowths on the primary hematite. Silica is rarely removed and replaced by fine-grained iron oxides. However, silica acts after magnetite in some sections attest to the mobility of both iron and silica under specific local conditions in this environment. Virtually all components except quartz are leached in some samples, leaving a flinty residue (Fig 8.27B). Preservation of the replacement texture in some micro and mesobands and the well-developed mineral pseudomorphs are compelling evidence that supports the weathering and secondary enrichment. The leaching of goethite in preference to hematite can result in high-grade hematite concentrations consisting essentially of residual martite and primary hematite.

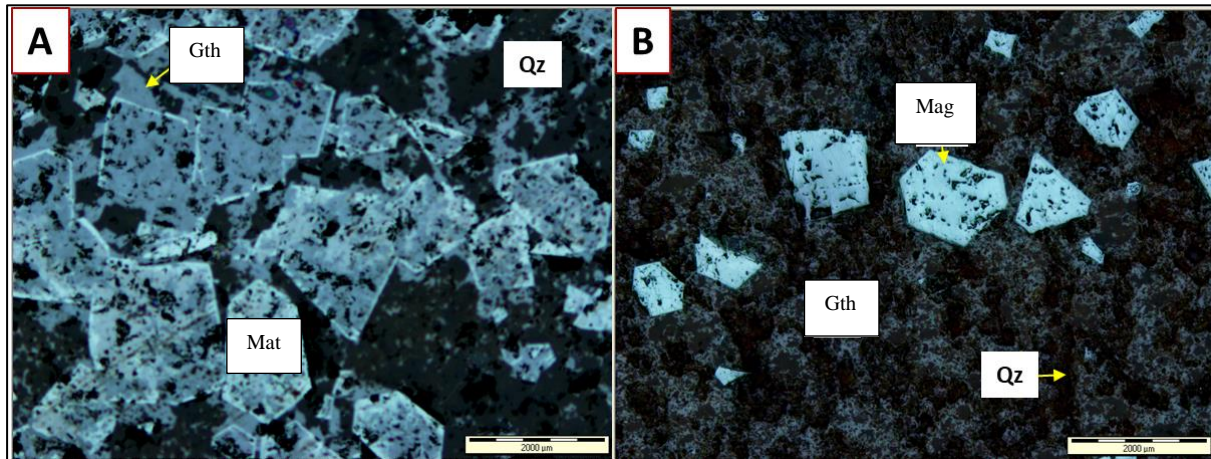
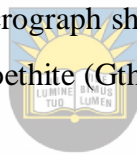


Figure 8. 24: Reflected light photomicrograph showing (A) weathering of magnetite to form goethite (Gth); (B) Leached skeletal goethite (Gth); and authigenic euhedral martite (Mat).



University of Fort Hare
Together in Excellence

8.4. Mineral paragenesis

The mineral paragenesis (Fig. 8.25) represents a genetic sequence or pathway of the mineral assemblages formed over geological time. The mineral paragenesis is deduced from the deposition and diagenetic events and arranged based on the formation time. Thus, the paragenesis sequence (Fig. 8.25) shows the primary and post-depositional minerals of the Prieska BIF and their relative formation time and the relationship among the different assemblages.

The study area's BIF mineral assemblages can be grouped into primary, diagenetic, low-grade metamorphic mineral assemblages, and weathering mineral assemblages (Fig. 8.) Field observations and petrographic evidence were used to distinguish between primary and secondary mineral species.




















MINERAL PHASES	MINERAL TYPE	PARAGENIC ASSEMBLAGE			
		PRIMARY MINERAL ASSEMBLAGE	DIAGENETIC MINERAL ASSEMBLAGE	LOW-GRADE MINERAL ASSEMBLAGE	WEATHERING MINERAL ASSEMBLAGE
Iron oxides	Hematite				
	Martite				
	Magnetite				
	Goethite				
	Limonite				
Silica	Quartz				
Carbonates	Siderite				
	Ankerite				
	Calcite				
Silicates	Calcrete				
	Stilpnomelane				
	Riebeckite				
	Smectite				
	Illite				
	Minnesotaite				

Figure 8. 25: Mineral paragenetic assemblages of the Kuruman BIF the in Prieska area. The line thicknesses and lengths correspond to the relative abundances of the indicated minerals. The chart represents the prevalent BIF mineral phases in different environments.

8.4.1. Primary mineral assemblage

The mineral assemblages of the rocks are composed of various primary and secondary minerals. These primary minerals include hematite, magnetite, chert (amorphous quartz), calcite, siderite, and smectite. Hematite and magnetite are interpreted as the primary mineral

from the petrographic evidence. Also, the cryptocrystalline to microcrystalline chert (quartz) indicates primary precipitation.

The optical zonation displayed by siderite from the petrographic study is evidence for siderite formation as a primary precipitate. This zonation reflects the immediate changes of the seawater or pore fluids chemistry (Konhauser et al., 2005). It indicates that siderite is one of the earliest mineral precipitates of the Prieska BIF sediment. Petrographic examination revealed no evidence for a carbonate precursor or significant grain replacement by the siderite. The siderite appears to have formed entirely through direct precipitation in the bottom water or intergranular pore water. The siderite zonation shown by the petrographic examination reflects the possibility of two principal siderite types (Fe-rich and Mg-rich). Paragenetic relationships in samples containing both types invariably indicate that the Fe-rich siderites formed before the Mg-rich variety.

Stilpnomelane formed as a primary silicate precipitate based on textural grounds and in the absence of a possible precursor. Stilpnomelane is stable at 25°C from low to high Eh at alkaline pH in the iron-formation system.



8.4.2. Diagenetic mineral assemblage

University of Fort Hare
Together in Excellence

The diagenetic mineral assemblage includes all those minerals formed from the primary or pre-existing minerals during diagenesis. These minerals are hematite cement, magnetite, quartz cement, ankerite, recrystallized clay mineral illite, riebeckite, and stilpnomelane.

Primary silica mineral chert recrystallized to quartz, and its crystalline size gradually changed from fine-grained to coarse-grained with the change from early to late diagenesis. The quartz veins are also associated with late diagenesis and metamorphism.

Hematite precipitated from the initial ferrihydrite, $\text{Fe}(\text{OH})_3$ (Ahn & Buseck, 1990; Glasby & Schulz, 1999). The ferrihydrite precipitates into goethite and small hematite at pH 4, while major hematite crystallizes at pH 7–8. Therefore, hematite is interpreted as a secondary mineral formed near-neutral pH conditions after initial precipitation.

Magnetite could be formed from hematite or ferrous carbonates such as siderite. Magnetite formation could be driven by partial reduction of hematite by organic carbon (Ohmoto, 2003;

Frost et al., 2007; Pecoits et al., 2009; Li et al., 2013). It could also be formed through partial oxidation of Fe (II) or Fe (III) minerals by CO₂. It could be produced by siderite oxidation at 450°C and 2kbar (French, 1971; McCollom, 2003; Marocchi et al., 2011).

The flaky or fibrous chalcedony was recrystallized from chert, and it will further to quartz. Chalcedony lines up parallel to deformation and local tectonic pressure. (Fig. 6.4B). These are interpreted as diagenesis or post-depositional recrystallized quartz varieties.

Some authigenic siderite growth occurred during early diagenesis and burial. The impure, Mg-enriched nature of the siderites is typical for early diagenetic siderites from marine depositional environments (Mozley 1989). Diagenetic maturation thus results in an increasing crystallinity of siderites. No sign or evidence reflects chert substitution by siderite within the Pieska BIF.

The coarser-grained ankerite represents the late diagenetic minerals. The data suggest that ankerite formed during the samples' deep burial and compaction, forming larger grains and distorting the primary microlamination. The ankerite could be representing a by-product from siderite dissolution and subsequent CO₂ release. The secondary calcite variety was formed during early to late diagenesis.

The minnesotaite represents the late stages of diagenesis, possibly being formed from stilpnomelane or primary greenalite at 200°C to 230°C temperatures (Ayres, 1972; Frost et al., 2007; Kleyenstuber, 1985). Minnesotaite and possibly riebeckite developed through the late stages of diagenesis or low-grade metamorphism that resulted from the rocks' deep burial.

Riebeckite formed in the course of late diagenesis or very low-grade metamorphism (around /150⁰C) on mineral assemblages and textural relationships (e.g., Trendall & Blockley, 1970; Gole & Klein, 1981). Riebeckite probably formed when iron-oxides reacted with silica and water (Gole & Klein, 1981). It could have formed through the reaction of carbonates (siderite), silica, and water. Through the reaction of iron-oxides, carbonates, silica, and water. Through the reaction of iron silicates (stilpnomelane), carbonates, and silica. Through the reaction of iron-oxides and stilpnomelane (Gole & Klein, 1981, Miyano, 1982). The first three reactions are the most likely for the formation of riebeckite in the area. Hematite and magnetite are the sources of iron, while quartz is the source of silica. The carbonates could be an important source of magnesium and iron for riebeckite. In general, riebeckite related to carbonates has a higher MgO content than that of carbonate-free associations. Siderite may be an important reactant among the carbonates during diagenesis because of its common existence. The common constituents of most riebeckite assemblages are ankerite and calcite. The massive riebeckite

bands result from riebeckite replacing the primary minerals in quartz-iron-oxide mesobands. Riebeckite used magnetite and other minerals as nucleation and growth sites. Riebeckite was affected by weathering and replaced by the iron oxides or leached out when exposed to the earth's surface

Illite formed from smectite through cation substitution, releasing Mg^{2+} and Fe^{2+} into solution (Burst, 1969; Perry & Hower, 1970; De Segonzac, 1970; Foscolos & Kodama, 1974; Hower et al., 1976; Boles & Franks, 1979; Inoue, 1988) at major depth during late diagenesis.

8.4.3. Low-grade metamorphic assemblage

The low-grade metamorphic mineral assemblage within the Prieska area includes riebeckite and minnesotaite. In contrast, the flaky and fibrous chalcedonic quartz have been interpreted as the later tectonic overprinting or deformation quartz.

Quartz is affected by burial stress conditions such as pH, temperature, and pressure (Choi et al., 2012). The flaky, fibrous quartz and long quartz fringes are more pronounced parallel to deformation and pressure shadows adjacent to the iron oxide micro-bands (Fig. 6.4B). These are late secondary diagenesis or post-depositional recrystallized quartz varieties.

Minnesotaite and riebeckite could have developed towards late diagenesis or low-grade metamorphism that resulted from the deep burial of the rocks. Minnesotaite developed during later low-grade metamorphism that resulted from the rocks' deep burial. It must have formed from primary greenalite and iron-rich chlorite during late diagenesis to early metamorphism at 200°C to 230°C temperatures (Ayres, 1972; Frost et al., 2007; Kleyenstuber, 1985).

Riebeckite formed during late diagenesis or very low-grade metamorphism (around 150°C) on mineral assemblages and textural relationships (e.g., Trendall & Blockley, 1970; Gole & Klein, 1981). The riebeckite formation may also be related to deformation, as evidenced by the petrographic examinations (Trendall & Blockley, 1970).

8.4.4. Weathering mineral assemblage

The weathering mineral assemblage involves all the minerals formed due to uplift, weathering, and oxidation (e.g., Bland & Rolls, 1998). These minerals include hematite, goethite, limonite, martite, and calcrete. The quartz shows no evidence of major alteration by weathering. Silica is rarely removed and replaced by fine-grained iron oxides. A rare alteration process in the area is the apparent volume for volume replacement of chert by iron minerals.

Hematite could be formed directly from magnetite through oxidation. At the same time, it could also be formed through maghemite replacing parts of magnetite grains, leaving islands of unreplaced magnetite (kenomagnetite) depending on crystallite size (see Colombo et al., 1965; Ghosh et al., 2013). Hematization of chert banding resulted from hematite replacing silicate minerals within cherty bands. The red hematite also forms from the yellow dehydrated goethite due to heat. Hematite replaces the carbonate minerals as well.

Goethite forms from the ferrihydrite at pH 4. A fine-grained groundmass is formed by widespread goethite that replaced hematite and remnant magnetite during weathering. Goethite probably formed at low temperatures by hydration of the partly oxidized magnetite, martite, maghemite, and hematite phases. Some carbonates were volumetrically replaced by goethite with minor textural changes. Some of the iron silicates were also replaced by goethite.

Magnetite was formed by converting hematite through hematite and siderite reaction (Burt, 1972). This conversion is evidenced by magnetite overgrowths along the boundaries between hematite- and chert + siderite-rich laminae. This reaction (FeCO_3 (siderite) + Fe_2O_3 (hematite) = Fe_3O_4 (magnetite) + CO_2) is favoured at relatively high temperatures and pressures (Kozioł, 1999).

In the supergene and weathering environment, magnetite oxidizes to martite and, in part, to goethite. Magnetite appears to diminish as supergene alteration and weathering intensifies, and it is replaced by hematite and goethite.

Quartz is hardly affected by weathering, and it shows no evidence of dissolution or being replaced by another mineral.

Siderite is chemically unstable in air and rapidly oxidizes to the secondary magnetite, maghemite, hematite, and goethite either before, during, or after uplift. Siderite is rapidly

destroyed by oxidation. It can be inferred that most post-diagenetic oxidizing effects, such as weathering during uplift and exposure of a sedimentary sequence, destroy the mineral.

The ankerite is depleted relative to siderite at low temperatures (at 25°C) (Dutton & Land, 1985; Fisher & Land, 1986). Like siderite, ankerite is replaced by the iron oxides during supergene processes and weathering or leached without replacement. The secondary calcite was later replaced by the iron oxide minerals or leached out of the system. This leaching and replacement were due to uplift or weathering. These rhomb-shaped minerals occur in different sizes, indicating different stages of formation. The iron silicates have been traced to the early stages of BIF formation. These were later compacted and replaced by the iron-oxides and quartz or leached out of the system.

8.5. The origin and formation process of the BIF

Multiple formation processes were involved in the banded iron formation origin within the Prieska area. The first process includes the deposition of iron-rich and silica (chert/quartz)-rich mud material in the deep ocean floor. This deposition was accompanied by the formation of a mixture of iron-rich mud (ferruginite) on the seafloor (Fig. 8.26A) (see Trendal, 2013).

The second process involves differentiation of the ferruginite and formation of disseminated iron-oxide from mud (Fig. 8.26B) (see Bekker & Konhouser 2014).

The third process includes cohesion and diagenesis of disseminated iron-oxide and formation of iron-rich (magnetite/hematite) and silica-rich (chert/quartz) patches, lenses (pod structures), microbands, and laminations (Fig. 8.26C & D) (see Trendal, 2005).

The fourth process is consolidation and compaction, leading to the final banded iron formation (BIF) (Fig. 8.26E & F) (see Erikson & Cantuneanu, 2005).

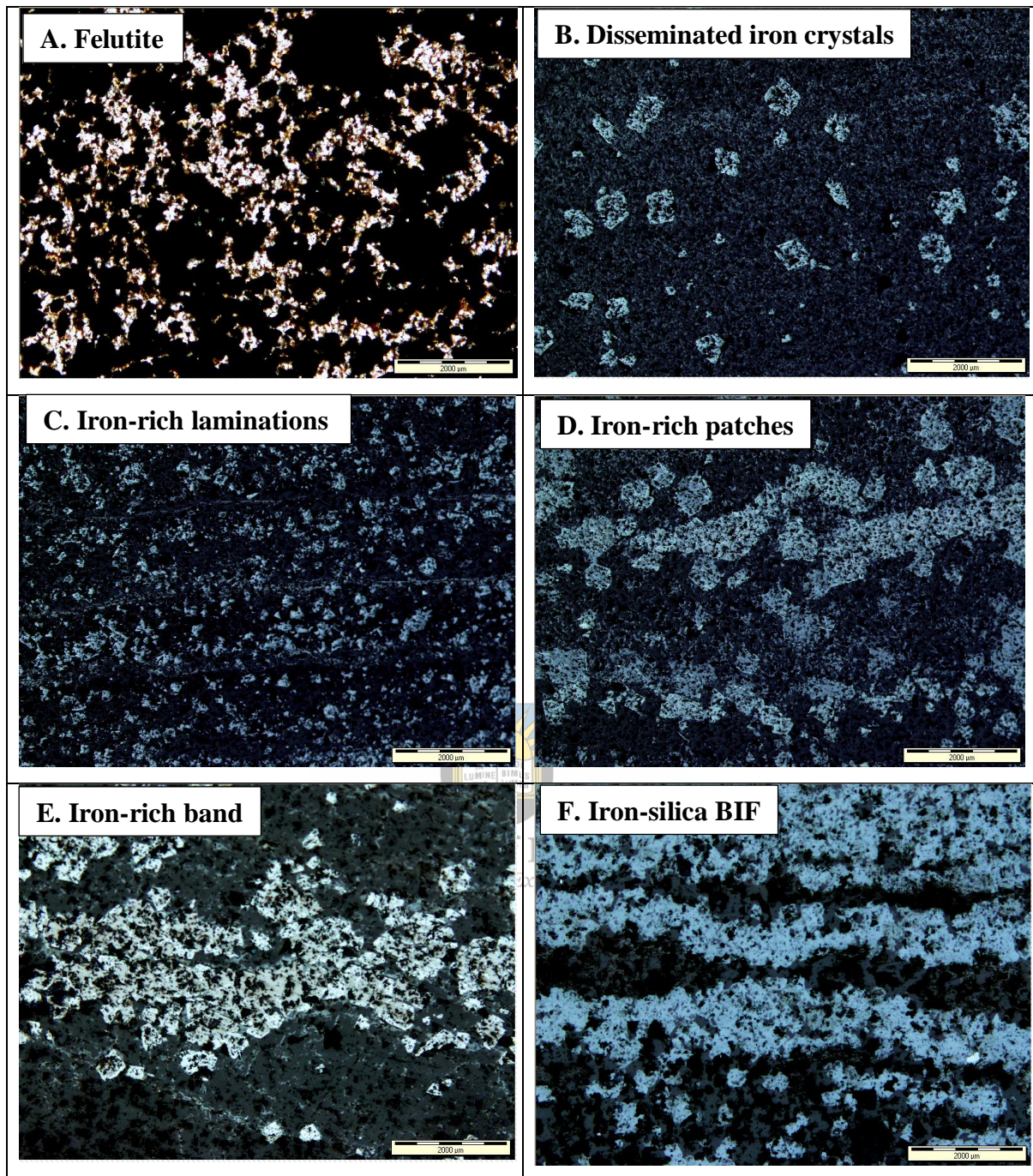


Figure 8. 26: Origin and formation processes of Banded Iron Formation: (A) Iron-rich mudstone (felutite) showing the mixture of iron oxides, chert (quartz) and silicate minerals; (B) Authigenic hematite grows up as disseminated crystals from felutite through recrystallization; (C) Hematite crystals cumulated together to form laminations; (D) Hematite clusters together to form iron-rich patches and lenses; (E) Hematite/goethite further grows to become various sized bands; (F) Iron-rich mesobands alternating with silica bands and finally the formation of banded iron formation.

CHAPTER 9: DISCUSSIONS AND CONCLUSION

9.1. Discussion

The Kuruman Formation in the study area comprises iron-bearing mudstone (falu-tite), quartz arenite, banded iron formation (BIF), and carbonate-stromatolite. The occurrence of the banded iron formation in the Prieska area can be classified into Horizontally laminated BIF facies, Horizontal thin to medium bedded BIF facies (Hbb), Ripple laminated BIF facies (Rlb), Thin to medium bedded mudstone facies (Mbm), Medium to thick-bedded mudstone facies (Tbm), Medium to thick-bedded fine-grained sandstone facies (mts), Laminated dolomite stromatolite facies (Ld), and dome-shaped stromatolitic banded iron formation facies (Dbif). The horizontal laminated BIF facies and horizontal thin to medium bedded BIF facies (Hbb) indicate a deep marine basin or deep marine plain environment. The ripple laminated mudstone, BIF facies, and the medium to thick-bedded fine-grained sandstone facies (mts) indicate continental shelf deposits. In contrast, the stromatolite carbonate facies and dome-shaped stromatolite BIF facies reflect subtidal to intertidal deposition.



Each lamination thickness of the horizontally laminated BIF facies (Hlb) is millimetre to a centimetre-scale, reflecting a slow deposition in a deep, quiet water depositional environment (Fig. 5.1). The horizontal thin to medium bedded BIF facies (Hbb) (Fig. 5.2) represents a stable deep water depositional environment. The ripples presence in the ripple laminated BIF facies (Rlb) possibly formed in a shallow marine depositional environment with stronger hydrodynamic energy than the horizontal lamination facies (Fig. 5.3). Such ripples also possibly formed in deep water by several possible mechanisms like contour currents or large storm waves, or tsunamis. The medium to thick-bedded mudstone facies (Tbm) could be representing a deep marine depositional environment (Fig. 5.5). The depositional environment of the medium to thick-bedded fine-grained sandstone facies (Mts) could be shifting from deep water to shallow water, probably closer to coastline environments such as a wide shallow marine environment or subtidal environment (Fig. 5.6). The laminated dolomite stromatolite facies (Ld) are formed in a relatively shallow marine environment, such as intertidal and subtidal environments, since algae growth needs sunlight (Fig. 5.7). If the water is too deep, sunlight cannot penetrate the floor of the deep water. The dome-shaped stromatolitic carbonate facies (Dbif) were formed in shallow water environments, such as intertidal and supratidal

environments by algae and bacteria (Fig. 5.8). They are usually carbonated in chemical composition, but iron, phosphorus, and manganese stromatolites are found in the geological records. It is not clear the iron, phosphorus, or manganese types of stromatolite were formed by replacement of carbonate stromatolite, or they were originally formed by iron, phosphorus, or manganese eating bacteria and algae in the geological past. This facies represents a shallow-water sub-tidal to supratidal depositional environment.

Ripples' presence represents a relatively shallow marine depositional environment with stronger hydrodynamic energy than the horizontal lamination facies. Such ripples also possibly formed in deep water by several possible mechanisms like contour currents or large storm waves, or tsunamis.

These facies and facies associations generally reflect a deep marine basin environment that gradually shifted to a shallow marine continental shelf environment and a shallow marine subtidal-intertidal environment.

Petrographic and diagenesis studies indicate felutites that contained a composite of iron oxide minerals, silica, carbonate, and silicate minerals. This felutites mixture experienced progressive differentiation, cohesion, and diagenesis. Then the iron-oxides and chert (quartz) gradually separated from mud (felutite). The quartz association with iron oxide assemblages indicates that these minerals were deposited mixed and underwent differentiation due to favourable precipitation conditions. This association also suggests that they were replacing each other in different conditions. The BIF micro and mesobands' arrangement into discrete bands, diffusive bands, patches, lenticular and pod-shaped bands, and laminations indicate the BIF development in different diagenetic stages. The realignment of the chert (quartz), silicate, and iron-oxides resulted from diagenesis or compaction.

The Prieska BIF is constituted by primary and secondary minerals such as hematite, magnetite, martite, goethite, limonite, quartz, stilpnomelane, riebeckite, minnesotaite, illite, siderite, ankerite, and calcite. The secondary origin of the minerals is a result of neomorphism, recrystallization, and replacement. The dominant quartz and iron oxides concentrations displayed by petrographic studies and geochemical data are attributed to their primary precipitation and replacement of the carbonates (siderite, ankerite, and calcite) and silicates (riebeckite, stilpnomelane, and illite) by those minerals during diagenesis and metamorphism.

A typical BIF generally consists of over 40 wt.% iron concentration (with varying proportions of FeO and Fe₂O₃), SiO₂ (up to 56 wt.%), CaO (up to 9 wt.%), Al₂O₃ (up to 1.8 wt.%), and

MgO (up to 6.7 wt.%) according to Klein (2005). The study area's BIF comprises iron and silica concentrations slightly higher than those reported by Klein (2005). These concentrations indicate the depletion of the iron silicates and carbonates within the BIF, which were replaced mainly by iron oxides and quartz. The silica and iron concentrations are comparable with those of the Kuruman protolith from Gutzmer et al. (2008). The same trend applies with the iron concentration of the high-grade superior type BIF published by McClung (2006) even though silica is slightly enriched.

This data supports the transformation and replacement of the carbonate and silicate minerals by quartz, hematite, and goethite supported by petrographic study and geochemical data. It also supports the weathering and leaching of the carbonates and silicates, as indicated by field observations and petrographic analysis.

The CaO, Al₂O₃, and MgO concentrations are below those reported by Klein (2005) for a typical BIF. The samples display complete depletion in MgO and CaO compared to the Kuruman protolith from Gutzmer et al. (2008) (Table 7.3, Fig 7.2). They are moderately depleted in P₂O₅ and MnO; meanwhile, the Al₂O₃ and K₂O concentrations have comparable averages. Compared to the high-grade Superior Type BIF published by McClung (2006), the samples are depleted in all the other components (Al₂O₃, MgO, P₂O₅, K₂O, Na₂O, CaO, and MnO) (Table 7.4, Fig. 7.3). This data reflects the effects of the post-depositional alteration processes such as diagenesis, weathering, and leaching that have affected the Prieska BIF.

The inverse relationship of Fe₂O₃ with SiO₂ and Al₂O₃ (Fig. 7.5) suggests the replacement of precursor quartz by goethite, which subsequently dehydrated to hematite. The positive correlation between Al₂O₃ and Fe₂O₃ (Fig. 7.4) accompanied by illite presence is evidence of clay minerals resulting from the parent rock's weathering.

The weak positive relationship of CaO+MgO and Na₂O+K₂O (Fig. 7.4C) suggests low contamination and marine origin of the BIF precipitation. Samples with high iron contents generally have low Mg, Al, Ca, K, and Na values. These trends reflect the presence of carbonates (siderite and ankerite) at the expense of iron oxides (hematite, goethite, and magnetite). The Al₂O₃ quantity is an indication of the presence of Fe-silicates like stilpnomelane, smectite, and illite.

The iron oxides contain large contents of trace metals within the samples, and the distribution of these trace metals is controlled by the relative proportion of the iron minerals. Iron silicates like riebeckite and stilpnomelane dominate samples with high Mg content, whereas Fe-oxides

dominate those with low Mg concentrations. The samples' negligible CaO content indicates that the carbonate is mainly siderite or ankerite, as Beukes (1983) reported. The minimal amounts of sodium indicate the leaching out or replacement of most of the riebeckite. The relatively low CaO, K₂O, and Na₂O contents imply that the source rocks may have been exposed to prolonged weathering. The minor Na and Ca contents are related to the absence or extremely low calcite modal abundances, a typical Na and Ca mineral constituent of the BIF. The depletion of highly mobile K₂O and NaO results from leaching during increased chemical weathering. The low Na, Ca, and Sr concentrations suggest that these elements were also leached away from the BIF after uplift since the alkali and alkali earth metal elements are typically mobile or soluble (Angerer et al., 2012; McLennan et al., 2003).

The weathered BIF is composed of significantly high SiO₂ but low MgO and CaO contents, whereas an oxidized supergene BIF comprises low MgO and CaO but has high Fe₂O₃ concentrations compared to weathered BIF. The Prieska BIF is moderate to highly weathered and low to moderately oxidized because it contains high SiO₂, relatively high Fe₂O₃, and low MgO and CaO contents.

The weathering indices indicate a very low, moderate to a relatively high degree of chemical weathering from different source materials (Fig. 7.11 & 7.12). This weathering intensity may not be accurate as these indices were never applied on chemical sedimentary rocks before; they were meant for clastic rocks. Again, getting weathering indices below 5 (P61) in those samples from the surface proves the indexes' inapplicability in the BIFs.

The highly enriched tungsten and cobalt contents are associated with the iron oxides (Table 7.5; Fig. 7.6). The tungsten was not reported by either Gutzmer et al. (2008) or McClung (2006) for the Kuruman protolith and the Superior Type BIF, respectively. Its enrichment within the Kuruman Formation in the Prieska area could be related to the BIF deformation by brittle fracture. The cobalt and tungsten in the study need attention in future studies. The sulfur concentrations reflect the common existence of minor iron sulfides (pyrite and pyrrhotite) within the samples. The chlorine concentrations indicate the presents of chloride within the samples. Chlorine and sulfur are closely associated, and they are common constituents in the marine environment like the BIFs.



University of Fort Hare
Together in Excellence

9.2. Conclusions

Through the stratigraphy, petrography, sedimentary facies, and geochemical studies of the weathered BIF outcrops near the Prieska area, the following conclusions were finally reached:

Four stratigraphic sections representing a continuous stratigraphic sequence of the Kuruman Formation in the Prieska area were measured. The stratigraphic sequence comprises BIF, mudstone, carbonate facies, and sandstone, and constitutes nine successional cycles with five-upward fining cycles and four upward-coarsening cycles, representing water level fluctuation, final basin shallowing, and filling-up processes.

Eight sedimentary facies were identified in the Prieska area. These facies include Horizontally laminated BIF facies (Hlb), Horizontal thin to medium bedded BIF facies (Hbb), Ripple laminated BIF facies (Rlb), Thin to medium bedded mudstone facies (Mbm), Medium to thick-bedded mudstone facies (Tbm), Medium to thick-bedded fine sandstone facies (Mts), Laminated dolomite stromatolite facies (Ld), and Dome-shaped stromatolitic BIF facies (Dbif). Five facies associations which include Facies association 1 (Hlb + Hbb), Facies association 2 (Hlb + Hbb + Mb + Tbm), Facies association 3 (Hlb + Hbb + Mb + Tbm + Rlb), Facies association 4 (Mb + Tbm + Mts), and Facies association 5 (Ld + Dbif + Mts) were established in the area. The FA1 was probably deposited in a deep marine basin environment; FA2 was probably deposited in a lower hydrodynamic environment, such as a deep marine plain, where lamination and horizontal bedding could be developed. FA3 could be a relatively shallower marine deposit, the water energy was higher than FA2 as the grain size became coarse and ripple structures occurred. FA4 was a relatively shallow marine depositional environment, comprising a coarser grain size than Facies association 3. FA5 was a shallow marine environment and could be near the subtidal to the intertidal environment. Thus the dome-shaped stromatolite developed.

Microscope petrography, XRD, SEM-EDX, and diagenesis studies revealed four groups of mineral paragenesis. These groups include primary mineral assemblages such as magnetite, hematite, siderite, chert/quartz, stilpnomelane, and smectite; diagenetic mineral assemblages like martite, quartz (cement), illite, calcite, and ankerite; low-grade metamorphic mineral assemblages including riebeckite and minnesotaite; and weathering/supergene mineral assemblages such as goethite, limonite, calcite (calcrete), quartz (silcrete), and clay minerals.

Mineralogy, petrography, and geochemical studies show that quartz dominates the mineral assemblages of BIF, constituting about 53 wt.%, followed by the iron oxides averaging about 44 wt.%. Other minerals such as carbonates and silicates occur in minor concentrations of less than 3 wt.% combined in BIF. The Prieska BIF is enriched in cobalt, tungsten, molybdenum, barium (Ba), and nickel.

Post-depositional and geochemical studies indicate three processes responsible for the mineralogy and geochemical changes of the Prieska BIF. These processes include diagenesis, low-grade metamorphism, and surficial weathering and oxidation. These studies also show that most of the mineral assemblages are of secondary origin. The majority of quartz and iron oxides are the primary precipitates' recrystallization products (cryptocrystalline chert, primary hematite, and magnetite). The carbonate fraction and iron silicates were commonly replaced by silica or iron oxides.

Multiple formation processes were involved in the origin of the banded iron formation: (1). Deposition of iron-rich mud material in the deep ocean floor and formation of a mixture of iron-rich mud (faluite) on the seafloor; (2). Differentiation of faluite and formation of disseminated iron-oxide and chert (quartz) from mud; (3). Cohesion and diagenesis of disseminated iron-oxide and formation of iron-rich (magnetite/hematite) and silica-rich (chert/quartz) patches, lenses (pod structures), microband, and laminations; (4). Consolidation and compaction, leading to the formation of final banded iron formation (BIF). (5) Secondary enrichment by weathering and leaching of some minerals after uplift and exposure to the Earth's surface. The iron oxide content could be more concentrated due to the dissolution of K_2O , Na_2O , CaO , and MgO and the accumulation of Fe_2O_3 in the supergene zone. Most carbonate and silicate minerals were replaced by quartz and iron oxides or leached out of the system.

9.3. Recommendations

Due to the lack of funds, a limited geochemical analysis was performed, more geochemical analyses could be done in the future. More borehole drilling is recommended, such as a deep borehole drilling at the centre of the synclines to verify the stratigraphic thickness and some shallow borehole drillings to verify the vertical effects of supergene and weathering on the BIF

to understand the ore grade and economic significance of the BIF. In addition, the cobalt and tungsten abundances need to be followed up using more sample analyses and get better geochemical data sets as these elements could have economic potential.



University of Fort Hare
Together in Excellence

REFERENCES

- Ahn, J. H., & Buseck, P. R. (1990). Hematite nanospheres of possible colloidal origin from a Precambrian banded iron formation. *Science*, 250(4977), 111-113.
- Alchin, D. J., & Botha, W. J. (2006). The structural/stratigraphic development of the Sishen South (Welgevonden) iron ore deposit, South Africa, as deduced from ground gravity data modelling. *Applied Earth Science*, 115(4), 174-186.
- Alchin, D., Lickfold, V., Mienie, P. J., Nel, D., & Strydom, M. (2008). An Integrated Exploration Approach to the Sishen South Iron Ore Deposit, Northern Cape Province, South Africa, and Its Implication for Developing a Structural and/or Resource Model for These Deposits. *Reviews in Economic Geology* 15, 317-338.
- Altermann, W. (1996). Discussion of zircon Pb-evaporation age determinations of the Oak Tree Formation, Chuniespoort Group, Transvaal Sequence: implications for the Transvaal – Griqualand West basin correlations. *S. Afr. J. Geol.* 99 (3), 337– 338.
- Altermann, W. (1997). Sedimentological evaluation of Pb–Zn potential of the Precambrian Griquatown fault zone in the Northern Cape Province. *S. Afr. – Mineral. Deposita* 32 (4), 382–391.
- Altermann, W. & Hälbich, I.W. (1990). Thrusting, folding and stratigraphy of the Ghaap Group along the south-western margin of the Kaapvaal Craton. *S. Afr. J. Geol.* 93, 553–556.
- Altermann, W. & Hälbich, I.W. (1991). Structural history of the south-western corner of the Kaapvaal Craton and the adjacent Namaqua realm: new observations and reappraisal. *Precambrian Research* 52, 133–166.
- Altermann, W. & Nelson, D.R. (1998). Sedimentation rates, basin analysis and regional correlations of three Neoproterozoic and Palaeoproterozoic sub-basins of the Kaapvaal craton as inferred from precise U–Pb zircon ages from volcanoclastic sediments. *Sediment. Geol.* 120, 225–256.
- Anderton, R. (1985). Clastic facies models and facies analysis. *Geological Society, London, Special Publications*, 18(1), 31-47.

Angerer, T., Hagemann, S. G. & Danyushevsky, L. V. (2012). Geochemical evolution of the banded iron formation-hosted high-grade iron ore system in the Koolyanobbing Greenstone Belt, Western Australia. *Economic Geology* 107, 599 - 644.

Appel, P.W.U. (1980). On the early Archaean Isua formation, West Greenland. *Precambrian Res.* 2, 73–87.

Ayres, D.E. (1972). Genesis of iron-bearing minerals in the Brockman Iron Formation, mesobands in the Dales Gorge Member, Hamersley Group, Western Australia, *Economic Geology and the Bulletin of the Society of Economic Geologists*, Vol. 67, pp. 1214-1233.

Bahlburg, H. & Dobrzinski, N. (2011). A Review of the Chemical Index of Alteration (CIA) and Its Application to the Study of Neoproterozoic Glacial Deposits and Climate Transitions. – In: Arnaud, E., Halverson, G. P., ShieldsZhou, G. A. (eds.) *The Geological Record of Neoproterozoic Glaciations*. Memoir 36, pp. 81–92. *Geological Society, London*.

Barley, M. E., Pickard, A. L., Hagemann, S. G., & Folkert, S. L. (1999). Hydrothermal origin for the 2-billion-year old Mount Tom Price giant iron ore deposit, Hamersley Province, Western Australia. *Mineral. Deposita*, 34, 784–789.

Bau, M. (1993). Effects of syn-depositional and post-depositional processes on the rare-earth element distribution in Precambrian iron-formations. *European Journal of Mineralogy* 5, 257-267.

Bau, M., Romer, R. L., Luders, V., & Beukes, N. J. (1999). Pb, O, and C isotopes in silicified Moodraai dolomite (Transvaal Supergroup, South Africa): implications for the composition of Paleoproterozoic seawater and 'dating' the increase of oxygen in the Precambrian atmosphere. *Earth and Planetary Science Letters* 174, 43-57.

Bekker, A., Holland, H.D., Wang, P.L., Rumble, D., Stein, H.J., Hannah, J.L., Coetzee, L.L., & Beukes, N.J. (2004). Dating the rise of atmospheric oxygen, *Nature*, Vol. 427, pp. 117-120.

Bekker, A., Slack, J. F., Plnavsky, N., Hoffman, A., Konhauser, K. O., & Rouxel, O. J. (2010). Iron formation: The sedimentary product of a complex interplay among mantle, tectonic, oceanic, and biospheric processes. *Econ. Geol.*, 105, 467–508.

Berge, G.L. (1966). Pyroclastic rocks in South African iron-formations. *Econ. Geol.*, 61:572-581.

Beukes, N.J. (1973). Precambrian iron-formations of Southern Africa. *Econ. Geol.*, 68:960-1005.

Beukes, N.J. (1977). Transition from siliciclastic to carbonate sedimentation near the base of the Transvaal Supergroup, Northern Cape Province, South Africa, *Sedimentary Geology*, vol. 18, 201-221.

Beukes, N.J. (1978). The Carbonate Rocks and Iron-Formations of the Ghaap Group of the Transvaal Supergroup in the Northern Cape Province. (Die karbonaatgesteentes en ysterformasie van die Ghaap Groep van die Transvaal Supergroep in Noord-Kaapland.) Unpubl. Ph.D. thesis, Dept. Geology, Rand Afrikaans University, Johannesburg, 580 pp.

Beukes, N.J. (1980a). Lithofacies and stratigraphy of the Kuruman and Griquatown Iron Formations, Northern Cape Province, South Africa. *Trans. Geol. Soc. S. Afr.*, 83:69-86.

Beukes, N. J. (1980). Stratigrafie en litofasies van die Campbellrand-Subgroep van die Proterofitiese Ghaap-Groep, Noord-Kaapland. *Transactions of the Geological Society of South Africa* 83, 141-170.

Beukes, N.J. (1983). Palaeoenvironmental setting of iron-formations in the depositional basin of the Transvaal Supergroup, South Africa, In: *Iron-Formation, facts and problems*, Developments in Precambrian Geology, vol 6, 131-209.

Beukes, N.J. (1984). Sedimentology of the Kuruman and Griquatown iron-formations, Transvaal Supergroup, Griqualand West, South Africa: *Prec. Res.*, v.24, p. 47-84.

Beukes, N.J. (1986). The Transvaal Sequence in the Griqualand West, In: C.R., Anhaeusser, and S., Maske, (Eds), Mineral Deposits of Southern African, *Geological Society of South Africa*, 819-828.

Beukes, N.J. (1986a). The Transvaal Sequence in Griqualand West, in: Mineral Deposits of Southern Africa, eds., C.R. Anhaeusser and S. Maske: *Geol. Soc. S. Afr.*, v. I, pp. 819-828.

Beukes, N. J. (1987). Facies relations, depositional environments and diagenesis in a major early proterozoic stromatolitic carbonate platform to basinal sequence, Campbellrand Subgroup, Transvaal Supergroup, Southern Africa. *Sedimentary Geology* 54, 1-46.

Beukes, N.J. & Gutzmer, J. (2008). Origin and paleoenvironmental significance of major iron formations at the Archean-Paleoproterozoic boundary, in Hagemann S., et al., eds., *Banded*

iron formation-related high-grade iron ore: *Society of Economic Geologists Reviews in Economic Geology* 15, p. 5–47.

Beukes, N. J. & Gutzmer, J. (2009). Precambrian manganese deposits: geological setting, metallogenesis and palaeoenvironmental implications. *Manganese in*, 21.

Beukes, N.J., Gutzmer, J., & Mukhopadhyay, J. (2003). The geology and genesis of high-grade iron ore deposits. *Applied Earth Sciences (Trans. Inst. Min. Metall. B)*, 112, B18-B25.

Beukes, N.J. & Klein, C. (1990). Geochemistry and sedimentology of a Facies transition from microbanded to granular iron-formation in the early Proterozoic Transvaal Supergroup, South Africa: *Precambrian Research*, vol. 47, 99-139.

Beukes, N. J. & Smit, C. A. (1987). New evidence for thrust faulting in Griqualand West, South Africa: Implications for stratigraphy and the age of red beds. *South African Journal of Geology* 90, 378-394.

Bland, W. & Rolls, D. (1998). *Weathering. An Introduction to the Scientific Principles.* – Arnold Publishers, London.

Boggs Jr, S., & Boggs, S. (2009). *Petrology of sedimentary rocks.* Cambridge university press.

Bolarinwa, T. A. (2018). Petrography and geochemistry of the banded iron formation of the Gangfelum area, Northeastern Nigeria. Earth Science Research. *Canadian Center of Science and Education*, 7(1), 2018.

Boles, J. R., & Franks, S. G. (1979). Clay diagenesis in Wilcox sandstones of Southwest Texas; implications of smectite diagenesis on sandstone cementation. *Journal of Sedimentary Research*, 49(1), 55-70.

Bordy, E.M. & Catuneanu, O. (2001). Sedimentology of the Upper Karoo fluvial strata in the Tuli Basin, South Africa. *Journal of African Earth Sciences*, 33, 605-629.

Bordy, E.M., Hancox, P.J., & Rubidge, B. (2005). The contact of the Molteno and Elliot Formations through the Main Karoo Basin, South Africa: A second-sequence boundary. *South Africa Journal of Geology*, 108, 351-364.

Burchell, W. J. (1822). *Travels in the Interior of South Africa*, 2 vols. II.(2nd ed. 1953.) London: Batchworth.

- Burley, S. D., & Kantorowicz, J. D. (1986). Thin section and SEM textural criteria for the recognition of cement-dissolution porosity in sandstones. *Sedimentology*, 33(4), 587-604.
- Burley, S., & Worden, R. (Eds.). (2009). *Sandstone diagenesis: recent and ancient* (Vol. 24). John Wiley & Sons.
- Burst, J. F. (1969). Diagenesis of Gulf Coast clayey sediments and its possible relation to petroleum migration. *AAPG bulletin*, 53(1), 73-93.
- Burt, D. M. (1972). *Mineralogy and geochemistry of Ca-Fe-Si skarn deposits* (Doctoral dissertation, Harvard University).
- Button, A. (1976). Iron formations as an end member in carbonate sedimentary cycles in the Transvaal Supergroup, South Africa. *Economic Geology* 71, 193-201.
- Button, A. (1986). The Transvaal sub-basin of the Transvaal Sequence, in: Mineral Deposits of Southern Africa, eds., C.R. Anhaeusser and S. Maske: *Geol. Soc. S. Afr.*, v. I, pp. 811-817.
- Carney, M. D. & Mienie, P. J. (2003). A geological comparison of the Sishen and Sishen South (Welgevonden) iron ore deposits, Northern Cape Province, South Africa. *Transactions of the Institute of Mining and Metallurgy B - Applied Earth Sciences* 112, B81 - B88.
- Catuneanu, O. & Eriksson, P.G. (1999). The sequence stratigraphic concept and the Precambrian rock record: an example from the 2.3-2.1 Ga Pretoria Group, Kaapvaal craton: *Precambrian Research* 97, 215-251.
- Catuneanu, O. & Eriksson, P.G. (2002). Sequence stratigraphy of the Precambrian Rooihogte-Timeball Hill rift succession, Transvaal basin, South Africa. *Sedimentary Geology* 147, 71-88
- Cheney, E.S. (1996). Sequence stratigraphy and plate tectonic significance of the Transvaal succession of Southern Africa and its equivalent in Western Australia, *Precambrian Research*, vol 79, pg. 3-24.
- Cheney, E. S. & Winter, H. D. L. R. (1995). The late Archean to Mesoproterozoic major unconformity-bounded units of the Kaapvaal Province of Southern Africa. *Precambrian Research*, 74(4), 203-223.
- Chisonga, B. C. (2012). Proterozoic mafic dykes and sills associated with BIF-hosted iron ore, South Africa: implications for the distribution of the Bushveld and Umkondo large igneous provinces (Doctoral dissertation, University of Johannesburg).

- Choi, J. H., Kimoto, K., & Ichikawa, Y. (2012). Quartz dissolution experiments at various pH, temperature and stress conditions: CLSM and ICP-AES investigations. *Environmental Earth Sciences*, 66(8), 2431-2440.
- Choquette, P. W., & Pray, L. C. (1970). Geologic nomenclature and classification of porosity in sedimentary carbonates. *AAPG bulletin*, 54(2), 207-250.
- Cilliers, J.J. le R. & Genis, J.H. (1964). Crocidolite asbestos in the Cape Province. In: S.H. Houghton The Geology of some Ore Deposits of Southern Africa, Vol. II. *Geol. Soc. S.Afr.*, Johannesburg, pp. 544-570.
- Cisne, J. L. (1984). A basin model for massive banded iron-formations and its geophysical applications. *The Journal of Geology*, 92(5), 471-488.
- Clout, J. M. & simonson, B. M. (2005). Origins of large high-grade iron ore deposits: Will one size ever fit all? In *2005 Salt Lake City Annual Meeting*.
- Colombo, U., Gazzarrini, F., Lanzavecchia, G., & Sironi, G. (1965). Magnetite oxidation: A proposed mechanism. *Science*, 147(3661), 1033-1033.
- Condie, K. C. (1981). *Archean greenstone belts*. Elsevier.
- Cornell, D. H., Schutte, S. S., & Eglinton, B. L. (1996). The Ongeluk basaltic andesite formation in Griqualand West, South Africa: Submarine alteration in 2222Ma Proterozoic sea. *Precambrian Research* 79, 101-124.
- Cornell, D. H., Minnaar, H., Frei, D., & Kristoffersen, M. (2018). Precise microbeam dating defines three Archaean granitoid suites at the southwestern margin of the Kaapvaal Craton. *Precambrian Research*, 304, 21-38.
- Council for Geoscience, 19.... 1:10 000 Geological map
- Cullen, D.J. (1963). Tectonic implications of banded ironstone formations. *J. Sediment. Petrol.*, 33: 387-392.
- Dalstra, H. & Flis, M. (2008). High-grade iron ore exploration in an increasingly steel-hungry world; the past, current, and future role of exploration models and technological advances. *Reviews in Economic Geology*, 15, 393-409.
- Dalstra, H. & Rosiere, C.A. (2008). Structural Controls on High-Grade Iron Ores Hosted by Banded Iron Formations: A Global Perspective. *Reviews in Economic Geology*, 15, 73-106.

De Kock, M. O., Evans, D. A., Gutzmer, J., Beukes, N. J., & Dorland, H. C. (2008). Origin and Timing of Banded Iron Formation-Hosted High-Grade Hard Hematite Deposits - A Paleomagnetic Approach. *Reviews in Economic Geology* 15, 49-71.

De Segonzac, G. D. (1970). The transformation of clay minerals during diagenesis and low-grade metamorphism: a review. *Sedimentology*, 15(3-4), 281-346.

De Villiers, P.R. (1960). Manganese Deposits of the Union of South Africa, *Geological Survey of South Africa*, Pretoria, Handbook 2, Vol. 280, pp. 7.

De Villiers, P.R. (1970). The geology and mineralogy of the Kalahari manganese-field north of Sishen, Cape Province. Mem. *Geol. Surv. S. Afr.*, 59, 84 pp.

Dimroth, E. (1975). Paleo-environment of iron-rich sedimentary rocks: *Geologische Rundschau*, v. 64, pp. 751-767.

Dimroth, E. & Chauvel, J.J. (1973), Petrography of the Sokoman iron formation in part of the Central Labrador Trough, Quebec, Canada: *Geol.*

Dorland, H. (1999). Paleoproterozoic laterite, red beds and ironstone of the Pretoria Group with reference to the history of atmospheric oxygen. MSc Thesis (unpublished), Rand Afrikaans University, Johannesburg.



University of Fort Hare
Together in Excellence

Du Toit, A.L. (1945). The origin of the amphibole asbestos deposits of South Africa. *Geol. Soc. S. Afr.*, 48: 161-206.

Dutton, S. P., & Land, L. S. (1985). Meteoric burial diagenesis of Pennsylvanian arkosic sandstones, southwestern Anadarko Basin, Texas. *AAPG bulletin*, 69(1), 22-38.

Engelbrecht, L.N.J. (1962). Markers in the Lower Griquatown Stage near Kuruman. *Ann. Geol. Surv. S. Afr.*, 1: 71-75.

Eriksson, P.G., Altermann, W., Catuneanu, O., Van Der Merwe, R., & Bumby, A.J. (2001). Major influences on the evolution of the 2.67-2.1 Ga Transvaal basin, Kaapvaal craton. *Sedimentary Geology*, 141-142, 205-231.

Eriksson, P.G., Altermann, W., & Hartzler, F.J. (2006). The transvaal supergroup and precursors. In: Johnson, M.R., Annhaeusser, C.R. Thomas, R.J. (Eds.). *The Geology of South Africa. Geol. Society of South Africa*, pp. 237–260 (Chapter 10).

Eriksson, P. G., Hattingh, P. J., & Altermann, W. (1995). An overview of the geology of the Transvaal Sequence and Bushveld Complex, South Africa. *Mineralium Deposita*, 30(2), 98-111.

Eriksson, P. G., Schweitzer, J. K., Bosch, P. J. A., Schreiber, U. M., Van Deventer, J. L., & Hatton, C. J. (1993). The Transvaal sequence: an overview. *Journal of African Earth Sciences (and the Middle East)*, 16(1-2), 25-51.

Evans, K. A., McCuaig, T. C., Leach, D., Angerer, T., & Hagemann, S. G. (2013). Banded iron formation to iron ore: A record of the evolution of Earth environments? *Geology* 41, 99 - 102.

Fedo, C. M., Nesbitt, H. W., & Young, G. M. (1995). Unraveling the effects of potassium metasomatism in sedimentary rocks and paleosols, with implications for paleoweathering conditions and provenance. *Geology* 23: 921–924.

Fisher, R. S., & Land, L. S. (1986). Diagenetic history of Eocene Wilcox sandstones, south-central Texas. *Geochimica et Cosmochimica Acta*, 50(4), 551-561.

Fockema, P. D. (1967). Crocidolite and associated rocks of the Kuruman area in the Northern Cape (Doctoral dissertation).



Folk, R. L. (1974). The natural history of crystalline calcium carbonate; effect of magnesium content and salinity. *Journal of Sedimentary Research*, 44(1), 40-53.

Foscolos, A. E., & Kodama, H. (1974). Diagenesis of clay minerals from lower Cretaceous shales of north eastern British Columbia. *Clays and Clay Minerals*, 22(4), 319-335.

French, B. M. (1971). Stability relations of siderite (FeCO₃) in the system Fe-CO. *American Journal of Science*, 271(1), 37-78.

Frost, C.D., von Blanckenburg, F., Schoenberg, R., Frost, B.R., & Swapp, S.M. (2007). Preservation of Fe isotope heterogeneities during diagenesis and metamorphism of banded iron formation. *Contrib. Mineral. Petrol.* 153, 211–235.

Garrels R. M. (1987). A model for the deposition of the microbanded Precambrian iron formations. *American Journal of Science* 287, 81–106.

Garrels, R. M., Perry, E. A., & MacKenzie, F. T. (1973). Genesis of Precambrian iron-formations and the development of atmospheric oxygen. *Economic Geology*, 68, 1173–1179.

- Ghosh, D., Dutta, T., Samanta, S. K., & Pal, D. C. (2013). Texture, microstructure and geochemistry of magnetite from the Banduhurang uranium mine, Singhbhum Shear Zone, India—implications for physico-chemical evolution of magnetite mineralization. *Journal of the Geological Society of India*, 81(1), 101-112.
- Gibson, W. (1892). The geology of the gold-bearing and associated rocks of the southern Transvaal. *Quarterly Journal of the Geological Society*, 48(1-4), 404-437.
- Glasby, G. P., & Schulz, H. D. (1999). Eh Ph diagrams for Mn, Fe, Co, Ni, Cu and as under seawater conditions: application of two new types of eh ph diagrams to the study of specific problems in marine geochemistry. *Aquatic geochemistry*, 5(3), 227-248.
- Gole, M.J. & Klein, C. (1981). Banded iron-formations through much of Precambrian time: *The Journal of Geology*, v. 89, p. 169–183, doi: 10.1086 /628578.
- Goodwin, A. M. (1973). Archean iron-formations and tectonic basins of the Canadian Shield. *Economic Geology*, 68(7), 915-933.
- Gressly, A. (1838). “Observations géologiques sur le Jura Soleurois,” *Neue Denkschr. Allg. Schweizerische Gesellsch. ges. Naturw.*, Vol. 2, pp. 1–112.
- Grobbelaar, W. S., Burger, M. A., Pretorius, A. I., Marais, W., & van Niekerk, I. J. (1995). Stratigraphic and structural setting of the Griqualand West and the Olifantshoek Sequences at Black Rock, Beeshoek and Rooinekke Mines, Griqualand West, South Africa. *Mineralium Deposita* 30, 152-161.
- Gross, G. A. (1965) Geology of iron deposits in Canada, Vol.1. General geology and evolution of iron deposits. *Geological Survey of Canada, Economic Report*, 22 p.
- Gross, G.A. (1980). A classification of iron formations based on depositional environments. *Can. Mineral.*, 18:215-222.
- Gutzmer, J., Beukes, N. J., de Kock, M. O., & Netshiozwi, S. T. (2005). Origin of high-grade iron ores at the Thabazimbi deposit, South Africa. *Australasian Institute of Mining and Metallurgy, Iron Ore 2005 conference*, Fremantle, Western Australia, 57-65.
- Gutzmer, J., Chisonga, B.C., & Beukes, N.J. (2008). The geochemistry of banded iron formation-hosted high-grade hematite-martite iron ores. In: Hagemann, S., Rosière, C., Gutzmer, J. and Beukes, N.J. (Eds), *Reviews in Economic Geology*, Vol. 15, *Society of Economic Geologists*, Littleton, 157-183.

Hagemann S. G., Angerer T., Duuringa P., Rosière C. A, Silva R. C., Lobato L., Hensler A. S., & Walde D. H. G. (2015). BIF-hosted iron mineral system: *A review*

Hagemann, S., Dalstra, H. I., Hodkiewicz, P., Flis, M., Thorne, W., & McCuaig, C. (2007). Recent Advances in BIF-related Iron Ore Models and Exploration Strategies. In "Proceedings of Exploration 07: *Fifth Decennial International Conference on Mineral Exploration*", 811-821.

Hagemann, S., Rosière, C., Gutzmer, J., & Beukes, N.J. (2008). Introduction: Banded iron formation-related high-grade iron ore. In: Hagemann, S., Rosière, C., Gutzmer, J. and Beukes, N.J. (Eds), *Reviews in Economic Geology*, Vol. 15, *Society of Economic Geologists*, Littleton, 1-4.

Halbich, L.W. & Altermann, W. (1992), The genesis of BIF in the Transvaal Supergroup, South Africa, in: *Source, Transport and Deposition of Metals*, eds., M. Pagel and J.L. Leroy: A.A. Balkema, Rotterdam, 841 p.

Halbich, I.W., Lamprecht, D., Altermann, W., & Horstmann, U.E. (1992). A carbonate-banded iron formation transition in the Early Proterozoic of South Africa. *J. Afr. Earth Sci.*, 15: 217-236.

Halbich, I.W., Scheepers, R., Lamprecht, D., van Deventer, J.L., & De Kock, N.J. (1993). The Transvaal-Griqualand West banded iron formation: geology, genesis, iron exploitation, *J. Afr. Earth Sci.*, 16: 63-120.

Harger, H. S. (1934). An early Transvaal geological map by Carl Mauch: *Transactions of the Geological Society of South Africa*, v. 37.

Harnois, L. (1988). The CIW index: a new Chemical Index of Weathering. *Sedimentary Geology* 55: 319–322.

Harrington, H. J. (1962). Paleogeographic development of South America. *AAPG Bulletin*, 46(10), 1773-1814.

Holland, H.D. (1973). The oceans: a possible source of iron in ironformation. *Econ. Geol.*, 68:1169-1172.

Holland, H.D. (1984). *The chemical evolution of the atmosphere and oceans*: Princeton, New Jersey, Princeton University Press, 582 p.

Holland, H. D., & Beukes, N. J. (1990). A paleoweathering profile from Griqualand West, South Africa: evidence for a dramatic rise in atmospheric oxygen between 2.2 and 1.9 bybp. *Am. J. Sci*, 290, 1-34.

Holland, H.D. (1999). When did the Earth's atmosphere become oxic? A reply. *The Geochemical News* 100, 20–22.

Horstmann, U.E. & Halbach, I.W. (1995). Chemical composition of banded iron-formations of the Griqualand West Sequence, Northern Cape Province, South Africa, in comparison with other Precambrian iron-formations: *Prec. Res*, v.72, p. 109-145.

Hower, J., Eslinger, E. V., Hower, M. E., & Perry, E. A. (1976). Mechanism of burial metamorphism of argillaceous sediment: 1. Mineralogical and chemical evidence. *Geological Society of America Bulletin*, 87(5), 725-737.

Inoue, A., Velde, B., Meunier, A., & Touchard, G. (1988). Mechanism of illite formation during smectite-to-illite conversion in a hydrothermal system. *American Mineralogist*, 73(11-12), 1325-1334.

Isley A. E. (1995). Hydrothermal plumes and the delivery of iron to banded iron formation. *Journal of Geology* 103, 169–185.

Isley, A. E. & Abbott, D. H. (1999). Plume-related mafic volcanism and the deposition of banded iron formation. *J. Geophys. Res.*, 104, 15461–15477.

Isley, A. E. & Abbott, D. H. (2009). Plumes and banded iron formation, In book: McGraw-Hill Yearbook of Science and Technology

Jacobsen, S.B. & Pimentel-Klose, M.R. (1988). A Nd isotopic study of the Hamersley and Michipicoten banded iron formations: the source of REE and Fe in Archean oceans. *Earth Planet. Sci. Lett.* 87, 29–44.

James, H.L. (1954). Sedimentary facies of iron-formation. *Economic Geology* 49, 235-293.

James, H.L. (1966). Chemistry of the iron-rich sedimentary rocks. *U.S. Geol. Survey Prof. Paper* 440-w.

James, H.L. & Trendall A. F. (1982). Banded Iron Formation: Distribution in Time and Paleoenvironmental Significance

Johnson, C.M., Beard, B.L., Beukes, N.J., Klein, C., & O'Leary, J.M. (2003). Ancient geochemical cycling in the Earth as inferred from Fe isotope studies of banded iron formations from the Transvaal Craton, *Contributions to Mineral Petrology*, Vol. 144, pp. 523-547.

Klein, C. (2005). Some Precambrian banded iron-formations (BIFs) from around the world: Their age, geologic setting, mineralogy, metamorphism, geochemistry, and origin. *American Mineralogist*, 90, 1473-1499.

Klein, C., & Beukes, N.J. (1989). Geochemistry and sedimentology of a facies transition from limestone to iron-formation deposition in the Early Proterozoic Transvaal Supergroup, South Africa. *Econ. Geol.* 84, 1733–1774.

Klein, C. & Beukes, N. J. (1992). Time distribution, stratigraphy, and sedimentologic setting, and geochemistry of Precambrian iron formations, in Schopf, J.W., and Klein, C, eds., The Proterozoic biosphere: Cambridge, *Cambridge University Press*. 139 - 146.

Klemm, D.D. (1979). A biogenetic model of the formation of the banded iron formation in the Transvaal Supergroup, South Africa. *Miner. Deposita*, 14: 381-385.

Kleyenstüber, A. S. E. (1985). A regional mineralogical study of the manganese-bearing Voëlwater Subgroup in the Northern Cape Province.

Knoll, A.H. & Beukes, N.J. (2009). Introduction: Initial investigations of a Neoproterozoic shelf margin-basin transition (Transvaal Supergroup, South Africa), *Precambrian Research*, Vol. 169, pp. 1-14.

Koehler, I., Konhauser, K., & Kappler, A. (2010). Role of microorganisms in banded iron formations. In *Geomicrobiology: molecular and environmental perspective* (pp. 309-324). Springer, Dordrecht.

Konhauser, K. O., Newman, D. K., & Kappler, A. (2005). The potential significance of microbial Fe (III) reduction during deposition of Precambrian banded iron formations. *Geobiology*, 3(3), 167-177.

Koziol, A. M. (1999, March). Experimental determination of siderite (iron carbonate) stability under moderate pressure-temperature conditions, and application to martian carbonate parageneses. In *Lunar and Planetary Science Conference* (p. 1226).

LaBerge, G. L. (1966). Altered pyroclastic rocks in South African iron-formation. *Economic Geology*, 61(3), 572-581.

Lantink, M.L., Davies, J.H.F.L., Mason, P.R.D., Schaltegger, U., & Hilgen, F. J. (2019). Climate control on banded iron formations linked to orbital eccentricity. *Nat. Geosci.* **12**, 369–374 . <https://doi.org/10.1038/s41561-019-0332-8>.

Lewy, Z. (2011). Banded Iron Formations (BIFs) and Associated Sediments Do Not Reflect the Physical and Chemical Properties of Early Precambrian Seas.

Li, W., Beard B.L., & Johnson C. M. (2015). Biologically recycled continental iron is a major component in banded iron formations

Liu, A. Y., & Cohen, M. L. (1990). Structural properties and electronic structure of low-compressibility materials: β -Si₃N₄ and hypothetical β -C₃N₄. *Physical Review B*, *41*(15), 10727.

Malherbe, S.J. (1970). Flat-pebble conglomerates in the Dolomite Series in the Northern Cape Province. *Ann. Geol. Surv. A.Afr.*, *8*: 89-94.

Marocchi, M., Bureau, H., Fiquet, G., & Guyot, F. (2011). In-situ monitoring of the formation of carbon compounds during the dissolution of iron (II) carbonate (siderite). *Chemical Geology*, *290*(3-4), 145-155.



University of Fort Hare
Together in Excellence

Martin, D. McB., Li, Z. X., Nemchin, A. A., & Powell, C. McA. (1998). A pre-2.2 Ga age for giant hematite ores of the Hamersley Province, Australia. *Econ. Geol.*, *93*, 1084-1090.

McClung, C. R. (2006). Basin analysis of the Mesoproterozoic Bushmanland Group of the Namaqua metamorphic province, South Africa. Ph.D. thesis (unpublished), University of Johannesburg, Auckland Park.

McCullom, T. M. (2003). Formation of meteorite hydrocarbons from thermal decomposition of siderite (FeCO₃). *Geochimica et Cosmochimica Acta*, *67*(2), 311-317.

McLennan, S.M., Bock, B., Hemming, S.R., Hurowitz, J.A., Lev, S.M., & McDaniel, D.K. (2003). The roles of provenance and sedimentary processes in the geochemistry of sedimentary rocks, in Lentz, D.R., ed., *Geochemistry of Sediments and Sedimentary Rocks: Evolutionary Considerations to Mineral Deposit-Forming Environments*. *Geological Association of Canada, GeoText* *4*, 7 - 38.

- Merriman, R. J. (2005). Clay minerals and sedimentary basin history. *European Journal of Mineralogy*, 17(1), 7-20.
- Meyer, C. (1985). Ore metals through geologic history. *Science*, 227, 1421–1428.
- Miall, A. D. (1977). Lithofacies types and vertical profile models in braided river deposits: a summary.
- Miall, A. D. (1983). Basin analysis of fluvial sediments. *Modern and ancient fluvial systems*, 277-286.
- Miall, A.D. (1988a). Facies architecture in clastic sedimentary basins. In: K. Kleinspehn and C. Paola (Eds.). *New Perspectives in basin analysis*. Springer-Verlag, New York, 63-81.
- Miall, A.D. (1988b). Architectural elements and bounding surfaces in channelized clastic deposits: notes on comparisons between fluvial and turbidite systems. In: A. Taira and F. Masuda (Eds.). *Sedimentary facies in the active plate margin*. Terra Scientific Publishing Company, Tokyo, Japan, 3-15.
- Miall, A.D. (1995). Description and interpretation of fluvial deposits: A critical perspective (Discussion). *Sedimentology*, 42, 379-384.
- Miall, A.D. (1996). *The Geology of Fluvial Deposits: Sedimentary Facies, Basin Analysis and Petroleum Geology*, Springer, New York, USA, 22pp.
- Miall, A.D. (1997). A review of the braided river depositional environment. *Earth Science Reviews*, 13, 1-62.
- Miall, A.D. (2000). *Principles of sedimentary basin analysis*: Springer, Berlin, 616 p
- Miyano T. (1982). Stilpnomelane, iron-rich mica, K-feldspar and hornblende in banded iron-formation assemblages of the Dales Gorge Member, Hamersley Group, Western Australia: *Can. Min.*, v. 20, pp. 189-202.
- Miyano, T. & Beukes, N.J. (1984). Phase relations of stilpnomelane, ferri-annite, and riebeckite in very low-grade metamorphosed iron-formations. *Trans. Geol. Soc. S. Afr.*, 87:111-124.
- Miyano, T. & Beukes, N.J. (1987). Physicochemical Environments or the Formation of Quartz-Free Manganese Oxide Ores from the Early Proterozoic Hotazel Formation, Kalahari Manganese Field, South Africa, *Economic Geology*, Vol. 82, pp. 706-718.

- Moffat, R. (1858). Report of a survey of a portion of the Orange River eastward of Little Namaqualand. *Parliamentary Report G1 – 1858*, Cape Town.
- Moore, J.M., Polteau, S., Armstrong, R.A., Corfu, F., & Tsikos, H. (2012). The age and correlation of the Postmasburg Group, southern Africa: Constraints from detrital zircon grains, *Journal of African Earth Sciences*, Vol. 64, pp. 9-19.
- Moore, J. M., Tsikos, H., & Polteau, S. (2001). Deconstructing the Transvaal Supergroup, South Africa: Implication for Palaeoproterozoic palaeoclimate models. *Journal of African Earth Sciences* 33, 437-444.
- Morey, G. B. (1983). Animikie Basin, Lake Superior Region, U.S.A, in *Iron-formations: Facts and Problems*, eds., A.F. Trendall and R.C. Morris. *Developments in Precambrian Geology* 6, 13-67.
- Mozley, P. S. (1989). Relation between depositional environment and the elemental composition of early diagenetic siderite. *Geology*, 17(8), 704-706.
- Mukhopadhyay, J., Gutzmer, J., Beukes, N.J., & Bhattacharya, H.N. (2008). Geology and Genesis of the Major Banded Iron Formation-Hosted High-Grade Iron Ore Deposits of India. *Reviews in Economic Geology*, 15, 291-316.
- Murphy, M. A. & Salvador, A. (1999). International subcommission on stratigraphic classification of IUGS international commission on stratigraphy-international stratigraphic guide-an abridged version. *Episodes*, 22(4), 255-271.
- Nel, B.P. (2013). Petrography and Geochemistry of Iron Formations of the Paleoproterozoic Koegas Subgroup, Transvaal Supergroup, Griqualand West, South Africa. Unp Thesis.
- Nel, T. (1929). The geology of the Postmasburg manganese deposits and surrounding country. An explanation of the geological map. Spec. Pub I. *geol. Surv. S. Afr.*, 7, 109pp.
- Nesbitt, H. W. & Wilson, R.E. (1992). Recent chemical weathering of basalts. *American Journal of Science* 292, 740 – 777.
- Nesbitt, H. W. & Young, G. M. (1982). Early Proterozoic climates and plate motions inferred from major element chemistry of lutites. – *Nature* 299: 715–717.
- Netshiozwi, S. T. (2002). *Origin of high-grade hematite ores at Thabazimbi mine, Limpopo Province, South Africa* (Doctoral dissertation, Rand Afrikaans University).

Obasi, R. A. & Madukwe H. (2016). Geochemistry, classification characteristics of pegmatites from Ejero-Ekiti, Ekiti-State, southwest Nigeria. *International research journal of Natural sciences* 4, 1-18.

Obasi, R. A., Madukwe, H. Y., & Nnabo, P. N. (2020). Geochemistry, weathering intensity and paleo-climatic conditions of soils around dumpsites from Ibadan, Oyo state, Nigeria. *European Journal of Basic and Applied Sciences* Vol, 7(1).

Obasi, R.A., Madukwe, H. Y., & Olaosun, T. (2019). Source Area Weathering, Paleo-Environment and PaleoClimatic Conditions of Soils from Bitumen Rich Ode Irele Area of Ondo State, Nigeria. *EJERS, European Journal of Engineering Research and Science*, Vol. 4, No. 3, 59-67.

Ohmoto, H. (1997). When did the Earth's atmosphere become oxic? *Geochem. News*, 93, 12–13, 26–27.

Ohmoto, H. (2003). Nonredox transformations of magnetite-hematite in hydrothermal systems. *Economic Geology* 98, 157 - 161.

Pecoits, E., Gingras, M.K., Barley, M.E., Kappler, A., Posth, N.R., & Konhauser, K.O. (2009). Petrography and geochemistry of the Dales Gorge banded iron formation: Paragenetic sequence, source and implications for palaeo-ocean chemistry, *Precambrian*



University of Fort Hare
Together we learn

Penning, W. H. (1885). A Sketch of the Goldfields of Lydenburg and De Kaap, in the Transvaal, South Africa. *Quarterly Journal of the Geological Society*, 41(1-4), 569-590.

Perry, E. D., & Hower, J. (1970). Burial diagenesis in Gulf Coast pelitic sediments. *Clays and Clay Minerals*, 18(3), 165-177.

Pettijohn, F. J., Potter, P. E., & Siever, R. (1987). Introduction and source materials. In *Sand and sandstone* (pp. 1-21). Springer, New York, NY.

Pickard, A. L. (2003). SHRIMP U–Pb zircon ages for the Palaeoproterozoic Kuruman iron formation, Northern Cape Province, South Africa: evidence for simultaneous BIF deposition of the Kaapvaal and Pilbara cratons. *Precambrian Research* 125, 275 - 315.

Pittman, E. D. (1979). Porosity diagenesis and productive capability of sandstone reservoirs.

Polteau, S., Moore, J. M., & Tsikos, H. (2006). The geology and geochemistry of the Paleoproterozoic Makganyene diamictite. *Precambrian Research* 148, 257-274.

- Rasmussen, B., Krapez, B., & Meier, D.B. (2014). Replacement origin for hematite in 2.5 Ga banded iron formation: Evidence for postdepositional oxidation of iron-bearing minerals. *Geol Soc Am Bull* 126(3-4):438–446.
- Robb, L. (2005). Introduction to ore-forming processes. Oxford: *Blackwell Publishing Research*, Vol. 172, pp. 163-187.
- Rogers, A.W. (1907). Geological survey of parts of Bechuanaland and Griqualand West. *Annu. Rep. 1906. Geol. Comn. Cape of Good Hope*, pp. 7-86.
- Rogers, A. W. & Du Toit, A. L. (1909). Geological survey of parts of Prieska, Hay and Britstown. *Annual Report, Geological Commission, Cape of Good Hope*, 13(8), 109.
- Romer, R. & Bau, M. (1998). 2.4 Ga secondary-lead age for the Mooidraai dolomite: implications for the early evolution of the atmosphere. ICOG-9. In *Chinese Science Bulletin*.
- Rosiere, C.A., Spier, C.A., Rios, F.J., & Suckau, V.E. (2008). The Itabities of the Quadrilatero Ferrifero and Related High-grade Iron Ore Deposits. *Reviews in Economic Geology*, 1, 223-24.
- Saggerson, E. P. & Turner, L. M. (1992). Metamorphic map of the Republics of South Africa. *Transkei, Bophuthatswana, Venda and Ciskei, and the Kingdoms of Lesotho and Swaziland, scale, 1, 1000000*.
- Schröder, S., Bedorf, D., Beukes, N.J., & Gutzmer, J. (2011). From BIF to red beds: Sedimentology and sequence stratigraphy of the Palaeoproterozoic Koegas Subgroup (South Africa), *Sedimentary Geology*, Vol. 236, pp. 25-44.
- Schoeder, S., Lacassie, J.P., & Beukes, N.J. (2006). Stratigraphic and geochemical framework of the Agouron drillcores, Transvaal Supergroup (Neoproterozoic - Palaeoproterozoic, South Africa), *South African Journal of Geology*, Vol. 109, pp. 23-54.
- Simonson, B.M. (2003). Origin and evolution of large Precambrian iron formations, In Chan, M.A., and Archer, A.W., (Eds.), Extreme depositional environments: Mega end members in geologic time, *Geological Society of America Special Paper*, Vol. 370, p. 231-244.
- Smith, A. J. B. (2007). The Paleo-environmental Significance of the Iron-formations and iron-rich Mudstones of the Witwatersrand-Mozaan Basin, South Africa. M.Sc. Thesis (unpubl.), University of Johannesburg, Auckland Park, 208pp. *Soc. Amer. Bull.*, v. 84, pp. 111-134.

Smith, A. J., & Beukes, N. J. (2016). Palaeoproterozoic Banded Iron formation hosted High-Grade Hematite Iron Ore Deposits of the Transvaal Supergroup, South Africa. *Episodes*, 39(2), 269-284.

Spier, C. A., de Oliveira, S. M., Sial, A. N., & Rios, F. J. (2007). Geochemistry and genesis of the banded iron formations of the Cauê Formation, Quadrilátero Ferrífero, Minas Gerais, Brazil. *Precambrian Research*, 152(3-4), 170-206.

Steno, N. (1687). 1669. De solido intra solidum naturaliter contento dissertationis prodromus. Florentiæ: Ex Typographia sub signo Stellæ.

Stow, G.W. (1874). Geological notes upon Griqualand West. *Q.J. Geol. Soc. London*, 30: 581-680.

Stowe, C.W. (1986). Synthesis and interpretation of structures along the north-eastern boundary of the Namaqua tectonic province, South Africa. *Transactions of the Geological Society of South Africa*, 89, 185-198.

Summer, D.Y., & Bowring, S.A. (1996). U-Pb geochronologic constraints on deposition of the Campbellrand Subgroup, Transvaal Supergroup, South Africa, *Precambrian Research*, Vol. 79, pp. 25-35.

Taylor, D. J., Page, D. C., & Geldenhuys, P. (1988). Iron and Steel in South Africa. *Journal of the South African Institute of Mining and Metallurgy* 88, 73-95.

Thorne, W., Hagemann, S., Webb, A. & Clout, J. (2008). Banded Iron Formation-Related Iron Ore Deposits of the Hamersley Province, Western Australia. *Reviews in Economic Geology*, 15, 197-222.

Trendall, A.F., (1965). Progress report on the Brockman Iron Formation in the Wittnoom-Yampire area. *Geol. Surv. West. Aust., Annu. Rep.*, 1965: 55-65.

Trendall, A.F. (1968). Three great basins of Precambrian banded iron-formation deposition: a systematic comparison: *Geol. Soc. Amer. Bull.*, v. 79, pp. 1527-1544.

Trendall, A.F. (1983). Introduction. In: Trendall, A.F. and Blockley (Eds), *Iron-formations: Facts and problems*, Elsevier, Amsterdam, 1-11.

Trendall, A. F. (2002). The significance of iron-formation in the Precambrian stratigraphic record. In Altermann, W., Corcoran, P. L. (eds.) *Precambrian Sedimentary Environments: A*

Modern Approach to Depositional Systems, volume. 33. *International Association of Sedimentologists Special Publication, Blackwell, Oxford, 33–66.*

Trendall, A. F. & Blockley, J. G. (1970). The iron formations of the Precambrian Hamersley Group, Western Australia, with special reference to the associated crocidolite. *Geological Survey of Western Australia Bulletin* 119, 353 p.

Tsikos, H. (1994). The mineralogy and geochemistry of the Voelwater banded ironformation, Northern Cape Province: MSc thesis (unpublished), Rhodes University, Grahamstown.

Tsikos, H. (1999). Petrographic and geochemical constraints on the origin and postdepositional history of the Hotazel iron-manganese deposits, Kalahari Manganese Field, South Africa. Rhodes University PhD thesis.

Tsikos, H., & Moore, J. M. (1997). Petrography and Geochemistry of the Paleoproterozoic Hotazel Iron-Formation, Kalahari Manganese Field, South Africa: Implications for Precambrian Manganese Metallogensis. *Economic Geology* 92, 87-97.

United States Geological Survey. (2015). Mineral Commodity Summaries.

Van Schalkwyk, J.F. & Beukes, N.J. (1986). The Sishen Iron Ore Deposit, Griqualand West. In: Anhaeusse, C.R., Maske, S. (eds) Mineral deposits of Southern Africa. *Geol. Soc. S. Afr., Johannesburg*, pp. 931-956.

Visser, D.J.L. (1944). Stratigraphic features and tectonics of portions of Bechuanaland and Griqualand West. *Trans. geol. Soc. S. Afr.*, 47, 197-254.

Visser, D.J.L. (1958). The geology and mineral deposits of the Griquatown area, Cape Province. Explan. Sheet 175 (Griquatown). *Geol. Surv. S. Afr., Pretoria*, 72pp.

Von Backstrom, J.W. (1963). Septarian concretions in the Lower Griquatown Stage of the Pretoria Series near Kuruman, Cape Province. *Ann. Geol. Surv. S. Afr.*, 2: 78--88.

Walker, R. G. (1976). Facies Models 2. Turbidites and associated coarse clastic deposits. *Geoscience Canada*.

Walker, R. G., & Cant, D. J. (1984). Sandy fluvial systems. In *Facies models* (Vol. 1, pp. 71-89). Geosci. Can., Repr. ser.

Woodward, W. F. & Knoll, A.H. (2009). An iron shuttle for deepwater silica in Late Archean and early Paleoproterozoic iron formation. *GSA Bulletin.*, 121 (1-2): 222–235. doi:

Worden, R. H., & Burley, S. D. (2003). Sandstone diagenesis: the evolution of sand to stone. *Sandstone diagenesis: Recent and ancient*, 4, 3-44.

Wronkiewicz, D. J. & Condie, K. C. (1987). Geochemistry of Archean shales from the Witwatersrand Supergroup, South Africa: Source-area weathering and provenance. *Geochim. Cosmochim. Acta* 51,2401-2416. Wronkiewicz D. J. and provenance. *Geochim. Cosmochim. Acta* 51,2401-2416.

Ye, Y., Khandrika, S. M., & Miller, J. D. (1989). Induction-time measurements at a particle bed. *International Journal of Mineral Processing*, 25(3-4), 221-240.

Ye, Y., & Miller, J. D. (1989). The significance of bubble/particle contact time during collision in the analysis of flotation phenomena. *International Journal of Mineral Processing*, 25(3-4), 199-219.

<https://www.google.com/maps/search/northern+cape+mines/@28.1251844,17.3024226,6z/data=!3m1!4b1>

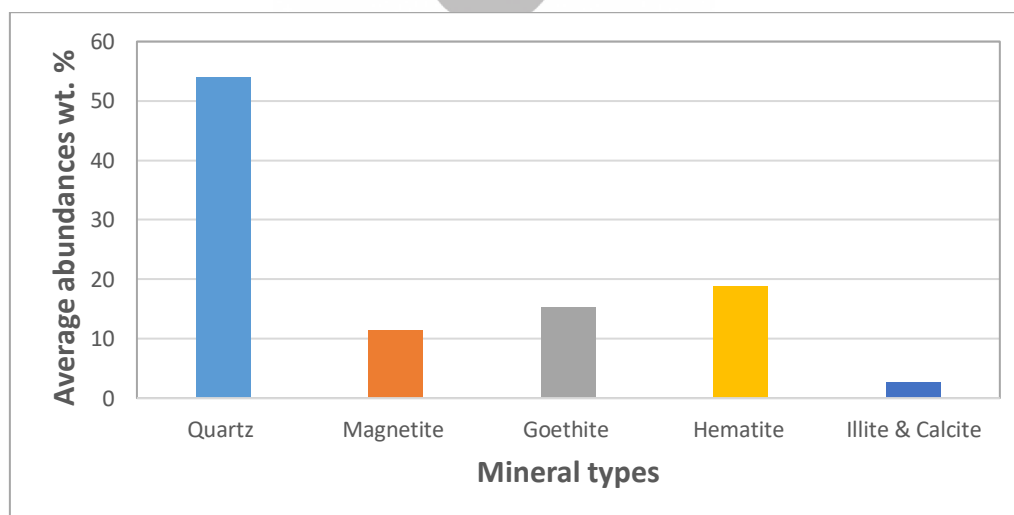


University of Fort Hare
Together in Excellence

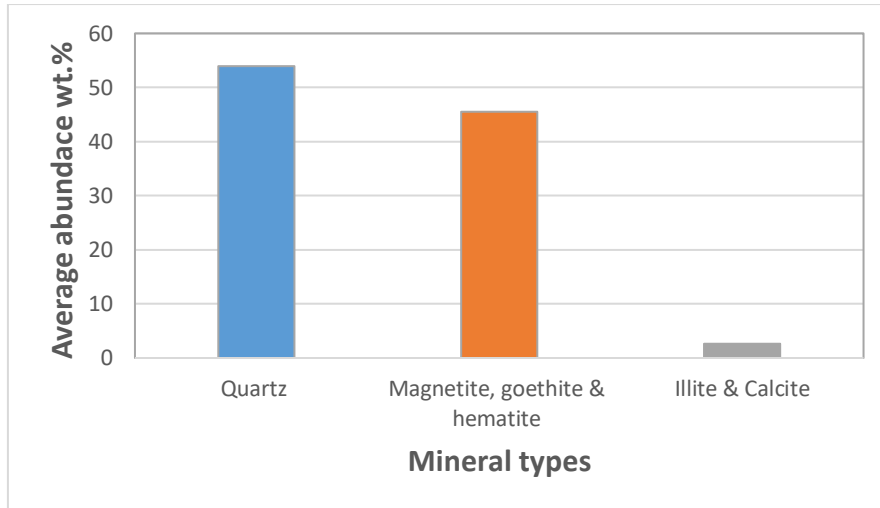
APPENDIX I

A. Approximate mineral abundances based on XRD results

Sample ID	Quartz wt. %	Magnetite wt. %	Goethite wt. %	Hematite wt. %	Illite wt. %	Calcite wt. %
P14	70.54	1.88	20.07	6.47	1.04	0.00
P17	49.80	15.11	22.90	12.19	0.00	0.00
P21	49.24	18.49	20.58	11.69	0.00	0.00
P25	60.09	9.64	14.88	15.39	0.00	0.00
P29	43.14	3.54	7.49	45.83	0.00	0.00
P33	41.83	12.12	18.30	27.75	0.00	0.00
P36	61.85	8.38	10.98	18.80	0.00	0.00
P42	54.20	9.08	16.34	20.37	0.00	0.00
P53	57.41	5.86	9.77	26.96	0.00	0.00
P61	51.42	29.67	11.38	3.30	0.00	4.23
Min	41.83	1.88	7.49	3.30	0.00	0.00
Max	70.54	29.67	22.90	45.83	1.04	4.23
Mean	53.95	11.38	15.27	18.88	0.10	0.42
Standard deviation	8.35	7.74	4.94	11.74	0.31	1.27

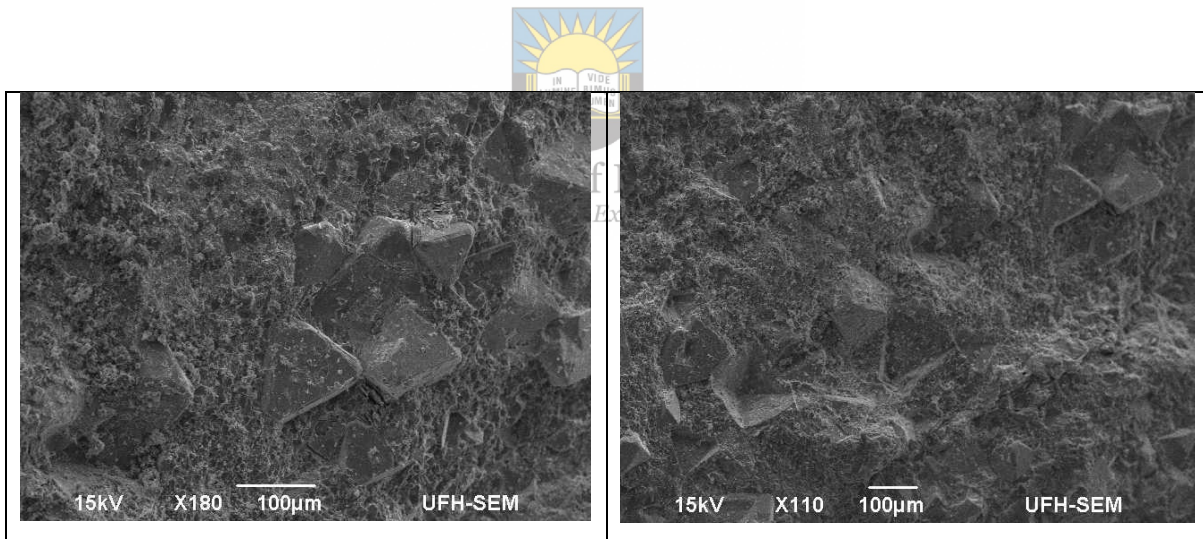


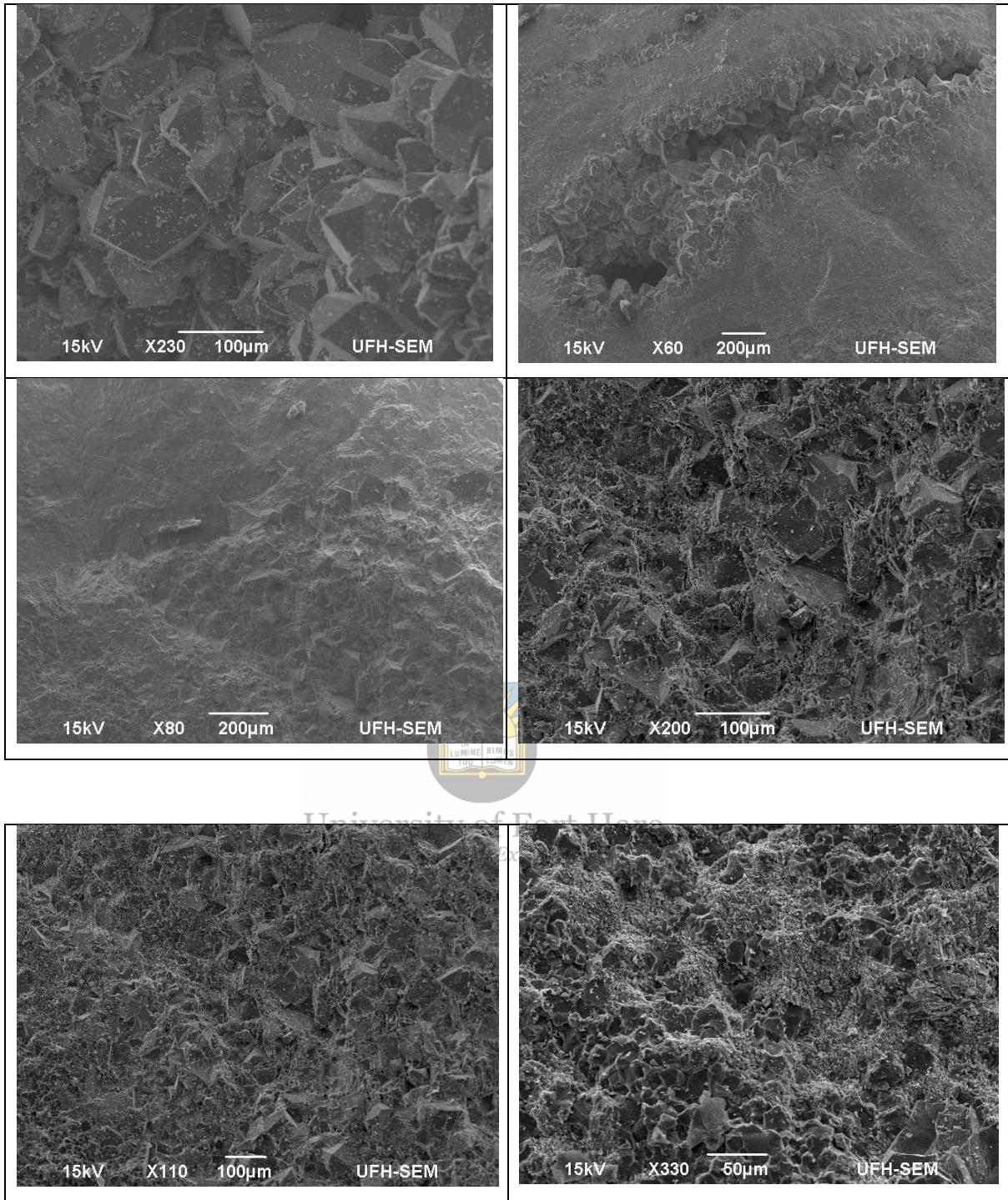
The average abundances of the minerals found from the Prieska BIF courtesy of XRD results.

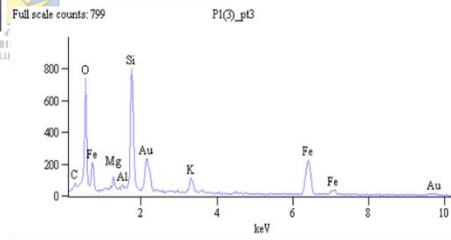
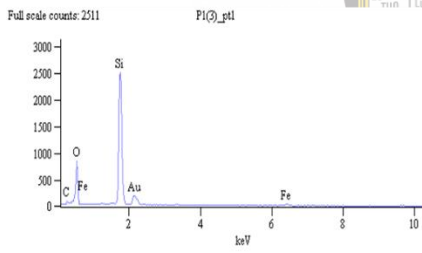
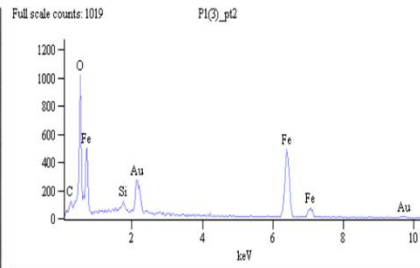
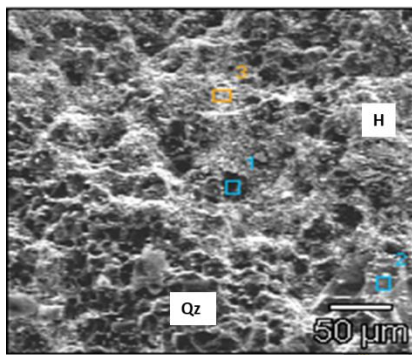
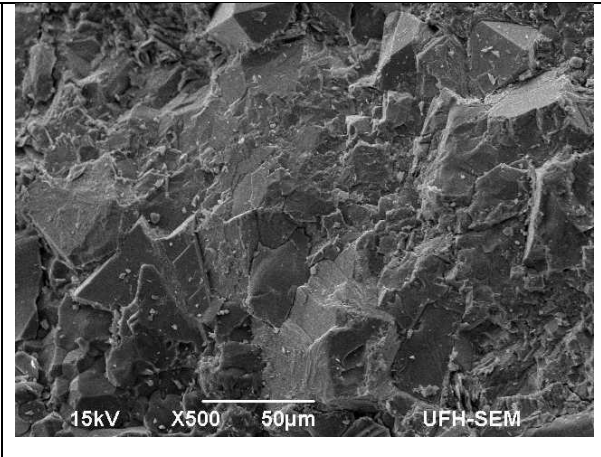
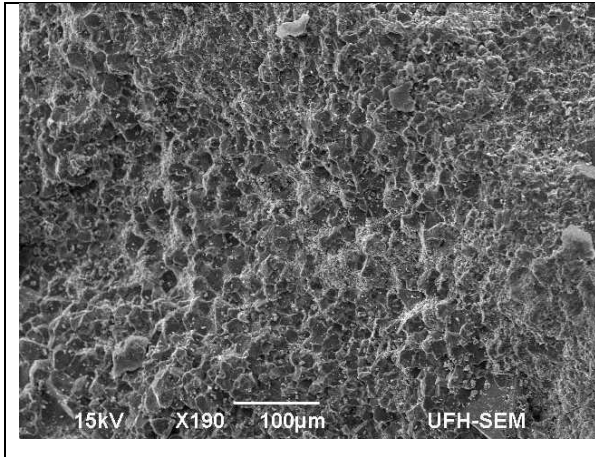


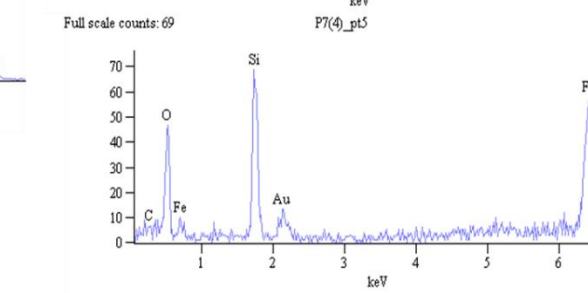
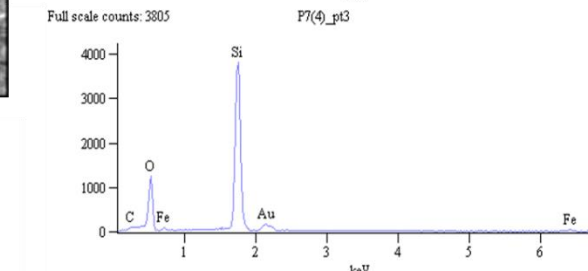
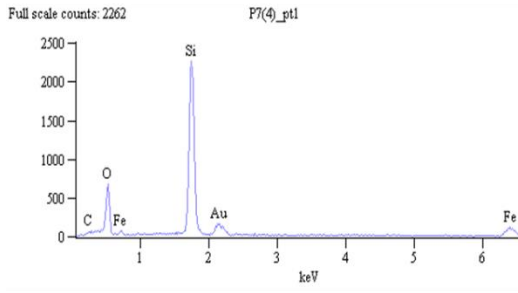
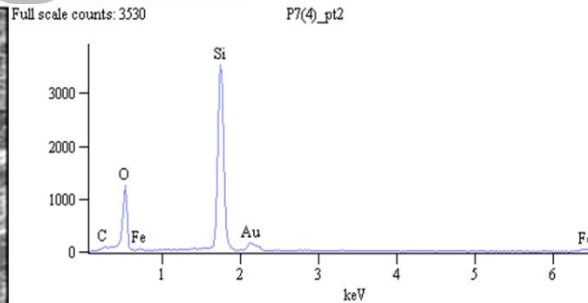
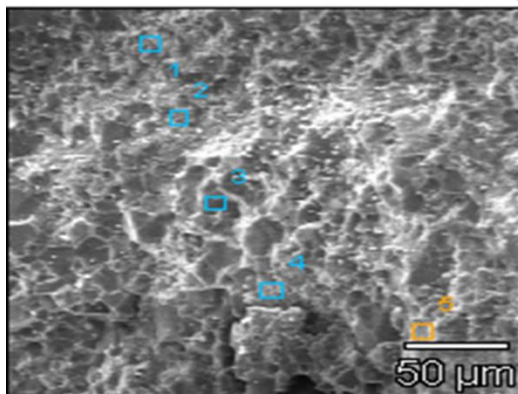
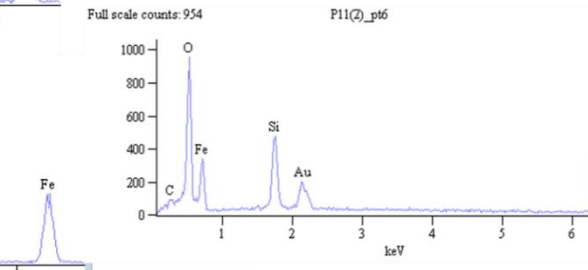
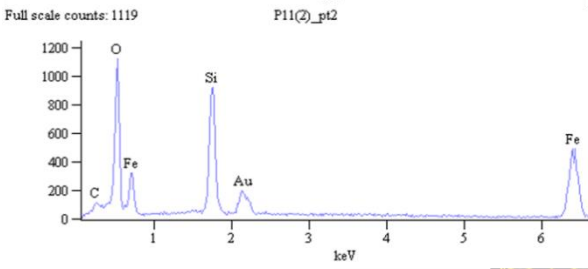
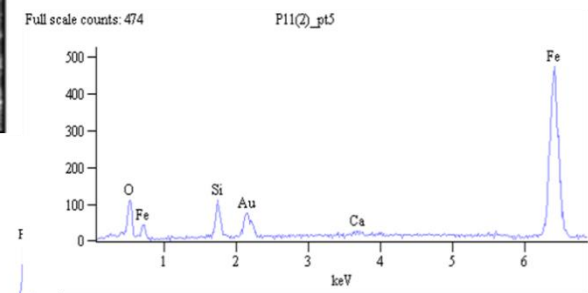
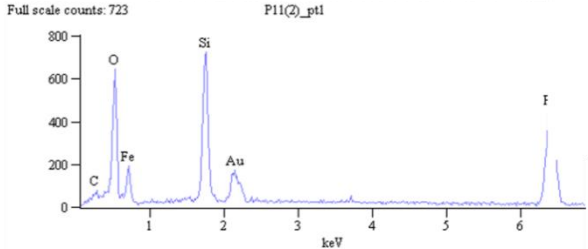
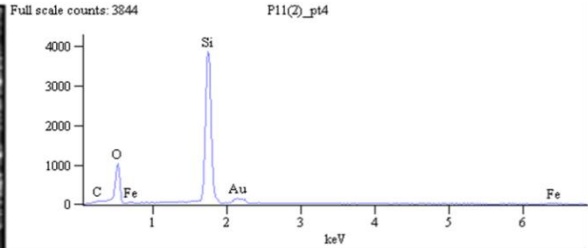
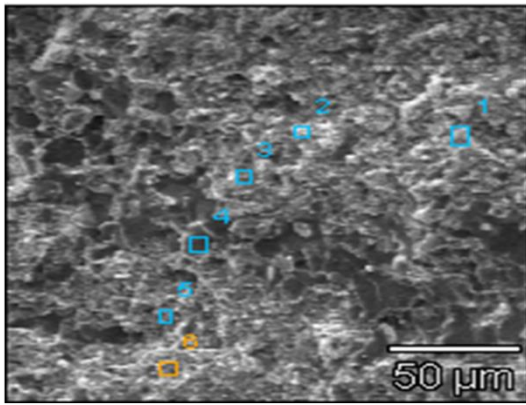
Mineral composition of the Prieska BIF. Comparison between silica. iron. and other mineral phases

B. Photomicrographs of the samples









APPENDIX II

A. Average major element chemical composition of the samples against published average data

Major oxides	This study (Prieska BIF) n = 10	Kuruman BIF N =	Superior type BIF n =
SiO ₂	53.71	51.68	47.30
Al ₂ O ₃	0.16	0.11	1.07
MgO	0.29	5.14	5.68
P ₂ O ₅	0.08	0.09	0.10
Fe ₂ O ₃	44.58	39.79	43.10
K ₂ O	0.09	0.03	0.27
Na ₂ O	0.02	-	0.33
CaO	0.47	5.65	3.03
MnO	0.42	0.30	0.44
TiO ₂	0.01	0.02	0.04

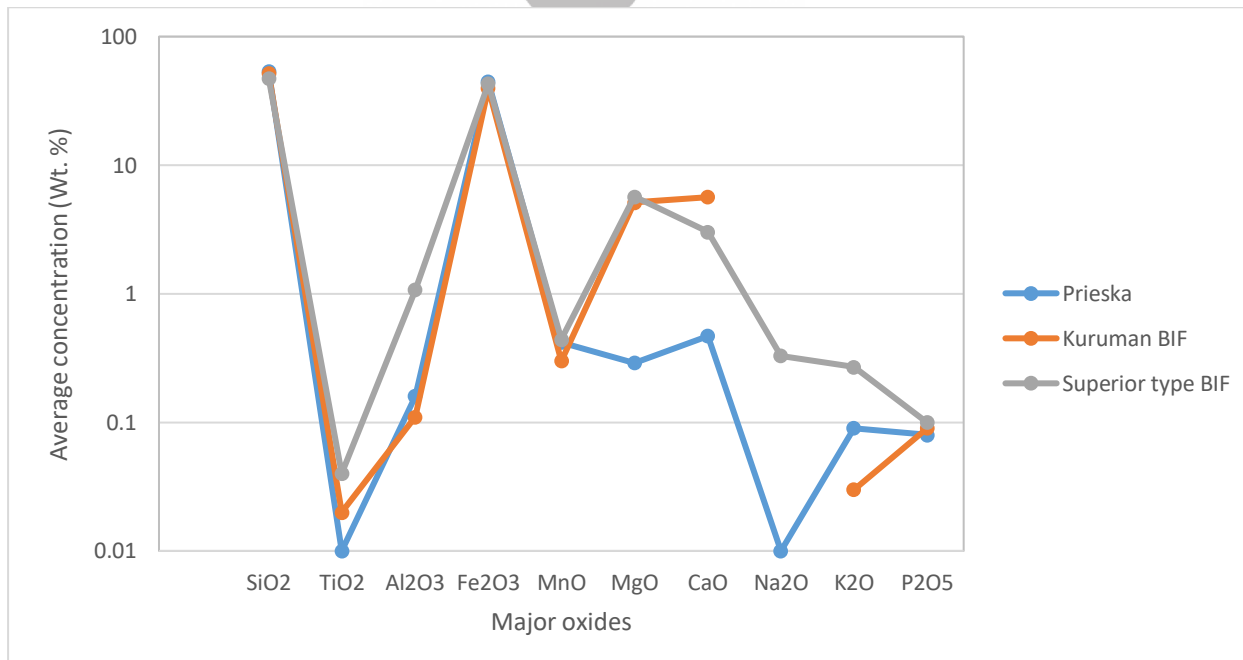


Figure 9. 1: Comparison of major element average compositions between Prieska BIF, Kuruman BIF (after Gutzmer et al. 2008), and Superior Type BIF (after McClung 2006).

B. Average trace element composition of the samples against published data

Trace element (ppm)	Prieska BIF n = 10	Superior type BIF n =	Kuruman BIF n=
Ni	17.5	18	29.3
Pb	2.3	5	2.25
Rb	7.3	36	2.15
Sr	16.9	25	3.45
Y	9.9	25	9.35
V	22.2	26	10
Co	372.4	24	0.16
Ba	139.6	108	7.13
Zn	3.68	-	25.4
Cl	79.5	-	-
S	158.9	-	-
Mo	62.2	-	-
W	437.3	-	-



University of Fort Hare

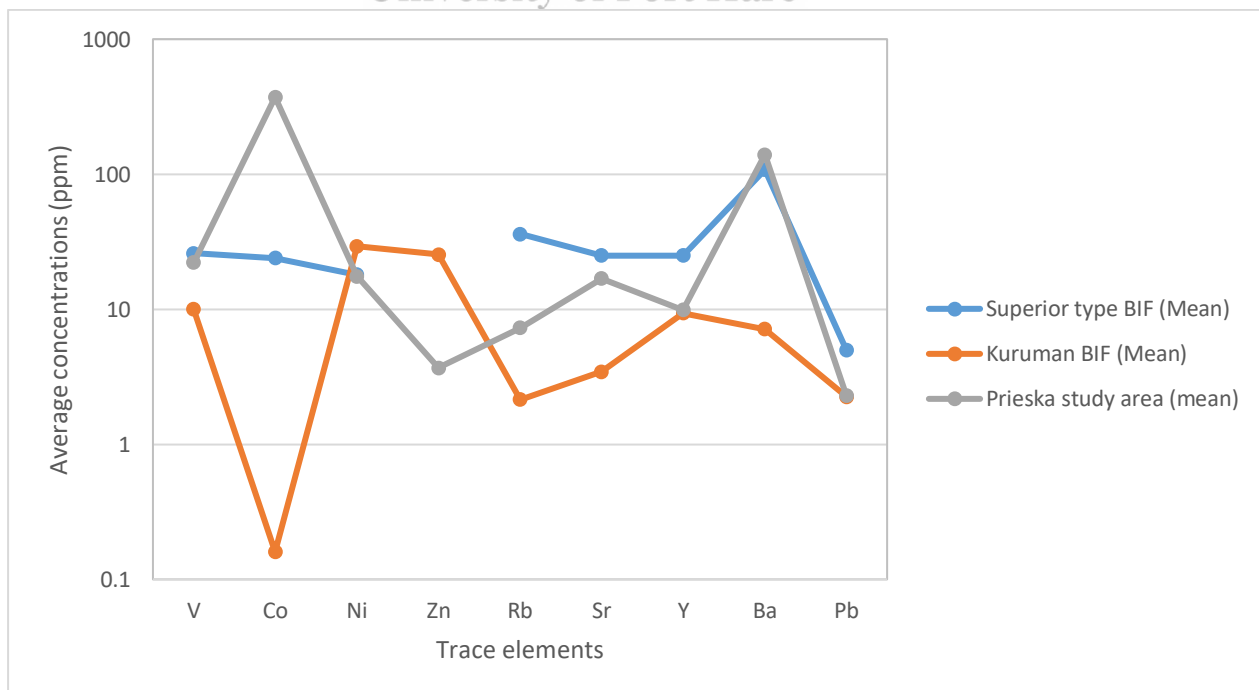
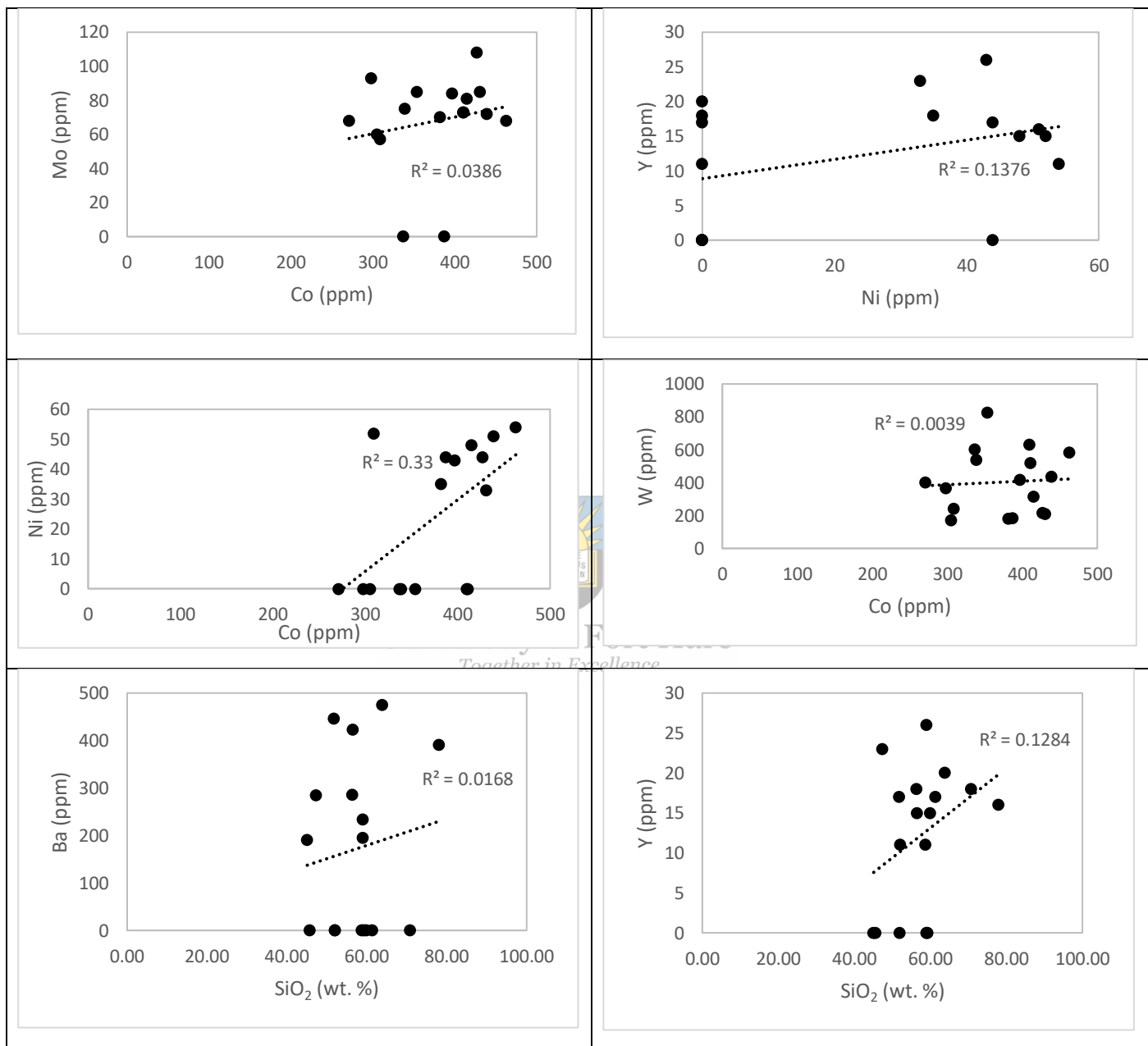
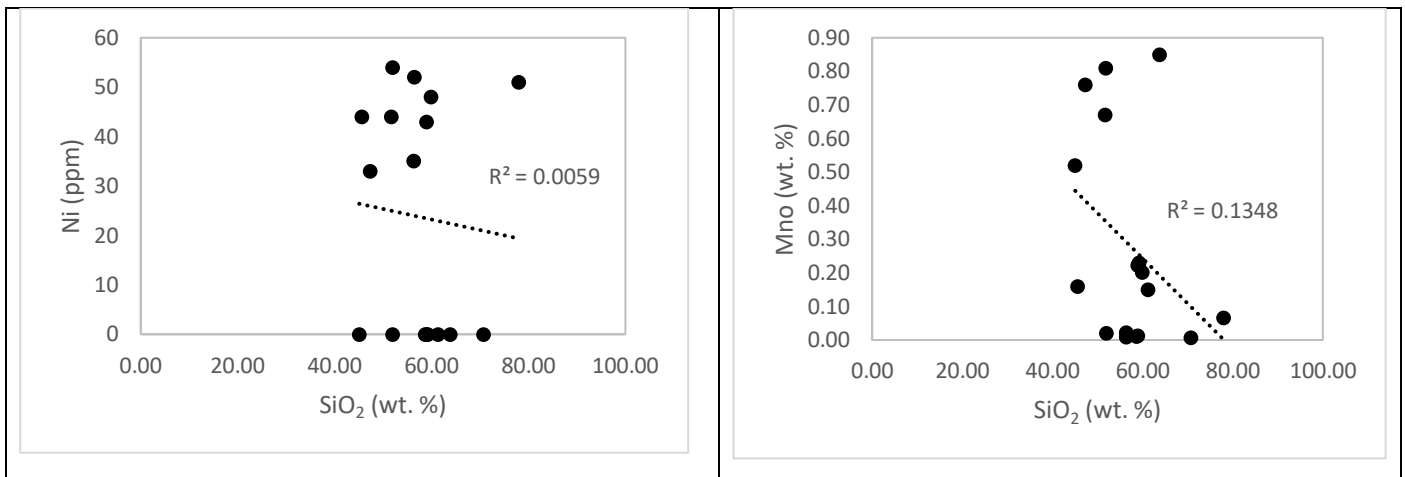


Figure 9. 2: Average trace element variations between Prieska BIF, Kuruman protolith (after Gutzmer et al. 2008), and Superior Type BIF (after McClung, 2006).

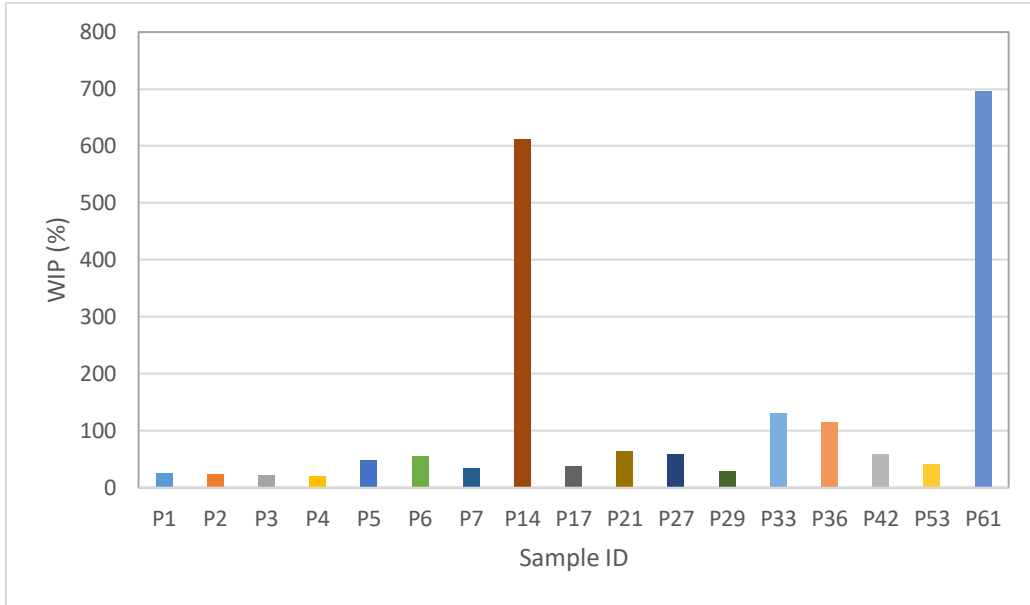
C. Scatter diagrams





D. Weathering Index of Parker (WIP)

Major oxides	WIP
P1	25.84127
P2	24.34921
P3	22.50794
P4	20.06349
P5	47.49206
P6	55.84127
P7	33.61905
P14	612.1651
P17	37.01587
P21	64.69778
P27	58.82857
P29	29.63683
P33	131.3365
P36	114.3079
P42	58.82889
P53	41.82127
P61	695.8768
Min	20.06349
Max	695.8768
Geometric mean	59.94054
Median	47.49206
Standard deviation	197.037



WIP variation plot across the samples.



University of Fort Hare
Together in Excellence